Artificial Materials for High Power Applications.

Author:
Aimée Hopper

Supervisor:
Professor R. Seviour

July 27, 2019

A thesis submitted to the University of Huddersfield in partial fulfilment of the requirements for the degree of Doctor of Philosophy.

Abstract

The aim of this research project was to design an $\varepsilon\mu$ Near Zero (EMNZ) Electromagnetic Artificial Material (EAM), optimised to operate in high power microwave environments. This was achieved by manipulating the geometry of sub-wavelength resonant periodic inclusions – unit cells – to create an effective material whose electromagnetic properties could be manipulated to enable high power operation with minimal losses for x-band operation. The optimised unit cell design comprised of a 500μm thick copper double-circular Complementary Split Ring Resonator (CSRR) arrangement with an operating frequency of 10.03GHz. Simulations were conducted in HFSS to determine the electromagnetic characteristics for an infinite array of the unit cell design, optimised to operate as an effective medium with an operating frequency of around 10GHz, demonstrating an absorption coefficient of below 0.1. This was then expanded to simulations where the optimised unit cell design was loaded into a 36x18mm waveguide (x-band waveguide would have only resulted in three of the unit cells being present in the waveguide, thus not adhering to the Effective Medium condition required for this design to be considered an Artificial Material). A comparison of the electromagnetic properties was conducted in COMSOL, with the intention of COMSOL conducting the simulations into the thermal properties of the unit cell design. The COMSOL results suggest that this new design can withstand incident pulsed powers of up to 10kW (a significant improvement on the previous incident power limit of 1W) thus expanding the capabilities of EMNZ materials for use in high power microwave environments.

Copyright Statement

Acknowledgements

Firstly I would like to thank my supervisor, Professor Rebecca Seviour, for being my mentor and guide over the course of this PhD. Also for her IOP talk on metamaterials and photonics in Lancaster; without that I'm pretty sure I wouldn't be here, completing a PhD in a topic I have found fascinating for many years.

I would also extend my gratitude to Dr Larry Ludeking for his help and guidance with MAGIC.

My thanks also to the EPSRC for funding this project.

My thanks are also extended to Dr Ray Davies of the Photonics Academy of Wales @ Bangor (PAWB). He introduced me to the topic of Metamaterials at the Photonics School at Optic Technium in 2008, sparking my interest in metamaterials and photonics and ultimately resulting in me walking the path I have. His raw enthusiasm and pure passion for physics, optics and the Good of Science is truly inspirational, and for that I will forever be grateful and thankful to his influence on my life.

I couldn't have arrived at this point without my friends and colleagues at the IIAA for their support, friendship and wine over the years we've had together, and for the fond memories they have left with me with along the way. You were there for me when times were rough and helped get me back on my feet. I will always appreciate that and you will always be in my thoughts for getting me through.

A massive thank you also goes out to all of my friends and family; it's amazing how far a soup and a brew, a friendly ear, a creepy fish or a reassuring kick up the rear end can help when times are tough. I will be forever grateful of their support, advice and guidance over, not just my PhD years, but throughout my life endeavours. An extra shout out goes to my CAM friends

and colleagues for their constant positivity and proactive pushing to make sure that giving up was never an option, even when gardening alternatives called to me. From the bottom of my heart, Thank you.

Specifically I want to give my thanks to everyone who read through my thesis and helped me put this document together in a way that is readable; Norman Turner, Sam Rowe, Gemma Hopper, my parents Marie and Alan Hopper and my mother-in-law Lesley Howard. I will be forever grateful for the time and effort you have put into checking this over for me!

Finally, my biggest shout out goes to my husband Adam. He has been my rock throughout this journey, my motivator to keep on going and my shoulder to cry on when times were hard. He has been my teacher and mentor for all things computery, giving me guidance and support from Python to Bash and beyond, my rubber duck for how to best progress with the project and with life, and has constantly given me drive to finish this PhD. We've had some pretty hard times along this road, too many, but we've gotten through them together. And together we shall continue on, heading straight into whatever lies ahead of us. Because whatever comes along, we can beat it.

Seeing such a strange laboratory in a place like this...
You're filled with determination.[1]

[1] *Undertale*, Toby Fox, 2015, Video Game

We may stumble and fall but shall rise again; it should be enough if we did not run away from the battle.

Mahatma Gandhi

Contents

List of Figures

List of Tables

Chapter 1

Introduction

The focus of this research was to design an optimised Electromagnetic Artificial Material (EAM) which operates in a high power environment, enabling energy exchange between a low energy electron beam and an incident x-band (microwave) RF wave. This is because, when designing a device for RF generation/particle acceleration, a number of key concerns become apparent very early on:

- How much power can the device produce/withstand?
- How much will the device cost to manufacture/maintain?
- How large will the device be?

One of the most recent developments in high power RF technologies are Solid State Transistors. These are easy to produce, can be manufactured to operate at a range of frequencies, can be swapped out of the system if a transistor breaks (reducing down-time), and the maximum achievable output power is predominantly limited by the number of transistors in the system. They do have their draw-backs though: they are very large, heavy, expensive systems which require constant maintenance. Figure 1.1a) shows

the ESRF RF generator system at Grenoble, showing the system at well over 2m tall while producing an output power of 75kW [1] in x-band operation. Figure 1.1b) however shows an x-band traveling wave tube (TWT), designed early on in the second world war [2]. This device is around a metre along the longest dimension and can produce powers of 100kW for around a fifth of the price of the solid state device for the same output power. The main drawback of a TWT type of system is the wavelength dependence on the size of the device, a drawback that can be mitigated by the use of EAMs.

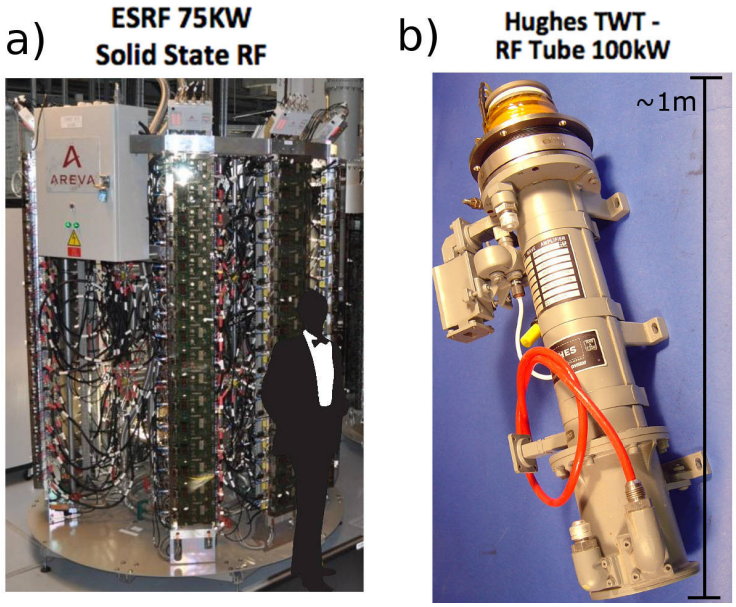

Figure 1.1: a) Image showing the ESRF solid state RF generator system at Grenoble [1]. b) Traveling Waveguide [2]. Both operate in x-band.

EAMs are materials made from periodic sub-wavelength unit cells, designed to have desirable electromagnetic properties as required by the user. These properties can be, for example, increasing the amount of energy exchange between an incident RF wave and a charged particle beam, achieved by manipulating the dispersion relation of the wave or adjusting the phase of the incident wave, reducing the sizes of equipment such as waveguides, or

simply by enabling a charged particle beam and incident wave interaction at a frequency not previously possible for a particular system.

Over the last 20 years there has been a growing interest in one type of EAM – metamaterials – to achieve this. Their ability to produce novel and interesting interactions with EM waves – such as negative refraction – has opened the doors to many new areas of physics and engineering [3]. These materials rely on a largely resonant design to produce a large negative refractive index. This unfortunately removes their ability to withstand high power operating environments due to the storage of energy in the resonant structures, creating substantial losses and limiting their usability in many environments where high levels of energy exchange are required.

This study focuses on the development of $\varepsilon\mu$ Near Zero (EMNZ) materials, structures which use the same resonant design as metamaterials but operate in a frequency region away from negative refraction. This significantly reduces the lossy behaviour whilst still allowing sufficient electromagnetic property manipulation [4]. By loading this type of material into a system like a TWT, the benefits of light weight, high power operation and cheaper costs may be retained whilst removing the wavelength dependence of the size of the device and increasing the high power capabilities of a system [5].

Chapter 2 focuses on the origins and development of EAMs, giving a more comprehensive discussion on the motivations behind this project and introducing the concept of a split ring resonator design for use as an EAM, along with highlighting some of the benefits and short fallings of the field. Chapter 2.5 discusses the current advances and limitations on existing high power applications of EAMs, highlighting the need to development of high power compatible devices. Chapter 3 discusses important theoretical considerations required for the full understanding of the EAM system, discussing Ef-

fective Media theory and Bloch-Floquet Theory. This section also compares the SRR design to a CSRR design. Chapter 4 covers the initial experimental work conducted on a pre-existing metamaterial design, demonstrating the usability of the theories discussed in Chapter 3 and showing that materials can indeed be designed with desirable qualities (in this case demonstrating Double Negative constitutive parameters in x-band).

The simulation software used (HFSS and COMSOL) are then discussed in Chapter 5, highlighting the advantages and limitations of the code used in each case. A comparison between the experimental setup discussed in 3 and a simulation of the same setup is then discussed in Section 5.2, demonstrating the usability of the software. The simulations run to determine the optimal unit cell design are then discussed in Chapter 5, where discussions regarding the meshing, the computational optimisations and the unit cell optimisations are made. The optimised design is studied in more detail in Chapter 6 where the thermal handling capabilities are also addressed. Chapter 7 discusses initial and potential fabrication methods, showing how these designs can be constructed easily and cheaply from easily accessible materials. Chapter 8 concludes this work, highlighting the successes of this research and discussing future work possibilities.

Chapter 2

Background

In the early 1860s J. C. Maxwell combined the workings of Faraday, Gauss and Ampére to determine a complete set of equations which describe the properties of electric and magnetic fields. For vacuum these are:

$$\nabla \cdot \mathbf{E} = \frac{\rho}{\varepsilon_0}, \tag{2.1}$$

$$\nabla \cdot \mathbf{B} = 0, \tag{2.2}$$

$$\nabla \times \mathbf{E} = -\frac{\partial \mathbf{B}}{\partial t}, \tag{2.3}$$

$$\nabla \times \mathbf{B} = \mu_0 \left(\mathbf{J} + \varepsilon_0 \frac{\partial \mathbf{E}}{\partial t} \right), \tag{2.4}$$

where $\mathbf{E}$ is the electric field, $\mathbf{B}$ is the magnetic induction, ρ is the charge density of the material and ε_0 and μ_0 are the permittivity and permeability of free space, equal to (in SI units) 8.854×10^{-12} m^{-3} kg^{-1} s^4 A^2 and $4\pi \times 10^7$ H/m respectively (a full discussion of the derivation of these equations can be found in [6]).

These equations are scale-invariant, meaning that phenomena predicted to occur at millimetre lengths are also predicted for lengths of kilometres when

scaled by the relevant factor (as λ increases by factor of a million, f decreases by a factor of a million due to the equation $c = f\lambda$, where c is the speed of light in vacuum). By modelling a system with macroscopically averaged electric and magnetic fields the **E** and **B** fields can be re-expressed using the macroscopic electric displacement **D** and the magnetic field **H**, given by:

$$\begin{aligned} \mathbf{D} &= \varepsilon_0 \mathbf{E} + \left(\mathbf{P} - \sum_{\beta} \frac{\partial Q'_{\beta}}{\partial x_{\beta}} + ... \right), \\ \mathbf{H} &= \frac{1}{\mu_0} \mathbf{B} - (\mathbf{M} + ...), \end{aligned} \tag{2.5}$$

where **P**, **M** and Q_{β} represent the macroscopically averaged electric dipole (electric polarisation), magnetic dipole (magnetic polarisation) and electric quadrupole [6].

By assuming small numbers of point charges (i.e. charged particles) and weak incident fields, the material can be regarded as linear (see Appendix A.1 for discussion) and the higher order terms in **D** and **H** can be disregarded (they represent the moment densities when the material experiences a significant external magnetic field, such as those found in ferro-electrics, ferro-magnets or other highly crystalline structures). **P** can then be written as $\varepsilon_0 \chi_e \mathbf{E}$ where χ_e is the electric susceptibility, and **M** can be written as $\chi_m \mathbf{H}$ where χ_m is the magnetic susceptibility. These susceptibilities represent the ability of a material to respond to an incident EM field, enabling Eqns. 2.5 to be re-written as:

$$\mathbf{D} = \bar{\varepsilon} \mathbf{E}, \tag{2.6}$$

$$\mathbf{B} = \bar{\mu} \mathbf{H}, \tag{2.7}$$

where $\bar{\varepsilon}$ represents the electric (permittivity) tensor and $\bar{\mu}'$ represents the inverse magnetic (permeability) tensor. If the material is isotropic as well as linear, then $\bar{\varepsilon}$ and $\bar{\mu}$ are diagonal with all elements equal, so **D** and **H** become:

$$\mathbf{D} = \varepsilon_0 \varepsilon_r \mathbf{E} = \varepsilon \mathbf{E}, \tag{2.8}$$

$$\mathbf{H} = \frac{1}{\mu_0 \mu_r} \mathbf{B} = \frac{1}{\mu} \mathbf{B}. \tag{2.9}$$

ε and μ are known as the constitutive parameters, with ε_r and μ_r representing the complex relative permittivity and permeability respectively. Equations. 2.6 and 2.7 are known as the constitutive relations.

By assuming that the wave is monochromatic and plane, travelling in the **r** direction, both **E** and **B** are proportional to $e^{i(\mathbf{k}\cdot\mathbf{r}-\omega t)}$, the Helmholtz Equation – relating the wavevector to the frequency of the wave – can be determined from Maxwell's equation as:

$$(-k^2 + \mu\varepsilon\omega^2) \begin{Bmatrix} \mathbf{E} \\ \mathbf{B} \end{Bmatrix} = 0. \tag{2.10}$$

The non trivial solution to this equation is:

$$(-k^2 + \mu\varepsilon\omega^2) = 0, \tag{2.11}$$

giving the relationship between the wavenumber k and the frequency ω as:

$$k = \omega\sqrt{\varepsilon\mu} = \omega\sqrt{\varepsilon_r\mu_r}\sqrt{\varepsilon_0\mu_0} = \frac{\omega n}{c} = nk_0, \tag{2.12}$$

where c is the speed of light in vacuum and k_0 is the free space wavenumber. This is the dispersion relation for the material, demonstrating that all of the electromagnetic physics of the material is encapsulated into ε and μ. In this equation n represents the refractive index of the material and is defined as:

$$n^2 = \varepsilon_r \mu_r = \left(\frac{c}{v}\right)^2. \tag{2.13}$$

As ε_r and μ_r are complex values n is also complex, where $n = n' - jn''$ where:

$$n' = \frac{1}{2n''}(\varepsilon'\mu'' + \varepsilon''\mu'), \tag{2.14}$$

is the real part of n and:

$$n'' = + \left\{ \frac{1}{2}(\varepsilon''\mu'' - \varepsilon'\mu') + \frac{1}{2}((\varepsilon'^2 + \varepsilon''^2) \cdot (\mu'^2 + \mu''^2))^{1/2} \right\}^{1/2}, \tag{2.15}$$

is the imaginary part of n [4], also known as the extinction coefficient. This is related to the absorption coefficient of a material by the equation:

$$AbsCoeff = \frac{4\pi f n''}{c}, \tag{2.16}$$

where f is the frequency of the incident wave and c is the speed of light in vacuum.

The normalised absorption (the absorptivity) in an idealised system can be determined by:

$$A(\omega) = NormP_{lost} = 1 - |S_{11}|^2 - |S_{21}|^2, \tag{2.17}$$

where S_{11} is related to the reflection coefficient of the material and S_{21} is related to the transmission coefficient of the material, as used by Smith in his 2002 paper as A_2 [7] and is discussed in Appendix A.3.

Figure 2.1 shows the plot of ε vs μ for all possible types of isotropic electromagnetic materials, as taken from page 3 in [8]. Most materials lie in the first quadrant of the plot, where $\mu = \mu_0$ and $\varepsilon > \varepsilon_0$. For some materials $\varepsilon < 0$ and $\mu > 0$ (for example in non-magnetic wires at low electron oscillation frequencies (electric plasmas)), as in quadrant 2. For others, $\varepsilon > 0$ and $\mu < 0$ (i.e. magnetic plasmas, such as anti-ferromagnetic materials like MnF_2 and FeF_2 [9, 10]) as in quadrant 4. In both of these cases, the refractive index $n = \sqrt{\varepsilon\mu}$ is imaginary, therefore only evanescent wave propagation can occur.

In quadrant 3 ε and μ are both negative. Contained within this quadrant is the point $-\varepsilon_0, -\mu_0$, otherwise called "anti-air" or "anti-vacuum" (refractive index $n = 1$) which produces a perfect lens [11]. The line where $\varepsilon = \mu$ represents impedance matching materials; materials with impedances perfectly matched to that of air, removing reflections at the air-material interface [12]. Materials with μ near zero (MNZ) or ε near zero (ENZ) are also interesting media, as is the point where $\varepsilon = \mu = 0$, called the nihility point [13]. Materials containing these properties were not discovered until the early 2000s (see Chapter 2.2).

For an electromagnetic wave the electric field strength $\mathbf{E}$, magnetic field strength $\mathbf{H}$ and wave vector $\mathbf{k}$ are related by:

$$\begin{aligned} \mathbf{k} \times \mathbf{E} &= \omega\mu\mathbf{H}, \\ \mathbf{k} \times \mathbf{H} &= -\omega\varepsilon\mathbf{E}. \end{aligned} \tag{2.18}$$

One can see here that when ε and μ are simultaneously positive, $\mathbf{k}, \mathbf{E}$ and

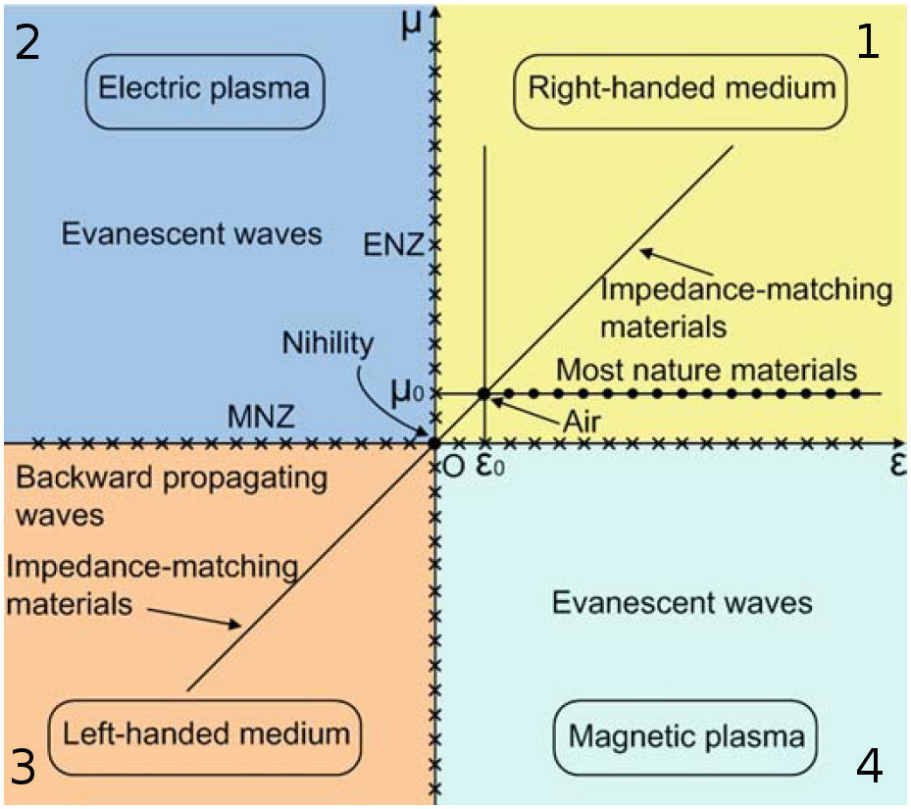

Figure 2.1: $\varepsilon - \mu$ plot showing all the different possible configurations for isotropic materials [8].

H form a right handed triplet; these are conventionally called Right Handed Materials (RHM). Conversely when ε and μ are simultaneously negative then $\mathbf{k}, \mathbf{E}$ and $\mathbf{H}$ form a left handed triplet, called Left Handed Materials (LHM). The energy flow per unit area per unit time, otherwise known as the Poynting Vector $\mathbf{S}$, is written as:

$$\mathbf{S} = \sqrt{\frac{\varepsilon}{\mu}|E_0|^2}\hat{\mathbf{n}}, \tag{2.19}$$

where $\hat{\mathbf{n}}$ is the unit normal vector of the plane of propagation of the wave. $\mathbf{S}$ *always* forms a right handed system with $\mathbf{E}$ and $\mathbf{H}$, shown by the relationship:

$$\mathbf{S} = \mathbf{E} \times \mathbf{H}. \tag{2.20}$$

When ε and μ are simultaneously positive, $\mathbf{S}$ and $\mathbf{k}$ are parallel to one another and the material behaves as conventionally observed. However, when ε and μ are simultaneously negative, $\mathbf{S}$ and $\mathbf{k}$ are anti-parallel to each other. As $\mathbf{k}$ points in the same direction as the phase velocity of the wave, it is apparent that the direction of energy propagation and phase velocity point in opposite directions. This has some very profound effects, resulting in phenomena such as dispersion manipulation [14], backwards wave propagation [15], inverse Cherenkov acceleration [16] and reverse Doppler effects [17]. Researchers such as Rayleigh [18], Bose [19], Lamb [20], Schuster [21] and Kock [22] had discussed ideas of negative ε and μ, even discussing backwards wave propagation, yet non did a thorough study of the behaviour of double negative materials. These effects were first discussed in significant detail by Veselago in the mid 1960s [23].

2.1 Veselago's Vision

Veselago discusses in [23] how the different signs for ε and μ would manifest themselves physically. He talks about a boundary between two materials, with a monochromatic wave incident through the first, right handed material. This is shown in Fig. 2.2. This wave can behave in one of three ways; it can be reflected off the boundary, it can refract through the boundary or it could do a combination of the two.

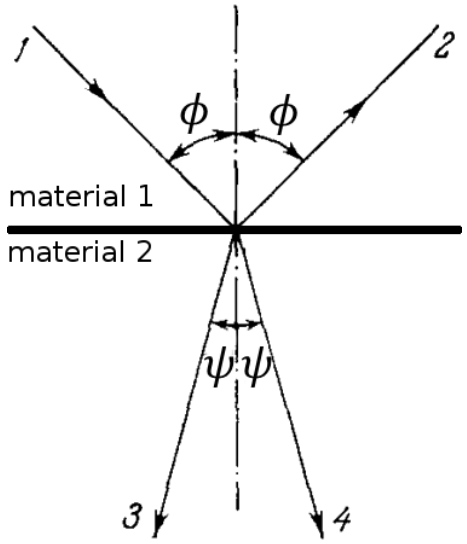

Figure 2.2: 1 - incident ray, 2 - reflected ray, 3 - refracted ray if the second medium is left handed, 4 - refracted ray if the second medium is right handed. ϕ (top) and ψ (bottom) represent the incident/reflected and refracted rays respectively [23].

If both materials have the same handedness, then the incident wave (ray 1) will either reflect of refract through the second material along ray paths 2 or 4. This is well known as conventional materials (both right handed), behave in this manner. However, if the materials have different handedness, then Veselago predicts that the incident wave will refract through the second

medium along ray path 3.

The refractive index of a material was defined in Eqn. 2.13 as $n^2 = \varepsilon_r \mu_r$, and Snell's law states that $n_1 sin\theta_1 = n_2 sin\theta_2$ (for $|n_1| > |n_2|$). Combining these equations for the two materials results in:

$$\frac{n_1}{n_2} = \frac{sin\theta_2}{sin\theta_1} = \pm\sqrt{\frac{\varepsilon_1 \mu_1}{\varepsilon_2 \mu_2}}. \tag{2.21}$$

Conventionally only the positive root was accepted as the negative root was deemed unphysical, however Veselago re-expressed Snell's Law to include the negative root:

$$\frac{n_1}{n_2} = \frac{sin\theta_2}{sin\theta_1} = \frac{p_1}{p_2}\left|\sqrt{\frac{\varepsilon_1 \mu_1}{\varepsilon_2 \mu_2}}\right|, \tag{2.22}$$

where p_1 and p_2 represent whether the material is Right Handed ($p_i = +1$) or Left Handed ($p_i = -1$) and ε_i and μ_i are the permittivity and permeability of material 1 and 2 respectively. This study was regarded as interesting but not relevant to the academic community at the time as there were no physical realisation of RHMs and so the study was no longer pursued.

2.2 Pendry's Proof

In the late 1990s Pendry and his team produced two papers; one demonstrating a possible realisation of a negative ε [24], (experimentally verified in [25]), and another showing a realisation of negative μ [26]. The first describes an array of thin wires arranged periodically to produce a reduced plasma frequency response, enabling plasmons to exist in the near infra-red to GHz range. Prior to this, the plasmons had only been observed in the visible or ultra-violet frequencies due to dissipative effects establishing dom-

inant Drude behaviour at lower frequencies[1]. The second paper describes a periodic array of resonant non-magnetic "microstructures" which exhibited behaviour in the microwave region as if they had an effective permeability. These were dubbed Split Ring Resonators (SRRs). At the resonant frequency, induced currents set up in the split rings cause the storage of energy from the incident wave, creating an opposing magnetic field, while the capacitive regions act to store the electric field. The greater the capacitance, the greater the induced current.

The equations for the resonant frequency for the split rings was determined as:

$$\omega_0^2 = \frac{3lc_0^2}{\pi ln\frac{2c}{d}r^3} = 7.1 \times 10^{21}, \tag{2.23}$$

where l is the distance between adjacent planes of rings, c_0 is the speed of light in vacuum, c is the width of each ring (assumed the same for both rings), d is the spacing between ring edges and r is the inner radius.

This equation assumes:

$$r >> c, \qquad r >> d, \tag{2.24}$$

$$l < r, \tag{2.25}$$

$$ln\frac{c}{d} >> \pi \tag{2.26}$$

A complete solution for the exact electromagnetic behaviour of a split ring resonator system is difficult due to the complexity of the inductances produced by the structures. Exact solutions for simple, idealised cases are possible but consist of complex expressions – for example, circular coaxial

[1] Drude behaviour is essentially where the electrons can be modelled as classical objects which "bounce" between their adjacent atoms, similar to a ball in a pinball machine.

filaments in a circuit require the use of elliptical integrals. Look-up tables can be used to determine the solutions to these expressions, however exemplary accuracy must be made when taking measurements of the individual terms for the equations for the calculated values for the inductance to have even a moderate precision. To determine the approximate resonant frequency for a split ring resonator with magnetic resonance applications, Hardy and Whitehead [27] determined:

$$\omega_0 = \frac{c}{r_0}\sqrt{\frac{t}{\pi w}} \tag{2.27}$$

where t is the split-width in the SRR, w is the ring width, c is the speed of light in vacuum and r_0 is the internal ring radius. These dimensions can be seen in Fig. 2.3.

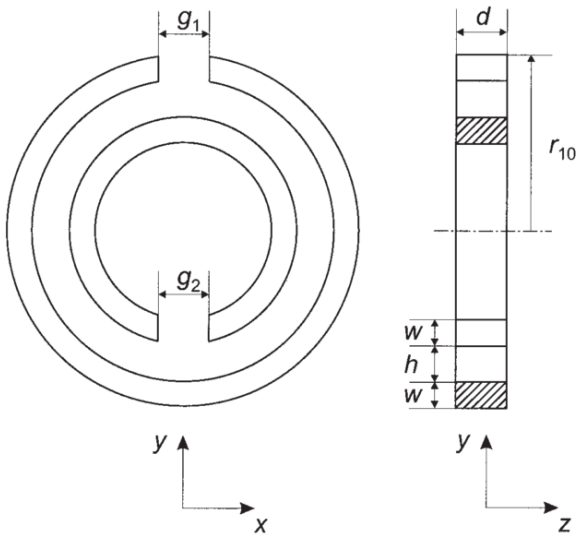

Figure 2.3: Hardy and Whitehead's determination of a resonant frequency for a SRR [27].

This enables the material engineer to easily determine an approximate op-

erating frequency for the SRR structure.

A more complete analysis for determining the analytic resonant frequency of the split rings were later produced by Shamonin *et. al.* [28, 29]. This models the SRR arrangement as a collection of distributed circuits – similar to those used in transmission-line theory – connected via two gap capacitances. The equivalent circuit model for the SRRs can be seen in Fig.2.4.

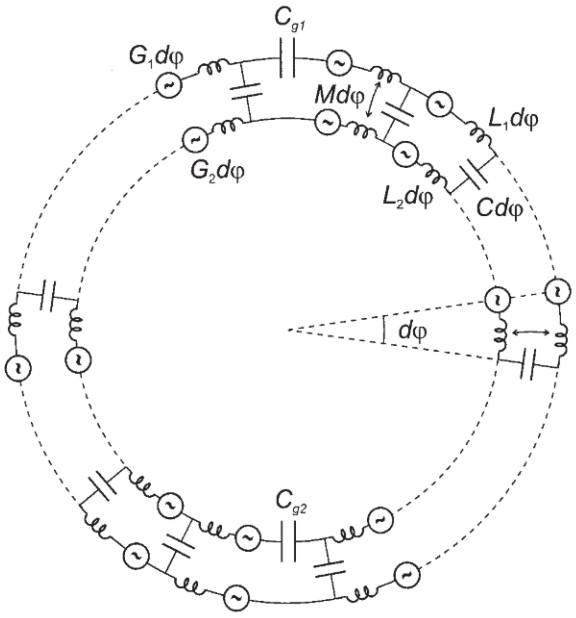

Figure 2.4: Inductances and Capacitances for SRR arrangement [29].

By assuming a lossless system the resonant frequencies of the system can be determined using the characteristic equation:

$$\kappa sin\kappa\pi \cdot [4\pi\kappa^2 - \pi\gamma_1\gamma_2 - 2\gamma_1\nu_2 - 2\gamma_2\nu_1] + cos\kappa\pi \cdot [\gamma_1\gamma_2(\nu_1 + \nu_2) - 2\pi\kappa^2(\gamma_1 + \gamma_2)] = -2\gamma_1\gamma_2(\nu_1\nu_2)^{1/2}, \quad (2.28)$$

where:

$$\kappa^2 = \omega^2 L_{eq} C, \qquad \gamma_1 = C/C_{g1}, \qquad \gamma_2 = C/C_g 2,$$
$$\nu_1 = [(L_1 - L_{12})/D]^2,$$
$$\nu_2 = [(L_2 - L_{12})/D]^2, \qquad L_{eq} = L_1 + L_2 - 2L_{12},$$
$$D = (L_1 L_2 - L_{12}^2)^{1/2} \tag{2.29}$$

The values for the inductances and capacitances can be determined using look-up tables given in [30, 31].

Due to the periodic nature of these designs, and because these structures were designed with unit cell dimensions significantly less than the wavelength of the incident radiation, the structure can be modelled as an Effective Media (see Chapter 3.1) where the wave propagation through the material can be modelled using Bloch-Floquet Theory (see Chapter 3.2).

2.3 Smith's Success

In the early 2000s, Smith *et. al.* [32] consolidated Pendry's work with wires and SRRs to produce a simultaneously negative material. Their numerical and experimental results are shown in Fig. 2.5. These results show that transmission occurs in the 5GHz frequency region, akin to the region where ε and μ have the same, negative sign. This is not a direct measure of negative refraction.

Negative refraction was directly demonstrated experimentally in 2001 by Shelby *et. al.* [33]. In their experiment they move to using the square split-ring arrangement, as shown in Fig. 2.6a), and use a Drude-Lorentz type model (based on the Nicolson-Ross [34] and Weir [35] extraction technique) to determine the effective ε and μ:

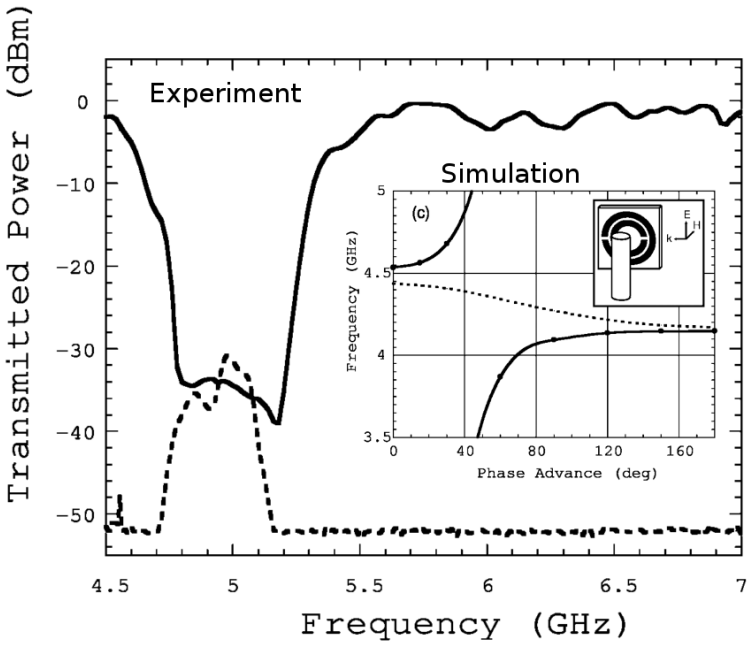

Figure 2.5: Plot showing the numerical results for the transmission of a wave over an SRR array with $a = 8mm$. Inset: Dispersion plot for the SRR and wire array [32].

$$\mu_r = \frac{\mu(\omega)}{\mu_0} = 1 - \frac{\omega_{mp}^2 - \omega_R^2}{\omega^2 - \omega_{mp}^2 + i\gamma\omega}, \tag{2.30}$$

$$\varepsilon_r = \frac{\varepsilon(\omega)}{\varepsilon_0} = 1 - \frac{\omega_{ep}^2 - \omega_{ER}^2}{\omega^2 - \omega_{ep}^2 + i\gamma\omega}, \tag{2.31}$$

where ω_{mp} is the magnetic plasma frequency, ω_R is the magnetic resonance frequency, ω_{ep} is the electric plasma frequency for the wires, ω_{ER} is the electric resonant frequency for the wires and γ is a damping factor. From this, they were able to determine a region where the index of refraction was -2.7 ± 0.1 at 10.5GHz. This can be seen in Fig. 2.6b).

Further discussion on this extraction method can be found in Appendix A.2.

Parazzoli *et. al.* conducted a similar experiment in 2003 with a modified structure (operating frequency at 12.6GHz) [36], and Houck *et. al.* also experimentally verified a negative index of refraction, also in 2003 [37]. This proved that a material which demonstrated a negative refractive index was realisable, completing the $\varepsilon - \mu$ graph and paving the way for new physics and technologies to be explored.

These materials were given the name "Metamaterials", a term coined by Rodger Walser in the early 2000s [38], and were defined in [39] as:

> macroscopic composites having a man-made, three-dimensional, periodic cellular architecture designed to produce an optimized combination, not available in nature, of two or more responses to specific excitation.

The idea of negative refraction has since been elaborated on further [40, 41] and used in phenomena from planar super-lensing [42, 43] to invisibility cloaking [44–47]. By coupling the unit cells in certain ways, properties like Electromagnetically Induced Transparency (EIT) [48–51], Fano-resonance

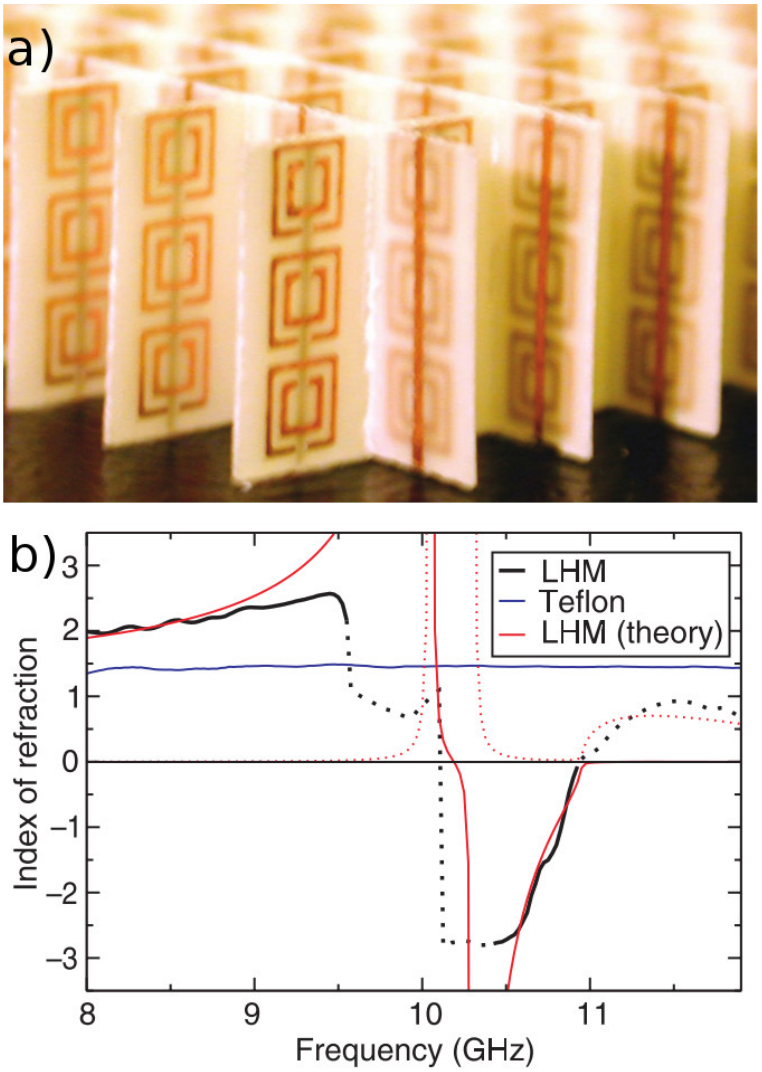

Figure 2.6: a)Image of the structure designed by Shelby *et. al.*. b) Plot of the refractive index of the material over a range of frequencies, showing a negative refraction of 2.7 ± 0.1 at 10.5GHz [33].

[52–55], and chirality [56–58] can be achieved; phenomena not known to occur in the original Pendry designs of metamaterials. However, for successful operation, it is imperative that these structures do not suffer from high losses or thermal breakdown.

A mention should also be made at this point, that there still remains some discrepancy in the literature as to what constitutes a "Metamaterial". Many literature sources treat any artificial material created with a specific, engineered EM behaviour as a Metamaterial, thus including structures with single negative or even dual positive constitutive parameters. This thesis uses the definition that a Metamaterial and a Left-Handed Material are synonymous i.e. both have a negative refractive index. Metamaterials are therefore a subset of Artificial Materials in this context.

2.4 Electromagnetic Artificial Materials

Metamaterials were not the first type of material to demonstrate interesting properties which do not exist naturally. Instead, they may be seen as successors of artificial dielectrics, pioneered by Bose [19], Lindman [59], Kock [60], Cohn [61], and Rotman [62] and typically existed as inclusions of spheres, discs or rods [62–64].

Artificial Dielectrics, or Electromagnetic Artificial Materials (EAMs), became a staple component for modern technology around the 1940s, with pioneering work produced by W. Kock of Bell Laboratories, in response to the then-recently developed radar microwave technologies, as lightweight structures and components were required for various forms of microwave delivery devices during the second world war. These structures used arrays of metallic strips to create an effective "metallic lens" by using the fact that the phase velocity of a wave is increased in waveguide. This essentially created

an artificial dielectric lens whose properties were determined by the spacing of the strips and the frequency of operation, producing low-loss, lightweight and cost effective lenses for use with radio-waves [22, 60].

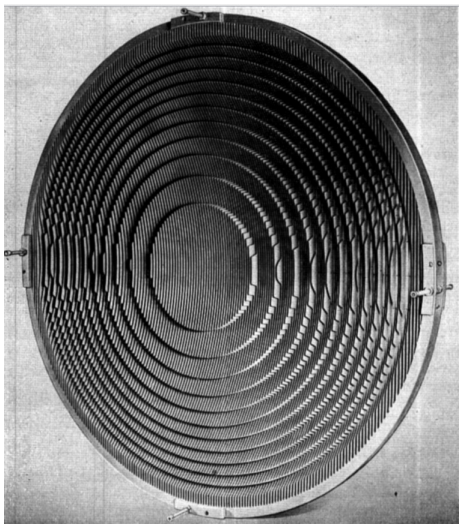

Figure 2.7: Kock's Metallic Lens [60].

The requirement of smaller, lighter microwave devices did not simply stop at the end of the second world war; the improvements in technologies were constantly requiring yet further reductions in the size of these devices and higher power operation. Vacuum Electronic Devices (VEDs) such as traveling-wave tubes, klystrons, magnetrons and backwards-wave oscillators currently hold the top-spot for high power capability, yet have the disadvantages of a large physical footprint (as the size of the VED is dependant on the wavelength of radiation being used), being heavy, being very limited in operational use and being expensive to manufacture and maintain. It is here that EAMs can help as their interesting, novel EM behaviour can be exploited to further reduce the size and cost of microwave devices [65].

2.5 High Power AMs

In 2002 N. Garcia *et. al.* [66] produced a comprehensive study questioning the validity of the experimental data produced by Smith *et. al.*, concluding that the introduction of metals into the unit cell arrangement would result in "unavoidable problems at microwave frequencies because of losses concomitant with dispersion that swamp any characterization of a net negative real refractive index".

P. Markus *et. al.* [67] however produced a numerical study analysing the origins of losses in Left Handed Materials (LHMs), concluding that very good transmission is possible in the region of negative refractive index in spite of the dispersion in μ and n. This study supposed that the high losses seen in the experiments could be due to the absorption of the dielectric board of the SRRs were located on, with the metallic components of the LH structures not contributing a significant source of loss.

J. Dimmock used Pendry and O'Brien's 2002 study [68] to continue this work into losses of LHMs [4]. By using the equations and results from the Pendry and O Brien's paper, Dimmock was able to deduce the material loss factor per wavelength, L_m, (for silver) as:

$$L_m \equiv \frac{4.8}{\lambda}. \tag{2.32}$$

The plot of this is seen in Fig 2.8, where L_a is the loss factor of the material per wavelength in air and is equal to:

$$L_a = 4\pi n'', \tag{2.33}$$

where n'' is the imaginary part of the refractive index as described in Eqn. 2.15.

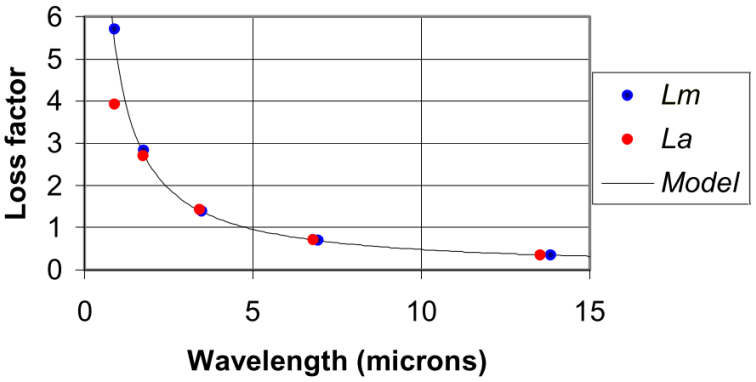

Figure 2.8: Plot showing the predicted material loss factor per wavelength as given in [4], based on the data given in [68]. L_m represents the material loss per wavelength in silver, and L_a is the loss factor of the material per wavelength in air.

Dimmock concludes that the losses in LHMs in the infrared and viable spectra are likely to be large, a result reiterated by Raynolds *et. al.* [69]. His results however suggests that the losses caused by the metal additions to the unit cells only produce a very small addition to the total losses experienced by the artificial structure for microwaves, therefore suggesting that the experimental setup or some other cause was to blame for the losses observed in experiment.

2.5.1 High Power Experiments

To test the ability of LHMs to withstand high power (required for operation in a VED) R.Seviour *et. al.* conducted a number of numerical simulations to determine whether the dielectric substrate was indeed the source of the losses [5, 70]. Through the use of HFSS and ePhysics (now ANSYS) they were able to demonstrate that the region of simultaneously negative ε_r and μ_r resulted in a peak in the absorption coefficient of the system. This is shown in Fig. 2.9.

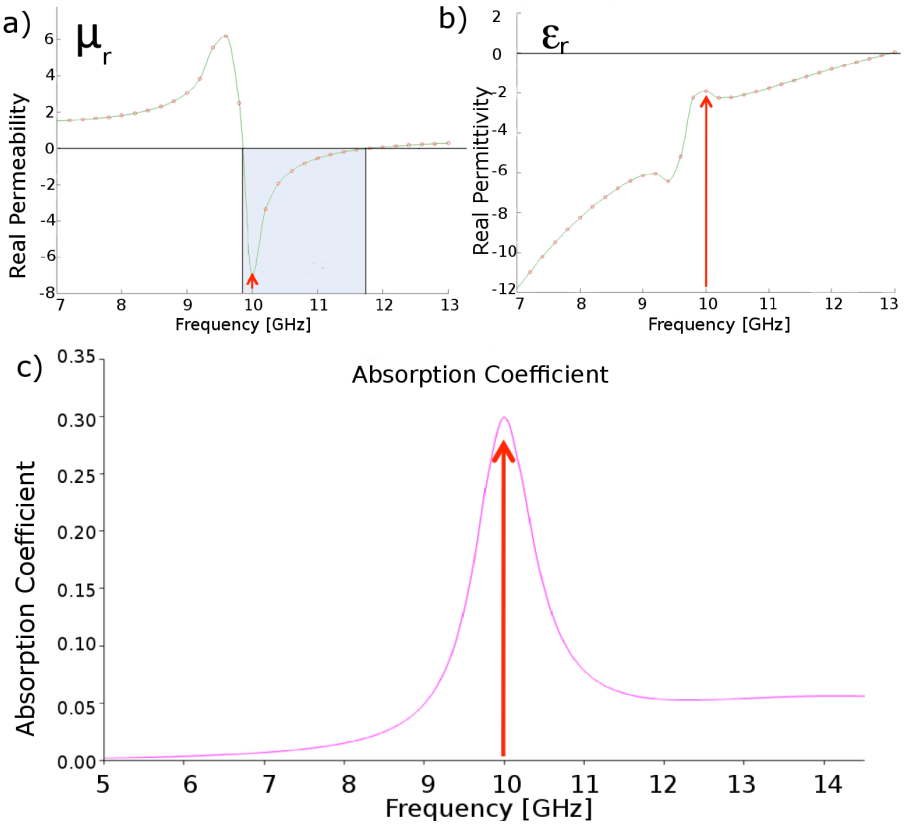

Figure 2.9: Plots of a) Re(ε_r), b) Re(μ_r) and c) absorption coefficient for the structure. These show that the region of simultaneously double negative response coincides with the peak in absorption [70].

The simulations determined the loss density and temperature rise of a bulk material made up of 2mm unit cell SRRs loaded into an x-band waveguide. The material was simulated to be exposed to 1W of RF at 10GHz, and suggested that temperatures exceeding the combustion point of the FR4 (600°C) would be reached after merely 15 seconds of exposure. This is shown in Fig. 2.10, indicating the loss density and the temperature rise for a unit cell located at the centre of the waveguide at the top of an array of 4 unit cells.

To verify these simulations, an experiment was made of the simulation setup,

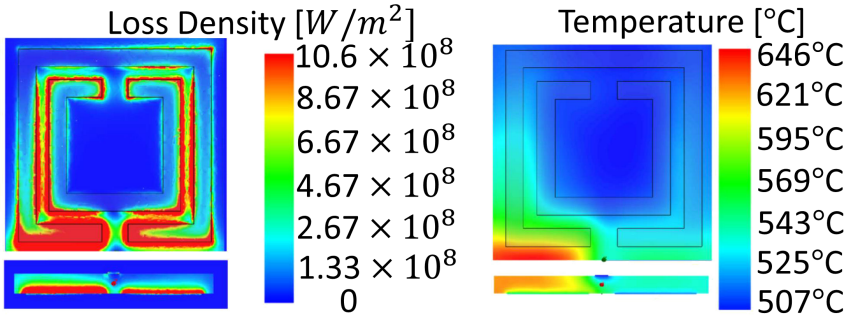

Figure 2.10: Left: Loss Density Map (HFSS). Right: Thermal Profile as produced in ePhysics (now ANSYS) produced using the Loss Density Map. Regions exceeding 600°C are predicted to occur in the bottom left of the unit cell [5].

and the material was exposed to a 10GHz 1W wave. After 15 seconds, the material began to combust, demonstrating temperatures exceeding the 600°C had occurred. This can be seen in Fig. 2.11, validating the simulation technique used.

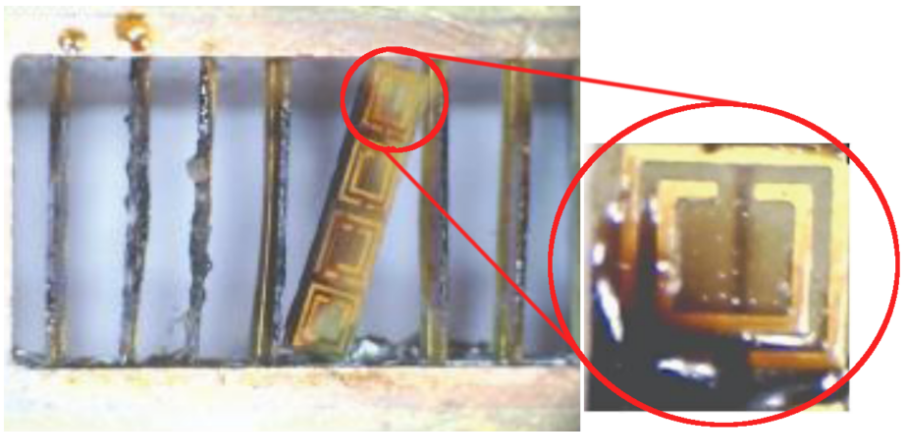

Figure 2.11: Image showing that after a 15 second exposure to a 1W 10GHz wave, the metamaterial suffered thermal breakdown.

Many other types of simulations were also conducted, for example varying the geometry of the unit cell and varying the substrate to name a couple.

However, all simulations concluded that operation in the region of negative refractive index resulted in very high predicted absorption coefficients which result in catastrophic failure of the structure either through deformation or melting/combustion. This demonstrates that LHM are not suitable for operation in high power VED environments.

Numerous studies have been conducted with varying degrees of success in order to identify methods to reduce these losses, for example by geometric tailoring [71], manipulating the coupling relationship between the electric and magnetic resonances [72, 73], using superconducting elements [74, 75] or operating away from resonance [76–78]. Many of these solutions actually move the operating frequency away from regions of negative refraction and use the LHM unit cell design in a frequency region where the bulk material is considered an ENZ/MNZ/EMNZ material. Active metamaterials have also been investigated [79–83], though more work needs to be done on these as the complex behaviour created when the gain materials are embedded into the metamaterial structure creates significant difficulties in creating a stable active metamaterial design [81, 84–87].

All that being said, there is considerable work being conducted into utilising these high absorption abilities for beneficial uses [12, 88–90]. Applications of these types of structures range from photovoltaics [91, 92], EM "pollution" absorbers [93, 94] or as a "perfect optical black hole" [95].

Chapter 3

Theory

In order to successfully design a high power electromagnetic artificial material, a number of concepts and derivations needed to be understood. The most important of these was being able to determine ε and μ from physically measurable quantities, thus ensuring that a material behaves in the desired manner. Typically, these measurable quantities are the scattering parameters (S-parameters) which are measures of the amount of the incident wave reflected from or transmitted through a material.

The most conventional method of doing this is by inserting the material (the Device Under Testing – DUT) between two ports (input - port 1, and output - port 2) in a Network. Exposing the DUT to an incident wave then enables the user to measure the amount of the wave from port 1 that is reflected back to port 1 (S_{11}), or transmitted through to port 2 (S_{21}), therefore allowing the electromagnetic properties of a material to be determined. A schematic of this can be seen in Fig. 3.1.

The actual values for the S-parameters are complex (as the incident wave is complex) so are expressed as $S_{ij} = |S_{ij}|e^{i\theta_{ij}}$ where $|S_{ij}|$ represents the amplitude or magnitude of the S-parameter, and θ_{ij} represents the phase.

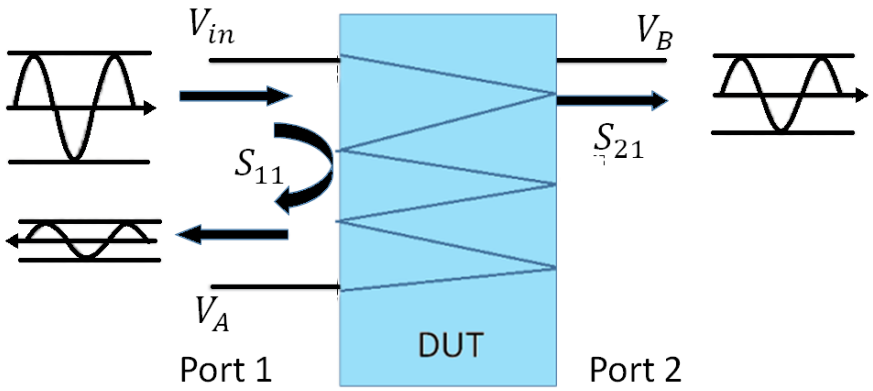

Figure 3.1: Schematic showing how the S_{11} and S_{21} parameters are related to the amount of wave being reflected off (S_{11}) or transmitted though (S_{21}) the DUT.

3.1 Effective Media Theory

Section 3 introduced the concept of averaging the electromagnetic properties of a microscopic system, enabling the system to be modelled using the macroscopic Maxwell's Equations. This leads to the question of where the limit between a microscopic and a macroscopic system lies; can an EM medium with physically realisable substructure be created which also ensures that the incident wave remains unaware of the fine detail - an "Effective Medium"?

Effective Media Theory (EMT) and the electromagnetic response of inclusions in a host medium have been a topic of interest since the time of Maxwell and Rayleigh [96–105]. For a composite material, EMT outlines the limitations of the size of a sub-wavelength periodic unit cell relative to the incident wave, resulting in the material appearing to the wave as a single, homogeneous bulk of material.

Here, a composite material is any material made up of two or more types of material, generally with one of the materials forming the main bulk of

the material, called the "host", with the other materials existing as "substructures" or "inclusions" within the host. These can exist in two forms; a cermet – substructures are complete isolated from one another, as shown in Fig 3.2a) – or an aggregate – substructures touch on one or more edges, as see in Fig 3.2b) [106].

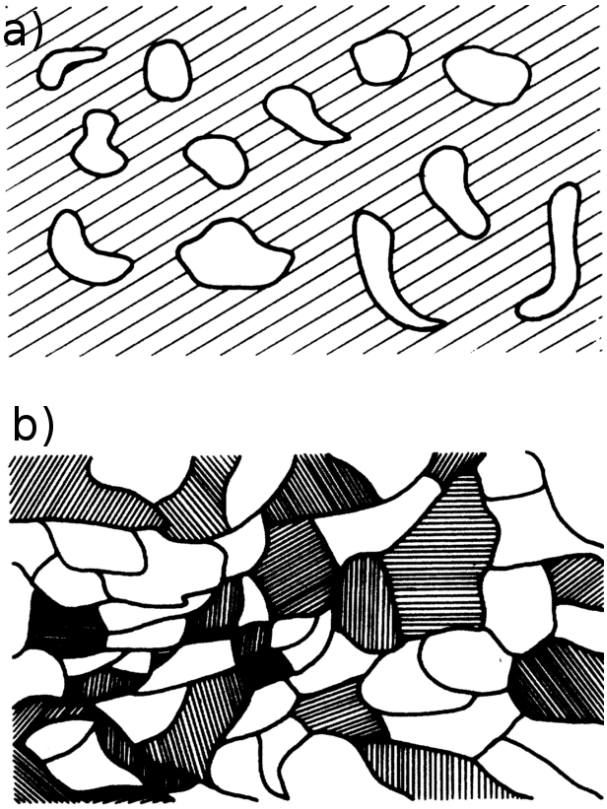

Figure 3.2: a) Cermet Topology (unit cells isolated from one another). b) Aggregate Topology (unit cells share boundaries) [106].

In a two-material cermet composite (typically a vacuum or air "host" and dielectric or metal "inclusion"), an incident wave will encounter five different conditions: $|k_1|a \ll 1$, $|k_2|a \ll 1$, $|k|a \ll 1$, $|k_1|b \ll 1$ and $|k|b \ll 1$. Here, k_i is the wavenumber in each material (1 is the host and 2 is the inclusion, where $k_i = \frac{2\pi\sqrt{\varepsilon_i \mu_i}}{\lambda_0}$), k is the average wavenumber for the bulk structure, a is the radius of the material inclusion and b is the largest length characterising

the unit cell spacing (i.e. the largest primitive lattice vector in a crystal). When the first condition is satisfied ($|k_1|a \ll 1$) the system is said to adhere to the long-wavelength limit. If all five conditions are satisfied, then the system is in the infinite wavelength (or quasi-static) limit.

Most theories of wave propagation through cermets are variations or extensions of the Maxwell-Garnett [107] or the Bruggeman [108] methods, with the Bruggeman theory becoming known as EMT. Both methods are based on Mie scattering (the scattering of EM waves within the material lattice) and on the the electric-dipole moment induced in the unit cell. When the fraction of the unit cell volume (Fr) occupied by the inclusion is suitably small (for example $Fr = 0.3$ [109]), the two theories become indistinguishable and the effective complex dielectric constant is determined as [110]:

$$\frac{\varepsilon_r - \varepsilon_1}{\varepsilon_r + 2\varepsilon_1} = Fr\frac{\varepsilon_2 - \varepsilon_1}{\varepsilon_2 + 2\varepsilon_1}, \tag{3.1}$$

where ε_1 and ε_2 represent the permittivities of the host and inclusion respectively.

Stroud and Pan [111] extended the Bruggeman theory to include the magnetic-dipole terms (important at long wavelengths), which, in the long wavelength limit, simplify to [112]:

$$\frac{\mu_r - \mu_1}{\mu_r + \mu_1} = Fr\frac{\mu_2 - \mu_1}{\mu_2 + mu_1}. \tag{3.2}$$

Discussions on the details of the different types of effective media approximations can be found in [104, 106, 113–115].

By enforcing that a medium is truly effective (i.e. the scattering within the bulk material tends to zero so $k_1 a \ll 1$ [109]), Wu *et. al.* showed that the long wavelength limit is:

$$\lambda_0 \equiv \frac{2\pi}{k_0} > 3.5a, \tag{3.3}$$

for magnetodielectric composites [112]. Wavelengths shorter than this produces scattering within the material, removing the purely refractive behaviour required for the material to be considered effective.

The long wavelength theory has been applied to various types of metamaterial [116–118]. The general "rule of thumb" technique is to use unit cell sizes of $\lambda/10$, though structures with sizes $\lambda/6$ [33] were sufficient to demonstrate negative refraction, and sizes of $\lambda/4$ have also been justified [119].

This defines the maximum size that the unit cell can have to be considered an effective medium. However, an effective medium cannot really be considered a medium at all if there are only a few unit cells in the arrangement. To determine the complete EM behaviour of the unit cells it is useful to model an infinite sheet of them, a technique easily achievable by the use of Bloch-Floquet theory.

3.2 Bloch-Floquet Theory

Bloch Floquet Theory describes how waves propagate in an infinite, linear, periodic medium. The theorem is stated in [120] as:

> For a given mode of propagation at a given steady-state frequency, the fields at one cross section differ from those one period away only by a complex constant.

This means that if one knows the properties of the initial wave, the periodicity of the system and the number of unit cells which need to be traversed to reach a particular point in the material, the electromagnetic properties at the point can be determined. This can be expressed as:

$$\Phi(r+p) = e^{\zeta r} F(r) = \Phi(r) \tag{3.4}$$

where Φ is the periodic function in the r direction, p is the periodicity of the material, ζ is the propagation constant of the wave and may be real, imaginary or complex, $F(r)$ is the general solution of the wave at position r. This shows that for any periodic system, knowing the general solution to a single periodic unit cell provides the solutions for all given periodic units, given ζ. For a more complete derivation of this theory see Appendix A.5.

Using the concepts described so far, one can design an effective medium for any desired operating frequency and model an infinite plane of the material to determine the effective values of ε and μ. However, the actual value of the operating frequency, and thus the required sizes of the unit cells still needs addressing.

3.3 SRR vs CSRR

So far only the Split Ring Resonator (SRR) and wire arrangement suggested by Pendry *et. al.* have been discussed. However, as time has progressed, researchers began investigating many other designs, for example the Complementary Split Ring Resonator (CSRR).

Figure 3.3 shows both an SRR and a CSRR [121], along with their equivalent circuit models. In this image $C_0 = 2\pi r_0 C_{pul}$ represents the total capacitance between the rings, C_{pul} is the capacitance between the rings per unit length, $f_0 = (L_s C_s)^{-1/2}/2\pi$ represents the resonant frequency of the SRR where $C_s = C_0/4$ is the series capacitance of the lower and upper halves of the SRR and L_s represents the inductance and can be approximated by that of a single ring with an averaged radius r_0 and width c.

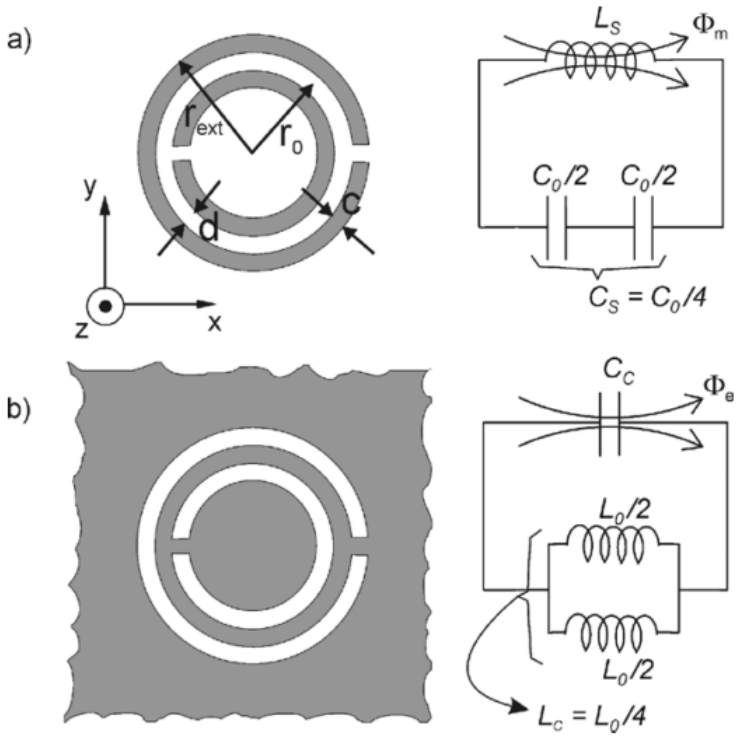

Figure 3.3: Images showing the difference between an SRR and a CSRR, alongside their corresponding equivalent circuit diagram. Grey zones represent metal regions [121].

This demonstrates that, where the SRR can be considered a resonant magnetic dipole which is excited by an axial magnetic field, an equivalent CSRR can be considered as a resonant electric dipole (with the same resonant frequency as the SRR) which is excited by an axial electric field. Therefore both designs can be used to create very similar electromagnetic responses. This enables the use of the formulas suggested by Pendry when creating a CSRR design.

Chapter 4

Experimental Work

To determine whether the Nicolson-Ross-Weir extraction technique is appropriate for obtaining ε_r and μ_r, an existing metamaterial design was experimentally characterised.

When deriving the extraction technique relating the scattering parameters to the constitutive parameters (specifically the technique developed by Nicolson, Ross [34] and Weir [35], and also Smith [32], as discussed in Chapter 2.3) certain assumptions were made which need to be addressed. The first assumption, that the technique requires an infinite sheet of unit cells, will never be possible to completely fulfil, however by filling the cross-section of the waveguide with the unit cells the edge effects caused by the finite size of the material can be reduced. The second assumption, that the incident wave is plane, is addressed by the use of a parallel plate waveguide system and ensuring that the structure is located a suitable distance away from the wave source ensures that the incident wave is plane at the structures surface. The final assumption, that the material is passive, is easily achievable as the structure is isolated from external energy sources.

The metamaterial used was a 2.4mm unit cell double square-SRR design,

lithographically etched onto an FR4 substrate, and with a copper stripwire along the back. These unit cells were stacked 4 high and 14 long to fill the 10.16mm x 22.86mm cross section of the x-band waveguide, creating a single row of artificial material. This design can be seen in Fig. 4.1. This design was used as it has the same geometry as the unit cell described in Chapter 2.5.1.

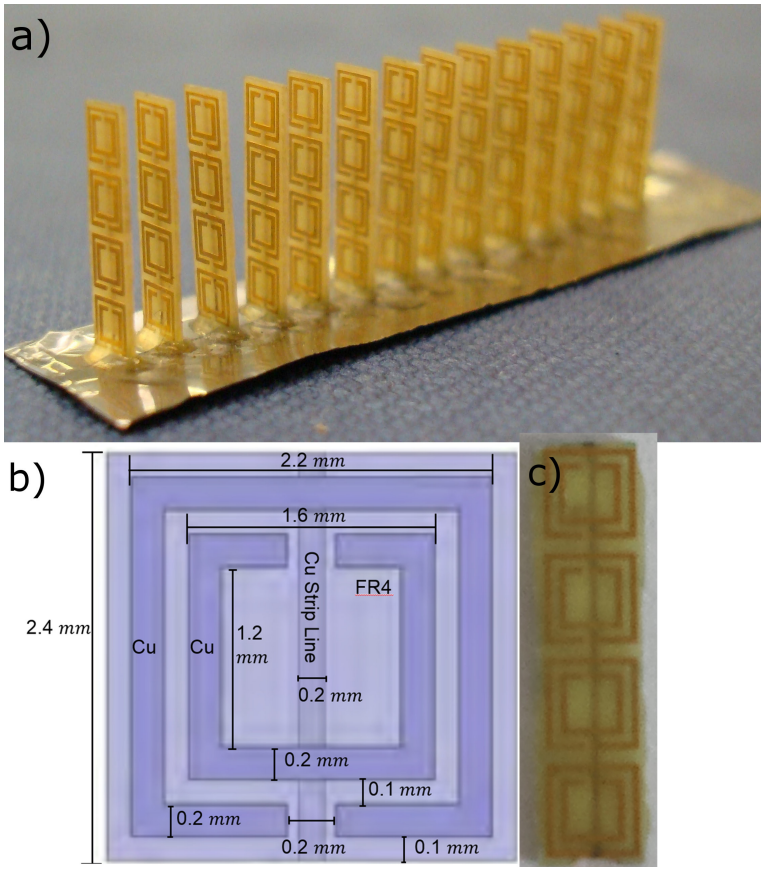

Figure 4.1: a)Metamaterial structure being experimentally characterised.b) Dimensions of the unit cell. c) Single strip of the material.

The experimental setup can be seen in Fig. 4.2, consisting of the material loaded into a parallel plate waveguide (see Fig. 4.2b); the top and bottom of the waveguide were made from aluminium plate and the sides were made from microwave absorber to ensure plane wave propagation of the incident

wave. At each end was an x-band launcher connected to an Agilent Technologies E Series Network Analyser (NA) via coaxial cable, set to record 20001 frequency points between 8GHz and 13GHz (covering the entire x-band range). A metal block was located at each port on top of the lid of the waveguide to ensure that there was minimal wave-leakage between the launcher and the waveguide. Each coaxial connection was impedance matched to a torque of 0.57Nm. The metamaterial structure was positioned at the centre of the waveguide, 29.0cm away from Port 1 (approximately 10 wavelengths) to ensure that the wave reaching the structure was a plane wave, see Fig. 4.2c).

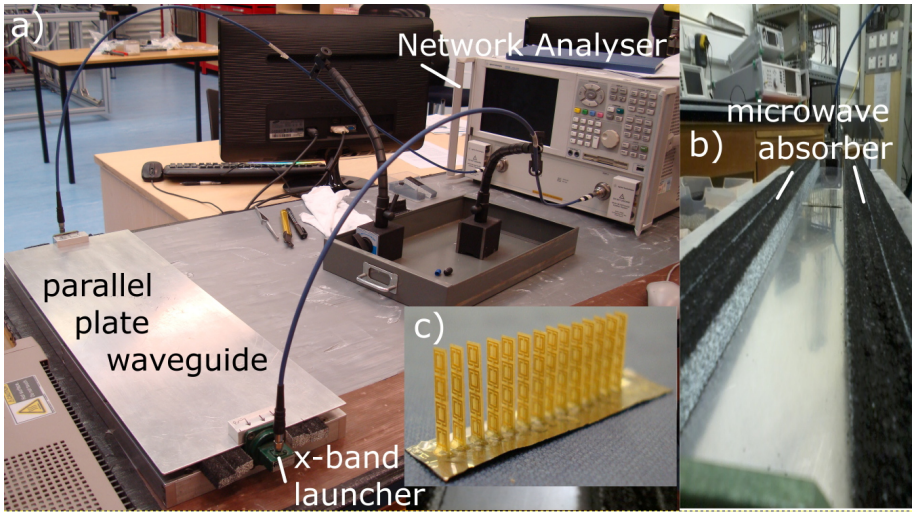

Figure 4.2: Experimental setup for characterising an existing metamaterial.

The cutoff frequency f_c of the waveguide was 6.56 GHz. This can be calculated from the equation:

$$f_c = \frac{c}{2\pi}\sqrt{\left(\frac{n\pi}{a}\right)^2 + \left(\frac{m\pi}{b}\right)^2}, \tag{4.1}$$

where the integers $n, m >= 0$ are the mode numbers, and a, b are the lengths of the sides of the waveguide. For fundamental mode propagation in x-band,

$n = 1$ and $m = 0$ where $a = 22.86$mm and $b = 10.16$mm.

4.1 Calibration of the Network Analyser

Before any experimental work could commence it was important to calibrate the network analyser. This ensures that the errors in the data obtained are kept to a minimum (as discussed in Chapter 4.1.1) and ensures reliability.

The experimental setup required the Parallel Plate Plane Wave Calibration Technique; this consists of two ports located at either end of a .60.0cm parallel plate waveguide, with a length of 29.0cm to the front of the Device Under Testing (DUT) loading region. It was very important to ensure that the front position of the DUT was maintained throughout the experiments as this distance from Port 1 effects the phase of both S_{11} and S_{21}, therefore could result in incomparable data if not recorded correctly.

The calibration used the standard open (nothing loaded into the waveguide), matched (absorber) and short (metal bar). These can be seen in Fig. 4.3.

To select the correct calibration kit, the options of "Calibration" $--> $ "Calabration Wizard" $--> $ "Unguided" $--> $ "TRL" $--> $ "Port 1-2" are required. At this point the user is able to select a specific type of calibration kit by selecting "View Calkit" and selecting "Plane Wave Kit" (for this experimental setup). At this point the three options for "open", "reflect" and "transmit" appear. Select "Reflect standard" $--> $ "System Impedance".

Open the lid to the experiment, insert the metal short into the waveguide exactly at 29.0cm and replace the lid, ensuring the metal blocks get replaced at the ports to ensure minimal wave-leakage. Select "Reflect" on the NA

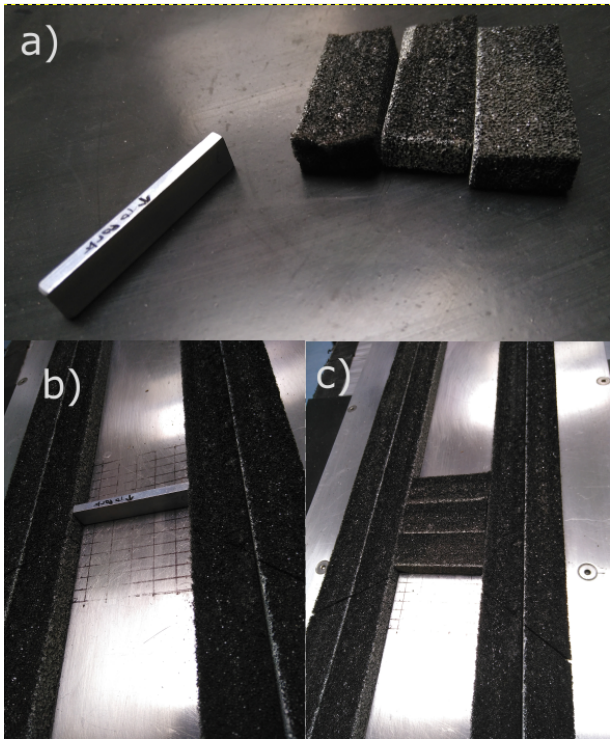

Figure 4.3: Calibration kit used for the Network Analyser. a) The short (metal bar - left) and the matched load (microwave absorber - right)

screen for Port 1 and wait for the screen to show that the measurement has been made. Remove the short and insert the matched load (the absorber). Select "line" on the NA screen for Port 1 and again wait for the measurement to be made. Finally, remove the load and replace the lid, then select "Thru" to measure the open system. Repeat for Port 2. Verify that the calibration has been successful checking S_{21}; if this doesn't equal 1 then either the calibration needs refreshing (turn "Cal" off then on again) or the calibration has not been conducted correctly.

4.1.1 Calibration Errors

There are 3 main types of error that can occur when calibrating the Network Analyser; Systematic Errors (caused by imperfections in the NA and the test setup), Random Errors (caused by issues like instrument noise) and Drift Errors (caused by the performance of the NA changing over time). Systematic errors are characterised during the calibration process and mathematically removed during measurements due to their predictable nature (they are assumed to be time invarient [122]. Random errors are much more difficult to account for as they are unpredictable by nature. The main contributor for this type of error is instrument noise (source phase noise, sampler noise, etc). Drift errors are predominantly caused by temperature variations and can be mitigated by ensuring that the ambient temperature of the experimental environment remains steady.

To explicitly address the issue of temperature variation, experiments were conducted to determine the time required for the Network Analyser to warm up sufficiently to produce stable readings and to determine how drift errors might be introduced over the course of an extended experiment. A frequency range of 0.1-20GHz was used, with scattering-parameter data being exported at various times over an hour (the previously assumed time required for the

NA to become stable). The room temperature remained a steady 24°C over the course of the experiment. The experimental setup was the same as in Fig. 4.2, though without the loaded structure. The results of the investigation can be seen in Fig. 4.4, with a subset of the data within the x-band frequency range being highlighted as this is the range we are most interested in stable results for. The first measurement (0925) was made as soon as the Network Analyser was turned on. Plot 4.4c) shows that there is an obvious difference between this measurement and the second time measurement 13 minutes later (0938). The later times show that there is then only slight fluctuations about the 0938 data – even after the completion of the hour – suggesting that the NA is stable for measurements by 13 minutes after being turned on and for at least an hour afterwards as long as the temperature of the room is kept stable. This will ensure that initial drift errors are kept to a minimum.

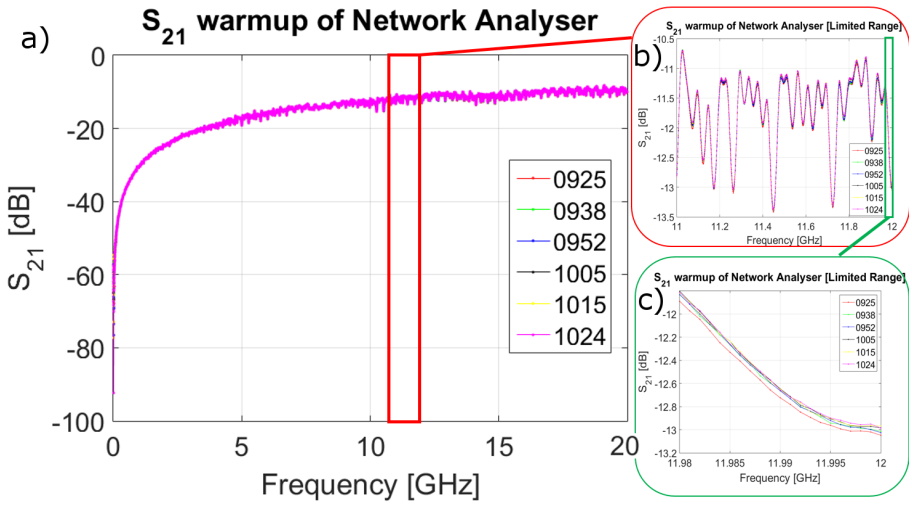

Figure 4.4: Data showing how fluctuations in the Network Analyser reduce over an hour.a) Data over the whole 0.1-20GHz range. b) Data from 11-12GHz. c) Data from 11.98-12GHz.

4.2 Experimental Results

For the 2.4mm unit cell being analysed, the approximate resonant frequency (based on Eqn. 2.27) is around 13.5GHz.

After calibrating the NA, the structure was loaded into the parallel plate waveguide and the magnitude and phase of S_{11} and S_{21} were extracted over an 8-15GHz frequency range. Figure 4.5 shows the plots produced by the NA, where the magnitudes of S_{11} and S_{21} are shown on the left of the figure and are given as Log$M$ (where M is the scattering parameter) and the phases in degrees are shown on the right. Note that in S_{21} the phase is wrapped around on itself, hence the large jump in phase. This jump is removed in the analysis of the data. This phase-wrapping unfortunately introduces a small amount of noise in the signal, as seen by the thickening of the line width of the data.

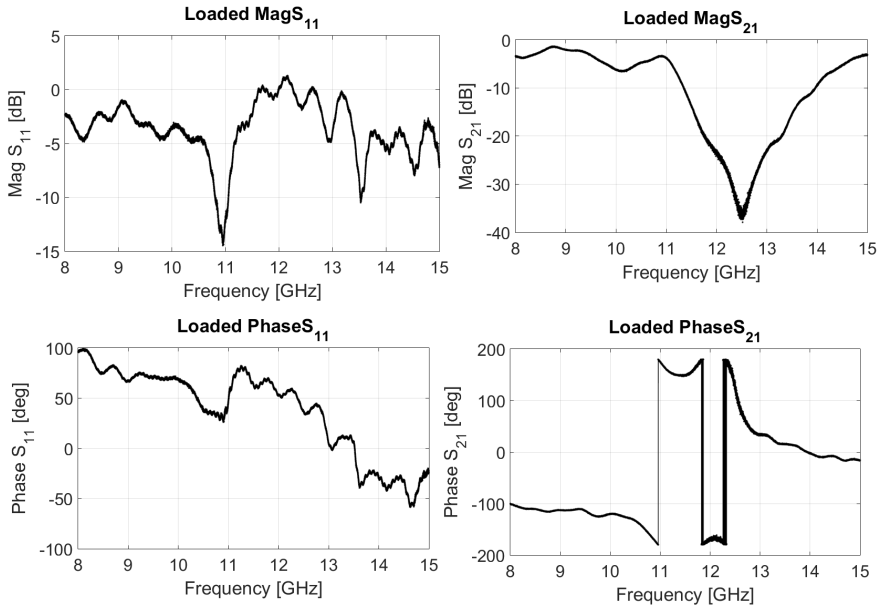

Figure 4.5: Data given by the Network Analyser: top left) Magnitude S_{11} [dB]; top right) Magnitude S_{21} [dB]; bottom left) Phase S_{11} [°]; bottom right) Phase S_{21} [°].

To ensure that the data acquisition method was reliable a number of measurements were taken of S_{11} and S_{21}. The plots comparing 6 separate experiments characterising the metamaterial between 9GHz and 13GHz can be seen in Fig. 4.6 showing the magnitudes [U] and phases [rads] of S_{11} and S_{21}. These plots show that the measured behaviour of the metamaterial structure is fairly consistent between experiments. The S_{11} plots show that fluctuations are present in the recorded signal, and that these fluctuations vary slightly between experiments. These fluctuations are caused by a number of issues; the alignment of the metamaterial relative to the incident wave, the positioning of the top plate of the waveguide and any oscillations or reflections in the coaxial cable to name a few. Attempts were made to mitigate these issues (aligning the metamaterial with a pre-set grid, see Fig. 4.2c), using aluminium blocks to better connect the top plate to the waveguide launcher plate to remove any gaps between the plate and the launchers, and by the use of clamps to hold the coaxial cables in place, see Fig. 4.2a)), however these sources of noise were not completely removable. There is also a spread in the S_{21} data in the region of 11.5GHz to 13GHz caused by the phase wrapping produced by the NA.

These experiments confirm that the scattering parameters for this metamaterial structure are reproducible, and so the smoothest data set was chosen to test the extraction technique discussed in Chapter 2.3. The magnitude and phase of S_{11} and S_{21} can be seen in Fig. 4.7.

From these plots one can observe that between 10.5GHz and 11.2GHz the magnitude of S_{21} exceeds that of S_{11}. A resonance peak is also observed in this region, shown by the minimum in the magnitude of S_{11} along with a corresponding phase shift. This suggests a region where full wave transmission is possible (instead of simply evanescent wave propagation), suggesting a region of negative refractive index and where ε_r and μ_r is negative.

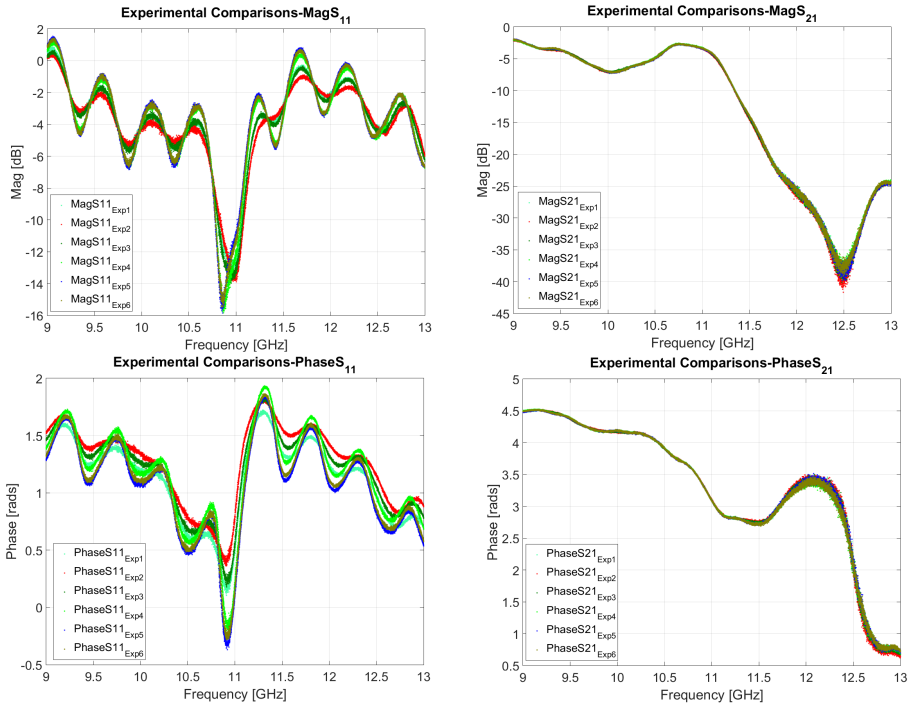

Figure 4.6: Plots comparing the scattering parameters of the metamaterial for 6 separate characterisation experiments: top left) Magnitude S_{11} [U]; top right) Magnitude S_{21} [U]; bottom left) Phase S_{11} [rads]; bottom right) Phase S_{21} [rads].

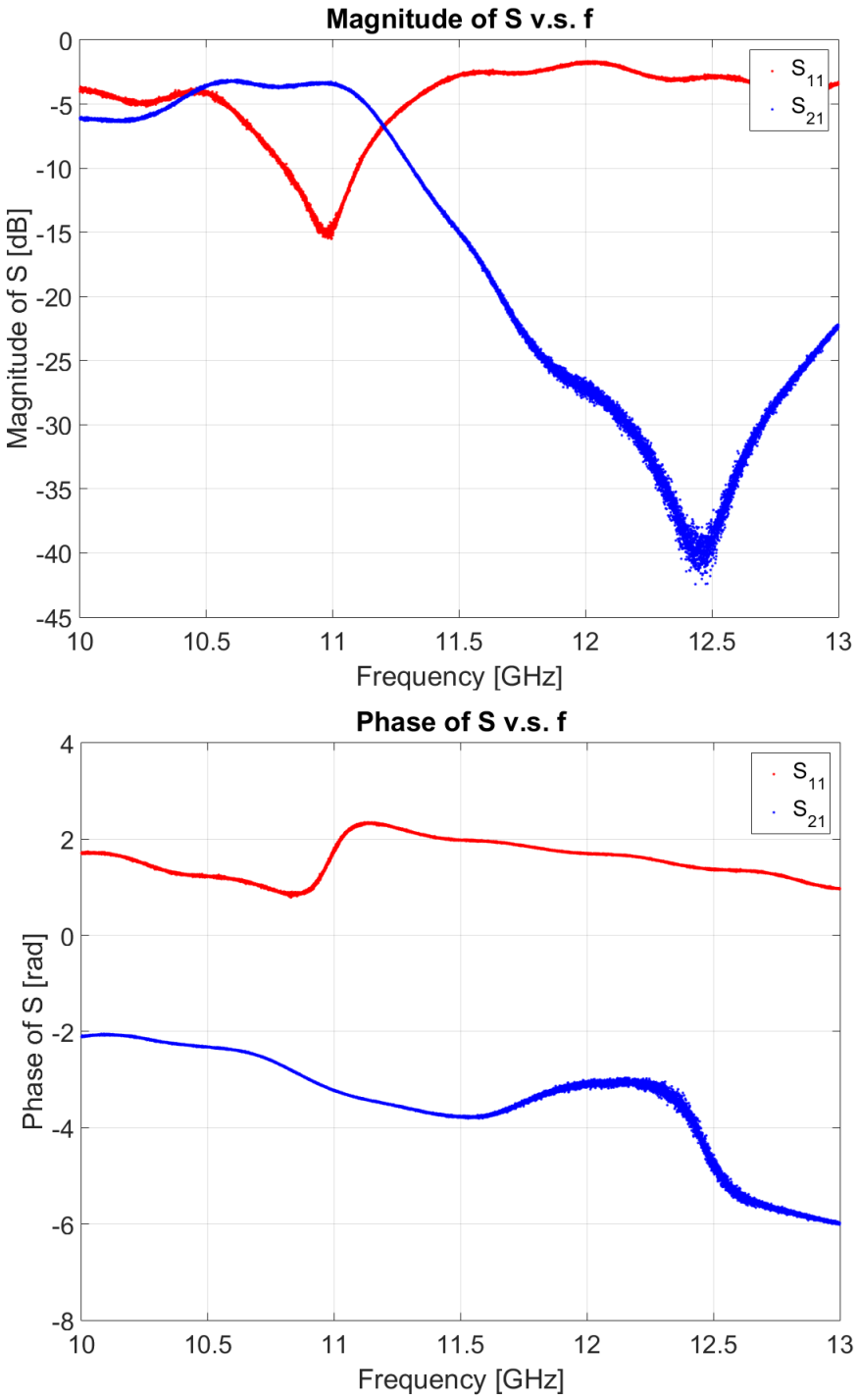

Figure 4.7: Plots showing the magnitude [dB] and phase [rads] of S_{11} (red) and S_{21} (blue) for the metamaterial.

The extraction technique was coded into MATLAB which produced the required plots of the constitutive parameters and other relevant graphs. Figure 4.8 shows the results of passing the experimental data through the extraction technique outlined in Chapter 2.3. The white region (10GHz - ≈11GHz) indicates the frequency region where the material acts as a Double Positive (DP) medium (both Re(ε_r) and Re(μ_r) are positive). In this region the magnitude of S_{11} and S_{21} are similar in value in Fig. 4.7. Notice that when the phase in S_{11} reaches its minimum value, a minimum in the magnitude in S_{11} is also observed and the constitutive parameters of the material both become negative. Between ≈11GHz and ≈11.3GHz – the green highlighted region – the material behaves as a Double Negative (DN) medium. This once again means that the wave can fully propagate across the material, that the refractive index is well defined and negative (as seen in Fig. 4.9) as is indicated by the region where S_{21} is greater than S_{11} in Fig. 4.7. The red region (≈11.3GHz - 13GHz) indicates where the material behaves as a Single Positive (SP) medium (Re(μ_r) is positive whereas the Re(ε_r) is negative). In this region, the medium acts as a barrier to full wave propagation; this is seen by the large reduction in the magnitude of S_{21} in this region. Notice here that the noise observed in the data previously presents itself here by the second, displaced line of data points.

The absorptivity of this material can be determined using Eqn. 2.17, shown in Fig. 4.10, where it becomes obvious that this type of design would struggle to operate in high power environments in the double negative frequency region as the absorption value peaks at nearly 0.6. This makes it unsurprising that the unit cell design discussed in Chapter 2.5.1 was unable to withstand significant incident powers.

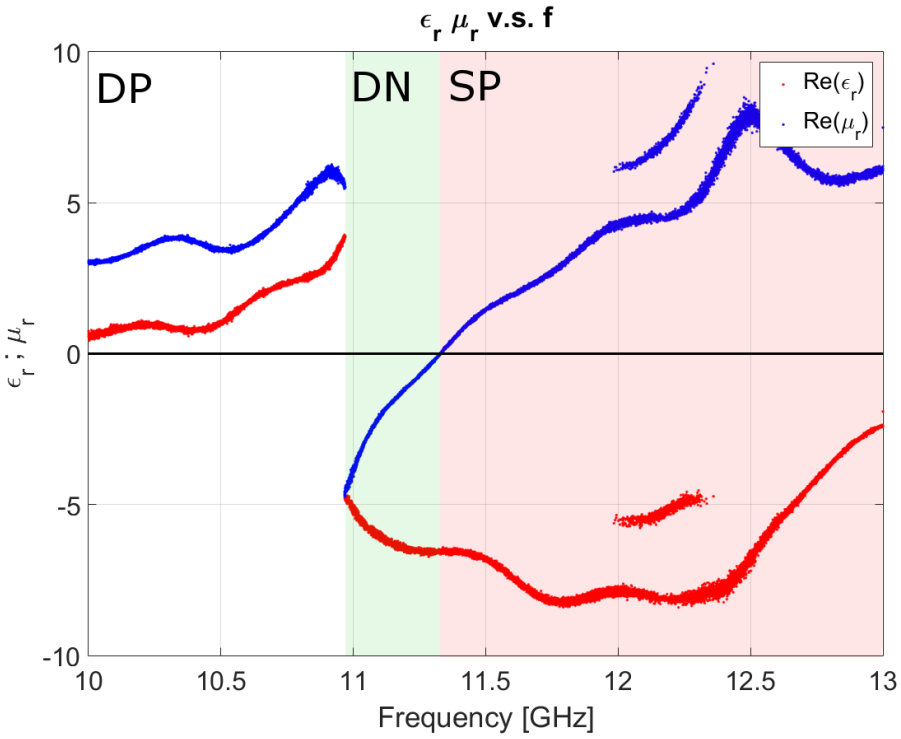

Figure 4.8: Figure showing the frequency regions where the material behaves as a Double Positive (DP) structure (white region), a Double Negative (DN) structure (green region) and a Single Positive (SP) structure (red region).

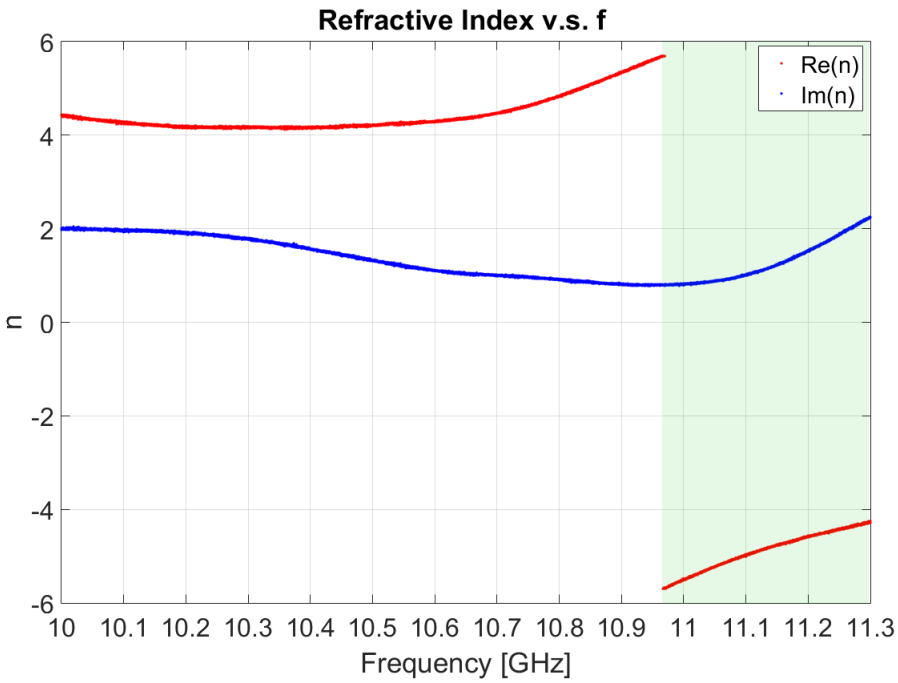

Figure 4.9: Refractive index for the material for regions where n is well defined, showing that the structure behaves as a negative index material in the region around 11GHz.

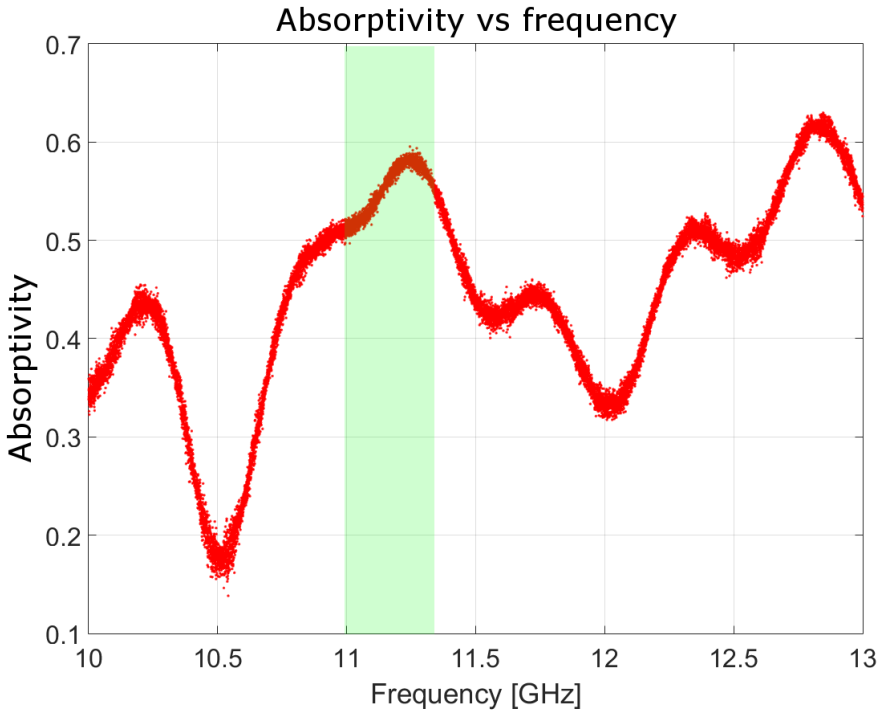

Figure 4.10: Absorption plot for the experimental setup, with the region of double negativity highlighted in green.

4.3 Experimental Conclusions

The aim of this chapter was to demonstrate that the extraction method discussed in Chapter 2.3 is a valid technique for extracting the constitutive parameters of a designed artificial material. Theory suggested that the resonant frequency for this unit cell design would exist in the regino of 13.5GHz, and the experiment demonstrates a resonant frequency at around 11GHz. The structure tested was based on a previous design of metamaterial that had previously demonstrated an inability to operate in high power environments [5, 70]. This experiment successfully demonstrated that the extraction technique is valid for this type of characterisation method.

The experimental system aimed to adhere to as many of the assumptions required by the extraction techniques as possible whilst also reducing many of the possible avenues for noise. Repeat experiments demonstrated that the technique of measuring S_{11} and S_{21} was reproducible, and showed that not all of the noise was able to be successfully removed from the experiment. However, the scattering parameters for the data set demonstrating the lowest noise was input into the extraction method, suggesting that this material design operates as a metamaterial (i.e. Double Negative material) in the frequency range of ≈11GHz to 11.3GHz. This corresponds to a region of high absorption, suggesting that this was the reason for the failure of the design discussed in [5, 70].

Chapter 5

Simulation Work

5.1 Simulation Packages

Various methodologies for analysis have been proposed and used for physical system simulations. Typical methods are the Method of Moments (MoM) [123], Spectral-Domain Methods (SDM) [124], Finite Difference Methods (FDM) [125, 126], and Finite Element Methods (FEM) [127–129].

This investigation uses computer modelling software packages HFSS and COMSOL, both FEM frequency-domain solvers (these were chosen due to the accessibility of the software). The simulations were run on an HP machine with a 1.6GHz quad core i7 processor with 16GB of RAM, though the simulations themselves only ran on single cores (enabling many simulations to be run simultaneously).

5.1.1 HFSS Theory

HFSS (High Frequency Structural Simulator) [130] is a commercially available 3D full-wave electromagnetic solver which uses the Finite Element

Method (FEM) with adaptive meshing to determine the electromagnetic behaviour of a structure. HFSS can determine [130]:

1. the electromagnetic behaviour of a system, including systems requiring open boundary conditions for near and far fields;
2. the characteristic port impedances and propagation constants the system;
3. generalised S-parameters and S-parameters renormalised to specific port impedances, and
4. the eigenmodes, or resonances, of a system.

To calculate required parameters, HFSS divides the problem space into many thousands of tetrahedra (called the finite element mesh) and creates a local function to describe the fields present within each tetrahedral. The electric field is determined from Maxwell's equations, expressed as:

$$\nabla \times \left(\frac{1}{\mu_r} \nabla \times \mathbf{E} \right) - k_0^2 \varepsilon_r \mathbf{E} = 0, \tag{5.1}$$

where $\mu_r(x, y)$ is the complex relative permeability, $k_0 = \omega/c$ is the wavenumber of free space, ω is the angular frequency, $\varepsilon_r(x, y)$ is the complex relative permittivity. $\mathbf{H}$ is determined by using the corresponding magnetic field equations.

HFSS continues by determining the area in the mesh where the exact solution has a strong error. In these regions the tetrahedra sizes are redefined, or adapted, with HFSS then determining another solution based on the refined mesh. The tetrahedrals which show low error do not get resized. HFSS then iteratively solves the system, analyses the error then refines the mesh until the convergence criteria (defined by the user) is met or until the requested number of adaptive passes (again defined by the user) are completed. This

process is known as adaptive meshing (schematic of this process shown in Fig. 5.1).

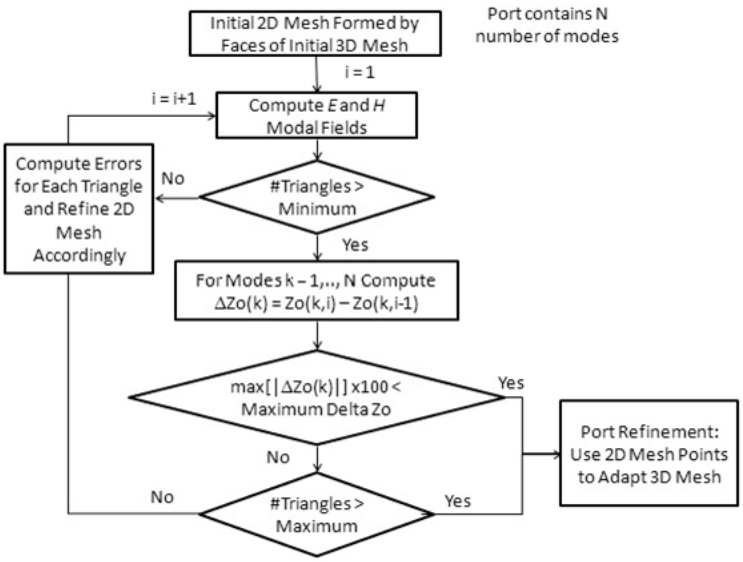

Figure 5.1: Schematic showing the mesh refinement mechanism used by HFSS [131].

HFSS Boundary Conditions

For the simulations run in this investigation, Port boundaries and Master/Slave boundaries were required. The Port boundaries that were used in these investigations were Floquet Ports (for infinite systems, these ports ensure that the E field on each of the outer edges of the geometry match to ensure a periodic system) and Wave Ports (for finite systems, ensure that the E field matches the constraints of the material properties at the port, i.e. go to zero for metal boundaries). Master/Slave boundaries simply ensure that the E fields along the boundary match, ensuring a periodic system is correctly simulated. This distinction is important as HFSS requires that the port is connected to a waveguide with the same cross section as the port (i.e. one cannot have a Wave Port connected to a Master/Slave boundary

as these only apply to infinite systems, nor can one have a Floquet Port surrounded by Perfect Electrical Conductor (PEC) boundaries).

The excitation field for a wave propagating in the z direction is expressed as:

$$\mathbf{E}(x, y, z, t) = Re\left[\mathbf{E}(x, y)e^{j\omega t - \gamma z}\right], \tag{5.2}$$

where $\gamma = \alpha + i\beta$ is the complex propagation constant where α is the attenuation and $\beta = k_z$ is the longitudinal wavenumber and is related to the phase constant of the wave.

The remaining boundary conditions of the simulations were limited to Master and Slave boundaries (for the infinite system) and PEC boundaries (for the finite system). Master and Slave boundary conditions use Bloch-Floquet periodicity to ensure that the electric fields located along the Slave boundary are equal to those determined at the Master boundary. PEC boundary conditions ensure that $\nabla \cdot \mathbf{E} = 0$ at the boundary.

5.1.2 HFSS Numerical Error

As with all simulations there is the possibility of numerical errors suggesting phenomena that are not real. HFSS deals with this by reducing the mesh size down until the predicted fields (or more correctly the S-parameters) differ by less than a pre-set tolerance. These tolerances are defined by the Maximum Percentage Error. Whether this value is achieved or not is determined by a couple of parameter variables; Maximum Number of Passes and Maximum Delta S. These are discussed in more detail in Chapter 6.2.1 and Chapter 6.2.2.

5.1.3 COMSOL Theory

COMSOL Multiphysics is a simulation package which uses the FEM method, together with adaptive meshing and error control, used to simulate many different types of physical and engineering systems [132]. This makes COMSOL similar to HFSS, especially as both programmes use similar meshing techniques to split up the problem-space. However where HFSS is optimised for fast, efficient High Frequency simulations, COMSOL's Multiphysics packages enables a much wider variety of simulations solving different types of physical problems simultaneously (for example solving EM systems with thermal heating analysis included).

For the EM system, COMSOL solves Maxwell's equations using:

$$\nabla \times (\mu_r^{-1} \nabla \times \mathbf{E}) - \frac{\omega^2}{c^2} \left(\varepsilon_r - \frac{i\sigma}{\omega \varepsilon_0} \right) \mathbf{E} = 0, \tag{5.3}$$

where μ_r represents the relative permeability, ε_r is the relative permittivity, σ is the electrical conductivity and c is the speed of light in free space.

By combining different partial differential equations, COMSOL solves for Thermal Heating by solving the rearranged first law of thermodynamics (including viscous heating and pressure work) as shown by the Heat Equation:

$$\rho C_p \left(\frac{\partial T}{\partial t} + (\mathbf{u} \cdot \nabla) T \right) = -(\nabla \cdot \mathbf{q}) + \tau : \mathbf{S} - \frac{T}{\rho} \frac{\partial \rho}{\partial T} \bigg|_p \left(\frac{\partial p}{\partial t} + (\mathbf{u} \cdot \nabla) p \right) + Q, \tag{5.4}$$

where ρ is the material density (SI unit: kg/m^3), C_p is the specific heat capacity at constant pressure (SI unit: $J/(kgK)$), T is absolute temperature (SI unit: K), u is the velocity vector (SI unit: m/s), q is the heat flux by conduction (SI unit: W/m^2), p is pressure (SI unit: Pa), τ is the viscous

stress tensor (SI unit: Pa), S is the strain-rate tensor (SI unit: $1/s$) and Q represents heat sources besides viscous heating (SI unit: W/m^3)

If viscous heating is ignored (as is typical for low speed thermal flows) and neglecting pressure work, this reduces down to the more commonly known equation:

$$C_p \frac{\partial T}{\partial t} + \rho C_p \mathbf{u} \cdot \nabla T = \nabla \cdot (k \nabla T) + Q, \tag{5.5}$$

where k is the thermal conductivity (SI unit: $W/(Km)$). The iterative computation cycle for determining the fields and heating for the "RF and Microwave Heating" physics is shown in Fig. 5.2.

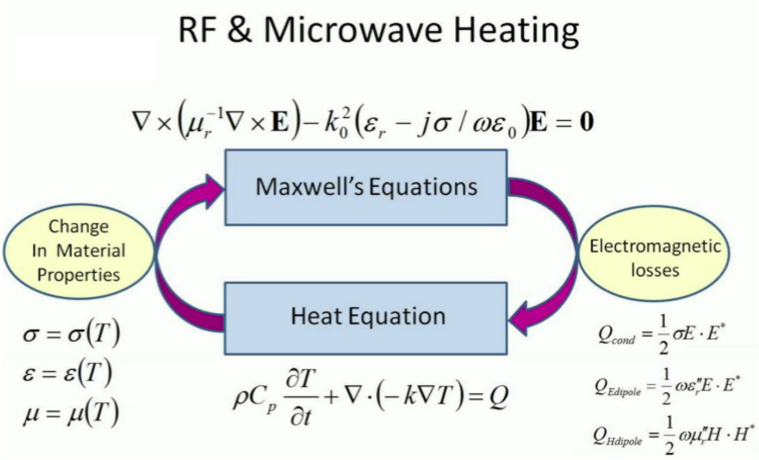

Figure 5.2: Schematic showing the way COMSOL determines heating in a simulation [132].

COMSOL Boundary Conditions

For the EM comparison simulations, boundary conditions of PEC (for the waveguide walls) and Ports (for the wave input and output ports) were required. The incident wave at port 1 is defined as a rectangular TE_{10} wave (normalised to 1W of incident power). The produced using:

$$S = \frac{\int_{\partial\Omega}(\mathbf{E} - \mathbf{E}_1) \cdot \mathbf{E}_1}{\int_{\partial\Omega} \mathbf{E}_1 \cdot \mathbf{E}_1}. \tag{5.6}$$

At Port 2 this equation changes slightly to:

$$S = \frac{\int_{\partial\Omega} \mathbf{E} \cdot \mathbf{E}_2}{\int_{\partial\Omega} \mathbf{E}_2 \cdot \mathbf{E}_2}. \tag{5.7}$$

The wave equation for the bulk of the waveguide is defined by:

$$\nabla \times \mu_r^{-1}(\nabla \times \mathbf{E}) - k_0^2 \left(\varepsilon_r - \frac{j\sigma}{\omega\varepsilon_0}\right) \mathbf{E} = 0, \tag{5.8}$$

where ∇ is the 3D spacial derivative operator, μ_r is the relative permeability, $\mathbf{E}$ is the electric field strength, k_0 is the free space wavenumber, ε_r is the relative permittivity, $j = \sqrt{-1}$ and highlights the imaginary component, σ is the electrical conductivity of the loaded material, ω is 2π times the frequency and ε_0 is the permittivity of free space.

For the PEC boundaries, COMSOL requires that at the boundary:

$$\mathbf{n} \times \mathbf{E} = 0, \tag{5.9}$$

where $\mathbf{n}$ is the unit vector normal to the boundary surface.

5.1.4 COMSOL Numerical Error

To ensure that COMSOL keeps numerical errors to a minimum, a “Factor in Error Estimate” parameter is assigned along with a “Maximum Number of Iterations”, defined by the user. This requires that the calculated field values converge within a set tolerance. If the simulation does not converge on the pre-assigned error tolerance within the Maximum Number of Iterations, the simulation will throw a “Did not converge” error.

One other significant difference in the meshing technique created by HFSS and COMSOL is that the user has to choose a minimum tetrahral size in COMSOL (Course, Normal, Fine etc) as opposed to defining a minimum error. This can add inaccuracies to the simulation if the chosen mesh size is not sufficiently small.

5.2 Experiment-Simulation Comparison

A comparison between the experimental data obtained and the simulation data was required to ensure that the simulation methodology is reliable. As the Square SRR on FR4 design had already been experimentally characterised, the same design was input into HFSS and a comparison study run. The geometry comparisons can be seen in Fig. 5.3.

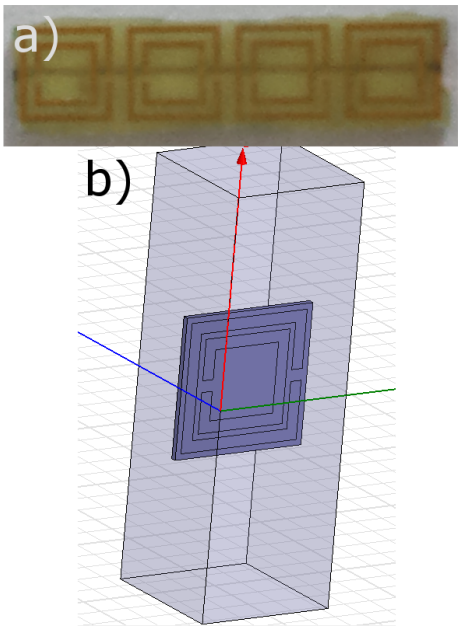

Figure 5.3: a) Experimentally tested Square SRR on FR4. b) Simulated Square SRR on FR4 design for the same geometry as the experimental setup.

The main differences between the experiment and the simulation were that the simulation ran for an infinite array of the SRRs as opposed to the 56 unit cells present in the experimental arrangement, and imperfections in the experimental system are not present in the simulations due to the nature of the simulation setup. This means that a certain amount of discrepancy is expected between the two data-sets, though the overall pattern of the data should still be the apparent. The experimental data was taken with 200001 frequency points over the range 10-13GHz; the simulation ran with a range of 9-15GHz to ensure that slightly more than the experimental range was covered to ensure differences in the resonant frequency of the structure are not overlooked. PEC boundaries were used to simulate the copper wires as this reduced the simulation run time from tens of hours to a few minutes, with only slight differences in the resonance results obtained (see Chap. 6.2.4 for a more in-depth discussion on this).

Figure 5.4 shows the experimental and simulation results for Mag S_{11} and Mag S_{21}, with the associated phases being shown in Fig. 5.5. These plots are interesting as the overall similarities can be seen between the two systems – both show a resonance occurring, with a lower frequency resonance and a higher frequency resonance clearly seen in MagS_{11} and both show a sharp decrease in Mag S_{21} after the resonance. However the resonant frequencies differ (11GHz for the experimental system and 10.3GHz for the simulation), the experimental data contains fluctuations in the data instead of a smooth plot and the peak values are not as high in the experiment. These differences are caused by a number of factors such as the simulation being a "perfect" system with perfect, lossless ports and PEC boundaries and the simulation modelling an infinite, boundless (i.e. no waveguide walls/edge affects) system.

On the whole this comparison study shows that the results obtained by the simulation demonstrate the behaviour of the experimental system ad-

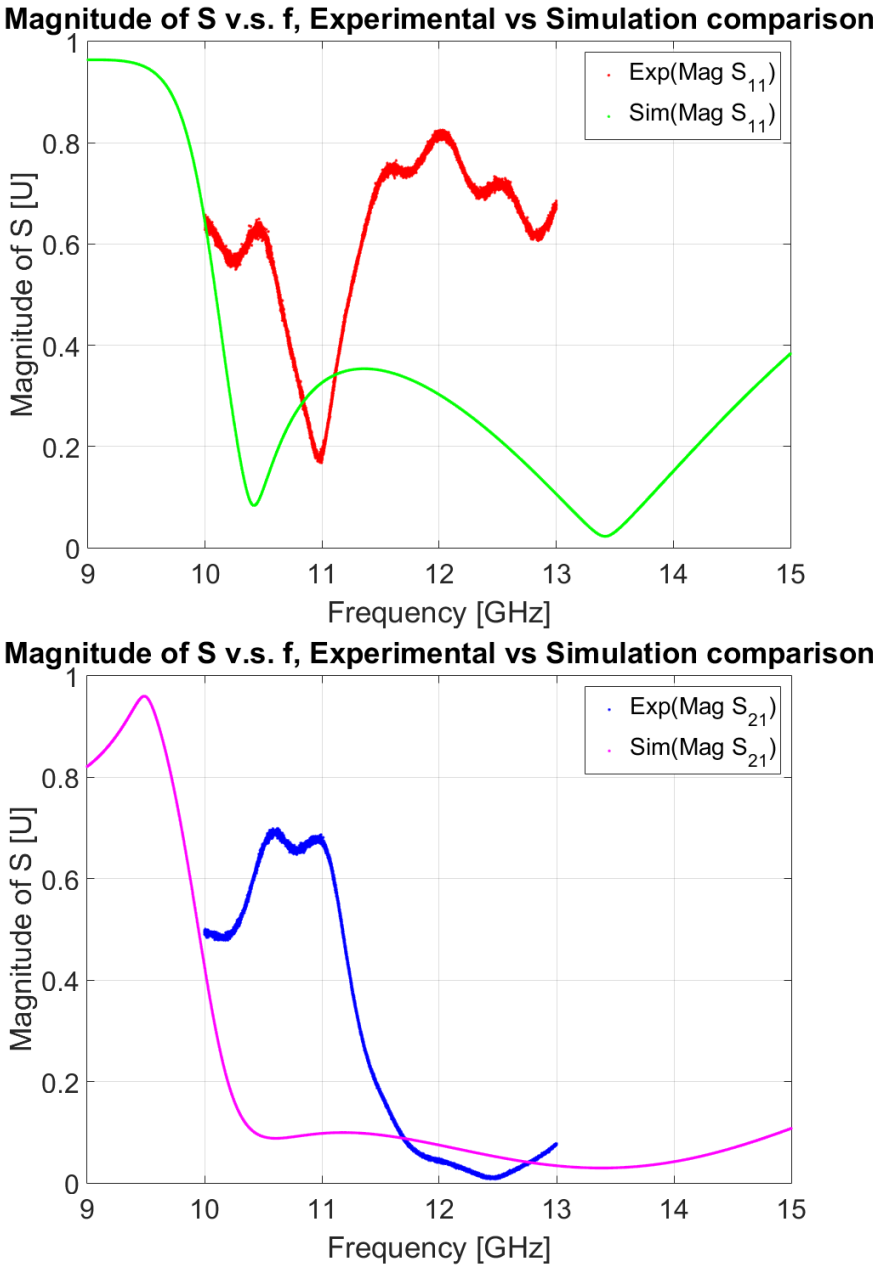

Figure 5.4: top) Mag S_{11} for the experiment (red) and the simulation (green) and b) Mag S_{21} for the experiment (blue) and the simulation (magenta). Both show agreement between the experiment and simulation results, though with some differences caused by differences between the perfect-infinite simulation and the real-life experiment.

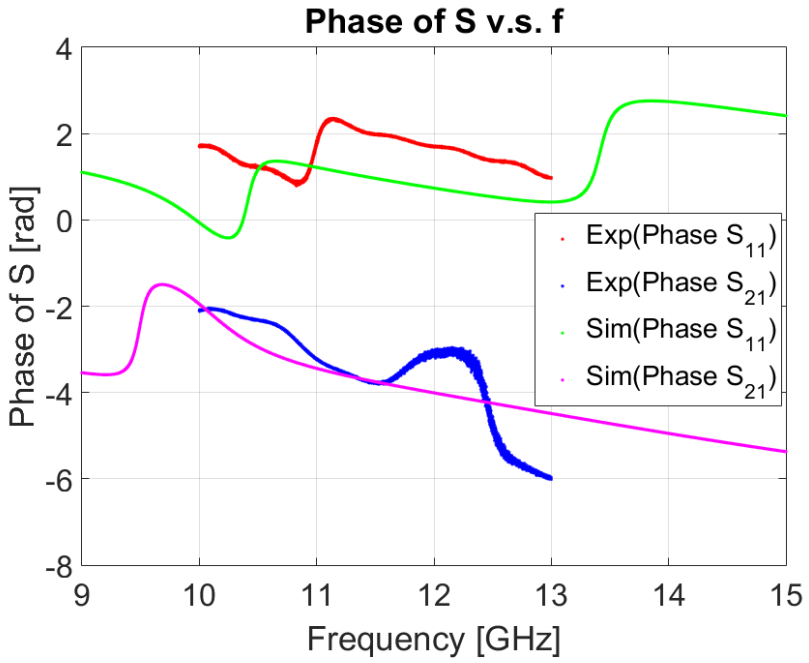

Figure 5.5: Experiment vs Simulation Comparison Phase.

equately as the general pattern of the data matches quite well. However finer resolution simulations and simulations of a more identical system compared to the experimental system need to be conducted to obtain a more well-matched value for the resonant frequency of the structure.

Chapter 6

Design Simulations

This section discusses the simulations which were run to obtain the final design specifications for the unit cell design. Initially the approximate dimensions for a 6mm complementary split ring arrangement was used to test the accuracy of the meshing. A number of parameter sweeps were then run to determine the optimal setup of the structure.

Points to note:

- Simulations of an infinite XY plane of the artificial material unit cells were initially run, therefore there was no cutoff frequency to be concerned about;
- All simulations were deembedded to the top/bottom surface of the unit cell to ensure that Only the behaviour of the unit cells were determined (i.e. no effects from the distance between the ports and the unit cell needed to be considered;
- Simulations were conducted with a frequency sweep ranging from 1 to 20GHz in steps of 0.1MHz to fully characterise the behaviour of the structures around the x-band frequency region of interest;

- Floquet boundary conditions (Master and Slave) were used to set up the infinite plane;
- Floquet ports were used to define the excitation port;
- Analysis was made on 2 modes, set perpendicular to one another to determine the TE and TM interactions between the wave and the structure.

6.1 Meshing

Before conducting simulations into the optimised design of the unit cell, simulations were run to test the meshing capabilities of HFSS for an infinite sheet of the square unit cell design discussed in Chapter 4. The different meshes can be seen in Fig. 6.1. The course mesh took 1 minute 9 seconds to complete, the normal mesh took 1 minute 50 seconds and the fine mesh took 8 minutes 56 seconds.

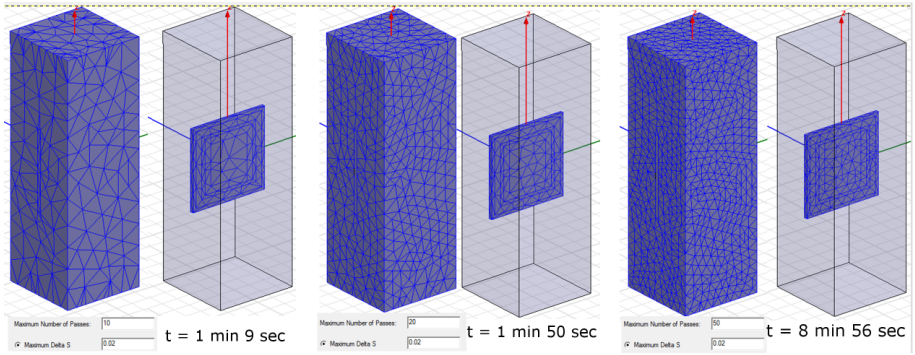

Figure 6.1: Image showing the various meshes used in HFSS along with their computation times.

Figure 6.2 shows the magnitude of S_{11} and S_{21} for the different meshing simulations. This makes apparent the resulting discrepancies in the predicted resonant behaviour of the infinite system based on the mesh size with

the larger mesh demonstrating the largest discrepancy from the other data sets. This is expected as the size of the tetrahedra used in the simulation will alter the predicted values for the electric and magnetic fields along the vertices which are then iterated on. However, the time for the finest mesh simulation to complete was around 4 times longer than that for the normal mesh, so this time will need to be taken into account if simulations are to be continuously conducted with the finest mesh.

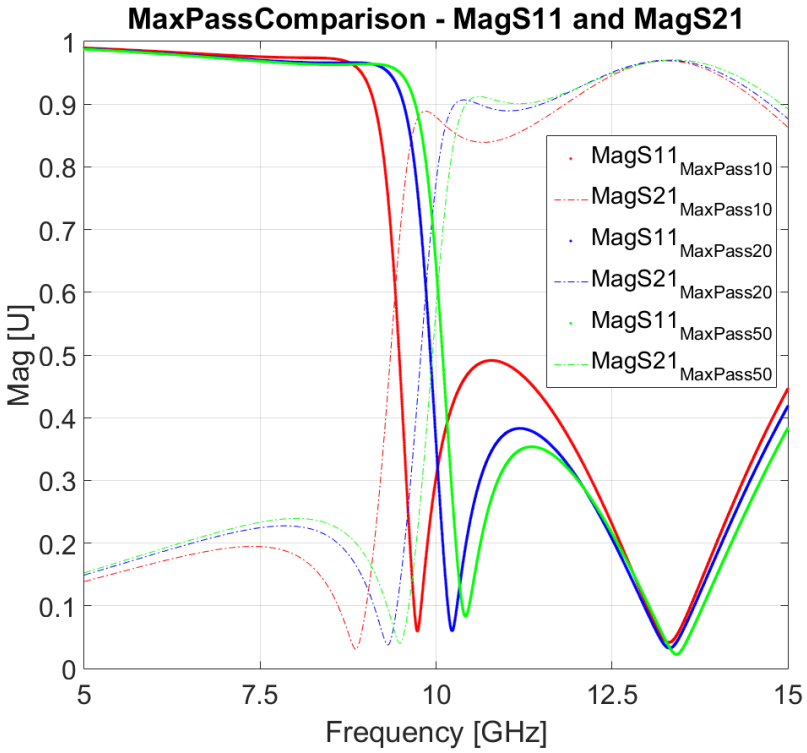

Figure 6.2: Plot showing Mag S11 and S21 for various meshes.

The initial geometry used can be seen in Fig. 6.3, showing a 6mm CSRR geometry design.

The setup for the boundary assignments can be seen in Fig. 6.4, where the dark blue diamond pattern highlighted in a) and b) represent the Master/Slave boundary conditions, the red diamond pattern highlighted in c)

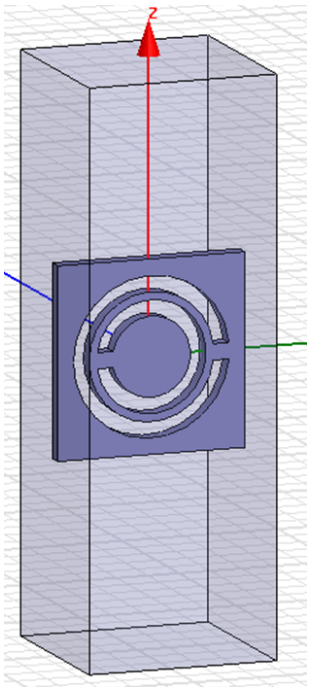

Figure 6.3: Original 6mm Unit Cell Design, used as the initial unit cell setup.

and d) represent the Floquet Ports. The blue arrows in c) and d) show the distance that the ports are deembedded i.e. from the port to the surface of the unit cell.

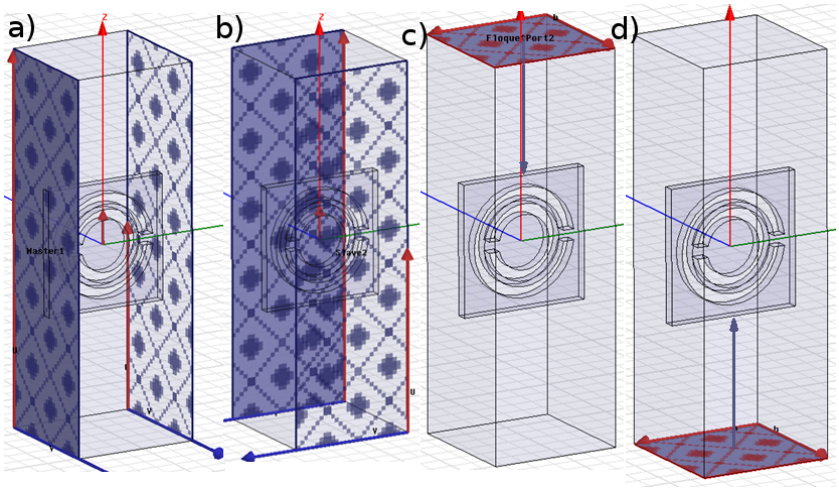

Figure 6.4: Plot showing the boundary conditions used for the design simulations. a) and b) The dark blue diamond pattern represents the Master/Slave boundaries, c) and d) the red diamond pattern highlights the Floquet Ports. The blue arrows in c) and d) shows the distance that the ports are deembedded.

6.2 Numerics - Computation Optimisation

These simulations were run to ensure that the simulation produced results which were dependable and did not cause issues due to numerical errors.

6.2.1 Max Number of Passes

As HFSS uses an iterative adaptive meshing algorithm, one can define the maximum number of iterations the simulation can undergo before a solution is determined. The maximum percentage error (convergence criteria) is also defined, and if a found solution is within that error before the maximum number of passes is reached then the simulation will stop.

The aim of this first set of simulations was to determine what the maximum number of passes should be for a pre-existing design. Table 6.1 lists the different values for the maximum number of passes used, and the time taken to for a solution to be reached.

Maximum Number of Passes	**Time Taken (mm.ss)**
6 (DNC)	03.02
10 (default)	02.52
15	03.24
20	03.11
30	03.14
50	03.18

Table 6.1: Table showing the time taken for Maximum Number of Passes simulations, where the 6 passes solution Did Not Converge (DNC).

Note here that a maximum number of passes of 6 resulted in a warning "Adaptive passes did not converge on the specified criteria".

Figure 6.5 shows the magnitude of the scattering parameters (also called S-parameters, S_{11} and S_{21}) for the different maximum numbers of passes, and Fig. 6.6 shows the phases.

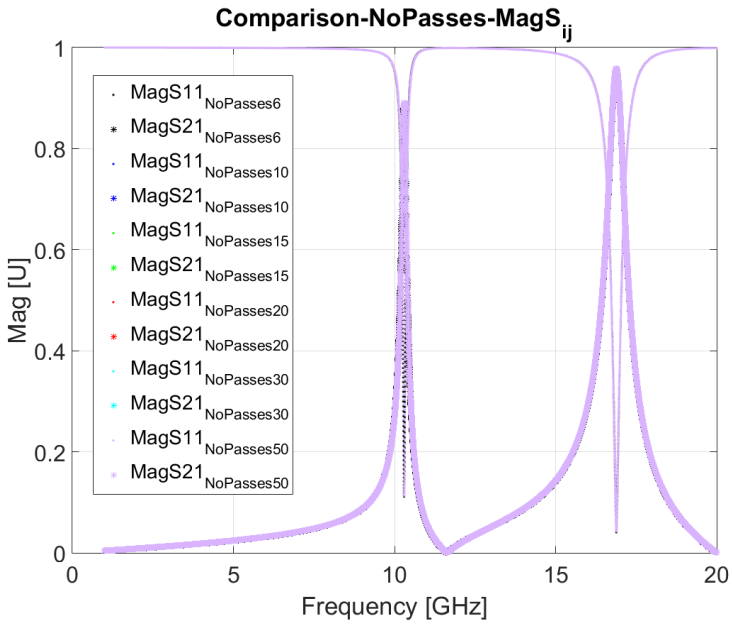

Figure 6.5: Plot showing the magnitude of S_{11} and S_{21} for varying numbers of passes.

One can see that the predicted behaviour of all of the runs is very similar for both the magnitude and phase of the S-parameters S_{11} and S_{21}, with the only slight difference being seen in the 6 passes run. This can be seen more clearly by zooming in to the Mag S_{11} peak, as shown in Fig. 6.7. This difference is incredibly small, but is still anomalous compared to the other runs, which are identical. The suggested (default) number of passes is 10, but as small geometries are being used a higher pass number is preferred to ensure that there are meshing no issues. Therefore a maximum number of passes of 20 was chosen as this took the next shortest time to reach a solution.

Number of Passes = 20.

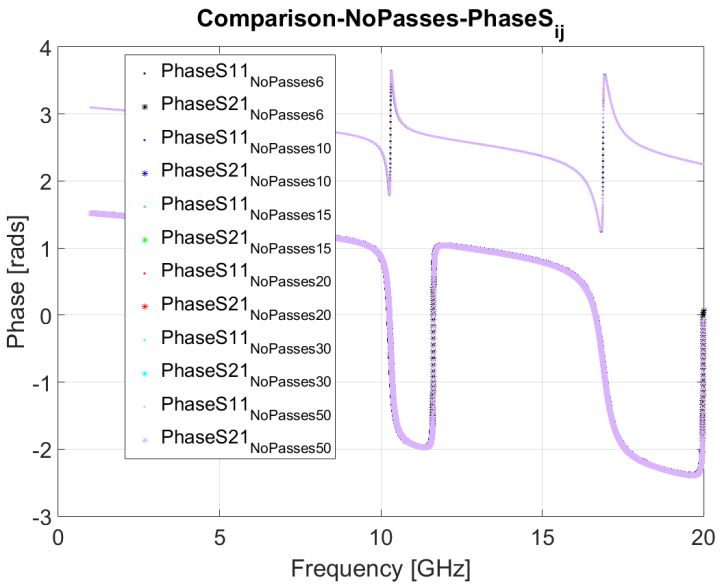

Figure 6.6: Plot showing the phase of S_{11} and S_{21} for varying numbers of passes.

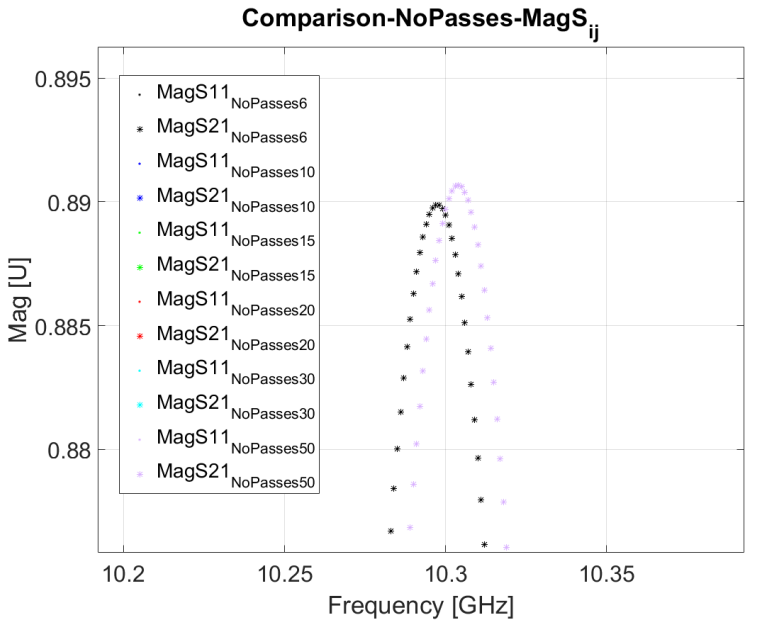

Figure 6.7: Plot zoomed into the S_{11} peak, showing that only the "6" run shows any difference in results.

6.2.2 Max Delta S

Since HFSS iteratively determines the S-parameters for a system, a value called the "Maximum Delta S" can be assigned. This stops the simulation if the change in the complex S-parameters from one iteration to the next is less than a predefined value. For example, if the Maximum Delta S is set to be 0.1, then the simulation will continue to refine the mesh until either the complex change of all S-parameters is less than 0.1, or until the maximum number of passes is reached.

Table 6.2 shows the values of Delta S simulated, along with the time taken for these simulations to run.

Maximum Delta S	**Time Taken (mm.ss)**
0.01	02.58
0.02 (default)	03.13
0.04	03.02
0.1	02.39
0.5	03.00
1	02.43

Table 6.2: Table showing the time taken for Maximum Delta S simulations.

Again both the magnitude and phase of the S-parameters were determined and can be seen in Fig. 6.8 and Fig. 6.9 respectively. Once again the results are very consistent with one another, though a slight discrepancy between the 0.01/0.02 data and the 0.04/0.1/0.5/1 data can be seen in Fig. 6.10.

Since the 0.04/0.1/0.5/1 data allows for larger variations in the S-parameters before a solution is determined, the finer stepped (and default) 0.02 for the Maximum Delta S is used for the simulations.

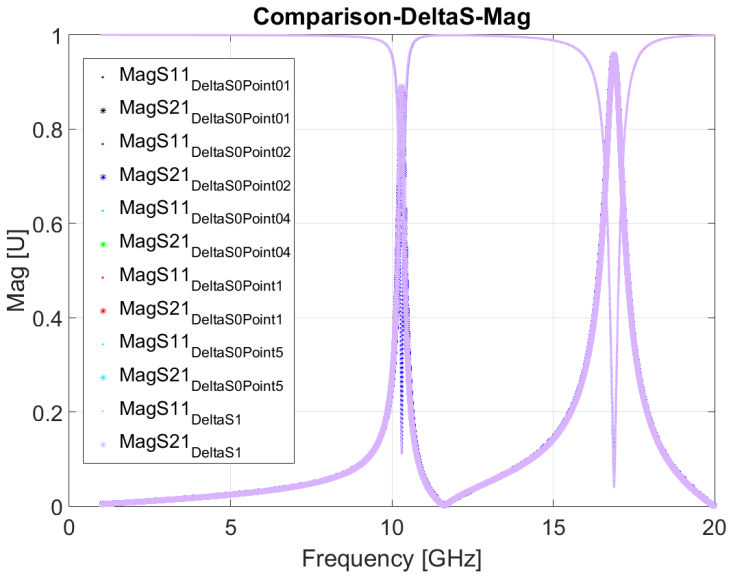

Figure 6.8: Figure showing the magnitude of the S_{11} and S_{21} S-parameters for different values of the Maximum Delta S.

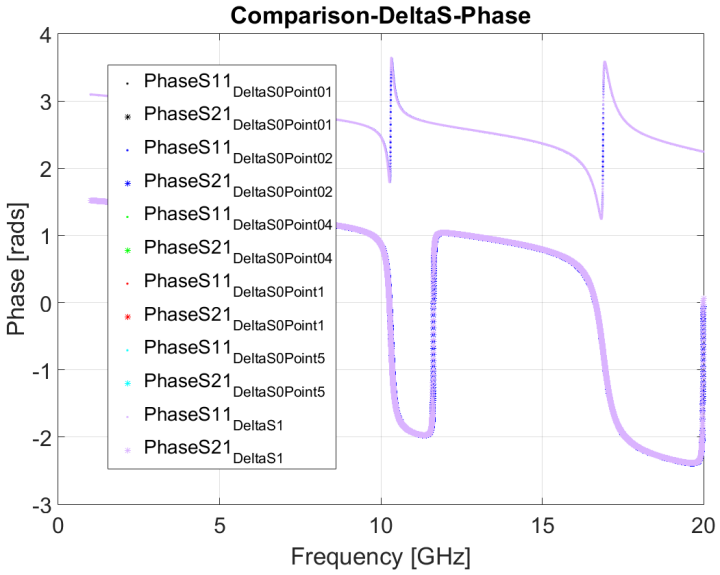

Figure 6.9: Figure showing the phase of the S_{11} and S_{21} S-parameters for different values of the Maximum Delta S.

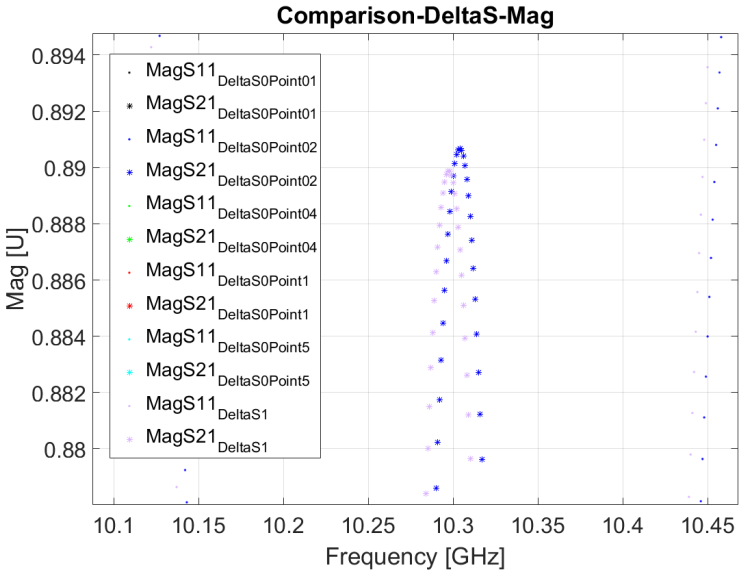

Figure 6.10: Zoomed in plot of the magnitude of the S_{11} peak, showing the slight discrepancy between the 0.01/0.02 data and the 0.04/0.1/0.5/1 data.

Maximum Delta S = 0.02.

6.2.3 Mesh Type

HFSS has the ability to alter the type of coordinate system the tetrahedral mesh is applied to; Cartesian or Curvilinear. Therefore simulations comparing the results of the two were conducted to see if there were any differences between the two methods. Table 6.3 shows the times the simulations took to reach a solution.

Coordinate System	**Time Taken (mm.ss)**
Cartesian	03.06
Curvilinear	03.40

Table 6.3: Table showing the time taken for the meshing on different coordinate systems.

The magnitude and phase of the S-parameters can be seen in Fig. 6.11 and 6.12, showing that there is a more substantial difference in the solutions predicted than with the previous numerical tests. This is not entirely unexpected - the integration volumes between the two coordinate systems will be very slightly different, resulting in very slightly different values of **E** and **B** determined on each of the vertices of the tetrahedra. From the ports, these values are then used to compute the fields in the rest of the simulation, therefore each slight difference is exacerbated over the simulations.

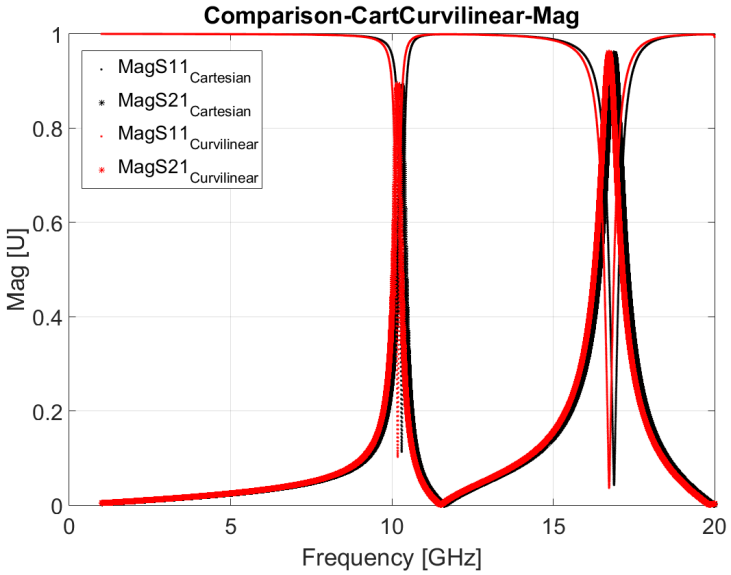

Figure 6.11: Figure showing the magnitude of the S_{11} and S_{21} S-parameters for different coordinate systems.

Therefore the coordinate system used in the later simulations was the Cartesian coordinate system. However the discrepancy between the results was noted, as this will need to be considered during experimental testing.

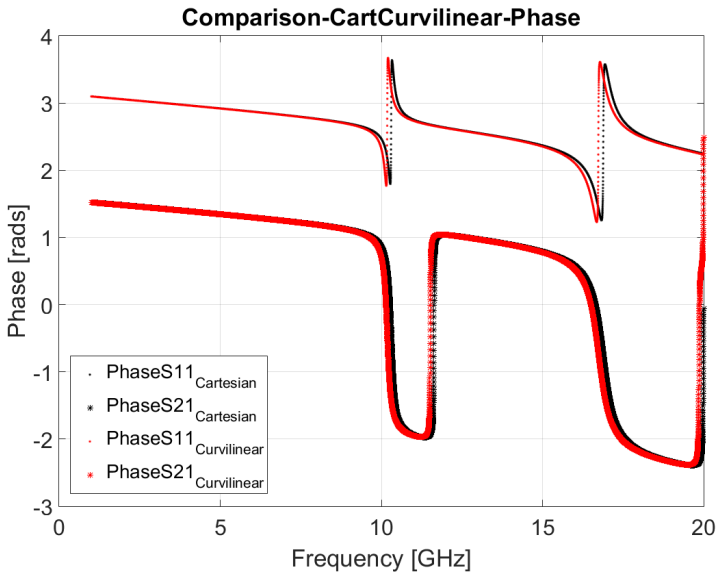

Figure 6.12: Figure showing the phase of the S_{11} and S_{21} S-parameters for different coordinate systems.

6.2.4 PEC or No PEC

As some of the geometry optimisation simulations investigation the use of wire Split Ring Resonators (SRRs) on some form of substrate, the final simulations run in the computation optimisation compared whether Perfect Electrical Conductor (PEC) was a suitable simulation alternative to copper wires of varying thickness's. A sample geometry of this setup can be seen in Fig. 6.13.

These comparisons, along with the time taken for each simulation to reach a solution, can be seen in Table 6.4.

This table shows that the 5μm-thick copper wire simulation crashed. This was due to the mesh being unable to refine significantly enough to determine a solution based on the maximum number of passes/convergence criteria defined (note a simulation with these values increased was also produced but the simulation time exceeded 24 hours and also crashed).

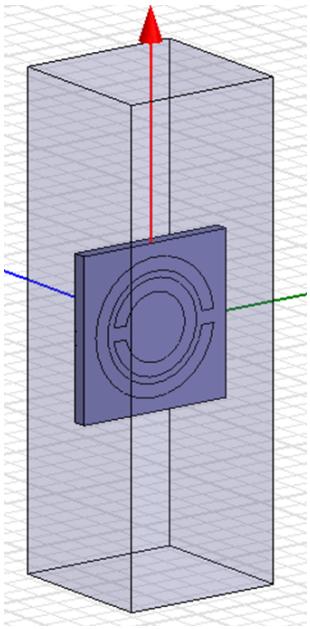

Figure 6.13: Figure showing an example of the wire/PEC on a substrate.

Wire Parameters	**Time Taken (mm.ss)**
0.5μm-thick copper wire	Crashed
5μm-thick copper wire	06.21
PEC wire (no thickness)	02.58

Table 6.4: Table showing the time taken for the different copper wire thickness/PEC SRRs simulations to complete.

Figure 6.14 shows the magnitude comparison of the S-parameters for the 5μm-thick copper wire and the PEC results, showing that there is a slight difference between the predicted behaviour, though for the x-band region there is very little to no difference in the position of the resonant peak.

This is not surprising as the PEC wire is purely a 2-dimensional construct, and so any currents or interactions of any form with the incident wave do not exist, whereas they do in the 5μm-thick copper. Also, PEC is, by definition, a Perfect Conductor, copper is not. This may result in small losses and eddy

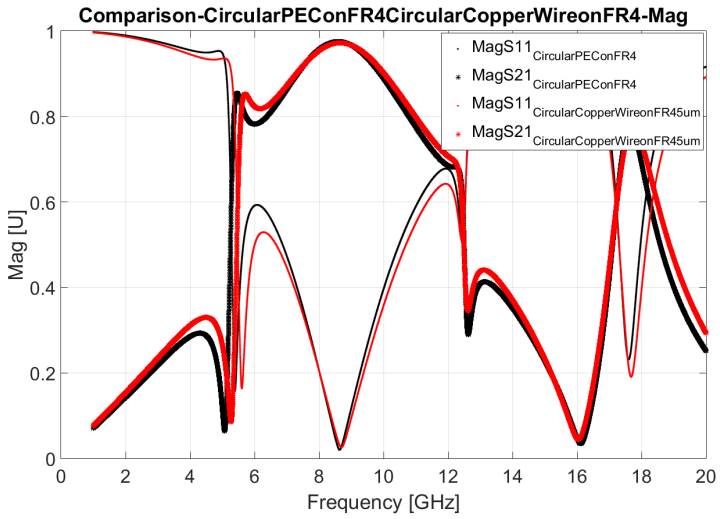

Figure 6.14: Figure showing there is a slight discrepancy in the magnitude of the scattering parameters between the 5μm and the PEC simulations. However there is very little difference in the region of interest.

currents being possible in the 5μm-thick copper and not in the PEC.

However, the time taken to simulate the PEC structure is less than half that taken to run the copper. Therefore, the simulations were conducted with the PEC wire, with note being made that the resulting behaviour may not occur at precisely the predicted manner when tested experimentally.

PEC wires for SRR designs.

6.3 Shape

This next section covers the geometric optimisation simulations, produced with the aim of creating a unit cell design for use in high power applications. The absorptivity predictions will be used in this discussion, determined using $A(\omega) = 1-|S_{11}|^2-|S_{21}|^2$ (Eq. 2.17) as a simple, quick measure of a unit-cells possible absorption characteristics.

A number of different unit cell arrangements were investigated; SRRs on FR4 Printed Circuit Board (PCB) and CSRRs for circular, square, a cog and a disc geometry. The thickness of the FR4 was 0.5mm, and the CSRRs were made from copper which also had a thickness of 0.5mm. These different designs can be seen in Fig. 6.15. As comparisons are being made between the SRR and CSRR systems, one could (incorrectly) presume that these designs should have simply the inverse behaviour of one another, as discussed in Chapter 3.3. However, a key point to note is that the SRR has a substantially different unit cell composition to the CSRR; the copper SRR is on a dielectric substrate compared to the pure copper composition of the CSRR.

Table 6.5 summarises the simulation time for each of these designs.

6.3.1 Square

The behaviour of both the magnitude and phase of S_{11} and S_{21} and the absorptivity were of interest in these simulations. Comparison plots can be seen in Fig. 6.16 and 6.17, showing that the behaviour of both systems are actually quite different.

This shows that the CSRR has a much simpler behaviour, showing 2 very clear resonance peaks in the magnitude of the S-parameters, coinciding with two very distinct phase shifts. The PEC on FR4 arrangement however predicts a much more complicated behaviour, demonstrating 4 drops in S_{11}

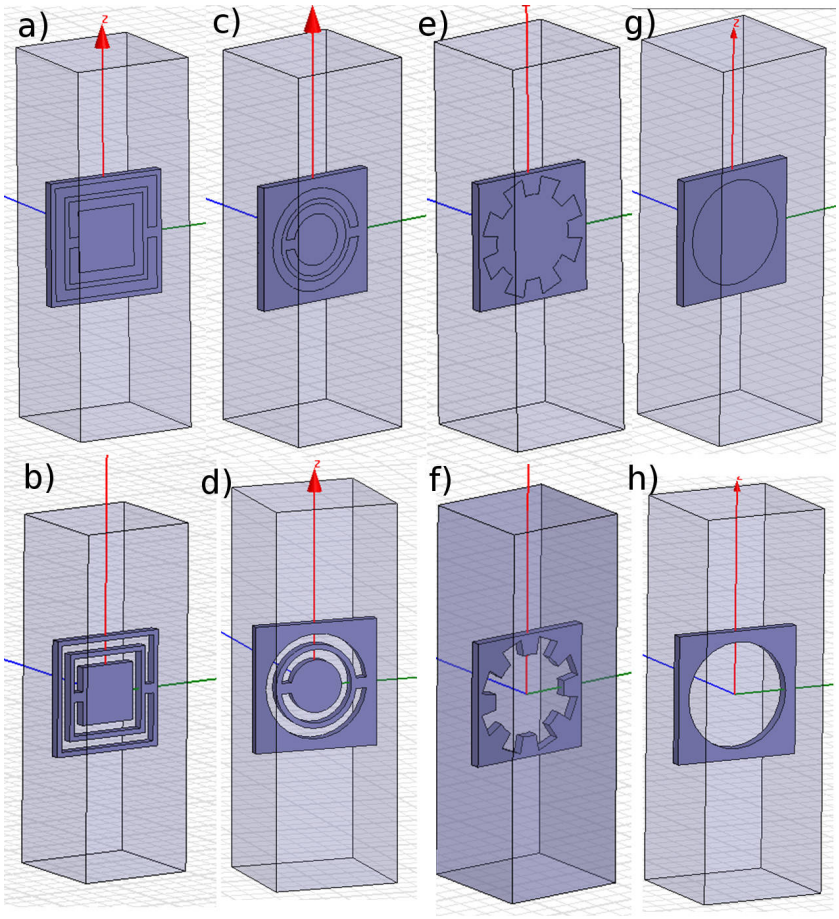

Figure 6.15: Geometries Simulated: a) Square SRRs on FR4, b) Square CSRR counterpart, c) Circular SRRs on FR4, d) Circular CSRR counterpart, e) Cog on FR4, f) Cog Complementary counterpart, g) Disc on FR4, h) Hole in Copper (Disc counterpart)

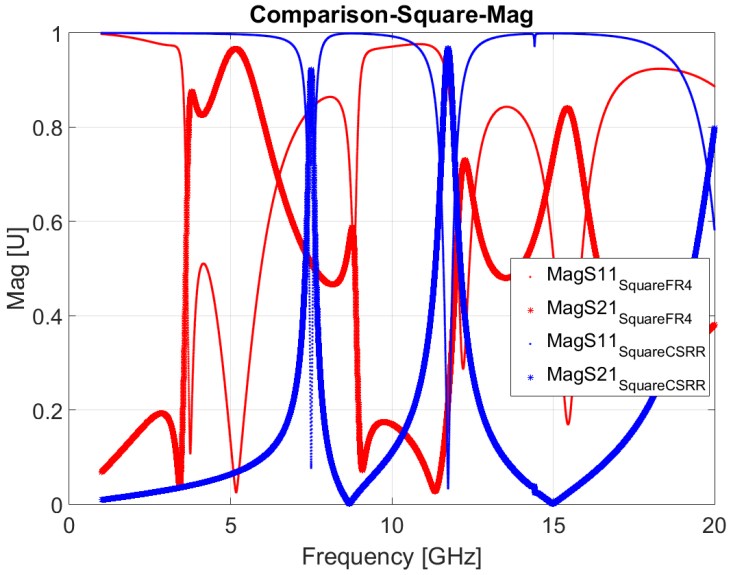

Figure 6.16: Plots comparing the magnitude of the S-parameters of the square geometries (SRR on FR4 and CSRR).

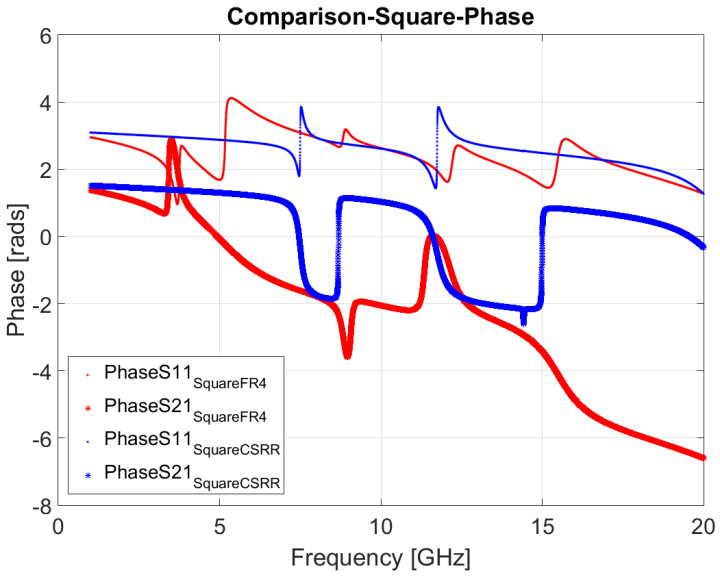

Figure 6.17: Plots comparing the phase of the S-parameters of the square geometries (SRR on FR4 and CSRR).

Shape	Time Taken (mm.ss)
Square SRR on FR4	02.48
Square CSRR	03.25
Circular SRR on FR4	02.54
Circular CSRR	02.17
Cog on FR4	01.54
Cog Complementary	01.29
Disc on FR4	01.29
Hole in Copper	01.50

Table 6.5: Table showing the time taken for the different geometry simulations to complete.

coinciding with 4 phase shifts over the frequency range simulated. These peaks are also seen in the absorptivity plots for the materials, shown in Fig. 6.18. The PEC on FR4 system is shows an almost consistently higher absorptivity compared to the copper CSRR system, suggesting that the CSRR system would be better at withstanding the higher power environments before suffering from break-down.

Therefore one can conclude that, although both geometries demonstrate interesting, engineered behaviours, the CSRR system would be most suited (out of the two shown here) for high power environments.

CSRR Square

6.3.2 Circular

Comparison plots of the magnitude and phase of the scattering parameters, along with the associated absorptivity plots, can be seen in Fig. 6.19, 6.20 and 6.21 respectively.

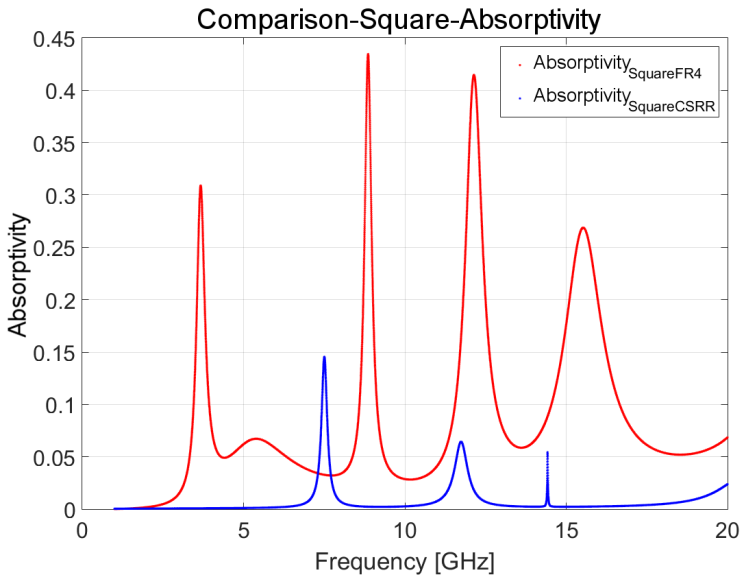

Figure 6.18: Plots comparing the absorptivity of the square geometries (SRR on FR4 and CSRR).

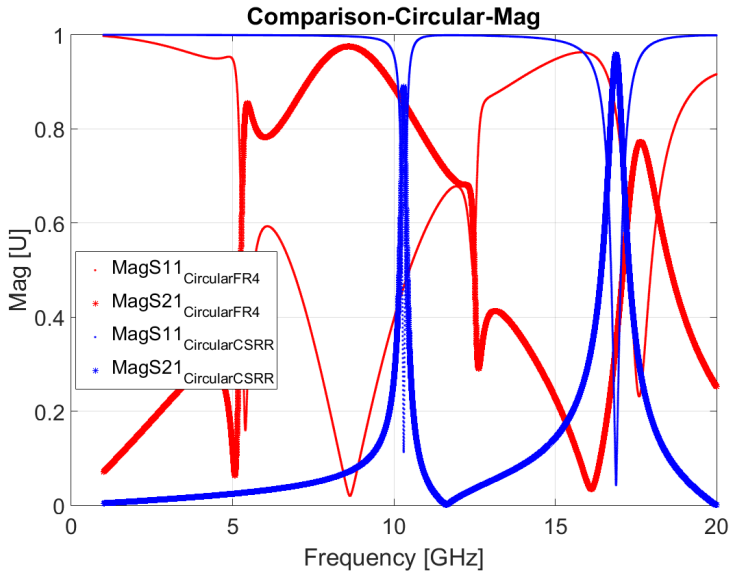

Figure 6.19: Plots comparing the magnitude of the S-parameters of the circular geometries (SRR on FR4 and CSRR).

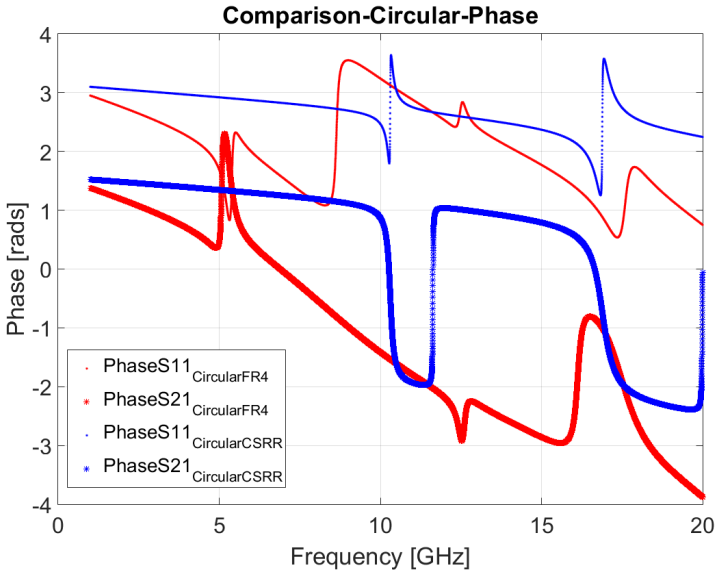

Figure 6.20: Plots comparing the phase of the S-parameters of the circular geometries (SRR on FR4 and CSRR).

Again the CSRR version of the geometry has resulted in 2 very distinct resonances in the magnitude of the scattering parameters, coinciding with two very clear phase shifts. The PEC on FR4 version is once again quite messy, though 3 resonant peaks in magnitude can be observed, each with corresponding phase shifts. Once again the absorptivity plots are used to show the feasibility of these designs for high power applications, once again showing that the frequencies of highest peaks correspond to the resonant frequencies of the unit cell.

One can conclude that, although both geometries are again interesting and demonstrate interesting, engineered behaviours, the CSRR system would be most suited (out of the two shown here) for high power environments.

CSRR Circular

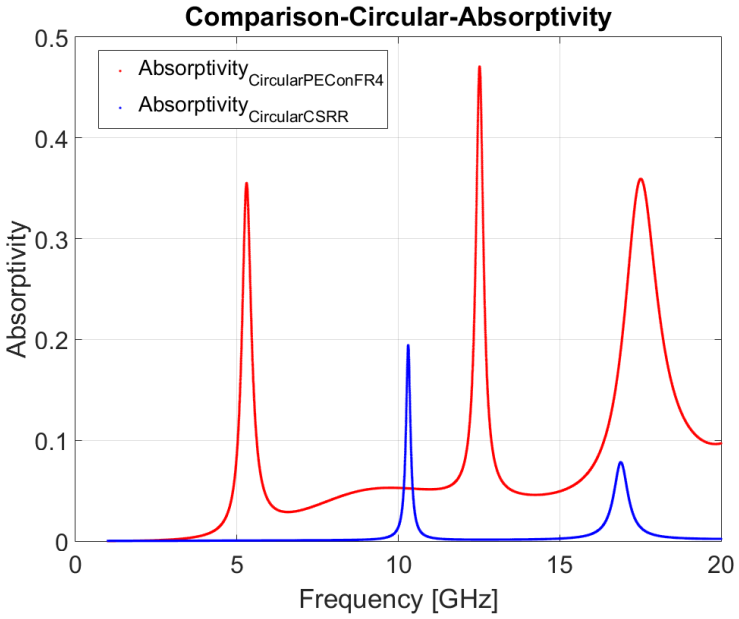

Figure 6.21: Plots comparing the absorptivity of the circular geometries (SRR on FR4 and CSRR).

6.3.3 Cog

The Cog design was also simulated and the S-parameters for both magnitude and phase of S_{11} and S_{21} were determined. The plots of these can be seen in Fig. 6.22 and Fig. 6.23. These plots show that there is no resonant peak near the x-band region for the CSRR design (though the plot hints to one being located at a higher frequency than 20GHz). There is however a significant peak in the x-band region for the PEC on FR4, along with an associated phase shift.

By looking at the absorptivity plots for this design a local peak for the PEC on FR4 design is observed with a value of just over 0.05. This suggests that this design may withstand high power environments.

Out of these two designs only the PEC on FR4 design suggests any engineered behaviour around the x-band region. This design also suggests low

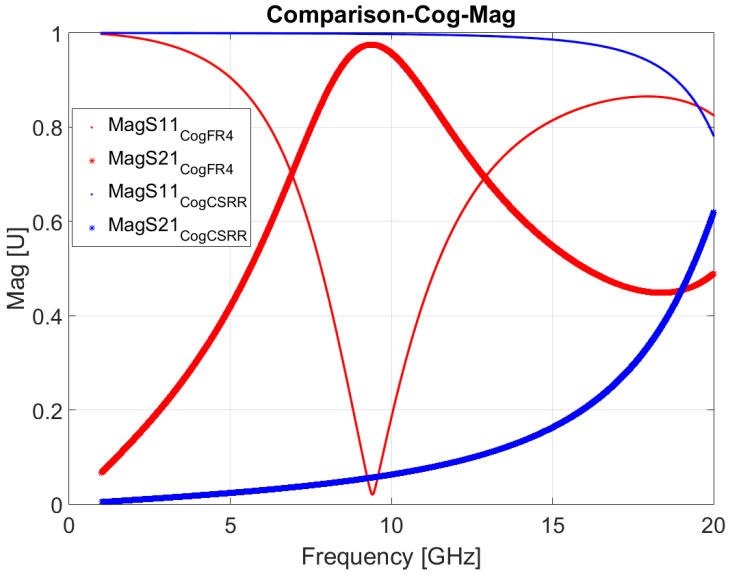

Figure 6.22: Plots comparing the magnitude of the S-parameters of the Cog geometries (SRR on FR4 and CSRR).

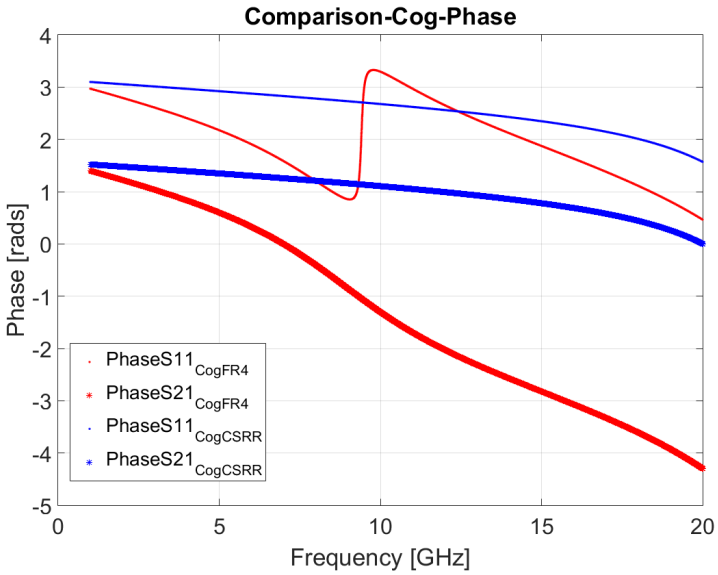

Figure 6.23: Plots comparing the phase of the S-parameters of the Cog geometries (SRR on FR4 and CSRR).

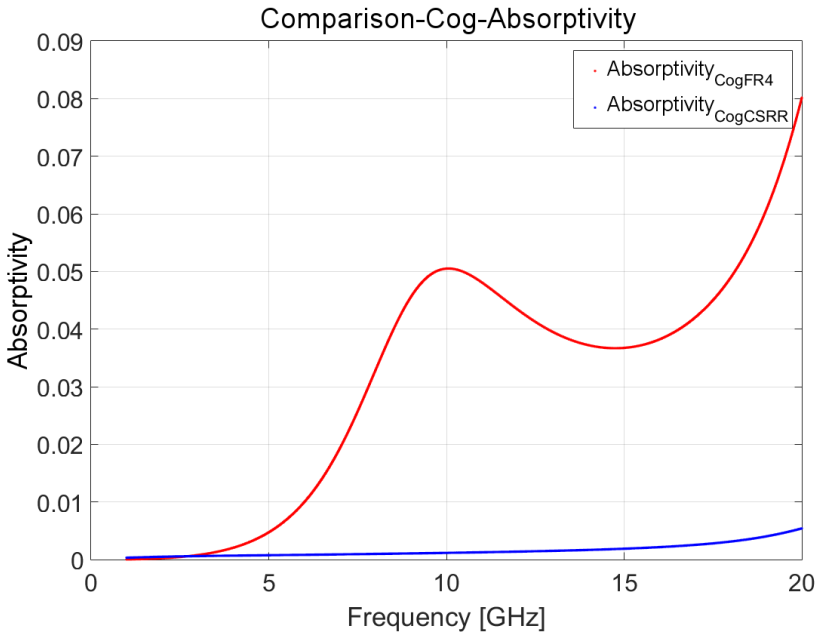

Figure 6.24: Plots comparing the absorptivity of the Cog geometries (SRR on FR4 and CSRR).

absorptivity, suggesting possible use for high power applications.

PEC on FR4 Cog

6.3.4 Disc

The final design simulated was the Disc design, again with the S-parameters for both magnitude and phase of S_{11} and S_{21} being determined. The plots of these can be seen in Fig. 6.25 and Fig. 6.26.

These plots show that there are no resonance peaks created in the frequency range simulated, nor any shifts in phase, therefore suggests no interaction occurring between the incident wave and the suggested geometry. This is re-iterated in the absorptivity plot, showing that there is very little absorption occurring over the range of interest.

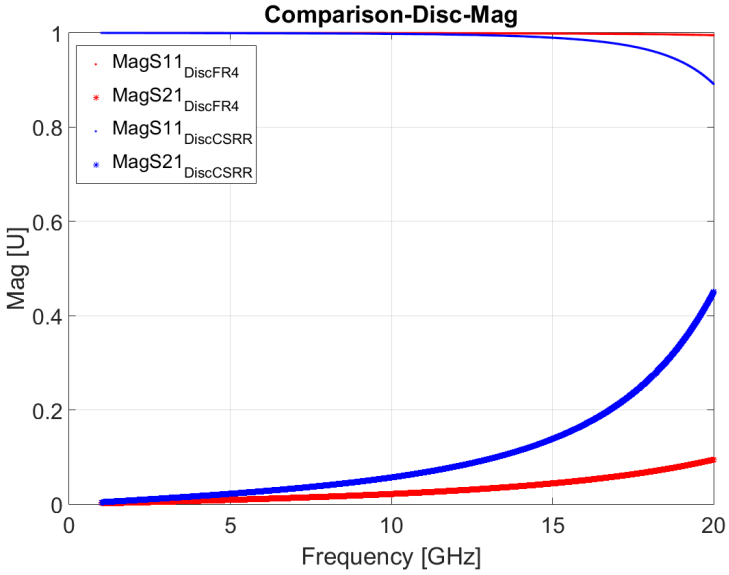

Figure 6.25: Plots comparing the magnitude of the S-parameters of the Disc geometries (SRR on FR4 and CSRR).

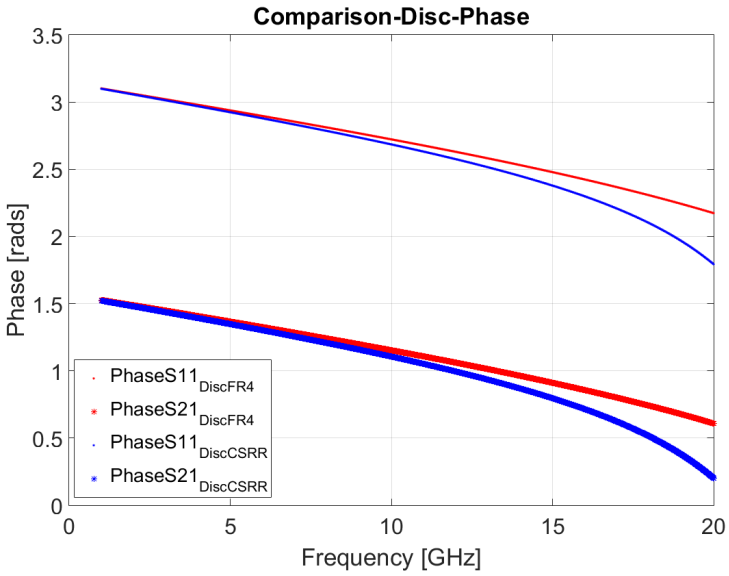

Figure 6.26: Plots comparing the phase of the S-parameters of the Disc geometries (SRR on FR4 and CSRR).

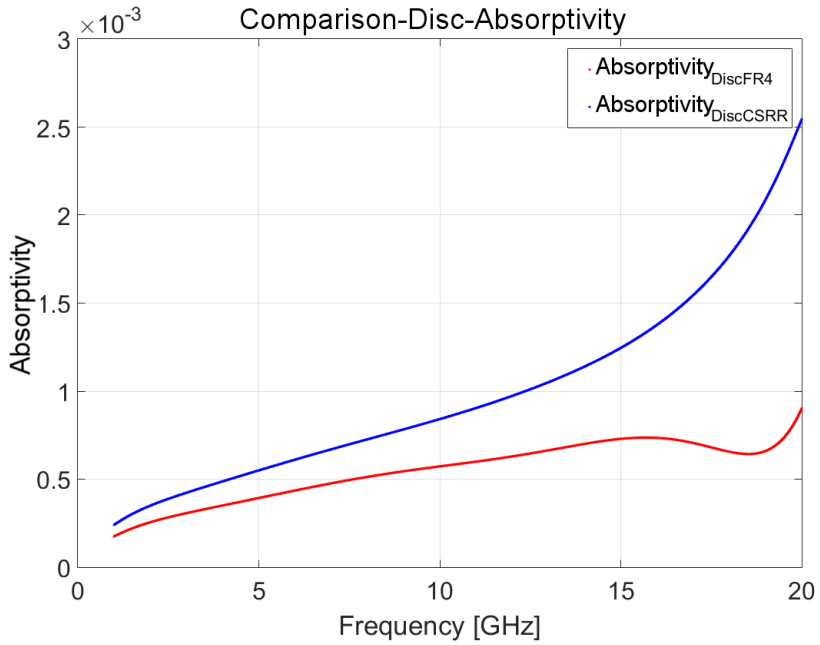

Figure 6.27: Plots comparing the absorptivity of the Disc geometries (SRR on FR4 and CSRR).

This shows that non of the disc geometries are worthwhile investigating further for operation in x-band, though the data does suggest a resonant peak at a higher frequency than the simulation covered.

6.3.5 Shape Summary

From the investigation into which shape would be most suitable for high power environments, these simulations suggest that the Square CSRR and the Circular CSRR are the most promising. The Square PEC on FR4 and Circular PEC on FR4 also demonstrate interesting behaviour, though would not be suitable for a high power environment due to the high absorption these structures demonstrate. The PEC on FR4 Cog geometry is also an interesting geometry, suggesting a single broad resonance peak located in x-band with low absorption.

However, only the circular CSRR design will be investigated further, as the final aim is to create these designs for experimental uses and the circular design is the easiest to manufacture.

Circular CSRR

6.4 Unit Cell Size

Simulations investigating a number of different unit cell sizes were conducted to determine what the best unit cell size would be. The unit cells are required to be significantly smaller than the incident wave so they can be treated as an effective medium. As x-band operation (8.2-12.4GHz, fundamental wavelength of 37-24mm) is required this would result in a free space cell size of around 2.4mm - 3.7mm. However, as the unit cells will eventually be operating in waveguide where the wavelength of the incident wave is effectively longer, this constraint can be increased slightly to 4.8mm - 7.4mm (5 unit cells per wavelength for this simulation). This gives a range of unit cell sizes to simulate, as seen in Table 6.6.

Unit Cell Size	**Time Taken (mm.ss)**
4.5mm	02.37
5.0mm	01.59
5.5mm	02.19
6.0mm	02.18
6.5mm	02.03
7.0mm	03.13
7.5mm	02.22

Table 6.6: Table showing the time taken for the different geometry simulations to complete.

The general geometry of the unit cells can be seen in Fig. 6.28, where the entire geometry was scaled up or down to result in the unit cell size simulated.

The S-parameters were once again determined, and the plots of the magnitude and absorptivity of the different unit cell sizes can be seen in Fig. 6.29, Fig. 6.30 and 6.31 respectively.

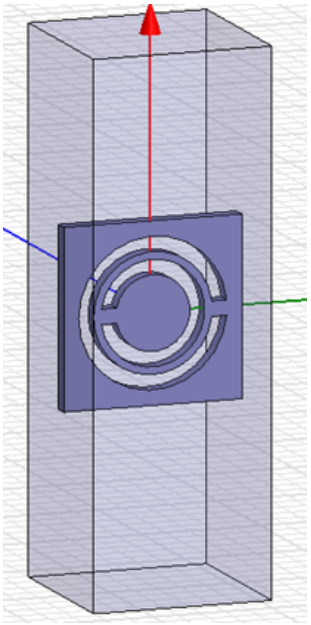

Figure 6.28: Image showing the geometry of the unit cell when simulating different Unit Cell Sizes. This geometry was scaled up or down depending on the desired unit cell size.

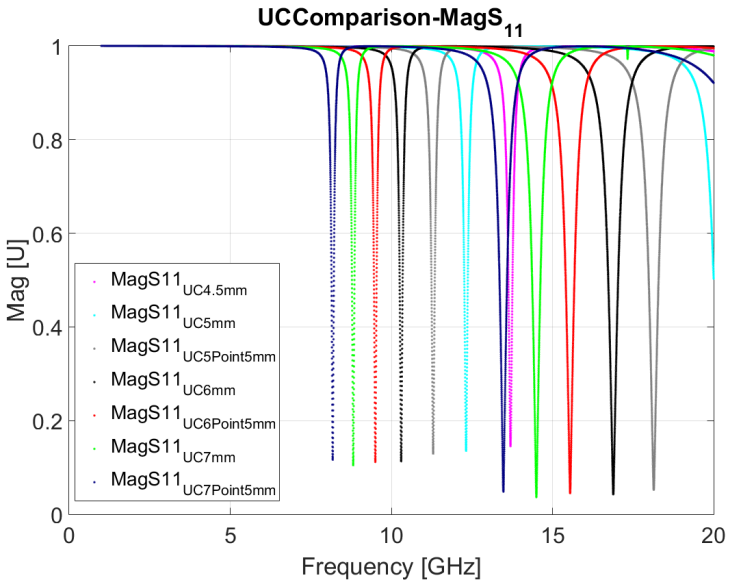

Figure 6.29: Plots comparing the magnitude of S_{11} of the different sized unit cells.

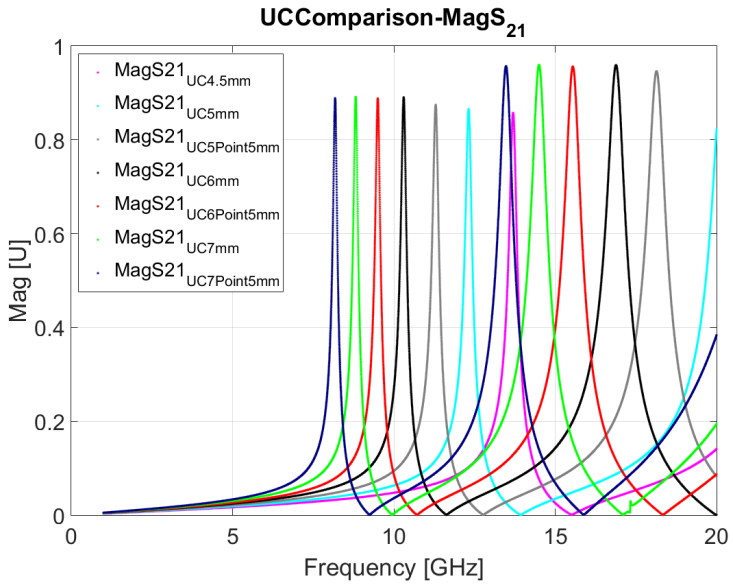

Figure 6.30: Plots comparing the magnitude of S_{21} of the different sized unit cells.

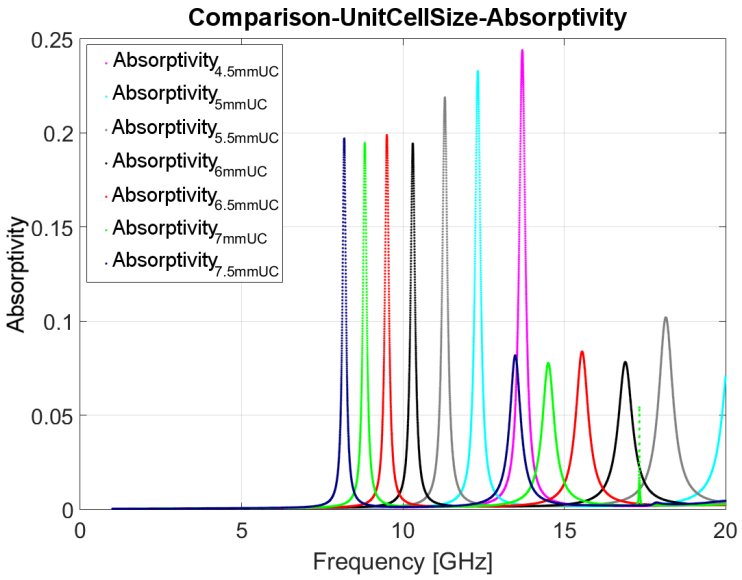

Figure 6.31: Plots comparing the absorptivity of the different sized unit cells.

6.4.1 Unit Cell Size Summary

From these plots two things can be deduced; increasing the unit cell size reduces the frequency of the resonant peak, slightly increasing the value of S_{21} as it does so, and increasing the unit cell size decreases the absorptivity until the unit cell size is 6mm or larger (then the value for absorption doesn't change much). Therefore the unit cell sizes of interest will be 6mm or larger, until the effective medium condition is no longer valid.

6.5 Rotation around Z axis

For this set of simulations the unit cell was rotated around the direction of wave propagation to see how being at an angle relative to the incident wave would affect the electromagnetic response of the unit cell. All of these simulations took a very similar amount of time to complete (around 2 minutes 10 seconds). Rotations of 0°, 45° and 90° can be seen in Fig. 6.32, though the complete number of rotations simulated can be seen in Table 6.7. Remember here that the simulations consist of 2 modes, orientated perpendicular to one another so as to not interfere with each other.

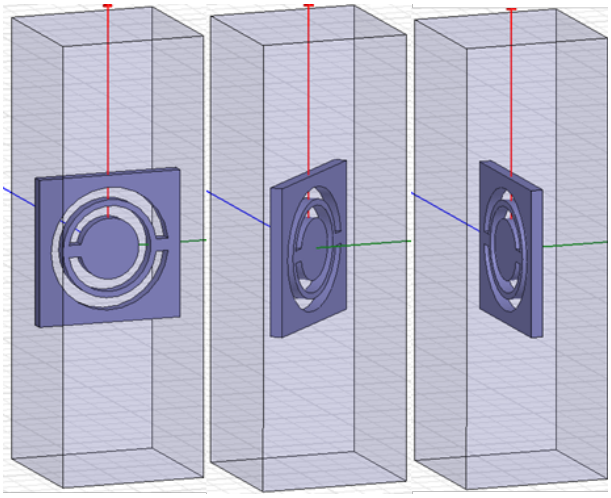

Figure 6.32: Image showing rotations of 0°, 45° and 90° around the Z axis.

Looking at the magnitude of S_{11} for the different modes of the incident wave shows that by rotating the unit cell the interacting mode is shifted from one mode to the other. This can be seen in Fig. 6.33a), where the magnitude in S_{11} for Mode 1 begins at a minimum (i.e. no resonant peak present), then increases until 90° where a strong resonance peak is present, before decreasing back to a minimum again. Figure 6.33b) shows where the value of S_{11} for Mode 2, starting off with a strong resonance peak, with the strength dropping until 90° rotation before increases again back to where it

Rotation Around Z axis
0°
15°
30°
45°
60°
75°
90°
105°
120°
135°
150°
165°
180°

Table 6.7: Table showing the time taken for the different rotations around Z simulations.

started.

6.5.1 Rotation Around Z Axis Summary

This shows that the orientation of the unit cell compared to the incident wave can be optimised to set up an interaction with either a TE or TM mode wave once the unit cells are loaded into waveguide.

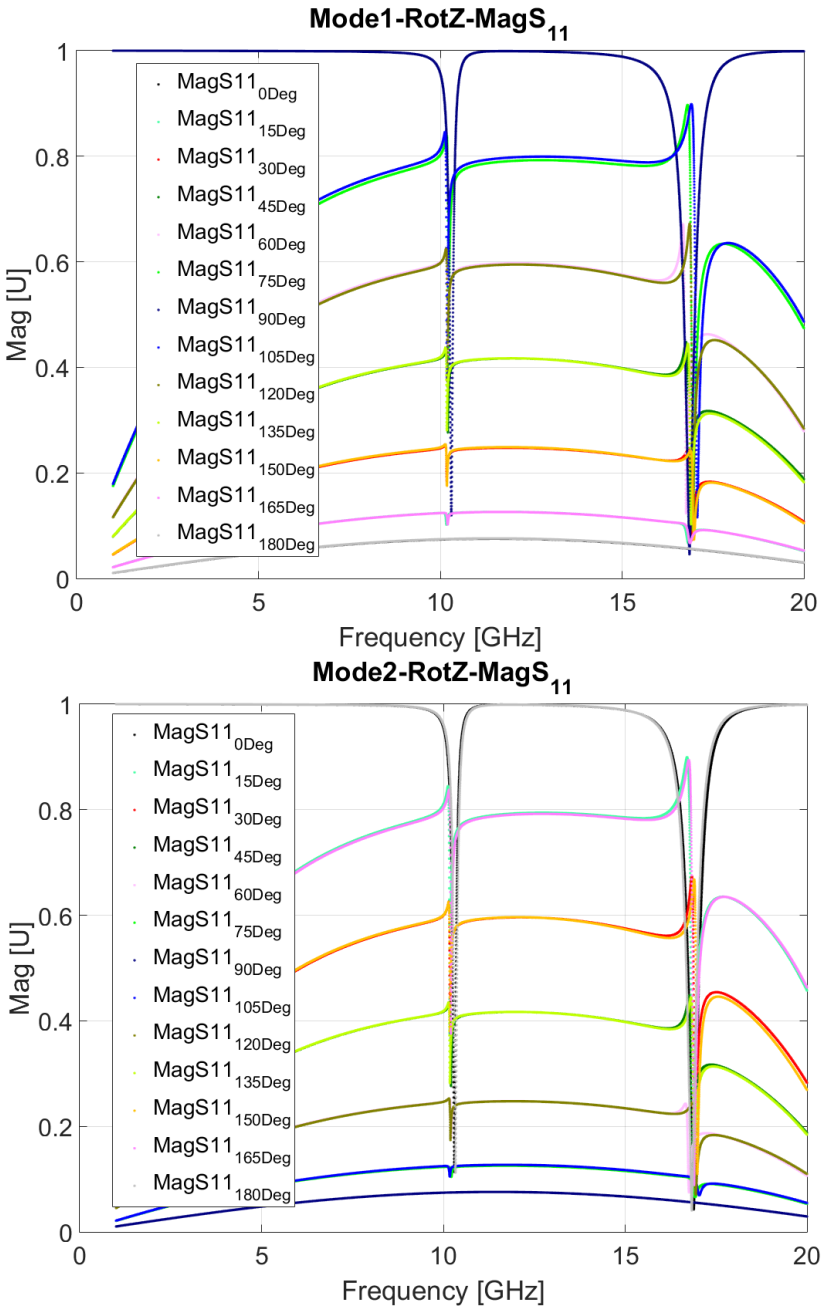

Figure 6.33: Plots of S_{11} for the two different modes of the incident wave. a), where the magnitude in S_{11} begins at a minimum (i.e. no resonant peak present), then increases until 90° before decreasing back to a minimum again. b) where the value of S_{11} initially drops until 90°, then increases again back to its original value.

6.6 Radius

Simulations optimising the radius of the split rings were run. Simulations comparing a single split ring to 2 and even 3 rings were run to determine the effect of each split ring on the overall behaviour of the unit cells. These simulations are discussed individually for 1 ring, 2 rings and the maximum of 3 rings for the unit cell dimensions chosen.

6.6.1 1 Ring

For the 1 ring simulations, radii of 1.00mm, 1.75mm, 2.35mm and 2.90mm were run; the geometries of these are shown in Fig. 6.34.

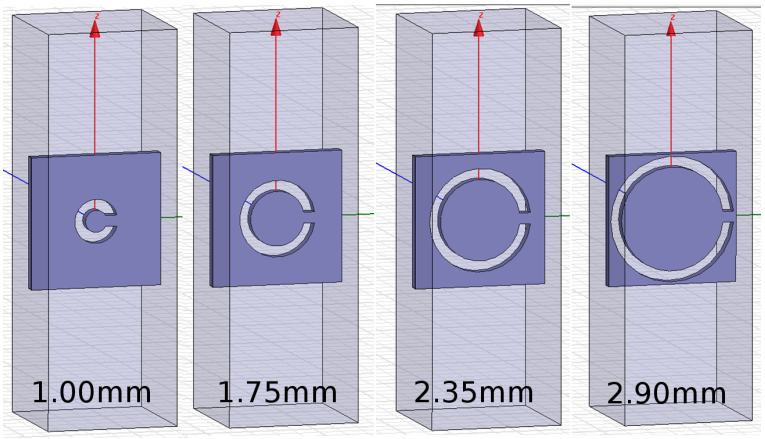

Figure 6.34: Image showing the geometry of the 1 ring radius alteration simulations, for rings with a 1mm, 1.75mm, 2.35mm and 2.90mm radius.

Looking at the plots of the magnitude of the S-parameters, Fig. 6.35, and the absorptivity plot, Fig. 6.36, shows how altering the radius size can manipulate the EM properties of the material.

These plots show that by increasing the ring radius the resonant frequency of the split ring is reduced, bringing it down from well above 20GHz (1.00mm

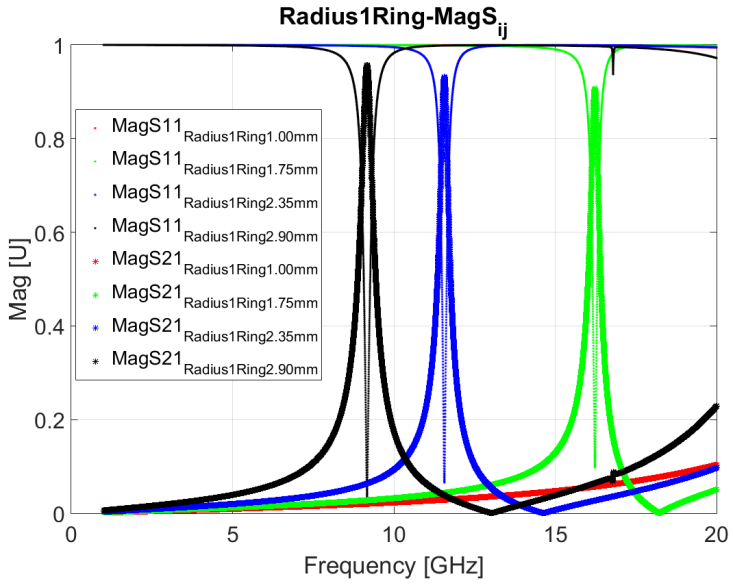

Figure 6.35: Plot of the magnitude of the S-parameters for a single split ring of different radii (1.00mm, 1.75mm, 2.35mm and 2.90mm)

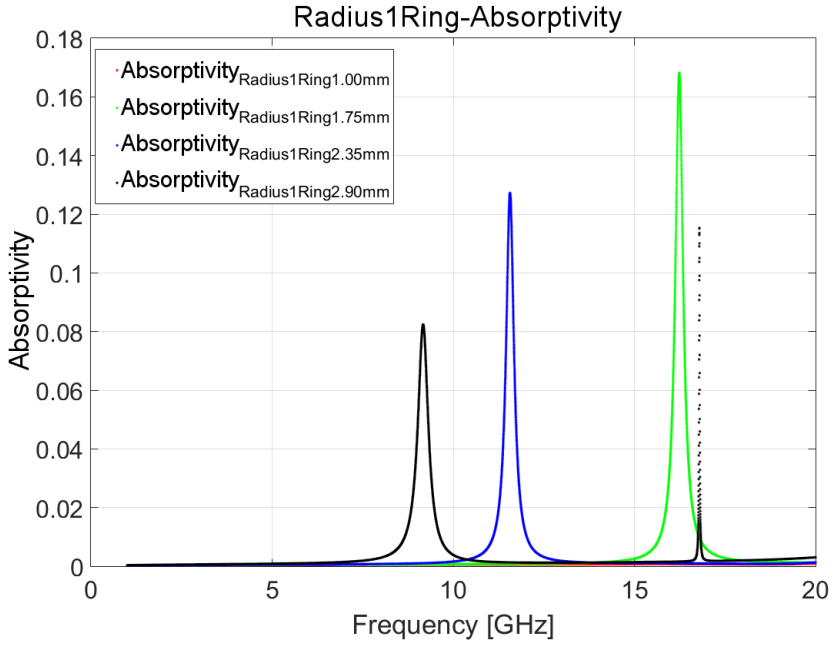

Figure 6.36: Plot of the absorptivity for a single split ring of different radii (1.00mm, 1.75mm, 2.35mm and 2.90mm)

ring) to the lower end of the x-band region (2.9mm ring). The larger ring also results in a lower absorption value.

6.6.2 2 Rings

6 simulations were run for the 2 ring simulations, as indicated by the 'x' in Table 6.8. The '-' signifies the simulations that were not possible (the inner ring would have been bigger than the outer ring!)

	Small In (1.00mm)	Mid In (1.60mm)	Big In (2.15mm)
Small Out (1.75mm)	x	–	-
Mid Out (2.35mm)	x	x	–
Big Out (2.9mm)	x	x	x

Table 6.8: Table showing different types of simulation run for 2 split rings in the unit cell arrangement. The 'x' signifies the simulations which were run, totalling 6.

Again, the magnitude of the S-parameters along with the absorptivity of the unit cells were determined and plotted. Figure 6.37 shows the magnitude results for the two ring system with the smaller ring set to 1.00mm and the outer ring varying in size, with Fig. 6.38 showing the absorptivity for the same setup. The results of the magnitude and absorptivity of the largest radius (2.90mm) single ring is also included showing how the addition of a second ring affects the overall behaviour of the unit cell.

These plots show that the adjustment of the inner ring radius seems to have a small effect on the position of the lowest frequency peak, moving it down in frequency by about 2GHz. However the largest effect is in the higher frequency peak, where increasing the radius of the inner ring drastically reduces the frequency where this peak is located.

Figure 6.39 shows the magnitude of the S-parameters for the system where

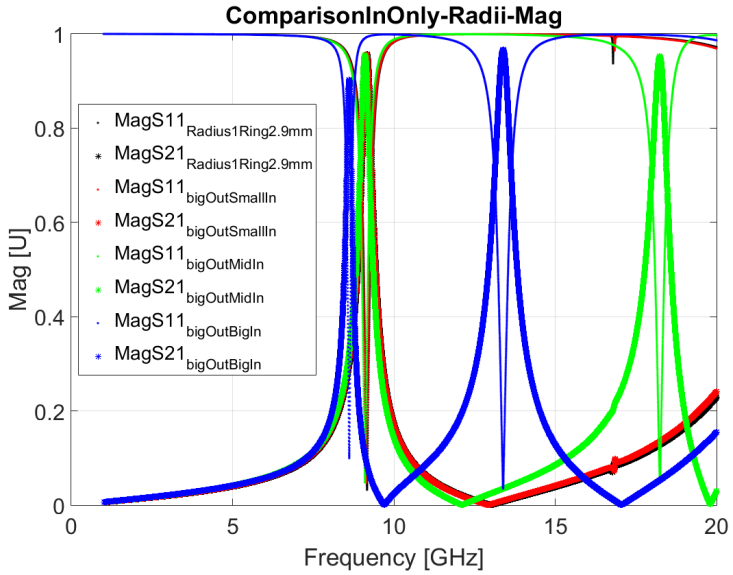

Figure 6.37: Plot of the magnitude of the S-parameters for two split rings of different radii with the inner ring set at the smallest value (1.00mm).

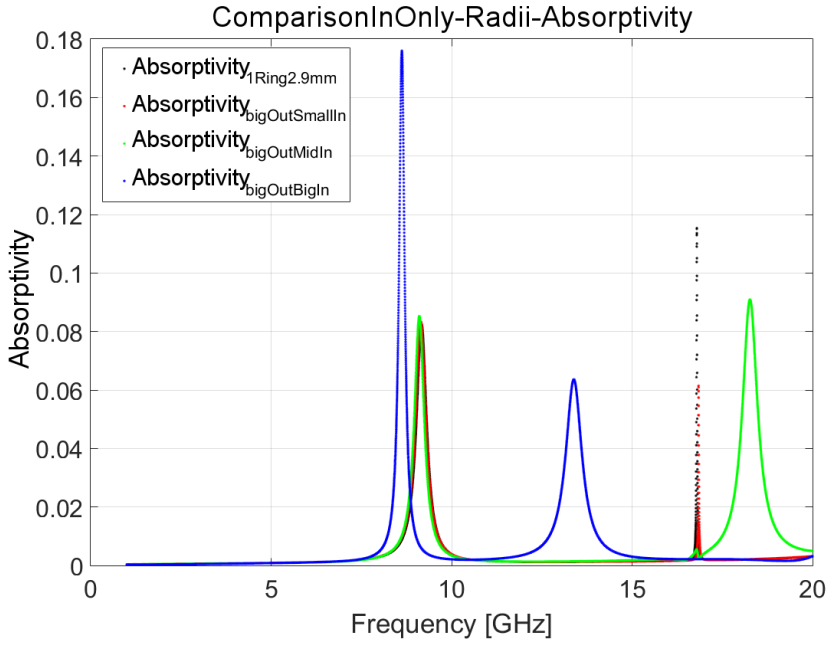

Figure 6.38: Plot of the absorptivity for two split rings of different radii with the inner ring set at the smallest value (1.00mm).

the outer ring is set to its largest value (2.90mm) and the outer ring varies in size. The absorptivity plot for this is seen in Fig. 6.40. The results of the magnitude and absorptivity of the smallest radius (1.00mm) single ring are also included, showing how the addition of a second ring affects the overall behaviour of the unit cell.

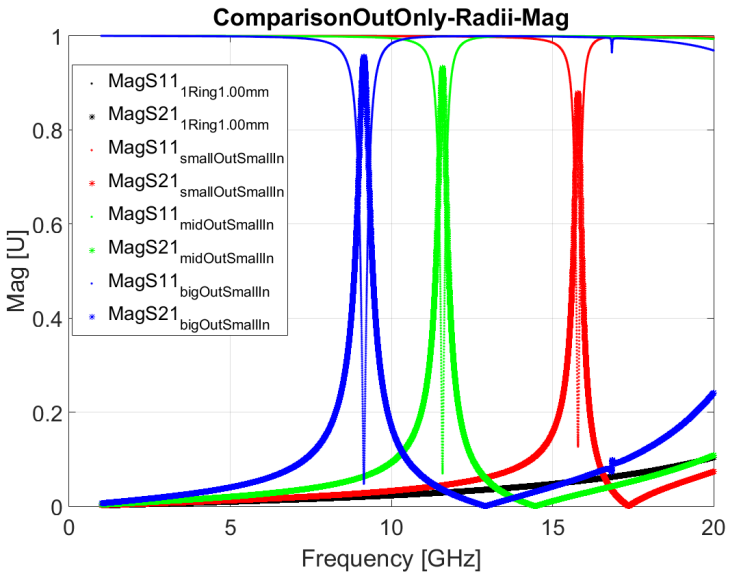

Figure 6.39: Plot of the magnitude of the S-parameters for two split rings of different radii with the outer ring set at the largest value (2.90mm).

These plots show that adjusting the outer ring radius has a substantial effect on where the lower resonance peak is located. The smaller inner ring has very little effect on the properties of this resonance peak.

6.6.3 3 Rings

The final simulation to be run in this section is the 3 Ring simulation. Only a single simulation was run for this, as the 6mm unit cell could not fit in more rings and only a single "middle" ring was suitable. The geometry of this can be seen in Fig. 6.41, where the radii are 1.40mm, 2.15mm and

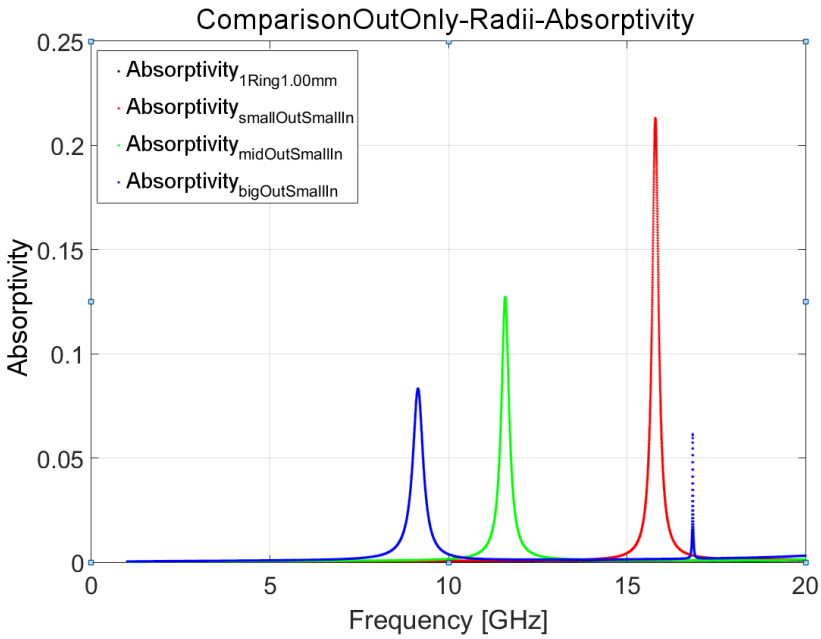

Figure 6.40: Plot of the absorptivity for two split rings of different radii with the outer ring set at the largest value (2.90mm).

2.9mm for the inner, middle and outer rings respectively.

Figure 6.42 compares the 3 ring simulation results with the 1 and 2 ring simulations, with all 3 simulations having the outer ring as large as possible (2.90mm). This plot shows that the addition of the third ring forces the lower frequency peak at an even lower value, though the middle ring creates a slightly higher peak where the 1 and 2 ring systems have none.

Figure 6.43 shows that the 3 ring system also suffers from significantly more absorption than the previous 1 and 2 row simulations. This is particularly troublesome at the lower frequency peak (this peak lies within x-band so could be useful) as the total absorption experienced by the structure is double that of the 1 and 2 row systems.

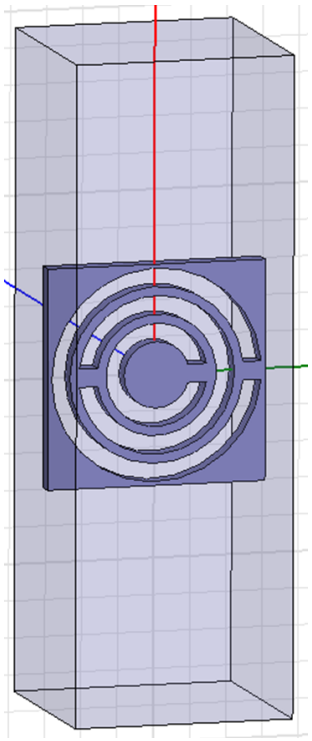

Figure 6.41: Image showing the geometry for the 3 ring simulation, where the radii are 1.40mm, 2.15mm and 2.9mm for the inner, middle and outer rings respectively.

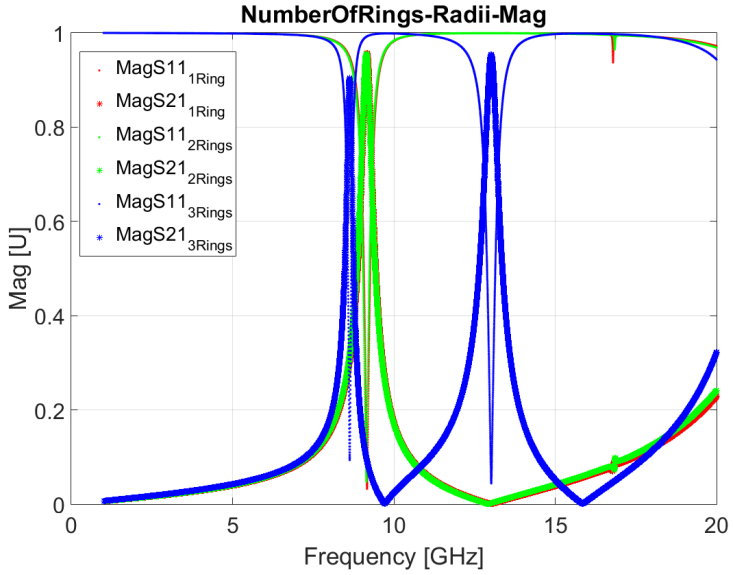

Figure 6.42: Plot of the magnitude of the S-parameters comparing the 1, 2 and 3 Ring unit cell designs for the largest possible outer ring (2.90mm).

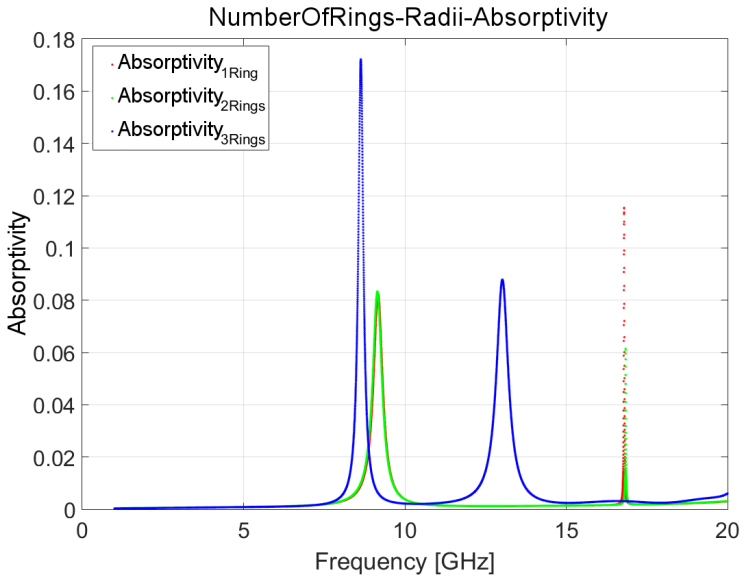

Figure 6.43: Plot of the absorptivity of the 1, 2 and 3 Ring unit cell designs for the largest possible outer ring (2.90mm).

6.6.4 Radii Summary

Based on the results of the simulations adjusting the radius of the split rings creating the unit cell design, the most suitable unit cell design is one with either 1 or 2 rings, where the outer most ring is as large as possible for the unit cell size. If 2 rings are required, then the inner ring should be as small as possible so as to not interfere with the created behaviour of the larger ring, as this increases the absorption, thus reducing the high power capabilities of the device.

6.7 Rotating Around Y axis

These simulations involved rotating the positions of the splits in the split ring resonators. 3 different types of simulations were run to achieve this: 1) a single split located in the inner ring only; 2) a single ring located in the outer ring only, and; 3) single splits in both rings.

6.7.1 Single Split In Inner Ring

A number of split locations were run and these are summarised in Table 6.9. The geometry of the -90°, 0° and +90° simulations can be seen in Fig. 6.44. Mention should be made at this point that this system is not physical; in real life, the lack of a split in the outer ring would result in a large hole in the material. However, the simulation does not need to concern itself with this, as the simulations are testing how the system would behave would this be the case.

The magnitude plot of the S-parameters, Fig. 6.45, shows a split in the inner ring results in a resonant peak at the high frequency end of the frequency range. Here one sees that the slight resonance which occurs at around 16GHz

Inner Ring Split Rotated Position
-90°
-67.5°
-45°
-22.5°
0°
22.5°
45°
67.5°
90°

Table 6.9: Table showing the different angles around Y the split in the inner ring was located.

comes into being as the split moves from -90° to 0°, disappearing again as the split continues to be rotated around the split ring, reaching its maximal value when the split in located at 0°.

The absorptivity plot, Fig. 6.46, also shows that there is the corresponding peak at the high frequency end also. The height of the peak increases as the resonance peak becomes more and more prevalent, reaching a maximum when located at +45° relative to the Y axis. This is possibly due to the split interacting with both Modes that the wave is producing, therefore storing energy in both x and y.

These simulations therefore suggest that the split in the inner ring should be located at 0° to the Y axis.

6.7.2 Single Split In Outer Ring

Once again, a number of split locations were simulated, summarised in Table 6.10. The geometry of the -90°, 0° and +90° simulations can be seen in Fig.

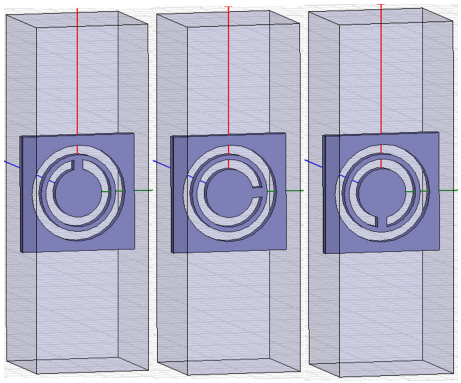

Figure 6.44: Plot of the geometry of the Rotating around Y simulations, showing the split located at -90°, 0° and +90° in the inner ring.

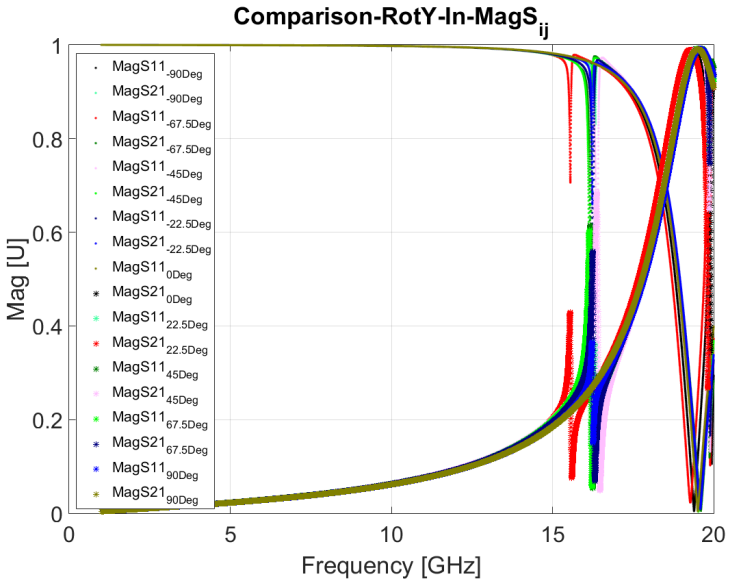

Figure 6.45: Plot of the magnitude of the S-parameters when the position of the split in the inner ring is rotated around the Y axis.

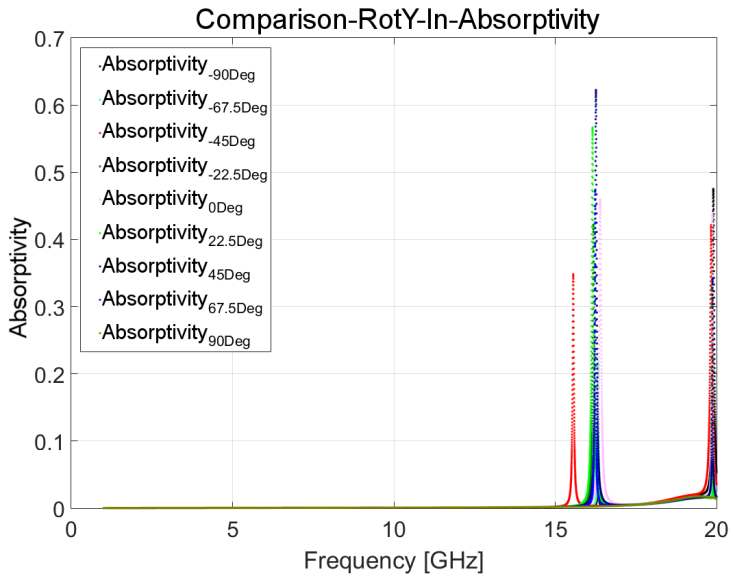

Figure 6.46: Plot of the absorptivity when the position of the split in the inner ring is rotated around the Y axis.

6.47. Mention should be made at this point that, again, this system is not physical; in real life, the lack of a split in the inner ring would result in a large hole in the material. However again, the simulation does not need to concern itself with this, as at the moment the simulations are testing how the system would behave would this be the case.

Again, looking at the magnitude of the S-parameters, Fig. 6.48, shows that a split in the outer ring results in a resonant peak at the lower frequency end of the frequency range. The slight resonance which occurs at around 16GHz comes into being and disappears again as the split is rotated around the split ring, reaching its maximal value when the split in located at 0°.

The absorptivity plot, Fig. 6.49, also shows that there is the corresponding peak at the high frequency end also, and that the height of the peak increases as the resonance peak becomes more and more prevalent.

These simulations therefore suggest that the split in the outer ring should

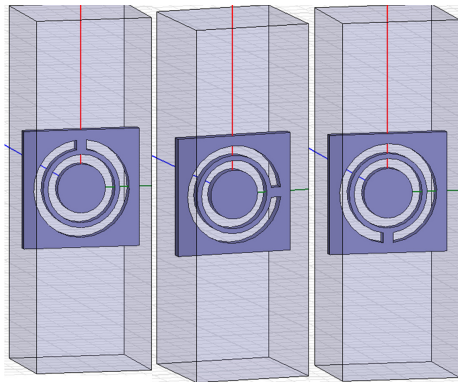

Figure 6.47: Plot of the geometry of the Rotating around Y simulations, showing the split located at -90°, 0° and +90° in the outer ring.

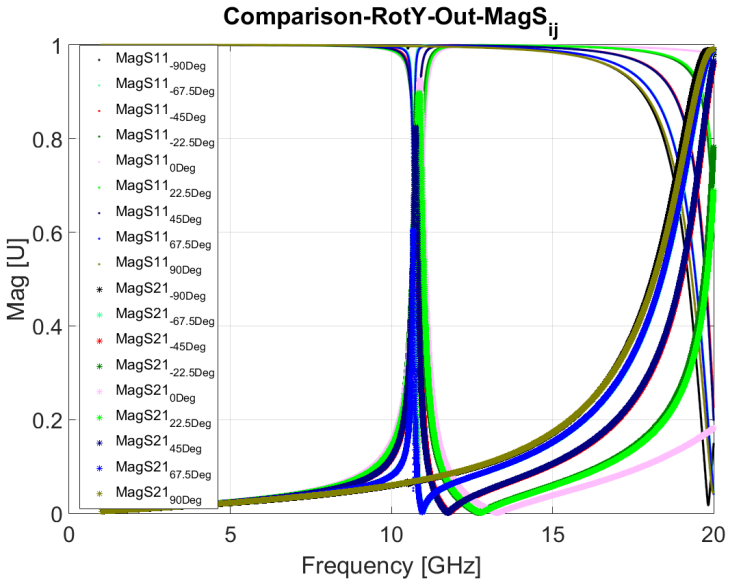

Figure 6.48: Plot of the magnitude of the S-parameters when the position of the split in the outer ring is rotated around the Y axis.

Outer Ring Split Rotated Position
-90°
-67.5°
-45°
-22.5°
0°
22.5°
45°
67.5°
90°

Table 6.10: Table showing the different angles around Y the split in the outer ring was located.

be located at 0° to the Y axis.

6.7.3 Single Split In Both Rings

Simulations were also conducted to test the EM behaviour of the unit cells when there was a split located in both split rings. Many simulations were run for this, so only a select few will be discussed here. A full view of all the simulations run can be seen in Table 6.50

The only set of results to be discussed will be when the outer split remains at 0°, as shown in Fig. 6.51.

The magnitude and phase of S_{11} can be seen in Fig. 6.52 (only S_{11} is shown so to not overfill the plot). This shows that as the rotation is increased from -90° to 90°, the resonant peak frequency is increased to a maximum point at 0°, then decreases again back to the point at which it originated.

The absorptivity plot for these simulations, Fig. 6.53, shows that as the

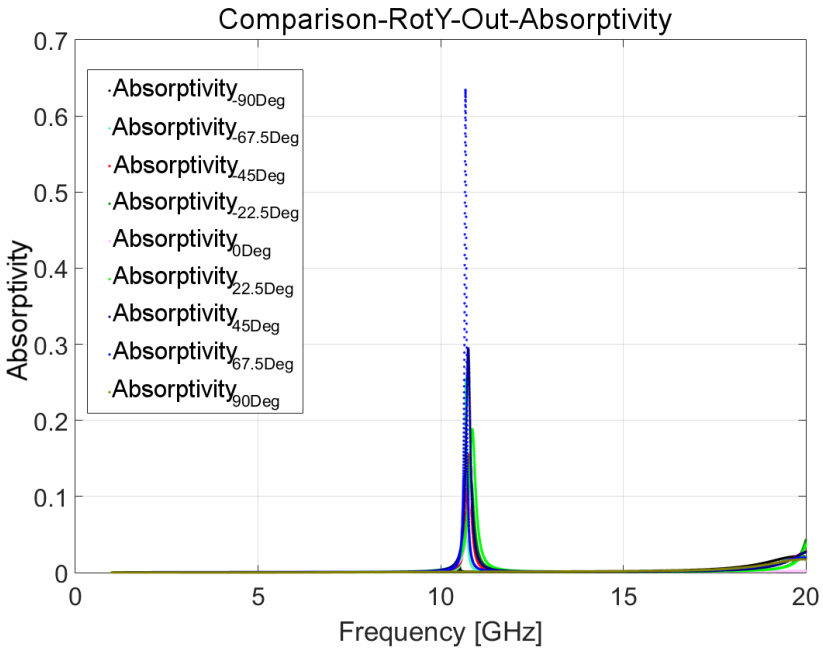

Figure 6.49: Plot of the absorptivity when the position of the split in the outer ring is rotated around the Y axis.

		In											
		-135	-90	-67.5	-45	-22.5	0	22.5	45	67.5	90	135	180
Out	-90		X	x	x	x	x	x	x	x	x		
	-67.5		x	x	x	x	x	x	x	x	X		
	-45	x										x	
	-22.5												
	0	x	x	x	x	x	x	x	x	x	x	x	x
	22.5												
	45	x	x	x	x	x	x	x	x	x	x	x	x
	67.5		x	x	x	x	x	x	x	x	x		
	90		x	x	x	x	x	x	x	x	x		
	180	-					x					-	-

Figure 6.50: Table showing all of the simulations run comparing splits located at different positions in each split ring, where the 'x' denoted simulations completed.

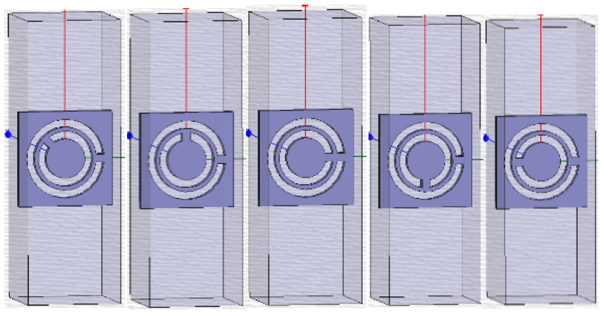

Figure 6.51: Image showing the rotation of the inner split when the outer split remains at 0°. Inner splits are located at -135°, -90°, 0°, 90° and 180°.

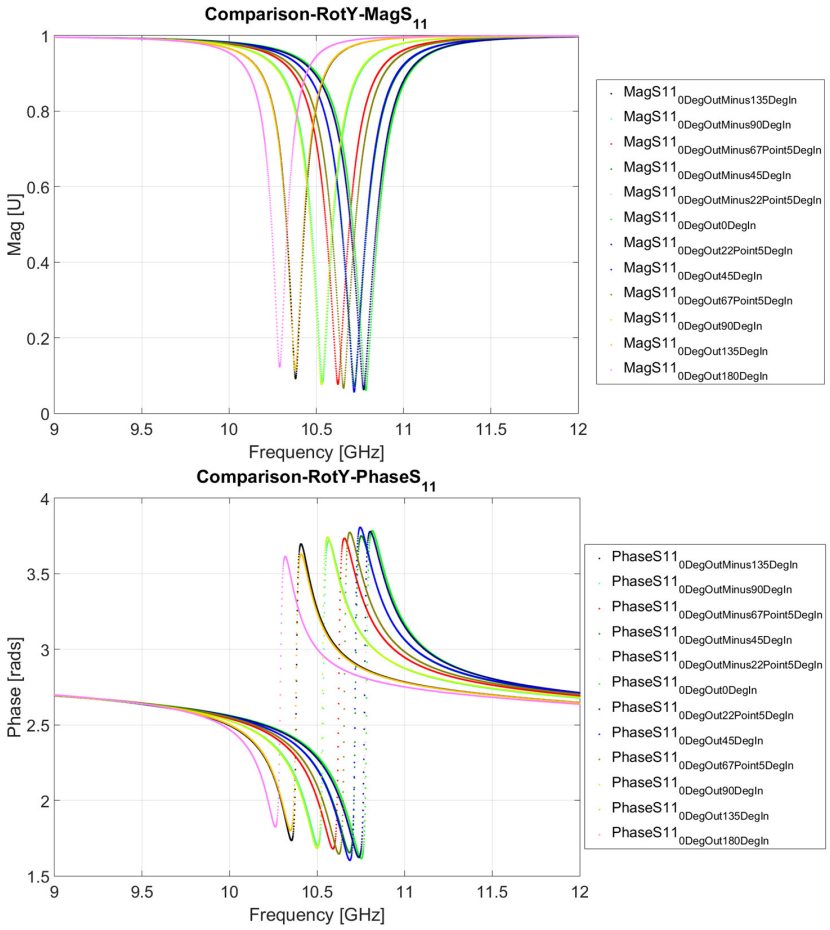

Figure 6.52: Plot showing how S_{11} is affected by the rotation of the inner split when the outer split remains stationary.

rotation increases the absorption experienced by the structure decreases to a minimum value of 0.12 at 0°.

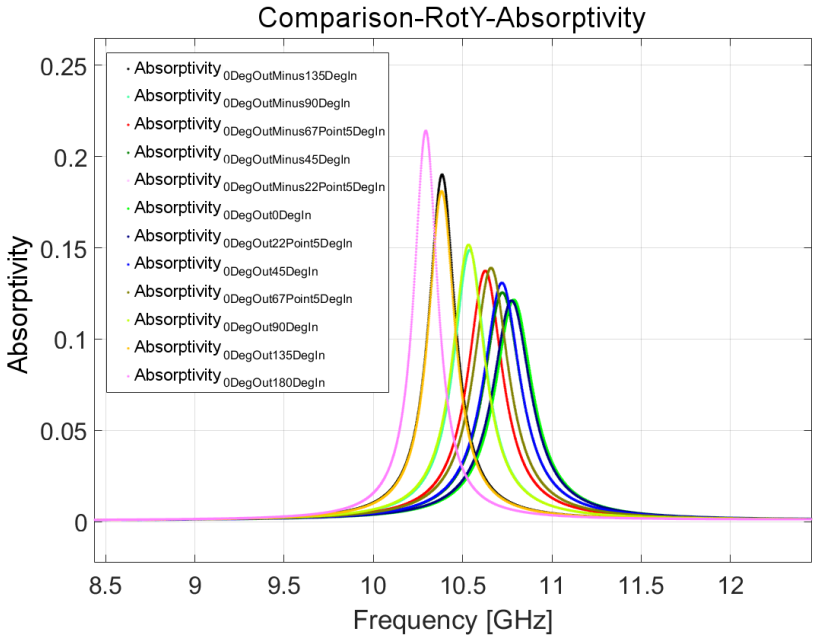

Figure 6.53: Plot showing how the absorptivity is affected by the rotation of the inner split when the outer split remains stationary.

6.7.4 Rotation Around Y Axis Summary

Moving the positions of the split in the inner ring effects the position and breadth of the higher peak whilst also having a significant effect on the lower peak. Moving the position of the split in the outer ring has a much larger effect on the position of the lower peak. By aligning the split positions, the absorptivity of the system is reduced, though this does also shift the peak frequency up by 0.5GHz compared to when the splits are located at opposite sides of the unit cell.

6.8 Material

A number of different materials were simulated to find the most suitable unit cell host material (i.e. good resonance response, low absorption etc). These can be seen in Table 6.11, along with the time taken for the simulation to complete. ε_r represents the relative permittivity of the host dielectric materials.

Material	**Time Taken (mm.ss)**
Brass	02.10
Copper	02.08
Tungsten	02.11
FR4 ($\varepsilon_r = 4.4$)	01.53
Glass ($\varepsilon_r = 5.5$)	01.34
Sapphire ($\varepsilon_r = 10$)	01.35
Rogers3010(tm) ($\varepsilon_r = 10.2$)	01.43

Table 6.11: Table showing the difference material simulations produced, along with the time taken for the simulation to complete. ε_r represents the relative permittivity of the dielectric materials.

The S-parameters S_{11} and S_{21} were extracted and the absorptivity of the system was calculated to determine which of the tested materials was best as the host material for the unit cell design. The geometry of this system is seen in Fig. 6.3, where the host material is the material that the CSRR is cut out of.

Dielectrics of different permittivity were tested to determine whether they had any effect on the EM properties of the unit cell. Figure 6.54 shows the magnitude of the S-parameters, showing that the dielectric material fails to allow a resonant peak in the frequency region of interest (this is probably why the simulations also took less time to run). All of the metal materials

produce a resonant peak at 10.5GHz.

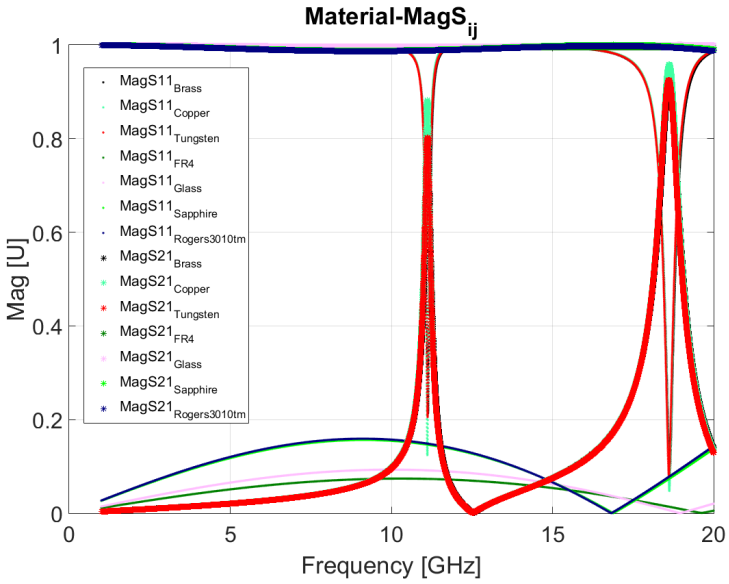

Figure 6.54: Plot showing how the magnitude of the S-parameters is affected when the host material is changed.

Plotting out the absorptivity of the different systems shows which of the materials are most suited for a high power environment. Figure 6.55 shows that the dielectric materials have very low absorption due to the lack of the presence of a resonance peak. The metals however do have increased absorption in the frequency region of interest. The lowest of these is caused by the copper.

6.8.1 Materials Summary

The copper arrangement can be seen to give the largest EM response as well as the lowest possible absorptivity for the metallic structures. The dielectric structures seem to not interact at this frequency range, though there is some interesting behaviour at the higher frequencies that may warrant further investigation. Therefore, copper is the material used for the final unit cell

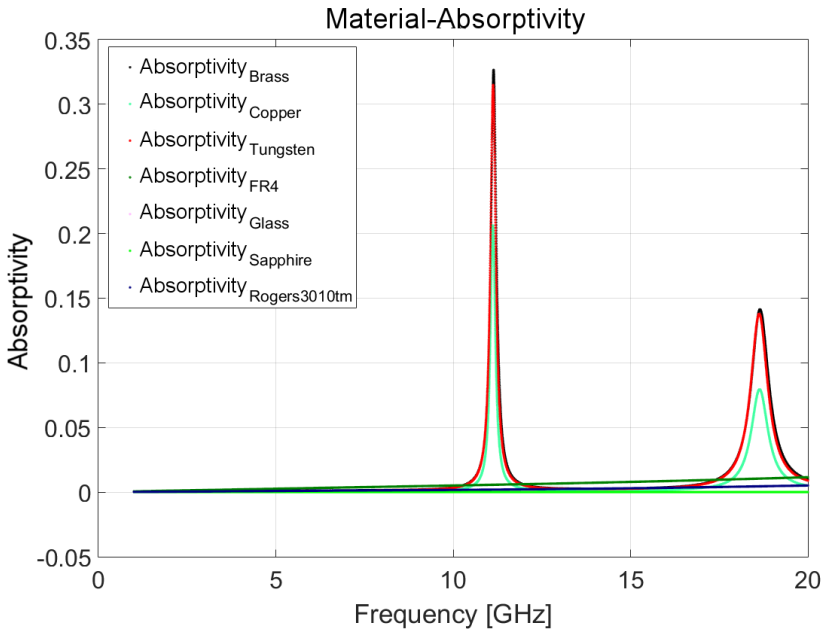

Figure 6.55: Plot showing how the absorptivity is affected when the host material is changed.

design.

6.9 Host Material Thickness

Simulations were run to determine how altering the thickness of the copper would affect the EM behaviour of the unit cell. 5μm, 50μm, 500μm, 1mm, 3mm and 5mm thicknesses were run, and the geometries of these can be seen in Fig. 6.56.

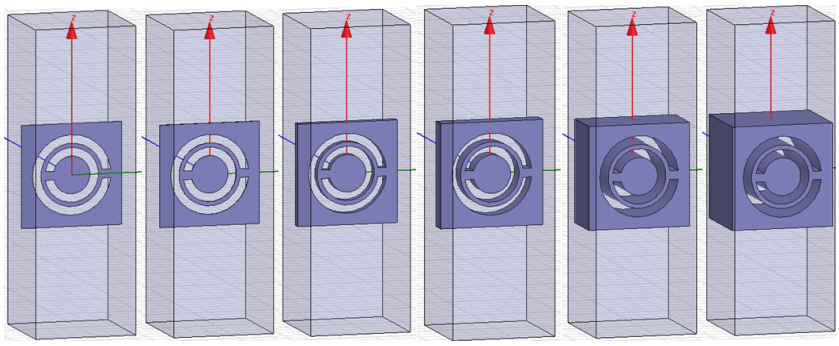

Figure 6.56: Geometry for the different thickness of the copper; 5μm, 50μm, 500μm, 1mm, 3mm and 5mm.

The magnitude of the S-parameters can be seen in Fig. 6.57, showing that the thicker the material, the higher but weaker the resonant peak frequency.

The absorptivity plot shows a similar picture; the thicker the material the higher the peak frequency, Fig. 6.58. This plot shows that the absorption for the 5μm thick copper is actually higher than that for the 50μm; this is probably due to the copper being so thin that the currents produced by the EM wave in the copper are fairly substantial as the resistivity of the material is fairly high. As the material gets to around 1mm in thickness, the bulk of the material is physically impeding the incident wave, so the absorption once again begins to increase, until eventually the thickness of the material overrides the resonant behaviour of the unit cell and the resonance is lost completely.

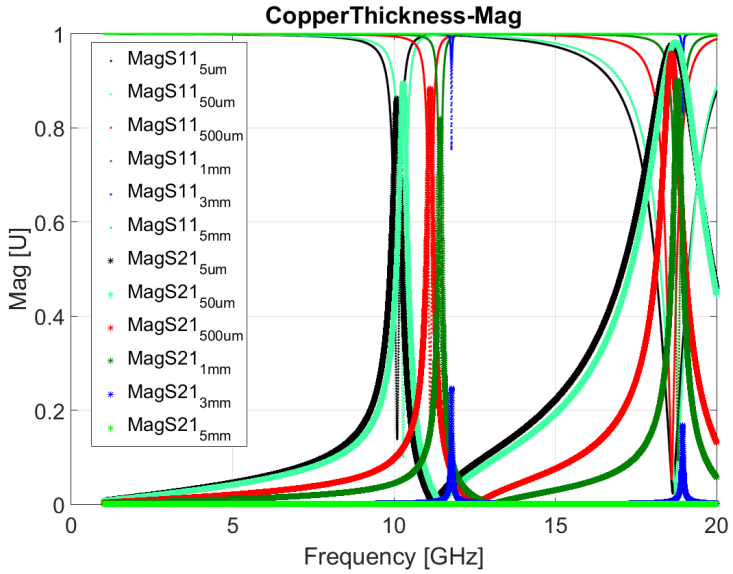

Figure 6.57: S_{11} and S_{21} plots showing how the different thickness of host material affect the frequency of the resonant peak.

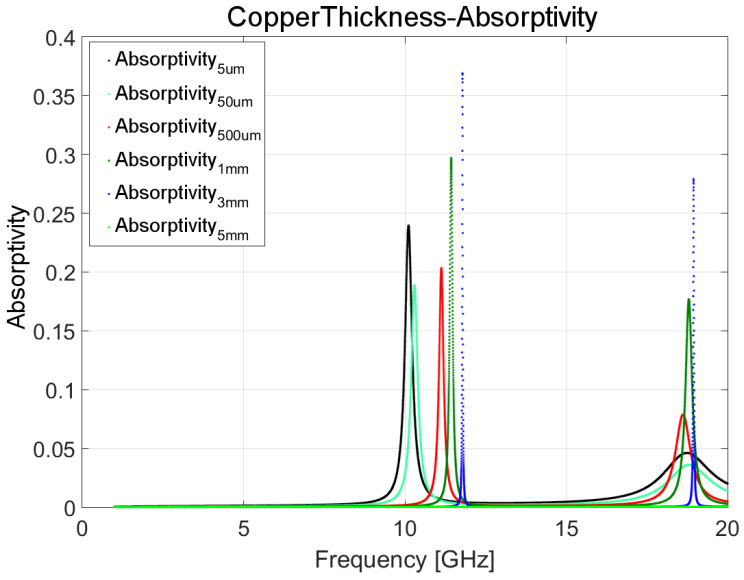

Figure 6.58: Plot showing the absorptivity for different thickness of copper host material.

6.9.1 Host Material Thickness Summary

From these simulations the copper thickness has been determined to have a significant effect on the position of the resonant peak, with the thinner material producing lowering the peak frequency. The thinner the copper, the better the EM response and the lower the absorption until the material is too thin to sustain the currents produced in the unit cell. Therefore, an ideal thickness of the copper host material lies between 50μm and 500μ. However, the thinner the material, the less structurally stable the material becomes; this needs to be accounted for when fabricating the structure.

6.10 Split Ring Width

The aim of these simulations was to determine the optimal width of the split rings. Figure 6.59 shows six of these simulation setups; the top images show where the inner ring is set to 0.25mm width and the outer ring varies in size (0.25mm, 0.50mm and 0.75mmm respectively). The bottom images show where the outer ring is set to 0.25mm width and the inner ring width is altered.

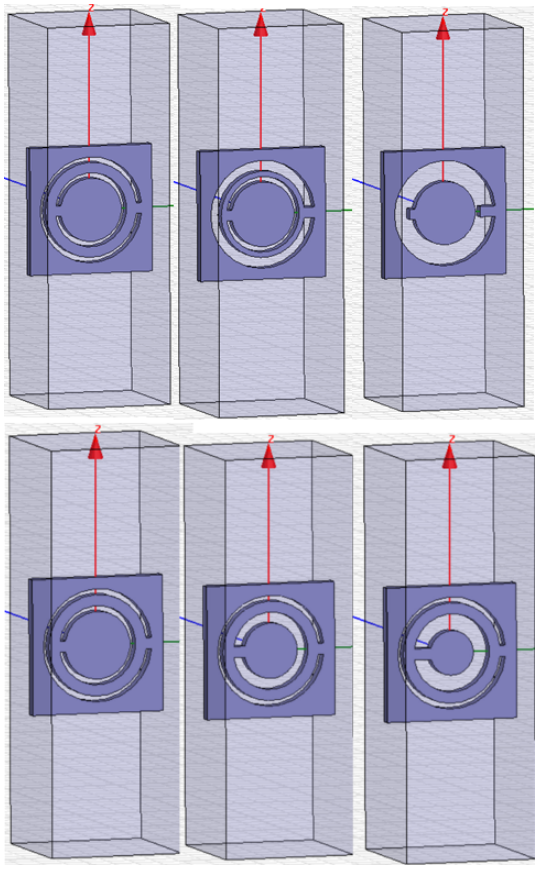

Figure 6.59: TOP: Inner ring kept at 0.25mm width and the outer ring varied between 0.25mm, 0.50mm and 0.75mm. BOTTOM: Outer ring kept at 0.25mm width and the inner ring varied between 0.25mm, 0.50mm and 0.75mm.

Table 6.12 shows all of the simulations which were run, where the 'x' shows that the simulations were completed.

	ThnIn (0.25mm)	MidIn (0.50mm)	ThkIn (0.75mm)
ThnOut (0.25mm)	x	x	x
MidOut (0.50mm)	x	x	x
ThkOut (0.75mm)	x	x	x

Table 6.12: Table showing different types of simulation run for different widths of the split rings.

6.10.1 Split Ring Width In = 0.25mm

By keeping the width of the inner ring the same the effect of altering the outer split ring width on the overall EM behaviour of the unit cell can be established. Figure 6.60 shows the magnitude of the S-parameters for the three simulations where the inner ring is thin. This plot shows that by increasing the outer ring width, one can fine tune the frequency position of the resonance peaks. The thickest ring width chosen overlaps with the inner ring, resulting in the loss of the resonant peak.

Figure 6.61 shows the absorptivity plot for these simulations, showing that as the split ring width increases, the absorption decreases.

Therefore the outer split ring width should be as thick as possible, without overlapping the inner ring.

6.10.2 Split Ring Width Out = 0.25mm

Keeping the width of the outer ring the same determines how the inner split ring width affects the overall EM behaviour of the unit cell. Figure 6.62 shows the magnitude of the S-parameters for the three simulations where the

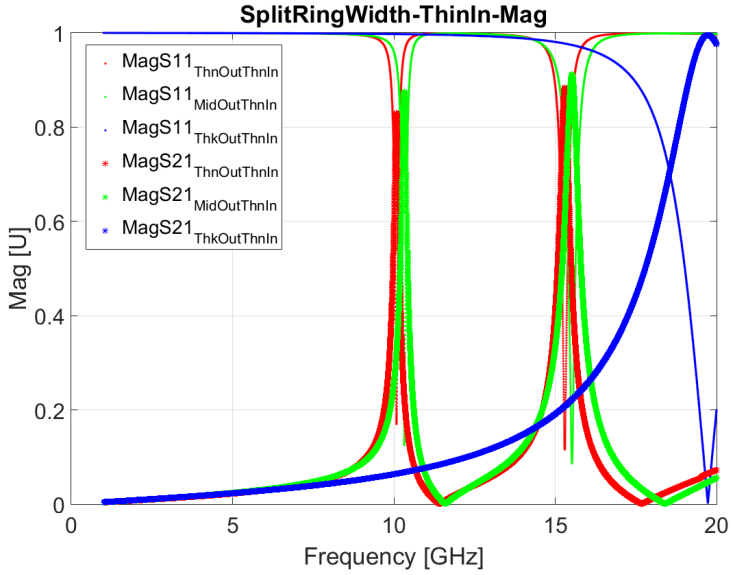

Figure 6.60: Plots showing the magnitude of the S-parameters for the varying outer split ring width (inner split ring width = 0.25mm).

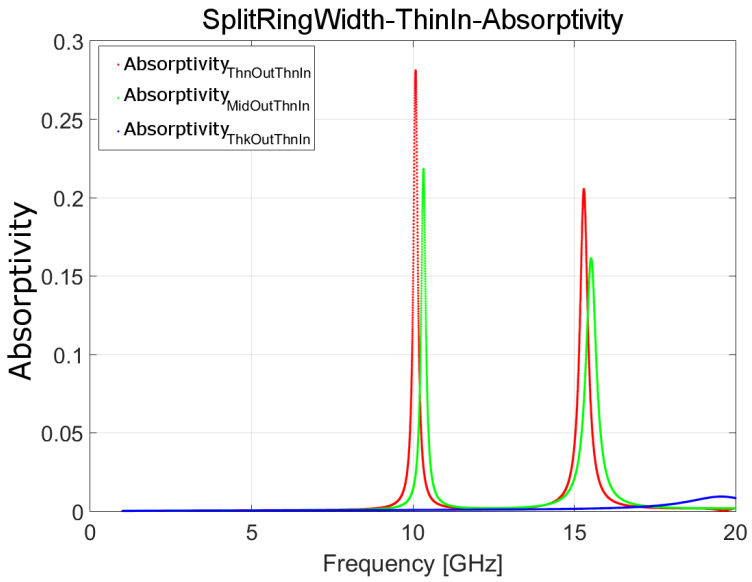

Figure 6.61: Plots showing the absorptivity for the varying outer split ring width (inner split ring width = 0.25mm).

outer ring is thin. This plot shows that by increasing the inner ring width, one can substantially increase the positions of the higher order resonance peaks without affecting the position of the lowest resonance.

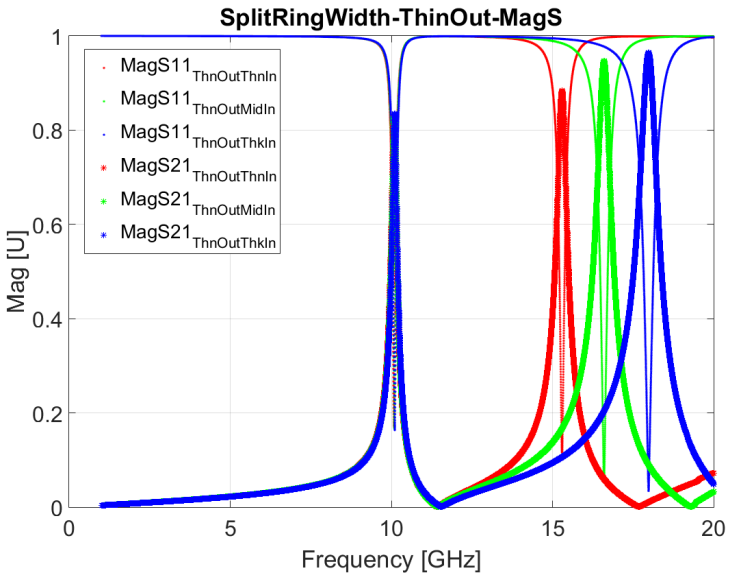

Figure 6.62: Plots showing the magnitude of the S-parameters for the varying inner split ring width (outer split ring width = 0.25mm).

Looking at the absorptivity plot for these simulations, Fig. 6.63, shows that as the split ring width increases, the peak of the lower frequency remains fairly constant, but the absorption of the higher peaks decreases.

Therefore the inner split ring width should be as thick as possible to ensure that the higher order resonance peak has the lowest possible absorption.

6.10.3 Split Ring Width Summary

These simulations show that the split ring widths need to be as thick as possible, without overlapping the other split ring, to ensure minimal absorption. Adjusting the width of the outer split ring offers a slight fine-tuning ability

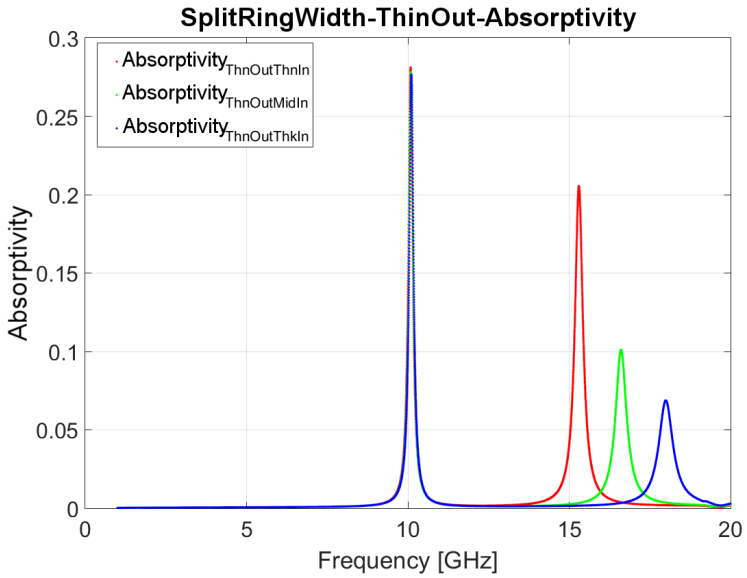

Figure 6.63: Plots showing the absorptivity for the varying inner split ring width (outer split ring width = 0.25mm).

on the frequency position of the resonance peak, whereas altering the width of the inner ring has minimal effect on the lowest resonance peak but a large effect on the higher order peak.

6.11 Split Width

The final set of optimisation simulations which were run determined the effect of the width of the split in the split ring on the EM behaviour of the unit cell. The geometries of a few of these simulations can be seen in Fig. 6.64, and the total number of simulations produced can be seen in Table 6.13, where the 'x' indicates a completed simulation.

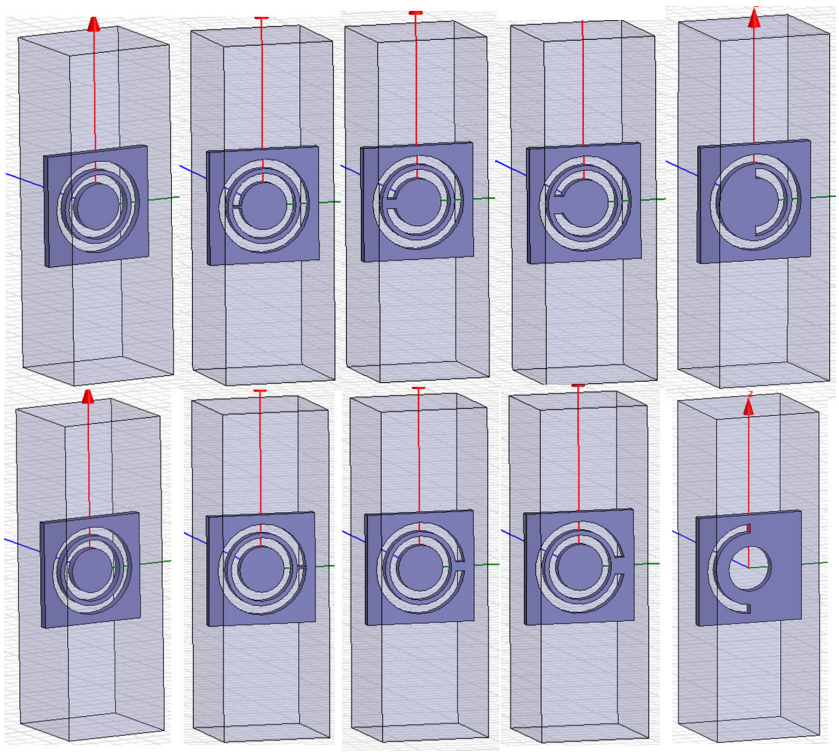

Figure 6.64: TOP ROW: Increasing the split width for the inner ring whilst keeping the outer ring with no split (Non, Small, Mid, Big, Max). BOTTOM ROW: Increasing the split width for the outer ring whilst keeping the inner ring with no split (Non, Small, Mid, Big) The final image shows the Maximum outer split width with a hole in the centre instead of an inner ring.

	Non	Small In (0.1mm)	Mid In (0.5mm)	Big In (0.9mm)	Max (1/2 split ring)	Hole
Non	x	x	x	x	x	-
Small Out (0.1mm)	x	x	x	x	x	x
Mid Out (0.5mm)	x	x	x	x	x	x
Big Out (0.9mm)	x	x	x	x	x	x
Max	-	x	x	x	x	x

Table 6.13: Table showing different types of simulation run for different widths of split in the split rings.

6.11.1 No Split Inner Ring

By keeping the inner ring set to have no split the effect that the split in the outer ring has on the EM behaviour of the unit cell can be determined. The magnitude of the S-parameters can be seen in Fig. 6.65, showing that the increasing in split width increases the resonant peak frequency of the unit cell. This is expected as the size of the split ring 'C' shape is decreased as the split increases, resulting in a higher resonant frequency.

Figure 6.66 shows the absorptivity associated with the increasing split width. The plot shows that as the split width increases the absorption decreases, with the lowest absorptivity of 0.12 resulting from the 'bigOutNonIn' simulation.

6.11.2 No Split Outer Ring

Keeping the outer ring set to have no split determines the effect the split in the inner ring has on the EM behaviour of the unit cell. The magnitude of the S-parameters can be seen in Fig. 6.67, showing that the increasing in split width increases the resonant peak frequency of the unit cell, though

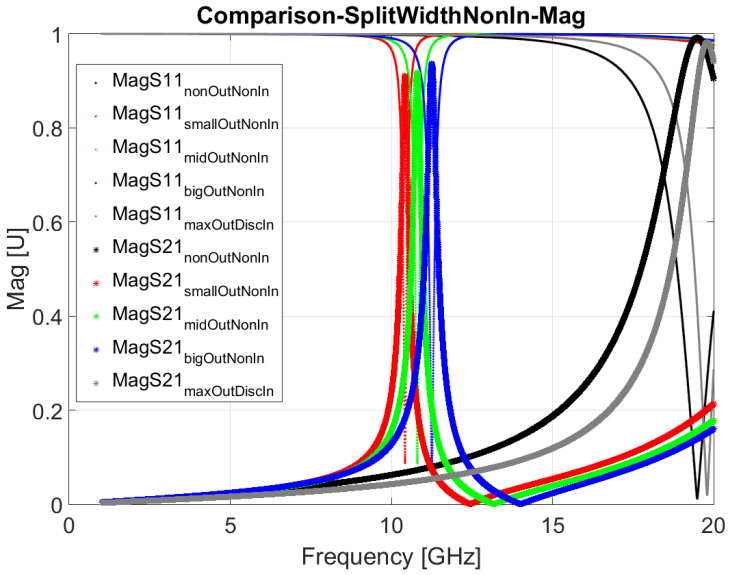

Figure 6.65: Plot of the magnitude of the S-parameters, showing the effects of increasing the split size in the outer ring.

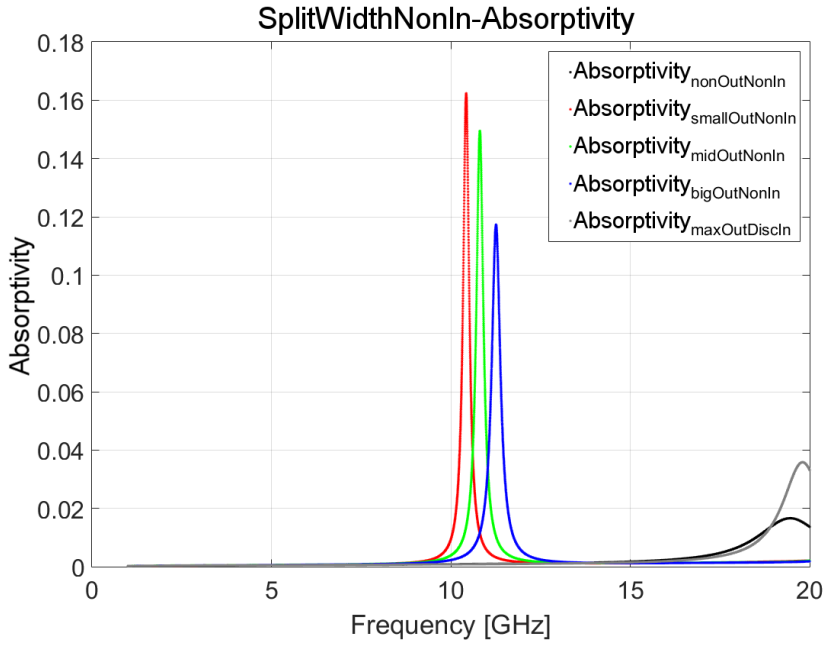

Figure 6.66: Plot showing the effect on absorption when increasing the outer split size.

this occurs at well above the x-band frequency region.

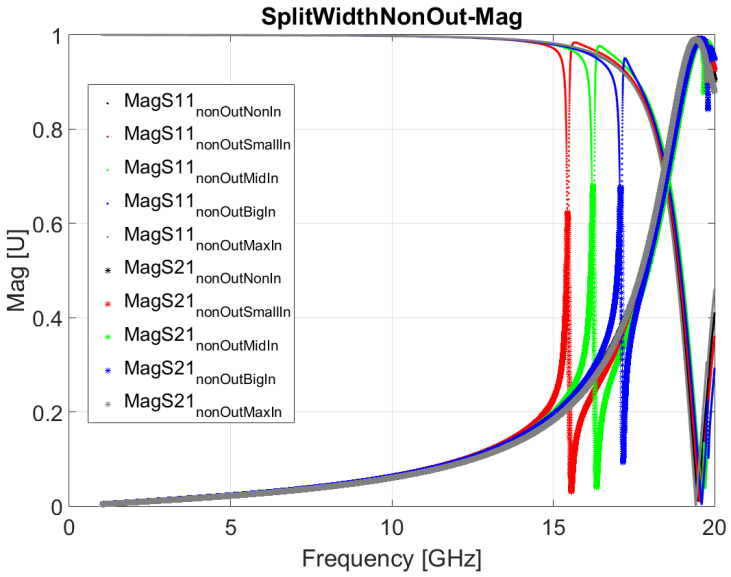

Figure 6.67: Plot of the magnitude of the S-parameters, showing the effects of increasing the split size in the inner ring.

Figure 6.68 shows the absorptivity associated with the increasing split width. The plot shows that the change in width has very little effect on the value of the absorption, with small, medium and big widths having absorptions of nearly 0.5.

6.11.3 Disc in Centre

The EM behaviour of the unit cell with a hole in the centre and altering the outer split ring width was also simulated. The magnitude of the S-parameters were extracted and can be seen in Fig. 6.69. This plot shows the resonant frequency peak is once again increased as the split width is increased.

The absorptivity plot, shown in Fig. 6.70, shows that the absorption once again reduces as the split width increases.

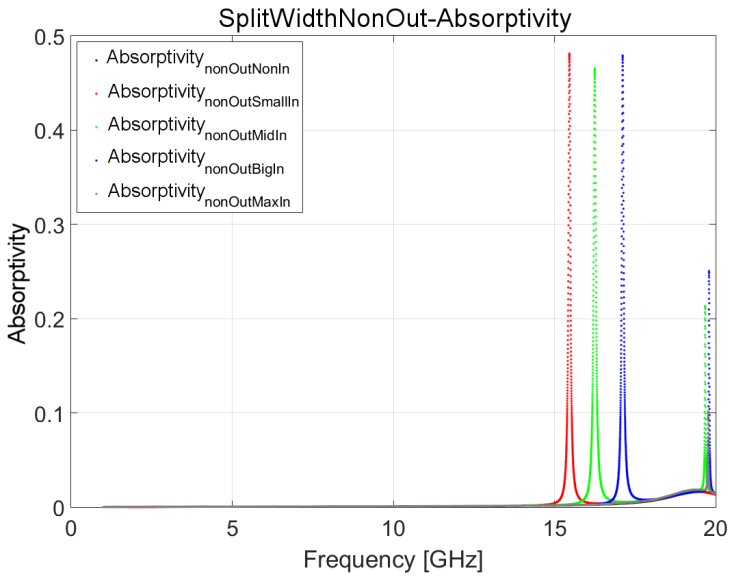

Figure 6.68: Plot showing the effect on absorptivity when increasing the inner split size.

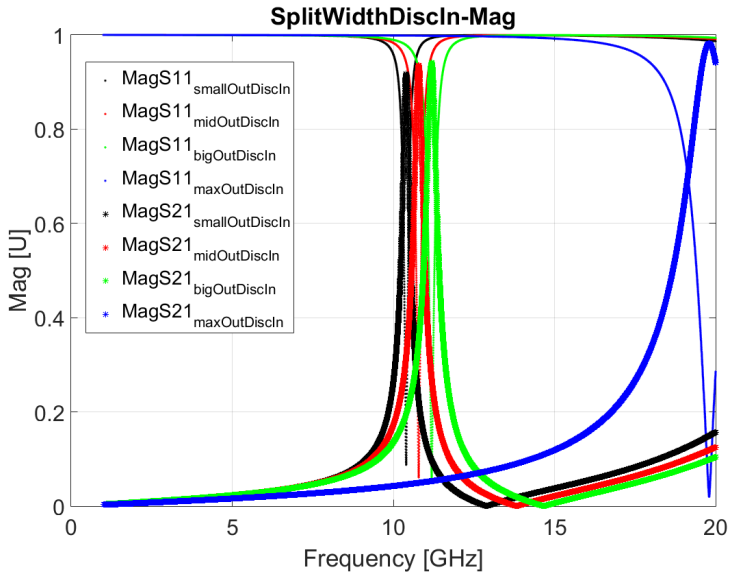

Figure 6.69: Plot of the magnitude of the S-parameters for the simulations where the split width in the outer split ring is increased with a hole present in the centre.

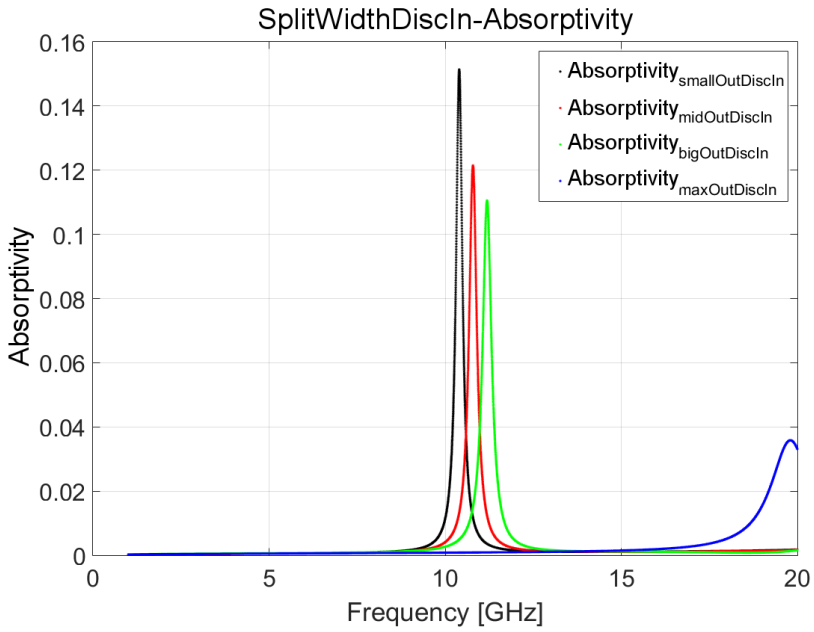

Figure 6.70: Plot of the absorptivity for the simulations where the split width in the outer split ring is increased with a hole present in the centre.

6.11.4 Split Width Summary

Simulations were conducted testing the effect of altering the width of the split on the resonant frequency and EM properties of the unit cell structure. These simulations show that increasing the split width, thus reducing the size of the resonant "C" shape, increases the resonant peak frequency position and the lower the associated absorption. Therefore, the splits should be as large as possible in the final design to keep absorption to a minimum.

6.12 HFSS - Methodology and Results

6.12.1 Material Design Specifications

The aims of this investigation were to design a material capable of high power operation, able to withstand more than 1kW of incident power with an absorption coefficient of less than 0.1 (ideally less than 0.05). The operating frequency required was between 8.2 and 12.5GHz (x-band).

A number of factors were looked at when the optimal geometry was being determined, such as unit cell shape, "complementary" (designed shape removed from material) vs "wire on substrate" (designed shape embedded onto material) split rings, wire thickness, split-gap thickness, number of rings and thickness of the unit cell material. Initially, the dimensions for an existing 6mm complementary split ring arrangement were used to test the accuracy of the meshing, followed by a number of parameter sweeps to determine the optimal design of the new structure. Simulations of an infinite XY plane of the unit cells were initially conducted to determine the behaviour of the unit cell itself. Floquet boundary conditions (Master and Slave) were used to set up the infinite system, along with Floquet ports. These are shown in Figs. 6.71a) and b), with the Floquet ports shown in Figs. 6.71c) and d). All infinite simulations needed to be de-embedded from the ports to the unit cell to ensure that the length of the air gap between the ports and the unit cell did not affect the predicted behaviour.

Simulation sweeps of 1-20GHz with a step size of 1MHz (20001 data points) were used to find the resonance peak of the structure, with this peak then being shifted into the x-band region when appropriate. 2 modes were analysed (TE and TM modes), set perpendicular to one another so the structures interaction with TE and TM modes could be determined. More details on the optimisation techniques used and the simulations produced are found in

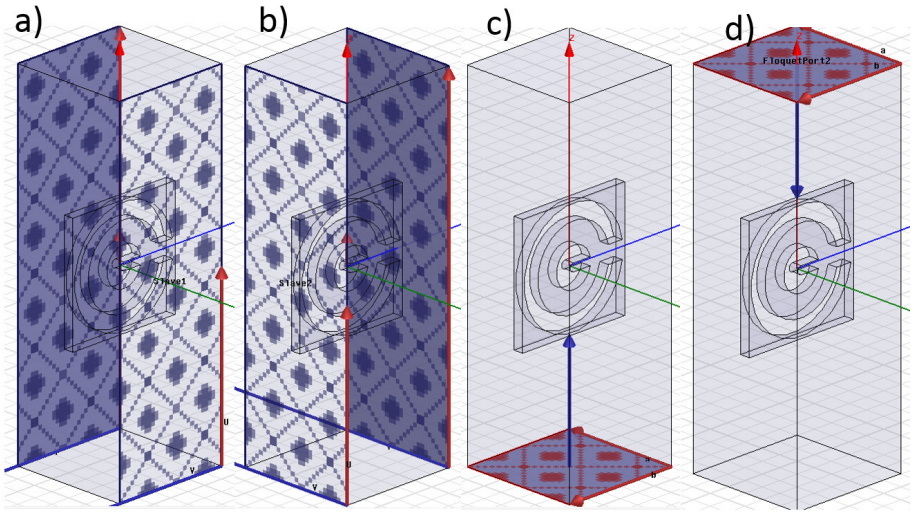

Figure 6.71: a) and b) Master and Slave (Bloch-Floquet) boundaries, used to create an infinite sheet of material. c) Floquet Port 1, deembedded to the unit cell edge as shown by the blue arrow. d) Floquet Port 2, de-embedded to the unit cell edge as shown by the blue arrow.

Chapter 6.

The final design specifications for the unit cell are found in Table 6.14.

Parameter	**Size (mm)**
Unit Cell Size	6.0
Outer Radius	2.9
Inner Radius	1.0
Split Ring Thickness	0.8
Split-Gap Width Outer	0.9
Split-Gap Width Inner	0.4
Material Thickness	0.5

Table 6.14: Table summarising the dimensions of the designed unit cell.

The unit cell size of 6mm give an approximate resonant frequency of 13.6GHz (using Eqn. 2.27). Copper was chosen as the unit cell construction mate-

rial due to its high melting temperature (around 1000°C) and low material absorption properties[1].

These dimensions are shown in Fig. 6.72.

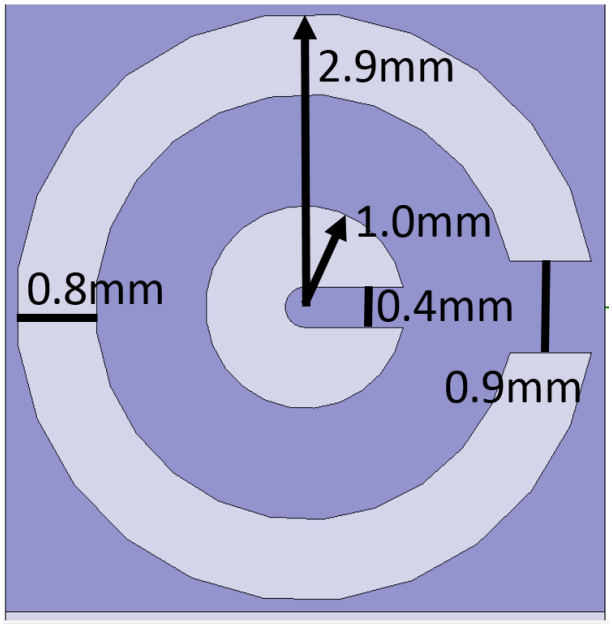

Figure 6.72: Dimensions for the split ring resonator design; Unit Cell size 6mm, copper thickness 0.5mm.

6.12.2 EM Characterisation Methodology.

A frequency sweep was conducted between 8 and 12GHz, covering the operating frequency range of interest. The simulation ran with a resolution of 0.2MHz (20001 data points over the 4GHz range). The "Maximum Number of Passes" was set to 20 and the "Maximum Delta S" was set to 0.02. This ensured that the meshing of the simulation was suitably accurate whilst

[1]Thinner copper actually gives a lower overall absorption but reduces the structural stability of the material. This also slightly alters the EM behaviour of the unit cell, but only for a range of around 1GHz. This needs to be taken into account when manufacturing the structure.

keeping the simulation time down (approximately 2 minutes) (more details on "Maximum Number of Passes" and "Maximum Delta S" in Appendices 6.2.1 and 6.2.2 respectively).

Values for S_{11} and S_{21} were determined, with the magnitude and phase plotted out in Fig. 6.73, where S_{11} is shown as the red line and can be seen to reach a minimum in magnitude at nearly 10GHz, corresponding to a phase shift of 2.5 radians ($\approx 4\pi/5$). S_{21} is shown as the blue line and can be seen to peak at in magnitude at around 10GHz. A phase shift in S_{21} also occurs though this is not nearly as sharp as the S_{11} phase shift and is drawn out over a larger frequency range.

By using Smith's adaptation of the Nicholson-Ross-Weir extraction technique, as discussed in Chapter 2.3, the permittivity ε_r and the permeability μ_r produced by the infinitely large sheet of a material composed of this unit cell design was determined.

Figure 6.74 shows the real and imaginary parts of ε_r. The real part of the permittivity moves from negative to positive in the region leading up to just below 10GHz, sharply reaching a peak at around 11GHz before drastically dropping to being negative once again. $Im(\varepsilon_r)$ remains at 0 until the peak in $Re(\varepsilon_r)$, where it drastically increases to a very large value before dropping off again. This shows that the material is well behaved away from the resonance peak, and that the losses of the material, which are related to the $Im(\varepsilon_r)$, increase around the resonance.

Figure 6.75 shows the real and imaginary parts of μ_r. $Re(\mu_r)$ is low (< 0.5) over the entire frequency sweep range, reaching a minimum at just under 11GHz. This corresponds to the frequency where $Im(\mu_r)$ becomes negative. The negative values are valid here because of the proximity to the resonance peak; away from resonance this behaviour would be non-physical. This is because the split rings are producing a magnetic response to oppose the

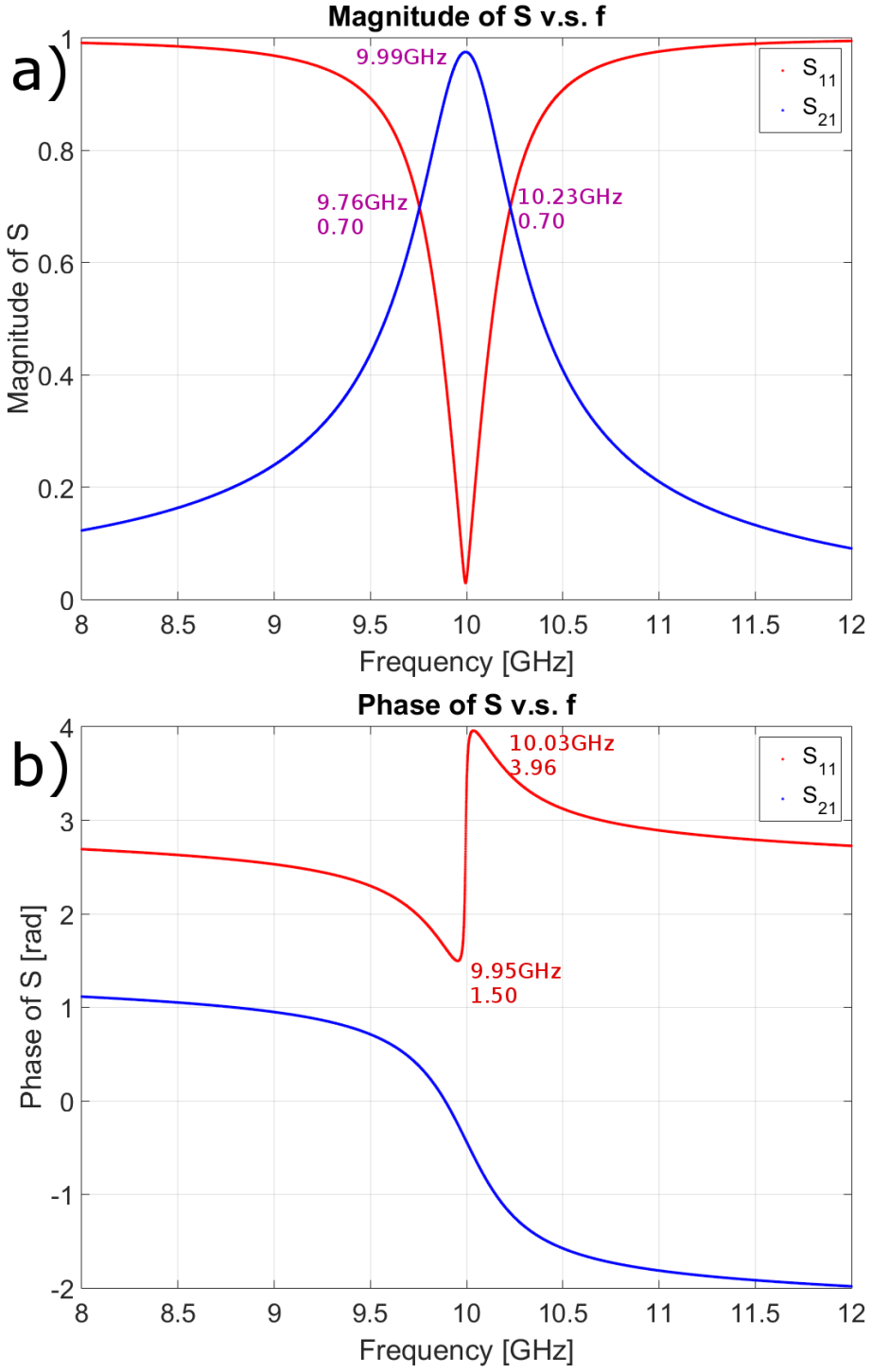

Figure 6.73: a) Plot showing the magnitude of S_{11} (red dotted) and of S_{21} (blue dashed), showing a resonance in S_{11} and S_{21}. b) Plot showing the phase of S_{11} and S_{21}, showing that S_{11} undergoes a π phase shift at 10GHz, and that S_{21} experiences a π phase shift over a range from 9-11GHz.

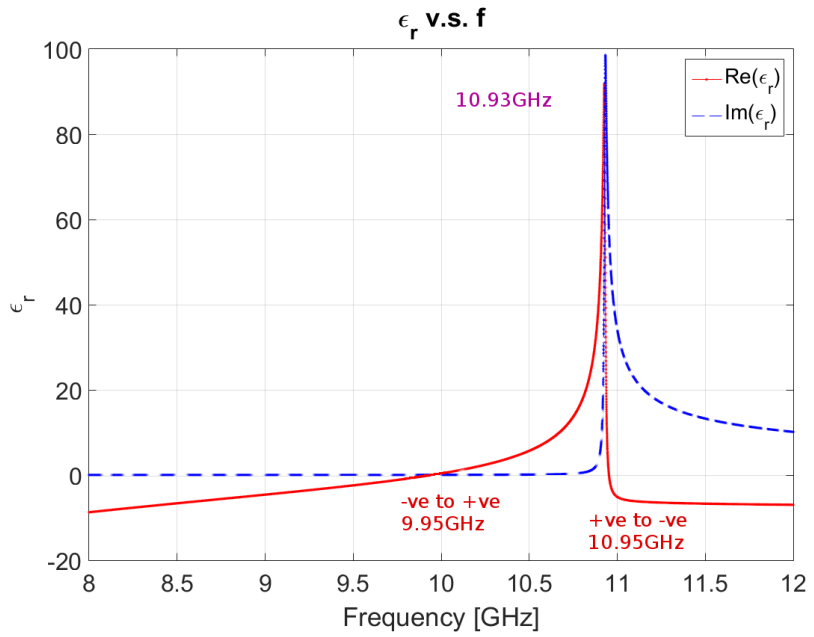

Figure 6.74: Plot showing the real (red) and imaginary (blue) parts of the permittivity (ε_r) for the infinite sheet of unit cells.

incident EM field, altering the way that the incident wave is responding magnetically.

Figure 6.76 shows the plot of the real components of ε_r (red dotted line) and μ_r (blue dashed line); the region where wave propagation is evanescent (i.e. ε_r and μ_r have opposite signs) is highlighted in light red. Full wave propagation is possible from just under 10GHz to just under 11GHz. In this region, $Re(\varepsilon_r)$ is positive and rising from 0 around 90 and $Re(\mu_r)$ is positive but reduces from around 0.4 towards zero. This shows that this material operates as an EMNZ material.

The refractive index (also known as the propagation index) of the material is determined from the equation $n^2 = \varepsilon_r \mu_r$, plotted in Fig. 6.77. As the designed material is passive, the imaginary part of the refractive index (shown in blue dashed, related to the total losses of the material) must al-

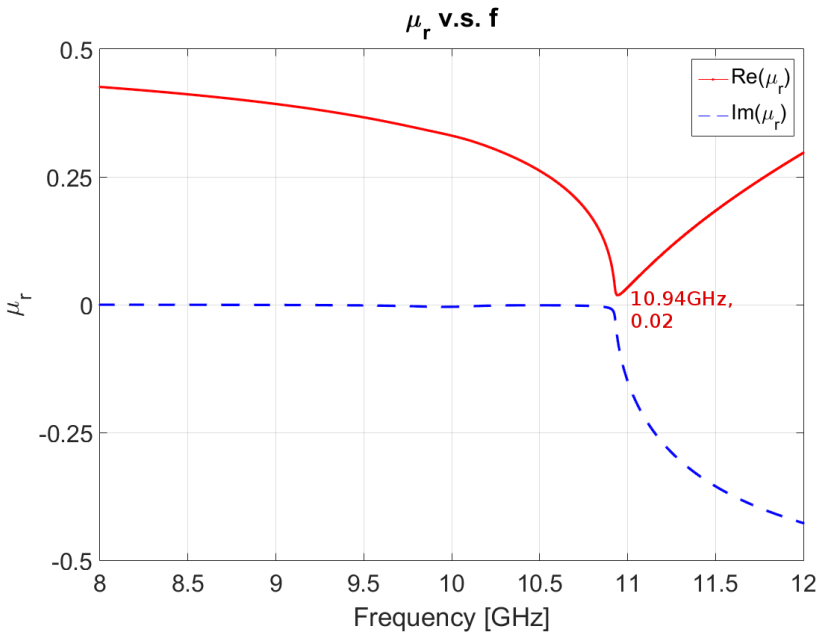

Figure 6.75: Plot showing the real (red) and imaginary (blue) parts of the permeability (μ_r) for the infinite sheet of unit cells.

ways remain positive to conform to energy conservation, which is observed. Below 10GHz the $Re(n)$ is zero; this is because ε_r and μ_r have opposite signs so n is not well defined, indicated by the large imaginary part of n. In this region, only evanescent waves may propagate. Between just under 10GHz to just under 11GHz n is well defined, rising from 0 to around 2.3, corresponding to a region where ε_r and μ_r have the same (positive) sign, allowing waves to propagate fully. From just under 11GHz, ε_r and μ_r once again have opposite signs, n is again no longer well defined and so $Re(n)$ drops off and $Im(n)$ increases once more.

A plot of the absorption coefficient, defined by Eqn. 2.16 as $AbsCoeff = \frac{4\pi f n''}{c}$ is shown in Fig. 6.78, showing a value of less than 0.05.

The phase velocity of the wave as it propagates over the structure is shown in Fig. 6.79, showing that the designed material does indeed slow down the

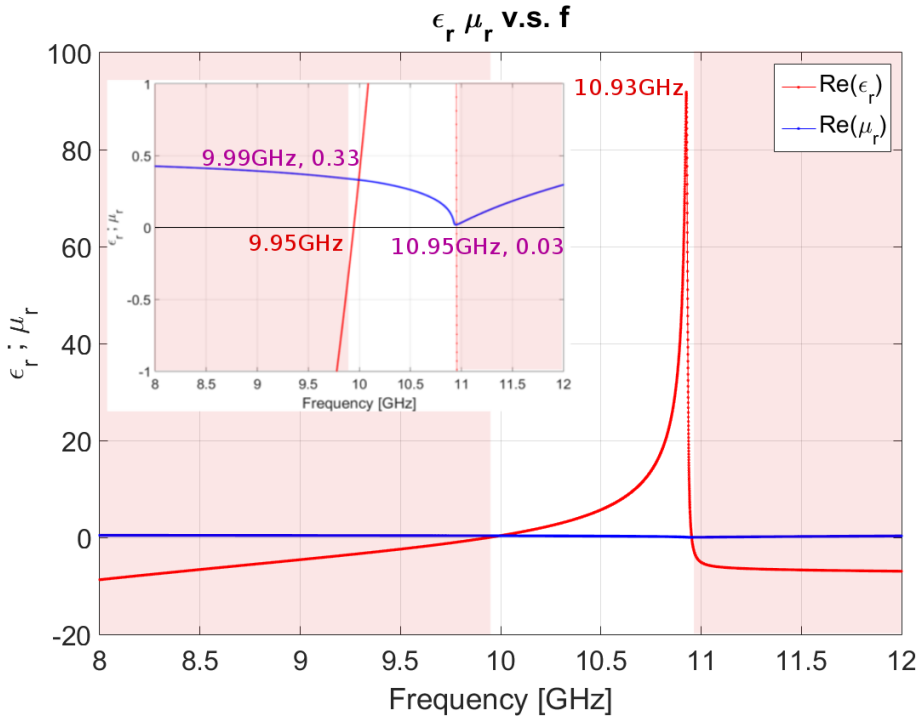

Figure 6.76: Plot showing the real components of ε_r and μ_r indicating that a region of double positive values exists between around 10 and 11GHz. At about 10GHz ε_r and μ_r have equal values of 0.3.

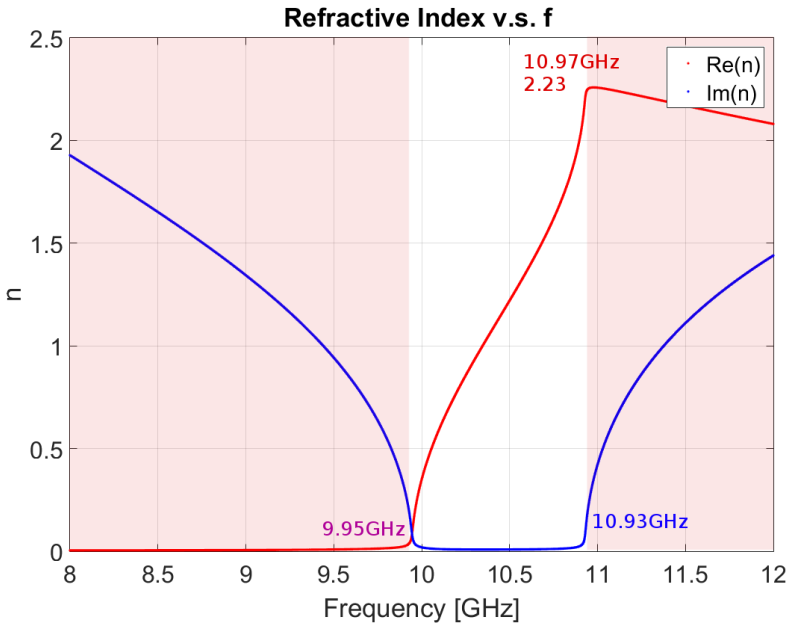

Figure 6.77: Refractive index (n) of the designed infinite material over 8-12GHz. The real part of n, shown by the red dotted line, can be seen to rise from 0 to around 2.2 for the frequency range where ε_r and μ_r have the same sign (from just under 10GHz to just under 11GHz). The imaginary part of n, shown by a blue dashed line, is significant for the frequency regions where ε_r and μ_r have opposite signs.

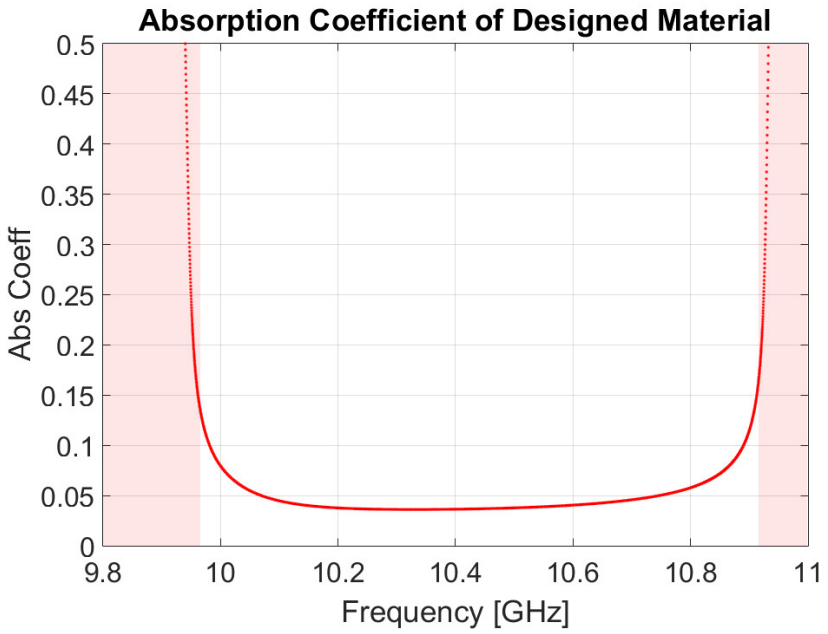

Figure 6.78: Plot showing the absorption coefficient of the designed material.

apparent speed of the wave to a fraction of the speed of light.

6.12.3 Initial Design: Infinite System Conclusions

This unit cell design has achieved many of the initial design criteria for an infinite 2D plane of this engineered unit cell; it has demonstrated an absorption coefficient of less than 0.05 and predicts an interaction frequency around 10.06GHz (well within x-band) between the incident RF and a low energy electron beam. It is worth noting here that the predicted interaction frequency is located on the high frequency side of the resonance peak. An operation frequency of around 10.06GHz predicts absorption in the region of 0.04.

The high power operation of this unit cell design requires simulations of the finite system to be investigated and are addressed in Chapters 6.12.4 and 6.13.

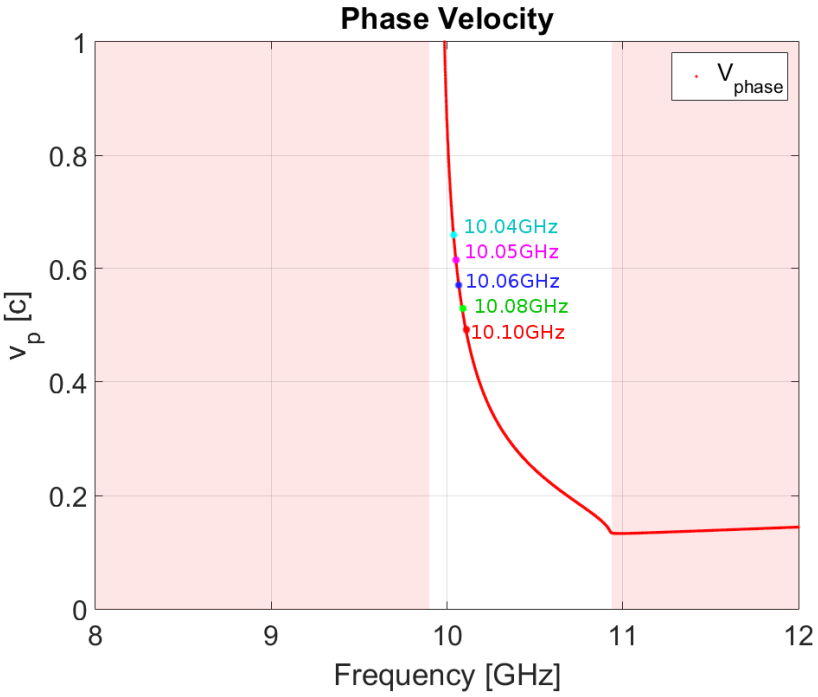

Figure 6.79: Plot showing the phase velocity of the wave as it passes over the designed material. In the region where interactions with an 80keV to 160keV are possible the wave has been slowed to around 0.50-0.65 times the speed of light.

6.12.4 Finite System - Waveguide

As this system was made for operation in x-band, simulations were run with this structure loaded into an x-band waveguide (dimensions 22.86mm x 10.16mm). However as this unit cell size is 6mm (1/6th of the waveguide wavelength at 10GHz) only 3 unit cells could be loaded into the waveguide; not really suitable for an effective medium description. Therefore simulations for a larger waveguide with dimensions 36mm (6 unit cells) x 18mm (3 unit cells) x 60mm (10x unit cell length) will be discussed here for initial testing of the finite, loaded waveguide. This enables a total of 18 unit cells to be loaded into the waveguide, better adhering to the effective medium requirements.

The incident wave originated from the bottom xy plane of the geometry (set as a Wave Port) and propagated in the +z direction. The waveguide walls (xz and yz planes) were set to PEC. The top xy plane was set to a Wave port.

This design can be seen in Fig. 6.80.

The simulation frequency sweep was originally set to 8-12GHz with step sizes of 0.2MHz, but this was later reduced to 9-10.5GHz in 0.1MHz steps to cover the range where an interaction has been predicted to occur. The simulation took around 30 minutes to run.

The plot of the magnitude and phase of the scattering parameters can be seen in Fig. 6.81, where the red line represents the magnitude and phase of S_{11} in a) and b) respectively, and the blue line represents the magnitude and phase of S_{21} respectively. A large resonance can be seen to occur at 10.07GHz, corresponding to the largest phase shift in S_{11}. This occurs at an increased frequency of 10.07GHz compared to the infinite simulation (resonance at 10GHz). There is more complicated EM behaviour apparent

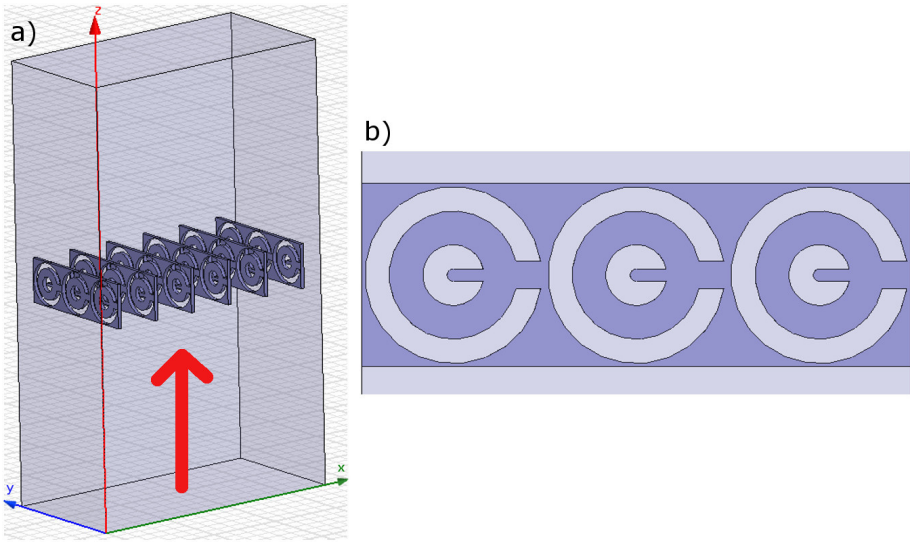

Figure 6.80: Geometric setup of the 36x18x60mm waveguide. a) Loaded 36x18mm waveguide, with the incident RF travelling in the +z direction. b) Image of the simulated strips of designed AM.

at the lower frequencies too compared with the infinite simulation; this is due to the finite nature of the system which results in extra reflections and excitations being produced within the waveguide.

By comparing the results of the scattering parameters for the infinite system and loaded systems, as shown in Fig. 6.82, the underlying trend of both the infinite and loaded waveguide systems are apparently very similar, except that the loaded waveguide behaviour has many more resonances present. The most influential of the new resonances is the anti-resonance that occurs at around 9.9GHz, resulting in the splitting of the previously simple resonance into 2 smaller, sharper resonances, one located 0.08GHz above the infinite resonance peak and one 0.13GHz below.

Figure 6.83 shows that the absorption coefficient for the loaded waveguide system is less than 0.07 around the 10GHz region. This is higher than the 0.05 predicted for the infinite system but is still less than the 0.1 originally

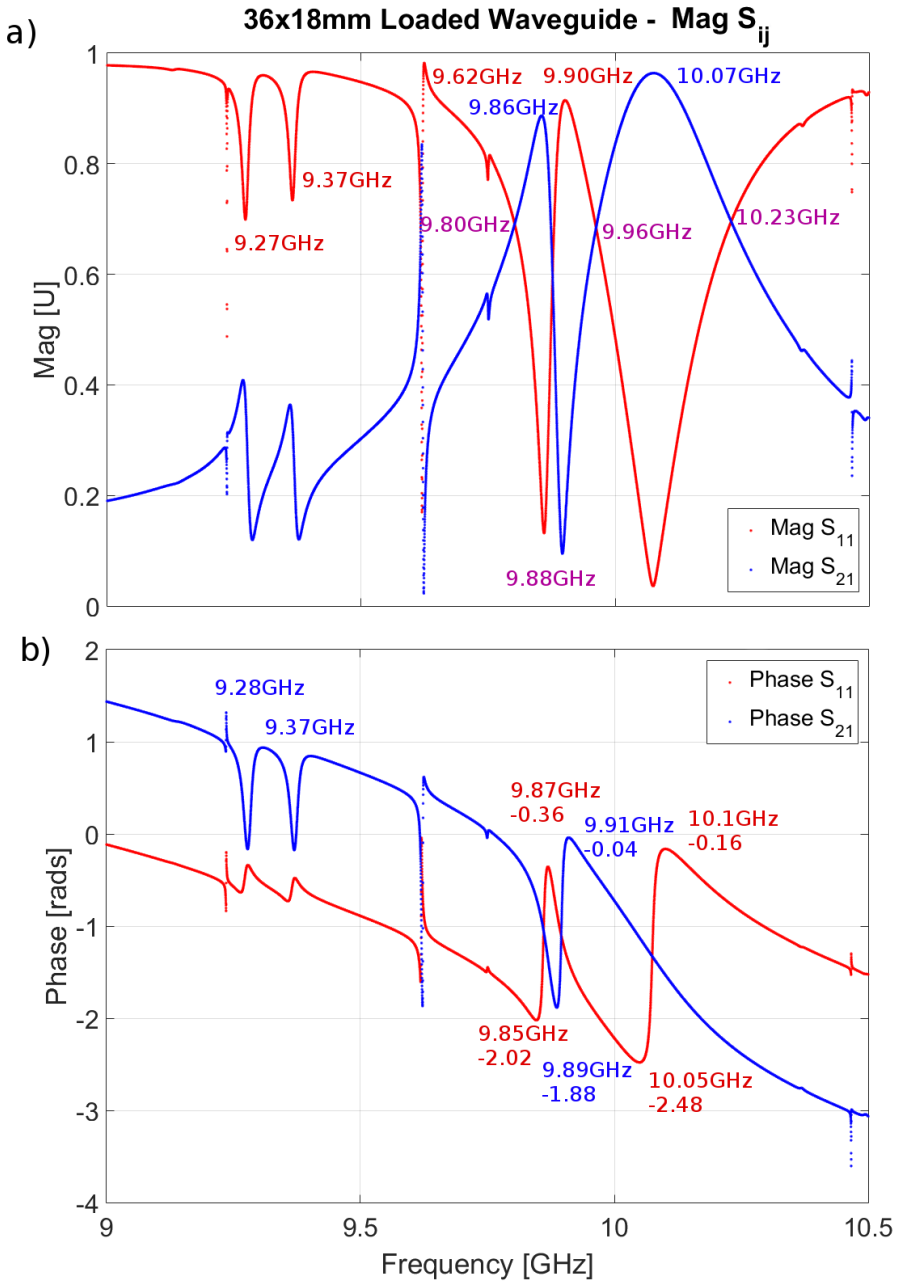

Figure 6.81: Plot showing S_{11} (red) and S_{21} (blue). a) Magnitude and b) Phase for the loaded 36x18x60mm waveguide. This behaviour is much more complex due to the finite nature of the simulation, and shows a small resonance at around 9.88GHz and a more substantial resonance in the region of 10.07GHz, along with the associated phase shifts.

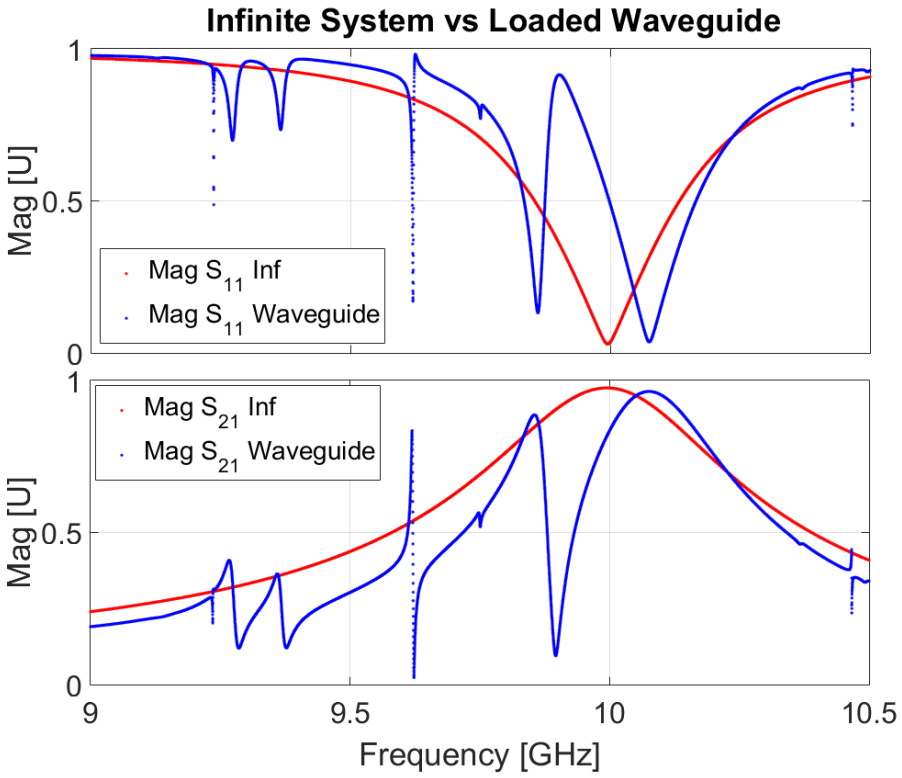

Figure 6.82: Plot showing the magnitude of the scattering parameters for the infinite and loaded waveguide systems.

required. Note that this could be reduced slightly by reducing the thickness of the copper.

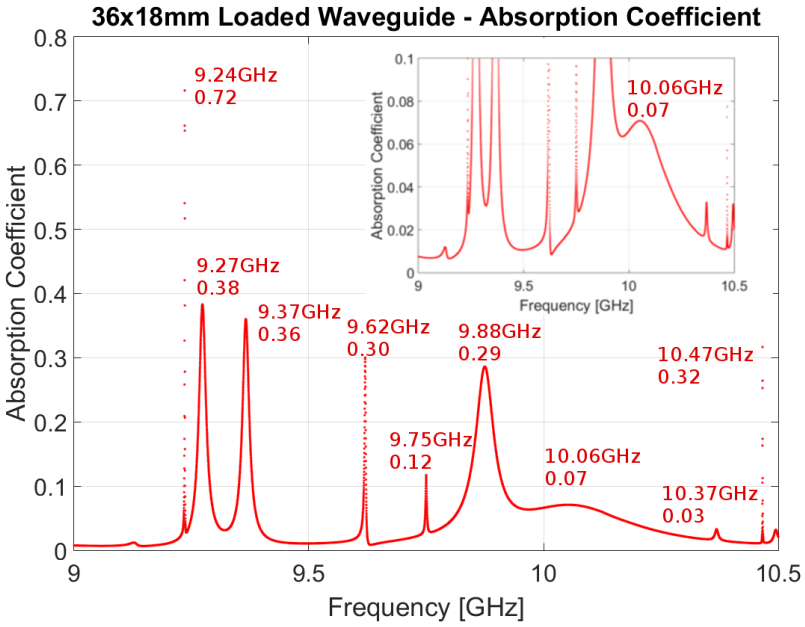

Figure 6.83: Plot showing the absorption for the loaded 36x18mm waveguide. The absorption has increased slightly for the region of interest (around 10GHz), but still remains lower than the required 0.1.

6.12.5 Initial Design: Waveguide Conclusions

The results from the simulation of a loaded 36x18mm cross section waveguide has predicted that key features of the unit cell material design have not been drastically changed compared to the initial infinite system. There is a slight increase in the frequency positions of the resonances present of around 0.07GHz (from 10GHz to 10.07GHz), and there are more resonances present in the lower frequency regions; this will be caused by edge effects of the AM structure and additional resonances present due to the waveguide.

6.13 COMSOL - Methodology and Results

6.13.1 Benchmarking : Comparing HFSS and COMSOL EM Characteristics

To determine the thermal behaviour of the structure, the loaded waveguide was modelled in COMSOL, a commercial Multiphysics Simulation Solver (for more information see Chapter 5.1.3). To check that COMSOL predicts the same or similar EM behaviour of the structure as HFSS, the loaded 36x18mm waveguide was created and simulated.

Figure 6.84 shows the position of the ports and the PEC boundaries.

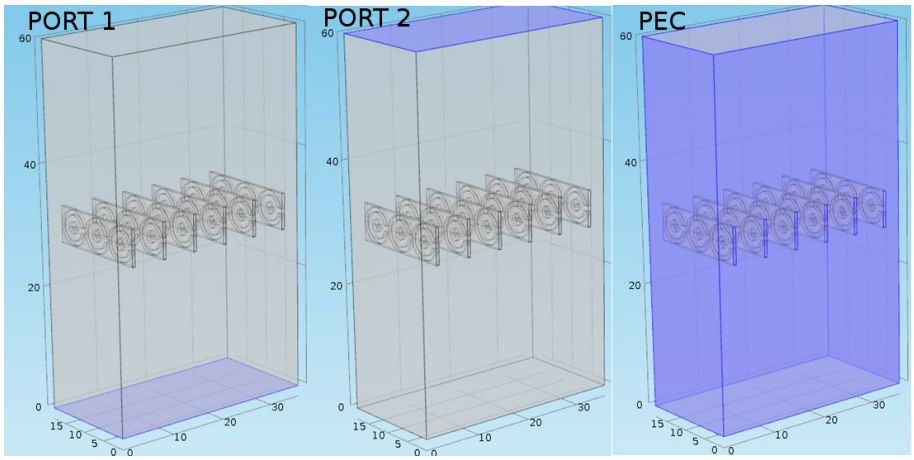

Figure 6.84: Images showing: left: Port 1, where the TE_{10} wave is incident from; middle: Port 2, exit port; right: PEC boundaries applied to the walls of the waveguide.

The simulation ran with a "Fine" mesh from 9GHz to 10.5GHz (see Fig. 6.85) with frequency steps of 0.01GHz and took 2 hours 8 minutes to complete[2]. This equated to a total of 150 data points, 1% of that run in

[2]Simulations of 9-10.5GHz were also attempted for frequency steps of 0.001GHz, however these simulations failed to converge. That said, many of the data points were obtained over the span of nearly 9 hours, and so these are shown and discussed in App. B.2.

HFSS.

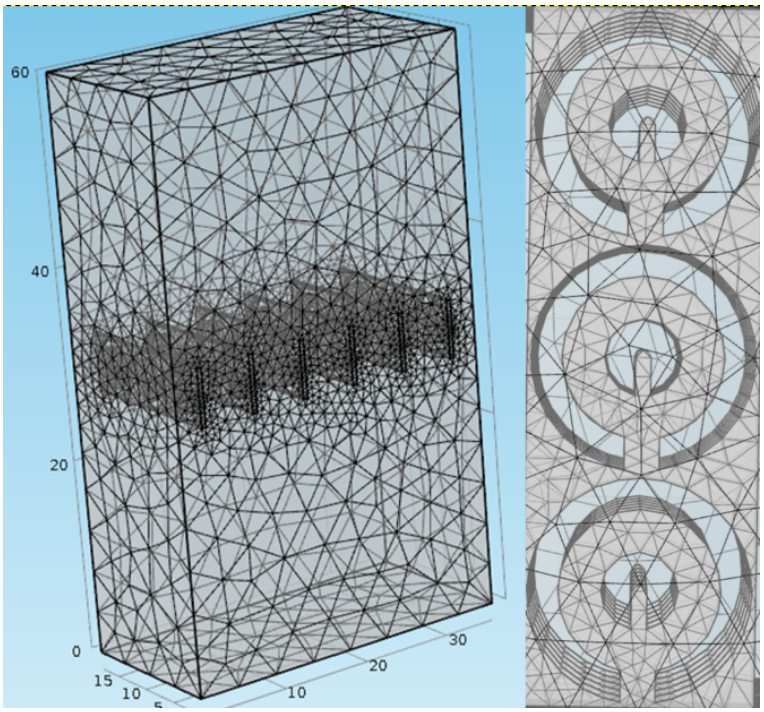

Figure 6.85: COMSOL Fine Mesh.

The plot comparing the magnitude of S_{11} and S_{21} for both HFSS and COMSOL in [dB] can be seen in Fig. 6.86.

From this comparison differences between the behaviour predicted by the two software packages become apparent. Points to note are the differences in the lower frequency resonances (2 resonances in HFSS compared to the single resonance in COMSOL) and there is a slight discrepancy between the frequency positions of all of the resonance peaks. These are 0.05GHz for the resonance where S_{21} first exceeds S_{11} over a reasonable range (around 9.8GHz), and 0.1GHz for where S_{21} becomes dominant for a second time (around 10GHz). Interestingly, the peak located at 9.62GHz coincide for both HFSS and COMSOL. This difference in the resonant peak positions would ultimately lead to differences in the calculated values of ε_r and μ_r

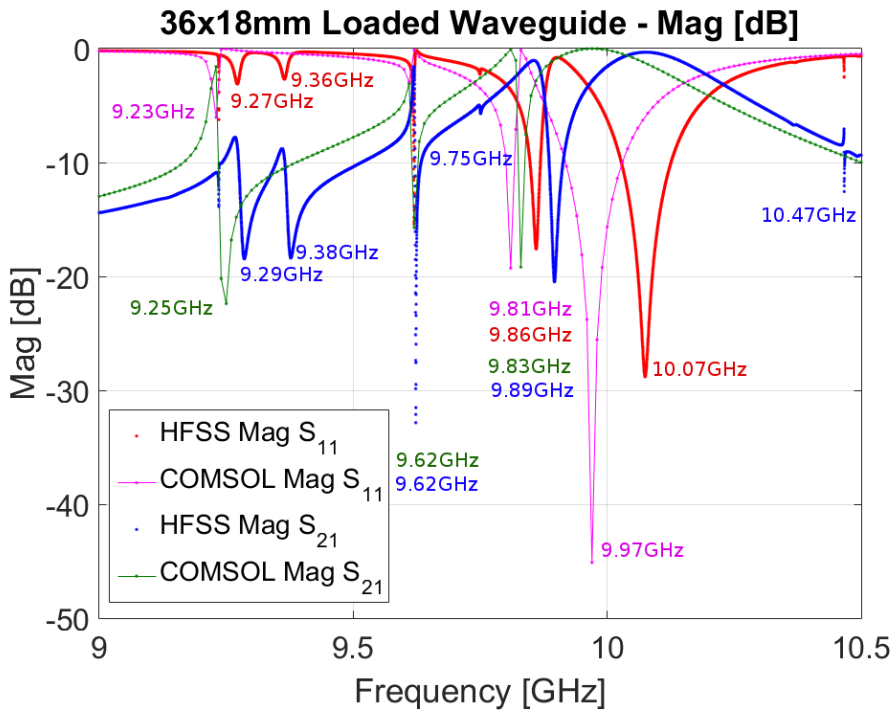

Figure 6.86: Plots comparing the magnitude of S_{11} and S_{21}, (in [dB]) outputs from HFSS and COMSOL.

as they are determined from S_{11} and S_{21}. Therefore a value of 10.03GHz was used for the COMSOL simulations as it lies between the HFSS and COMSOL predicted resonances.

6.13.2 1W Incident Power

To determine whether this structure was suitable for high power operation, it was important to determine how long the structure would take to heat up when exposed to an RF wave.

The aim was to ensure that this design could withstand powers higher than 1W for a duration exceeding 15 seconds, as previous work [5] had resulted in these parameters causing breakdown of the structures. The simulations produced exposed the structures to a 10.03GHz wave for 20 seconds for a range of powers from 1W to 100kW. The eventual aim is to demonstrate that this structure can withstand over 1kW of incident power.

As the unit cell material was set to copper, simulations which predicted a temperature exceeding 1000°C (the melting point of copper) were considered to have reached breakdown.

The first simulation had 1W of incident power with a "Fine" mesh at 10.03GHz from 0 to 20 seconds in steps of 1 second. Initially a heat plot of the structure was produced to indicate suitable locations to determine the maximum temperature in the system. This summary of the plots produced over time can be seen in Fig. 6.87, with the full 20 second time evolution found in Appendix B.9.

These plots quite clearly show that the regions of highest temperature rise occur in the Port 1-side unit cells of the central two slices of unit cells. The temperature of a number of points around one of these unit cells was taken (see positions in Fig. 6.88) and the temperatures reached at those points

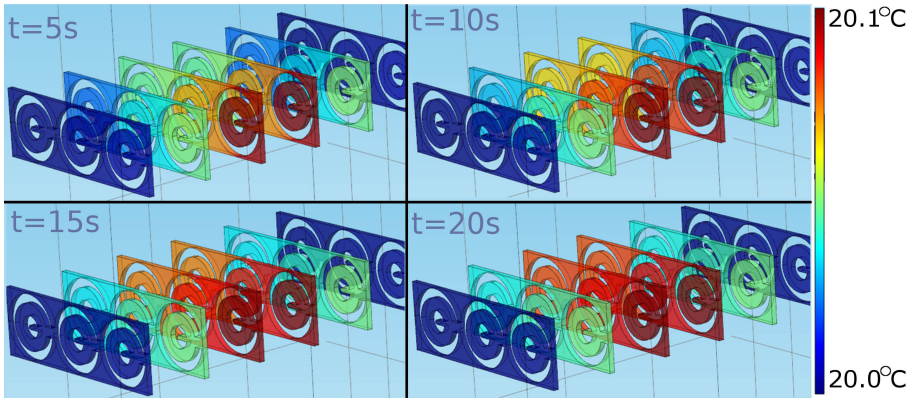

Figure 6.87: Surfaces showing heating in the structures after a 20 second exposure to a 1W 10.03GHz wave for 5 to 20 seconds in 5 second intervals.

are plotted in Fig. 6.89.

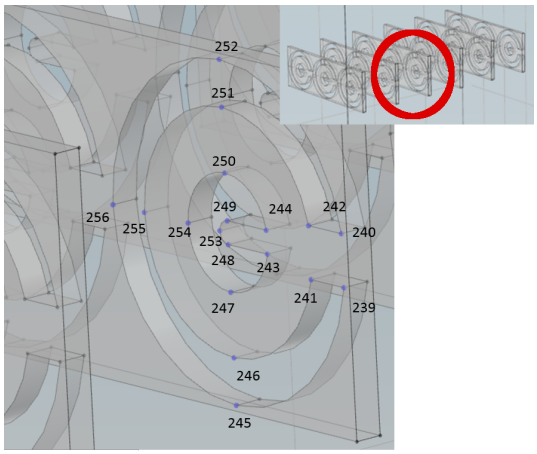

Figure 6.88: Points where the temperature of the structure was recorded.

The plot of the temperature at these recorded points can be seen in Fig. 6.89, and show that the sections of the structure located at the centre of the waveguide increase to the higher temperatures as the centre of the waveguide is the location of the highest electromagnetic fields. The predicted temperature rise for the structure when exposed to 1W of power is around 0.09°C after 20 seconds.

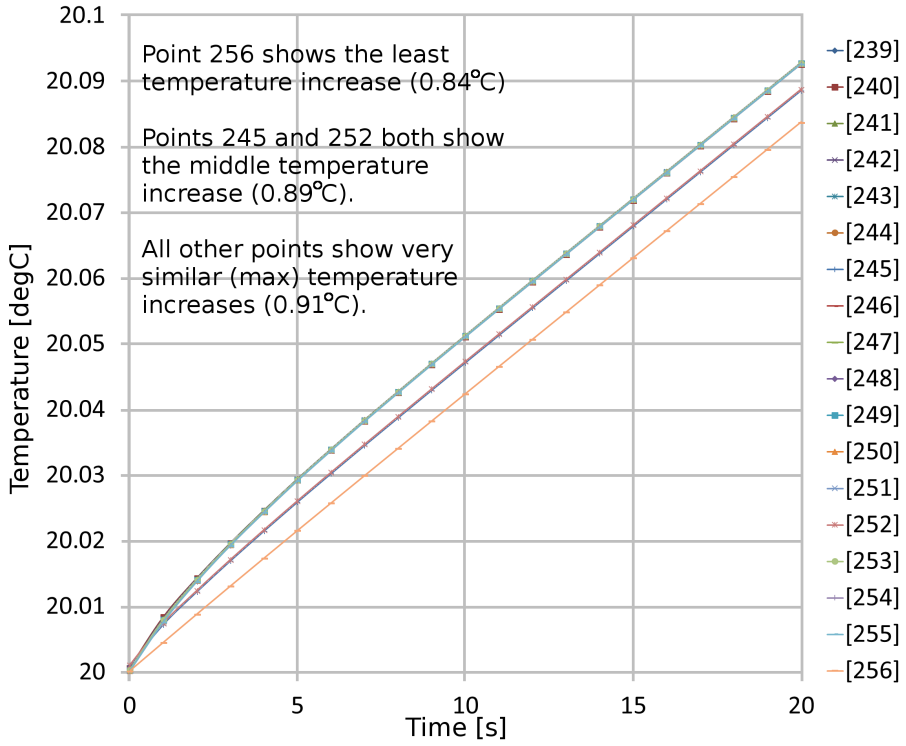

Figure 6.89: Plot produced by COMSOL showing the temperature rise of the structure over 20 seconds for the data points marked out in Fig 6.88.

Therefore point 244 will be taken as the point where the maximum temperature rise is determined for all power simulations.

6.13.3 Varying the Power

By looking at the temperature rise for a number of different powers, the power vs the maximum temperature experienced by the structure was plotted. This can be seen in Fig. 6.90, showing that the maximum temperature of the structure increases linearly as the incident power increases when exposed to the 10.03GHz wave for 20 seconds. This suggests that the maximum operating power for a 20 second exposure to RF at 10.03GHz for this structure lies in the region of 10kW. Each of the simulations took around 15minutes to run, increasing slightly as the power increased.

This is a significant conclusion as this is a 10000x increase in the potential high power abilities of these types of structure compared to initial high power investigations into AM material designs (see Ref. [5]).

6.13.4 Heating Conclusions

By simulating the loaded 36x18mm waveguide in both HFSS and COMSOL the predicted EM behaviour for the structure was directly compared for the two software packages. A discrepancy of 1% was found between the two packages caused by the difference in frequency-steps between the systems (resulting in slightly different calculated EM properties). This limitation was caused by issues with the computing power available, therefore was only able to produce 1% of the data points HFSS could create. The positions of the resonance peaks in the frequency region of interest (around 10GHz) seemed to show good behavioural agreement, though shifted down in frequency by 0.1GHz. This led to the conclusion that the interaction

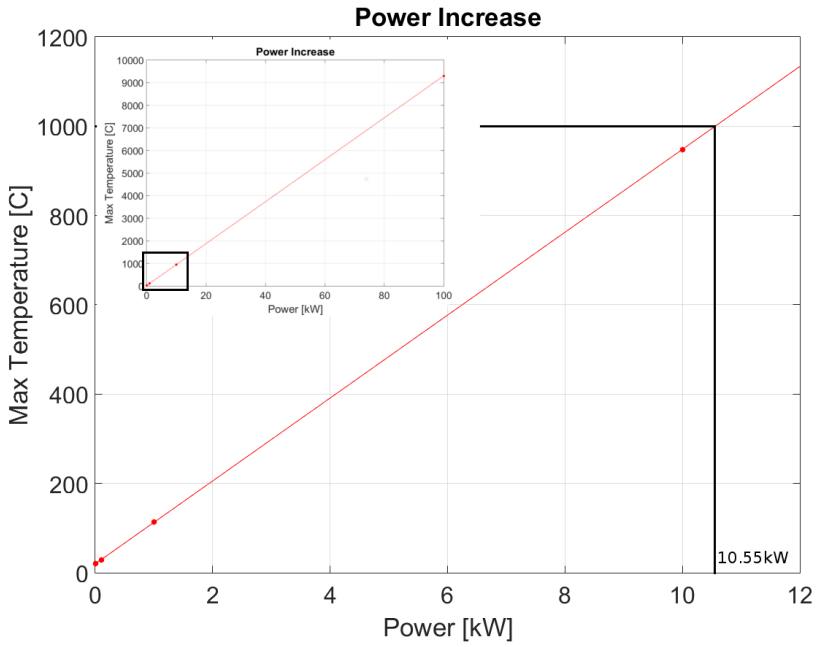

Figure 6.90: Plot showing that the maximum temperature reached at the centre of the structure increases as the power on the structure increases for a 20 second exposure. Breakdown of the copper is predicted to occur at an incident power of just over 10kW (T=1000°C).

frequency according to COMSOL would be located 0.1GHz below that predicted by HFSS, leading to the use of 10.03GHz as the operating frequency for the thermal simulations.

From the COMSOL heating simulations, for 20 second exposures to the incident RF operating at 10.03GHz, the maximum power this structure can withstand is in the region of 10kW; this shows that the designed structure adheres to the required design condition of coping with powers exceeding 1kW.

Chapter 7

Fabrication

To manufacture the designed structures a number of methods were proposed such as

1. Electrical Discharge Machining (EDM)
2. Water Jet Manufacturing (WJM)
3. Lithography
4. Laser cutting/printing
5. PCB Etching
6. Printed Circuit Board (PCB) Milling
7. Engraving

1, 2) EDM and WJM

EDM and WJM would require external companies, and thus were not explored at the time of writing due to additional costs and limited time constraints.

3) Lithography

Lithography is a more conventional for manufacturing these types of structures; however the university does not have access to these facilities on campus. Therefore an external company would again be required if manufacturing this way is required.

4) Laser Cutting and Laser Printing

Laser cutting is technically available at the university; however they are unable to cut material greater than 10s of microns in thickness. Laser printing has been suggested, though this avenue for manufacture has currently not been explored.

5) PCB Etching

Etching was another process suggested. Possible issues with this method include, due to the small dimensions of the structures, bleed through of the photoresist chemical into the areas where the copper is to be removed. This would mean that the structures are not made exactly to specifications. An example structure was created using this method – see Fig. 7.1 – and shows that the photo-resist bleeding is not a significant issue within the CSRR design, though there does seem to be a slight curve in the outer shape of the design where the CSRR geometry gets close to the edges of the design.

6) Printed Circuit Board (PCB) Milling

At the time of writing PCB milling is the manufacturing option of choice due to its ease of access on campus (Engineering Labs), the relative cheapness of the materials required (test runs can be made on discarded pieces of FR4 PCB) and the valuable assistance of David Upton, the departmental expert person on the PCB milling machine. This method again has its issues. The first is that the PCB mill is designed to cut out tracks for a circuit board (thickness of copper of around 34μm) therefore has issues with the required thickness of the copper (500μm). Therefore thinner copper is required if

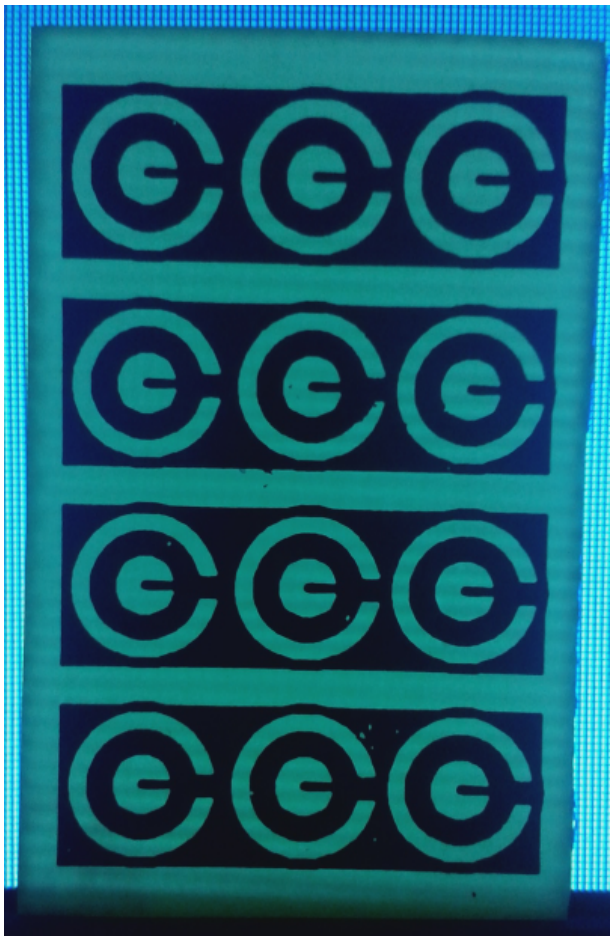

Figure 7.1: Etched optimised CSRR designs with a blue back-light to show inaccuracies in the geometry.

this is to be our primary source of manufacture. Secondly the drill piece is actually slightly conical in shape, with a 45 degree angle on the drill tip. This causes issues when drilling thicker pieces of copper as the top of the cut will be wider than the base. One method to possibly get around this is by cutting the copper from both sides: this has yet to be tested.

Initial tests involved ensuring that the computer can correctly program the mill to correctly cut the designed shape; the initial structures to be presented here are on 1 ounce copper clad FR4. This immediately brought out an issue

with the way that the files were being saved (as .DXF), as the PCB software was unable to correctly assign a drilling path. The results of this can be seen in Fig. 7.2a), where the drill seems to have cut directly on the outline of the split rings. The corrected drill path can be seen in Fig. 7.2b).

Figure 7.2: a) 1st PCB milling attempt, showing that the drilling path was defined incorrectly. This was due to issues with the file save-format. b) Milled structure with correct drill path.

Simulations had been run which had determined that between 50 and 500μm thick copper would be suitable for this material design (any thinner and the EM response is reduced, thicker results in higher losses). Originally 500μm copper was decided upon due to its accessibility, however there was concern that the metal would be too thick for the drill bit. 200μm copper also produced the same concerns, so 100μm copper was decided upon.

100μm copper was purchased and glued to a sheet of acetate; the acetate provides support for the copper during the milling process and can be easily dissolved after milling. However, upon milling, this setup was found to have insufficient adhesive strength, resulting in the drill bit ripping up the copper and heating the acetate to its melting point, as seen in Fig. 7.3.

Figure 7.3: 100μm thick milled copper, showing that the adhesive sticking the copper to the acetate was not sufficient and that the acetate could not withstand the heat produced by the drill bit.

This issue was mitigated by using the drill to re-trace the CSRR shapes a number of times instead of removing the copper in a single trace. This produced a much better quality finish of the CSRR, as shown in Fig. 7.4, and is easily reproducible.

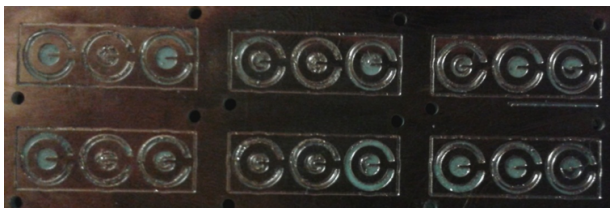

Figure 7.4: Many CSRRs drilled using the re-trace milling method on acetate.

3oz copper-clad (102μm thickness) FR4 was also used for testing the re-trace method as the FR4 can be dissolved using formic acid. This can be seen in Fig. 7.5.

This is most likely the method to be used going forwards with the fabrication of these structures.

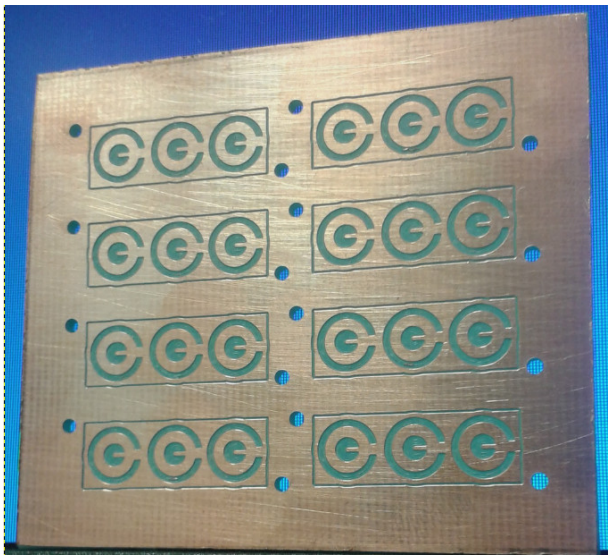

Figure 7.5: Many CSRRs drilled using the re-trace milling method on FR4.

Chapter 8

Conclusions and Future Work

The aim of this research project was to design and create an artificial material which is operable in high power RF environments. The focus was to minimise the absorption coefficient of the structure, enabling microwave energy transfer devices to become smaller, cheaper and operational in higher power environments compared to existing technologies. By using HFSS and COMSOL (commercial Finite Element Method software), a 6mm Copper Complementary Split Ring Resonator (CSRR) unit cell of 0.5mm thickness was designed, producing a significant electromagnetic response around 10GHz whilst withstanding incident powers of up to 10kW for exposures of up to 20 seconds. This is a substantial improvement on existing AM designs, which can currently only withstand in the region of 1W.

The optimisation designs began by manipulating an existing SRR design. This consisted of a 2.4mm double-square split ring resonator setup etched into 1oz copper clad FR4 Printed Circuit Board (PCB). This design was optimised to reduce the absorption coefficient of the material, resulting in

a 6mm double-ringed circular CSRR unit cell design. This reduces the magnetic response of the unit cell creating a material which behaves as an $\varepsilon\mu$ Near Zero (EMNZ) structure instead of producing the Double Negative response of the metamaterial. This ensured that the high losses associated with a large negative in μ_r were substantially reduced. Initial simulations used an infinite 2D plane of the unit cell structures, though simulations were later conducted using a 36x18mm design waveguide which operates in x-band (this was decided to ensure that more than 3 of the unit cells were contained within the waveguide, ensuring the effective media conditions were met).

The absorption coefficient of an infinite sheet of the designed structure in the 10GHz region was found to be below 0.05 – below 0.1 when loaded into 36x18mm waveguide – with COMSOL showing that incident powers in the region of 10kW for a 20 second exposure of 10.03GHz incident RF could be handled without additional cooling when the material is loaded into a 36x18mm waveguide.

Initial investigations have begun into simulating an electron beam/RF wave interaction (using the FDTD code MAGIC), and this currently suggests successful energy transfer between a continuous electron beam and incident x-band RF, though further simulations need to be conducted before any conclusive remarks can be made.

This investigation increases the current possibilities of uses of artificial materials into that of High Power Vacuum Electronic Devices, as research up to this date cumulated in the destruction of this type of designed material with only 1W of power. Future work would therefore begin by completion of the fabrication of the structures. These would then be characterised using a network analyser to ensure adequate adherence to the simulation parameters. Cold testing (exposure of the structure to very low powers) would determine

the scattering parameters of the material enabling the determination of the relative permittivity and permeability of the material. There will most likely be some slight discrepancies between the operating frequency predicted by the simulations and those obtained from experiment as the simulations use idealised conditions and the test-waveguide may not have the specific dimensions specified in the simulations. A slight amount of noise would be expected from the experimental equipment originating from, for example, reflections in the the coaxial cables (due to bending of the cable). However, the electromagnetic behaviour of the structure should be in good agreement with the simulations, though shifted in frequency or peak width slightly due to the experimentally introduced errors.

Next, the 36x18mm waveguide would need to be designed and constructed – along with the appropriate coaxial to waveguide wave launchers – to ensure that the structure could be exposed to the same conditions as those produced in the simulations. Again, cold testing of this system would be conducted to ensure that the simulations and experimental data agree on the EM behaviour of the system. Again, slight discrepancies are expected between the experimental setup and the simulations due to errors and noise in the experimental setup. Upon completion of the cold tests, the structure would to be exposed to high power testing (hot testing) to confirm whether the COMSOL simulations were correct in their predictions of the thermal behaviour of this structure. This would test the structure exposed to a number of different operational environments, such as with continuous and pulsed high power exposure, and also test for different exposure times.

Bibliography

[1] RF operation at the ESRF and EBS upgrade (EBS = Extremely Brilliant Source), author=Jörn Jacob, booktitle=21st ESLS RF Meeting - SOLARIS, Krakow, 15 16, year=2017, month=November.

[2] Hughes TWT. `http://www.dudleylab.com/surplus10.html` (Accessed 23-12-2017).

[3] John Pendry. Metamaterials, transformation optics, and the science of invisibility. In *APS Meeting Abstracts*, 2012.

[4] JO Dimmock. Losses in Left-Handed Materials. *Optics Express*, 11(19):2397–2402, 2003.

[5] R Seviour, YS Tan, and A Hopper. Effects of High Power on Microwave Metamaterials. In *Advanced Electromagnetic Materials in Microwaves and Optics (METAMATERIALS), 2014 8th International Congress on*, pages 142–144. IEEE, 2014.

[6] JD Jackson and RF Fox. *Classical Electrodynamics, 3rd Edition.* American Association of Physics Teachers, 1999.

[7] DR Smith, S Schultz, and P Markoš *et. al.* Determination of Effective Permittivity and Permeability of Metamaterials from Reflection and Transmission Coefficients. *Physical Review B*, 65(19):195104, 2002.

[8] TJ Cui, DR Smith, and RP Liu. *Metamaterials: Theory, Design, and Applications*. Springer, 2010.

[9] DL Mills and E Burstein. Polaritons: The Electromagnetic Modes of Media. *Reports on Progress in Physics*, 37(7):817, 1974.

[10] SC Lim, J Osman, and DR Tilley. Theory of a Gyromagnetic Fabry-Pérot Resonator. *Journal of Physics: Condensed Matter*, 9(39):8297, 1997.

[11] JB Pendry. Negative Refraction Makes a Perfect Lens. *Physical Review Letters*, 85(18):3966, 2000.

[12] NI Landy, S Sajuyigbe, and JJ Mock *et. al.* Perfect Metamaterial Absorber. *Physical Review Letters*, 100(20):207402, 2008.

[13] A Lakhtakia. An Electromagnetic Trinity from "Negative Permittivity" and "Negative Permeability". *International Journal of Infrared and Millimeter Waves*, 23(6):813–818, 2002.

[14] A. Sihvola, H. Wallen, and H. Kettunen. Dispersion manipulation of isotropic media through indefinite route. *2013 7th International Congress on Advanced Electromagnetic Materials in Microwaves and Optics, METAMATERIALS 2013*, pages 220–222, 2013.

[15] A. Grbic and G.V. Eleftheriades. Experimental verification of backward-wave radiation from a negative refractive index metamaterial. *Journal of Applied Physics*, 92:5930–5935, 2002.

[16] R. Seviour. Towards photonic crystal and metamaterial high-power microwave applications. 2009.

[17] Sam Hyeon Lee, Choon Mahn Park, Yong Mun Seo, and Chul Koo Kim. Reversed Doppler effect in double negative metamaterials. *Physical Review B*, 81(24):241102, 2010.

[18] JW (Lord Rayleigh) Strutt. On the Maintenance of Vibrations by Forces of Double Frequency, and on the Propagation of Waves Through a Medium Endowed with a Periodic Structure. *Phil. Mag.*, S.5, vol.24(147):145–59, 1887.

[19] JC Bose. On the Rotation of Plane of Polarisation of Electric Waves by a Twisted Structure. *Proceedings of the Royal Society of London*, 63(389-400):146–152, 1898.

[20] H Lamb. On Group-Velocity. *Proceedings of the London Mathematical Society*, 2(1):473–479, 1904.

[21] A Schuster. *An Introduction to the Theory of Optics*. E. Arnold, 1904.

[22] WE Kock. Metal-Lens Antennas. *Proceedings of the IRE*, 34(11):828–836, Nov 1946.

[23] VG Veselago. The Electrodynamics of Substances with Simultaneously Negative Values of ε and μ. *Physics-Uspekhi*, 10(4):509–514, 1968, (Russian 1967).

[24] JB Pendry, AJ Holden, and WJ Stewart *et. al.* Extremely Low Frequency Plasmons in Metallic Mesostructures. *Physical Review Letters*, 76(25):4773, 1996.

[25] JB Pendry, AJ Holden, and DJ Robbins *et. al.* Low Frequency Plasmons in Thin-Wire Structures. *Journal of Physics: Condensed Matter*, 10(22):4785, 1998.

[26] JB Pendry, AJ Holden, and DJ Robbins *et. al.* Magnetism From Conductors and Enhanced Nonlinear Phenomena. *Microwave Theory and Techniques, IEEE Transactions on*, 47(11):2075–2084, 1999.

[27] WN Hardy and LA Whitehead. Split-ring resonator for use in magnetic resonance from 200–2000 mhz. *Review of Scientific Instruments*, 52(2):213–216, 1981.

[28] M Shamonin, E Shamonina, and V Kalinin *et. al.* Properties of a Metamaterial Element: Analytical Solutions and Numerical Simulations for a Singly Split Double Ring. *Journal of Applied Physics*, 95(7):3778–3784, 2004.

[29] M Shamonin, E Shamonina, and V Kalinin *et. al.* Resonant Frequencies of a Split-Ring Resonator: Analytical Solutions and Numerical Simulations. *Microwave and Optical Technology Letters*, 44(2):133–136, 2004.

[30] P Hammond and J Sykulski. *Engineering electromagnetism: Physical processes and Computation.* Oxford University Press, Oxford, 1994.

[31] F.W. Grover. *Inductance calculations: Working formulas and tables.* Instrument Society of America, Research Triangle Park, NC, 1981.

[32] DR Smith, WJ Padilla, and DC Vier *et. al.* Composite Medium with Simultaneously Negative Permeability and Permittivity. *Physical Review Letters*, 84(18):4184, 2000.

[33] RA Shelby, DR Smith, and S Schultz. Experimental Verification of a Negative Index of Refraction. *Science*, 292(5514):77–79, 2001.

[34] AM Nicolson and GF Ross. Measurement of the Intrinsic Properties of Materials by Time-Domain Techniques. *Instrumentation and Measurement, IEEE Transactions on*, 19(4):377–382, 1970.

[35] WB Weir. Automatic Measurement of Complex Dielectric Constant and Permeability at Microwave Frequencies. *Proceedings of the IEEE*, 62(1):33–36, 1974.

[36] CG Parazzoli, RB Greegor, and K Li *et. al.* Experimental Verification and Simulation of Negative Index of Refraction Using Snells Law. *Physical Review Letters*, 90(10):107401, 2003.

[37] AA Houck, JB Brock, and IL Chuang. Experimental Observations of a Left-Handed Material that Obeys Snells Law. *Physical Review Letters*, 90(13):137401, 2003.

[38] RM Walser. Metamaterials: What are they? What are they good for? In *APS March Meeting Abstracts*, 2000.

[39] WS Weiglhofer and A Lakhtakia. *Introduction to Complex Mediums for Optics and Electromagnetics*, volume 123. SPIE press, 2003.

[40] C Argyropoulos, NM Estakhri, and F Monticone *et. al.* Negative Refraction, Gain and Nonlinear Effects in Hyperbolic Metamaterials. *Optics Express*, 21(12):15037–15047, 2013.

[41] T Xu, A Agrawal, and M Abashin *et. al.* All-Angle Negative Refraction and Active Flat Lensing of Ultraviolet Light. *Nature*, 497(7450):470, 2013.

[42] A Poddubny, I Iorsh, and P Belov *et. al.* Hyperbolic Metamaterials. *Nature Photonics*, 7(12):948–957, 2013.

[43] Z Wang, Y Feng, and J Zhao *et. al.* Analog Study of Near-Field Focusing and Subwavelength Imaging with Nonlinear Transmission-Line Metamaterial. *Science China Information Sciences*, 56(12):1–8, 2013.

[44] D Schurig, JJ Mock, and BJ Justice *et. al.* Metamaterial Electromagnetic Cloak at Microwave Frequencies. *Science*, 314(5801):977–980, 2006.

[45] F Zolla, S Guenneau, and A Nicolet *et. al.* Electromagnetic Analysis of Cylindrical Invisibility Cloaks and the Mirage Effect. *Optics Letters*, 32(9):1069–1071, 2007.

[46] T Ergin, N Stenger, and P Brenner *et. al.* Three-Dimensional Invisibility Cloak at Optical Wavelengths. *Science*, 328(5976):337–339, 2010.

[47] S Xu, Y Wang, and B Zhang *et. al.* Invisibility Cloaks from Forward Design to Inverse Design. *Science China Information Sciences*, 56(12):1–11, 2013.

[48] C Du, H Chen, and S Li. Quantum Left-Handed Metamaterial from Superconducting Quantum-Interference Devices. *Physical Review B*, 74(11):113105, 2006.

[49] J Gu, R Singh, and X Liu *et. al.* Active Control of Electromagnetically Induced Transparency Analogue in Terahertz Metamaterials. *Nature Communications*, 3:1151, 2012.

[50] J Shao, J Li, and J Li *et. al.* Analogue of Electromagnetically Induced Transparency by Doubly Degenerate Modes in a U-Shaped Metamaterial. *Applied Physics Letters*, 102(3):034106, 2013.

[51] BB Jin, JB Wu, and CH Zhang *et. al.* Enhanced Slow Light in Superconducting Electromagnetically Induced Transparency Metamaterials. *Superconductor Science and Technology*, 26(7):074004, 2013.

[52] N Papasimakis and NI Zheludev. Metamaterial-Induced Transparency: Sharp Fano Resonances and Slow Light. *Optics and Photonics News*, 20(10):22–27, 2009.

[53] B Luk'yanchuk, NI Zheludev, and SA Maier *et. al.* The Fano Reso-

nance in Plasmonic Nanostructures and Metamaterials. *Nature Materials*, 9(9):707, 2010.

[54] W Cao, R Singh, and IAI Al-Naib *et. al.* Low-loss Ultra-High-Q Dark Mode Plasmonic Fano Metamaterials. *Optics Letters*, 37(16):3366–3368, 2012.

[55] C Meng, R Peng, and R Fan *et. al.* Making Structured Metals Transparent for Broadband Electromagnetic Waves. *Science China Information Sciences*, 56(12):1–9, 2013.

[56] H Husu, BK Canfield, and J Laukkanen *et. al.* Chiral Coupling in Gold Nanodimers. *Applied Physics Letters*, 93(18):183115, 2008.

[57] S Zhang, Y Park, and J Li *et. al.* Negative Refractive Index in Chiral Metamaterials. *Physical Review Letters*, 102(2):023901, 2009.

[58] E Plum, J Zhou, and J Dong *et. al.* Metamaterial with Negative Index due to Chirality. *Physical Review B*, 79(3):035407, 2009.

[59] KF Lindman. Über eine Durch ein Isotropes System von Spiralförmigen Resonatoren Erzeugte Rotationspolarisation der Elektromagnetischen Wellen. *Annalen der Physik*, 368(23):621–644, 1920.

[60] WE Kock. Metallic Delay Lenses. *Bell System Technical Journal*, 27(1):58–82, 1948.

[61] SB Cohn. The Electric and Magnetic Constants of Metallic Delay Media Containing Obstacles of Arbitrary Shape and Thickness. *Journal of Applied Physics*, 22(5):628–634, 1951.

[62] W Rotman. Plasma Simulation by Artificial Dielectrics and Parallel-Plate Media. *IRE Transactions on Antennas and Propagation*, 10(1):82–95, 1962.

[63] RE Collin. *Field Theory of Guided Waves*. IEEE, 1991.

[64] GG MacFarlane. Surface Impedance of an Infinite Parallel-Wire Grid at Oblique Angles of Incidence. *Journal of the Institution of Electrical Engineers-Part IIIA: Radiolocation*, 93(10):1523–1527, 1946.

[65] YS Tan and R Seviour. Wave Energy Amplification in a Metamaterial-Based Traveling-Wave Structure. *EPL (Europhysics Letters)*, 87(3):34005, 2009.

[66] N Garcia and M Nieto-Vesperinas. Is There an Experimental Verification of a Negative Index of Refraction Yet? *Optics Letters*, 27(11):885–887, 2002.

[67] P Markoš, I Rousochatzakis, and CM Soukoulis. Transmission Losses in Left-Handed Materials. *Physical Review E*, 66(4):045601, 2002.

[68] S Obrien and JB Pendry. Magnetic Activity at Infrared Frequencies in Structured Metallic Photonic Crystals. *Journal of Physics: Condensed Matter*, 14(25):6383, 2002.

[69] JE Raynolds, BA Munk, and JB Pryor *et. al.* Ohmic Loss in Frequency-Selective Surfaces. *Journal of Applied Physics*, 93(9):5346–5358, 2003.

[70] R Seviour. Energy Amplification and Losses in Metamaterials and Photonic Structures. In *High-power Metamaterials for Accelerators and Microwave Applications, Boston*, 2010.

[71] DÖ Güney, T Koschny, and CM Soukoulis. Reducing Ohmic Losses in Metamaterials by Geometric Tailoring. *Physical Review B*, 80(12):125129, 2009.

[72] X Zhou, Y Liu, and X Zhao. Low Losses Left-Handed Materials with

Optimized Electric and Magnetic Resonance. *Applied Physics A: Materials Science & Processing*, 98(3):643–649, 2010.

[73] L Zhu, F Meng, and F Zhang *et. al.* An Ultra-Low Loss Split Ring Resonator by Suppressing the Electric Dipole Moment Approach. *Progress In Electromagnetics Research*, 137:239–254, 2013.

[74] F Magnus and B Wood *et. al.* A DC Magnetic Metamaterial. *arXiv preprint arXiv:0710.1227*, 2007.

[75] BG Ghamsari, J Abrahams, and S Remillard *et. al.* High-Temperature Superconducting Spiral Resonator for Metamaterial Applications. *IEEE Transactions on Applied Superconductivity*, 23(3):1500304–1500304, 2013.

[76] R Liu, Q Cheng, and JY Chin *et. al.* Broadband Gradient Index Microwave Quasi-Optical Elements Based on Non-Resonant Metamaterials. *Optics Express*, 17(23):21030–21041, 2009.

[77] X Wang and E Semouchkina. Microwave Cloaking Using Resonant and Non-Resonant Dielectric Materials. In *Advanced Electromagnetic Materials in Microwaves and Optics (METAMATERIALS), 2013 7th International Congress on*, pages 298–300. IEEE, 2013.

[78] DB Burckel, EA Shaner, and JR Wendt *et. al.* 3D Non-Resonant-Inclusion IR Metamaterials. Technical report, Sandia National Laboratories (SNL-NM), Albuquerque, NM (United States), 2011.

[79] Y Yuan, BI Popa, and SA Cummer. Zero Loss Magnetic Metamaterials using Powered Active Unit Cells. *Optics Express*, 17(18):16135–16143, 2009.

[80] SA Tretyakov. Metamaterials with Wideband Negative Permittiv-

ity and Permeability. *Microwave and Optical Technology Letters*, 31(3):163–165, 2001.

[81] RRA Syms, L Solymar, and IR Young. Three-Frequency Parametric Amplification in Magneto-Inductive Ring Resonators. *Metamaterials*, 2(2):122–134, 2008.

[82] BI Popa and SA Cummer. An Architecture for Active Metamaterial Particles and Experimental Validation at RF. *Microwave and Optical Technology Letters*, 49(10):2574–2577, 2007.

[83] P Weis, JL Garcia-Pomar, and M Rahm. Towards Loss Compensated and Lasing Terahertz Metamaterials Based on Optically Pumped Graphene. *Optics Express*, 22(7):8473–8489, 2014.

[84] AD Boardman, YG Rapoport, and N King *et. al.* Creating Stable Gain in Active Metamaterials. *JOSA B*, 24(10):A53–A61, 2007.

[85] A Fang, Th Koschny, and M Wegener *et. al.* Self-Consistent Calculation of Metamaterials with Gain. *Physical Review B*, 79(24):241104, 2009.

[86] B Nistad and J Skaar. Causality and Electromagnetic Properties of Active Media. *Physical Review E*, 78(3):036603, 2008.

[87] P Kinsler. Refractive Index and Wave Vector in Passive or Active Media. *Physical Review A*, 79(2):023839, 2009.

[88] X Liu, T Starr, and AF Starr *et. al.* Infrared Spatial and Frequency Selective Metamaterial with Near-Unity Absorbance. *Physical Review Letters*, 104(20):207403, 2010.

[89] X Liu, T Tyler, and T Starr *et. al.* Taming the Blackbody with Infrared Metamaterials as Selective Thermal Emitters. *Physical Review Letters*, 107(4):045901, 2011.

[90] PV Tuong, VD Lam, and JW Park *et. al.* Perfect-Absorber Metamaterial Based on Flower-Shaped Structure. *Photonics and Nanostructures-Fundamentals and Applications*, 11(1):89–94, 2013.

[91] C Wu, B Neuner III, and J John *et. al.* Metamaterial-based Integrated Plasmonic Absorber/Emitter for Solar Thermo-Photovoltaic Systems. *Journal of Optics*, 14(2):024005, 2012.

[92] Y Wang, T Sun, and T Paudel *et. al.* Metamaterial-Plasmonic Absorber Structure for High Efficiency Amorphous Silicon Solar Cells. *Nano Letters*, 12(1):440–445, 2011.

[93] I Huynen, N Quievy, and C Bailly *et. al.* Multifunctional Hybrids for Electromagnetic Absorption. *Acta Materialia*, 59(8):3255–3266, 2011.

[94] P Bollen, T Pardoen, and C Bailly *et. al.* Multifunctional Metamaterial Absorber Based on Honeycomb Filled with Epoxy-Carbon Nanotube Nanocomposite and Split Ring Resonator. In *Advanced Electromagnetic Materials in Microwaves and Optics (METAMATERIALS), 2013 7th International Congress on*, pages 349–351. IEEE, 2013.

[95] EE Narimanov and AV Kildishev. Optical Black Hole: Broadband Omnidirectional Light Absorber. *Applied Physics Letters*, 95(4):041106, 2009.

[96] JC Maxwell. Treatise on Electricity and Magnetism, 2 vols., reprint by Dover. *New York*, 1954.

[97] Lord Rayleigh. LVI. On the Influence of Obstacles Arranged in Rectangular Order upon the Properties of a Medium. *The London, Edinburgh, and Dublin Philosophical Magazine and Journal of Science*, 34(211):481–502, 1892.

[98] XC Zeng, PM Hui, and DJ Bergman *et. al.* Correlation and Clustering in the Optical Properties of Composites: A Numerical Study. *Physical Review B*, 39(18):13224, 1989.

[99] JP Clerc, G Giraud, and JM Laugier *et. al.* The Electrical Conductivity of Binary Disordered Systems, Percolation Clusters, Fractals and Related Models. *Advances in Physics*, 39(3):191–309, 1990.

[100] DM Grannan, JC Garland, and DB Tanner. Critical Behavior of the Dielectric Constant of a Random Composite Near the Percolation Threshold. *Physical Review Letters*, 46(5):375, 1981.

[101] AP Vinogradov, AM Karimov, and AT Kunavin *et. al.* Investigation of the Critical Behavior of the Dielectric Constant of Granular Materials. In *Dokl. Akad. Nauk SSSR*, volume 275, page 590, 1984.

[102] HJ Herrmann, B Derrida, and J Vannimenus. Superconductivity Exponents in Two- and Three-Dimensional Percolation. *Physical Review B*, 30(7):4080, 1984.

[103] AL Efros and BI Shklovskii. Critical Behaviour of Conductivity and Dielectric Constant near the Metal-Non-Metal Transition Threshold. *Physica Status Solidi (b)*, 76(2):475–485, 1976.

[104] GA Niklasson and CG Granqvist. Optical Properties and Solar Selectivity of Coevaporated Co-Al2O3 Composite Films. *Journal of Applied Physics*, 55(9):3382–3410, 1984.

[105] AP Vinogradov, AM Karimov, and AK Sarychev. Permittivity of Composite Percolation Materials: Similarity Law and Equations of State. *Sov. Phys. JETP*, 67(10):2129–2133, 1988.

[106] W Lamb, DM Wood, and NW Ashcroft. Long-Wavelength Electro-

magnetic Propagation In Heterogeneous Media. *Physical review B*, 21(6):2248, 1980.

[107] JC Maxwell-Garnett. Colours in Metal Glasses, in Metallic Films, and in Metallic Solutions. II. *Philosophical Transactions of the Royal Society of London. Series A, Containing Papers of a Mathematical or Physical Character*, pages 237–288, 1906.

[108] Von DAG Bruggeman. Berechnung Verschiedener Physikalischer Konstanten von Heterogenen Substanzen. I. Dielektrizitätskonstanten und Leitfähigkeiten der Mischkörper aus Isotropen Substanzen. *Annalen der Physik*, 416(7):636–664, 1935.

[109] ST Chui and L Hu. Theoretical Investigation on the Possibility of Preparing Left-Handed Materials in Metallic Magnetic Granular Composites. *Physical Review B*, 65(14):144407, 2002.

[110] GD Mahan. Long-Wavelength Absorption of Cermets. *Physical Review B*, 38(14):9500, 1988.

[111] D Stroud and FP Pan. Self-consistent Approach to Electromagnetic Wave Propagation in Composite Media: Application to Model Granular Metals. *Physical Review B*, 17(4):1602, 1978.

[112] Y Wu, J Li, and ZQ Zhang *et. al.* Effective Medium Theory for Magnetodielectric Composites: Beyond the Long-Wavelength Limit. *Physical Review B*, 74(8):085111, 2006.

[113] R Burridge, S Childress, and G Papanicolaou. Macroscopic Properties of Disordered Media. In *Macroscopic Properties of Disordered Media*, volume 154, 1982.

[114] JC Garland and DB Tanner *et. al. Electrical Transport and Optical*

Properties of Inhomogeneous Media. American Institute of Physics, 1978.

[115] P Sheng. Theory for the Dielectric Function of Granular Composite Media. *Physical Review Letters*, 45(1):60, 1980.

[116] AN Lagarkov, VN Semenenko, and VN Kisel *et. al.* Development and Simulation of Microwave Artificial Magnetic Composites Utilizing Nonmagnetic Inclusions. *Journal of Magnetism and Magnetic Materials*, 258:161–166, 2003.

[117] CL Holloway, EF Kuester, and J Baker-Jarvis *et. al.* A Double Negative (DNG) Composite Medium Composed of Magnetodielectric Spherical Particles Embedded in a Matrix. *IEEE Transactions on Antennas and Propagation*, 51(10):2596–2603, 2003.

[118] Th Koschny, P Markoš, and EN Economou *et. al.* Impact of Inherent Periodic Structure on Effective Medium Description of Left-Handed and Related Metamaterials. *Physical Review B*, 71(24):245105, 2005.

[119] C Caloz and T Itoh. *Electromagnetic Metamaterials: Transmission Line Theory and Microwave Applications.* John Wiley & Sons, 2005.

[120] DA Watkins. *Topics in Electromagnetic Theory.* Wiley, 1958.

[121] JD Baena, J Bonache, and F Martin *et. al.* Equivalent-Circuit Models for Split-Ring Resonators and Complementary Split-Ring Resonators Coupled to Planar Transmission Lines. *IEEE Transactions on Microwave Theory and Techniques*, 53(4):1451–1461, 2005.

[122] Agilent Network Analyzer Basics. Agilent technologies. *URL: http://cpliterature. product. agilent. com/litweb/pdf/5965-7917e. pdf*, 2004.

[123] CG Williams and GK Cambrell. Numerical Solution of Surface Waveguide Modes Using Transverse Field Components (Short Papers). *IEEE Transactions on Microwave Theory and Techniques*, 22(3):329–330, 1974.

[124] T Itoh. Spectral Domain Immitance Approach for Dispersion Characteristics of Generalized Printed Transmission Lines. *IEEE Transactions on Microwave Theory and Techniques*, 28(7):733–736, 1980.

[125] E Schweig and WB Bridges. Computer Analysis of Dielectric Waveguides: A Finite-Difference Method. *IEEE Transactions on Microwave Theory and Techniques*, 32(5):531–541, 1984.

[126] N Schulz, K Bierwirth, and F Arndt. Finite-difference Analysis of Integrated Optical Waveguides Without Spurious Mode Solutions. *Electronics Letters*, 22(18):963–965, 1986.

[127] RB Wu and CH Chen. A Variational Analysis of Dielectric Waveguides by the Conformal Mapping Technique. *IEEE Transactions on Microwave Theory and Techniques*, 33(8):681–685, 1985.

[128] P Daly. Hybrid-Mode Analysis of Microstrip by Finite-Element Methods. *IEEE Transactions on Microwave Theory and Techniques*, 19(1):19–25, 1971.

[129] BMA Rahman and JB Davies. Finite-Element Analysis of Optical and Microwave Waveguide Problems. *IEEE Transactions on Microwave Theory and Techniques*, 32(1):20–28, 1984.

[130] Ansoft Corporation. High Frequency Structure Simulator (HFSS). 2010.

[131] Ansoft Collaboration. HFSS Online Help Version 9.2. *American: Ansoft Inc*, 2004.

[132] C Pinciuc and V Marra. Simulating and Modeling RF and Microwave Heating. `www.comsol.com/video/simulating-modeling-rf-microwave-heating` (Accessed: 12-11-2016).

[133] DA De Wolf. *Essentials of Electromagnetics for Engineering*. Cambridge University Press, 2001.

[134] R Ludwig and P Bretchko. *RF circuit design: theory and applications, 2nd Edition*. Prentice-Hall, 2000.

[135] PZ Peebles Jr and TA Giuma. *Principles of Electrical Engineering*. McGraw-Hill, 1991.

[136] RP Feynman, RB Leighton, and ML Sands. *The Feynman Lectures on Physics: Vol. 2: The Electromagnetic Field*. Addison-Wesley, 1965.

[137] UC Hasar and CR Westgate. A Broadband and Stable Method for Unique Complex Permittivity Determination of Low-Loss Materials. *Trans. Microw. Theory Tech.*, 57(2):471–477, 2009.

[138] DM Pozar. *Microwave Engineering, 4th Edition*. John Wiley & Sons, 2012.

[139] J Baker-Jarvis, EJ Vanzura, and WA Kissick. Improved Technique for Determining Complex Permittivity with the Transmission/Reflection Method. *IEEE Transactions on Microwave Theory and Techniques*, 38(8):1096–1103, 1990.

[140] AH Boughriet, C Legrand, and A Chapoton. Noniterative Stable Transmission/Reflection Method for Low-Loss Material Complex Permittivity Determination. *IEEE Transactions on Microwave Theory and Techniques*, 45(1):52–57, 1997.

[141] K Chalapat, K Sarvala, and J Li *et. al.* Wideband Reference-Plane Invariant Method for Measuring Electromagnetic Parameters of Materials. *IEEE Transactions on Microwave Theory and Techniques*, 57(9):2257–2267, 2009.

[142] JB Pendry. Photonic Band Structures. *Journal of Modern Optics*, 41(2):209–229, 1994.

[143] JB Pendry. Calculating Photonic Band Structure. *Journal of Physics: Condensed Matter*, 8(9):1085, 1996.

[144] DR Smith, DC Vier, and T Koschny *et. al.* Electromagnetic Parameter Retrieval from Inhomogeneous Metamaterials. *Physical Review E*, 71(3):036617, 2005.

[145] NI Landy, CM Bingham, T Tyler, N Jokerst, DR Smith, and WJ Padilla. Design, theory, and measurement of a polarization-insensitive absorber for terahertz imaging. *physical review B*, 79(12):125104, 2009.

Appendix A

Derivations

A.1 Linear Materials

In this context a "linear" material means a material whose polarisation density, **P** scales linearly with the electric field strength **E** (Electrically Linear) and whose magnetisation **M** scales linearly with the magnetic field strength **H** (Magnetically Linear). Setting this condition makes the system a lot simpler to model and enables the use of simple constitutive relations in Maxwell's Equations:

$$\nabla \cdot \mathbf{E} = \frac{\rho}{\varepsilon}, \tag{A.1}$$

$$\nabla \cdot \mathbf{B} = 0, \tag{A.2}$$

$$\nabla \times \mathbf{E} = \frac{-\partial \mathbf{B}}{\partial t}, \tag{A.3}$$

$$\nabla \times \mathbf{B} = \mu \left(\varepsilon \frac{\partial \mathbf{E}}{\partial t} + \mathbf{J} \right), \tag{A.4}$$

A.1.1 Electrically Linear

In a dielectric material, the presence of an external electric field results in a slight separation of the atomic nuclei and electrons. This induces a polarising local electric dipole moment, and results in the total volume charge density being re-expressed as $\rho = \rho_f + \rho_b$, where ρ_f and ρ_b are the free and bound charge densities [133].

Equation A.1, for free space, then becomes:

$$\begin{aligned} \nabla \cdot \mathbf{E} &= \frac{\rho_f + \rho_b}{\varepsilon_0}, \\ \nabla \cdot \varepsilon_0 \mathbf{E} &= \rho_f - \nabla \cdot \mathbf{P}, \\ \nabla \cdot (\varepsilon_0 \mathbf{E} + \mathbf{P}) &= \rho_f, \\ \nabla \cdot \mathbf{D} &= \rho_f, \end{aligned} \tag{A.5}$$

where $\rho_b = -\nabla \cdot \mathbf{P}$, $\mathbf{P}$ is the (macroscopic) density of the permanent or induced electric dipole moments in the material ($\sum_m \mathbf{p}_m = \mathbf{P}dv$), and $\mathbf{D}$ is the electric displacement field, defined as:

$$\mathbf{D} \equiv \varepsilon_0 \mathbf{E} + \mathbf{P}. \tag{A.6}$$

For an electrically linear material, the polarisation density $\mathbf{P}$ scales linearly with the electric field strength $\mathbf{E}$:

$$\mathbf{P} = \varepsilon_0 \chi_e \mathbf{E}, \tag{A.7}$$

where χ_e is the electric susceptibility of the material (this represents the degree of polarisation the material undergoes in response to an incident electric field).

Inserting this into Eqn. A.6 gives:

$$\begin{aligned}
\mathbf{D} &= \varepsilon_0\mathbf{E} + \mathbf{P}, \\
\mathbf{D} &= \varepsilon_0\mathbf{E} + \varepsilon_0\chi_e\mathbf{E}, \\
\mathbf{D} &= \varepsilon_0(1+\chi_e)\mathbf{E}, \\
\mathbf{D} &= \varepsilon_0\varepsilon_r\mathbf{E}, \\
\mathbf{D} &= \varepsilon\mathbf{E}, \qquad \text{(A.8)}
\end{aligned}$$

where $\varepsilon = \varepsilon_0\varepsilon_r$ and $\varepsilon_r = (1+\chi_e)$ and may both be complex.

A.1.2 Magnetically Linear

To determine the magnetic behaviour of a material, it is useful to think of the atom as a nucleus with electrons revolving around it, with each electron having its own intrinsic magnetic moment $\mathbf{m}_i$. Summing these intrinsic magnetic moments gives an averaged magnetisation $\sum_i N_i < \mathbf{m}_i >= \mathbf{M}$ [6].

This magnetisation contributes to the current density, so $\mathbf{J}$ is replaced by $\mathbf{J} \rightarrow \mathbf{J} + \mathbf{J}_m$ where $\mathbf{J}_m = \nabla \times \mathbf{M}$.

This results in:

$$\begin{aligned}
\nabla \times \mathbf{B} = \mu_0(\mathbf{J} + \mathbf{J}_m) &= \mu_0(\mathbf{J} + \nabla \times \mathbf{M}), \\
\nabla \times (\frac{1}{\mu_0}\mathbf{B} - \mathbf{M}) &= \mathbf{J}, \\
\nabla \times \mathbf{H} &= \mathbf{J}, \qquad \text{(A.9)}
\end{aligned}$$

where $\mathbf{H} \equiv \frac{1}{\mu_0}\mathbf{B} - \mathbf{M}$ and $\mathbf{B} = \mu_0\mathbf{H} + \mu_0\mathbf{M}$.

For a magnetically linear material, the magnetisation $\mathbf{M}$ scales linearly with the magnetic field strength $\mathbf{H}$ giving:

$$\mathbf{M} = \chi_m \mathbf{H}, \tag{A.10}$$

where χ_m is the magnetic susceptibility of the material (this represents the degree of magnetisation the material undergoes when exposed to an external magnetic field). Therefore $\mathbf{B}$ is re-expressed as:

$$\begin{aligned} \mathbf{B} &= \mu_0 \mathbf{H} + \mu_0 \mathbf{M}, \\ \mathbf{B} &= \mu_0 \mathbf{H} + \mu_0 \chi_m \mathbf{H}, \\ \mathbf{B} &= \mu_0 (1 + \chi_m) \mathbf{H}, \\ \mathbf{B} &= \mu_0 \mu_r \mathbf{H}, \\ \mathbf{B} &= \mu \mathbf{H}, \end{aligned} \tag{A.11}$$

where $\mu = \mu_0 \mu_r$ and $\mu_r = (1 + \chi_m)$ and may both be complex.

A.2 NRW Extraction Technique

The main aim of the Nicolson-Ross paper is to determine an easy direct method for extracting the values of the permittivity ε and the permeability μ of a material.

The extraction technique begins by considering a system of an annulus of material, with permittivity $\varepsilon = \varepsilon_0\varepsilon_r$, permeability $\mu = \mu_0\mu_r$ (i.e. linear) and impedance Z, loaded into a coaxial cable with characteristic impedance Z_0, as shown schematically in Fig. A.1.

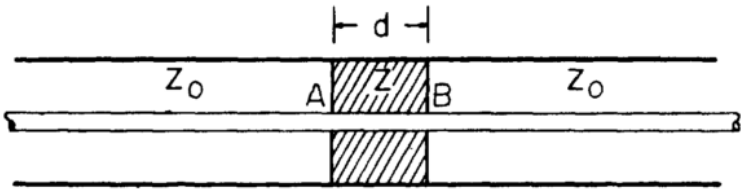

Figure A.1: Setup of the Nicolson-Ross Extraction of permittivity and permeability from scattering parameters. This consists of a coaxial cable with an annular disk of material loaded between A (z=0) and B (z=d) [34].

The impedance Z can be determined by modelling the system using an equivalent circuit model as an LCR transmission line circuit. By modelling the loaded coaxial cable as a lumped transmission line (see Ref. [134] for more details), an equivalent circuit model can be used to determine the electromagnetic parameters of the system. As can be seen in Fig. A.2, the transmission line is modelled as an infinite number of repeatable elements; one of these units, located between z and $z + \Delta z$, consists of a distributed resistance R, a distributed inductance L, a capacitance C and conductance G. By taking Δz to 0, the behaviour for the complete transmission line can be determined using Kirchoff's Laws.

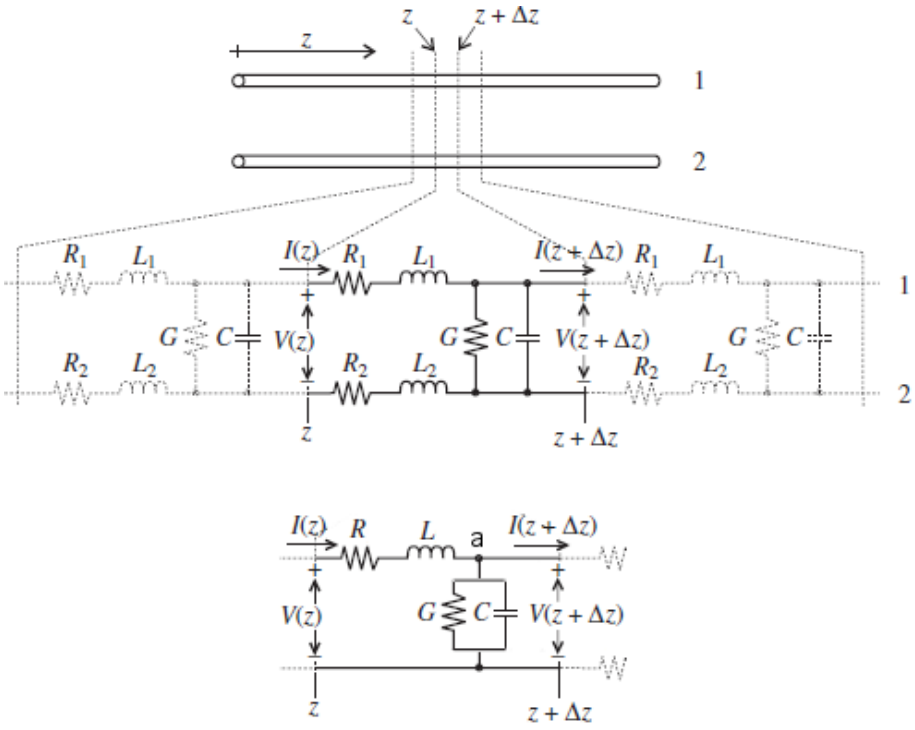

Figure A.2: Image showing the equivalent circuit model for the infinite transmission line [134]. Bottom image shows the simplified version of the repeating element.

A.2.1 Kirchoff's Voltage Law

From Kirchoff's Voltage law (voltage around a closed loop = zero) the voltage at z is determined as:

$$V(z) = V_R + V_L + V(z + \Delta z) = V_{R+L} + V(z + \Delta z), \tag{A.12}$$

where $V(z), V_R, V_L$ and $V(z + \Delta z)$ are the initial voltage, the voltage drop over R, the voltage drop over L and the remaining voltage at $V(z + \Delta z)$ respectively [135]. As R and L are connected in series, their associated voltages can be combined as V_{R+L}. Knowing that:

$$V_{R+L} = Z_{R+L} I_{R+L}, \tag{A.13}$$

where $I_{R+L} = I(z + \Delta z)$ is the current per unit length through R and L, the combined impedance Z_{R+L} is determined as:

$$Z_{R+L} = Z_R + Z_L = R + i\omega L,$$

where Z_R and Z_L are the impedances of R and L. This enables the determination of V_{R+L} as:

$$V_{R+L} = (R + i\omega L) I(z + \Delta z) \Delta z.$$

Inserting these values into the equation for $V(z)$, Eqn. A.12, gives:

$$V(z) = (R + i\omega L) I(z + \Delta z) \Delta z + V(z + \Delta z).$$

Rearranging this gives:

$$\frac{V(z+\Delta z)-V(z)}{\Delta z} = -(R+i\omega L)I(z+\Delta z).$$

Taking the limit of $\Delta z \rightarrow$ results in:

$$\frac{dV(z)}{dz} = -(R+i\omega L)I(z). \tag{A.14}$$

This is the first of two general transmission line equations.

A.2.2 Kirchoff's Current Law

From Kirchoff's current law (conversation of charge) the current through point "a" is:

$$I(z) = I(z+\Delta z) + I_{G+C}, \tag{A.15}$$

where I_{G+C} is the current that flows into the section modelling the conductance and capacitance part of the circuit.

Again by using Eqn. A.13 (replacing $(R+L)$ with $(G+C)$) and combining G and C in parallel using [135]) the combined impedance of the $(G+C)$ part of the circuit is determined as:

$$Z_{G+C} = (1/Z_G + 1/Z_C)^{-1} = (G+i\omega C)^{-1}.$$

Knowing that $V_{G+C} = V(z+\Delta z)$, the current per unit length through the $(G+C)$ part of the system can be determined as:

$$I_{G+C} = V_{G+C}/Z_{G+C} = V(z+\Delta z)(G+i\omega C)\Delta z.$$

Therefore the current at z is determined as:

$$I(z) = I(z + \Delta z) + V(z + \Delta z)(G + i\omega C)\Delta z.$$

Rearranging and taking the limit $\Delta z \to 0$ obtains:

$$\frac{dI(z)}{dz} = -V(z)(G + i\omega C). \tag{A.16}$$

This is the second of two general transmission line equations.

One can quite clearly see that Eqns. A.14 and A.16 are coupled to one another as both have either the differential of $I(z)$ or $V(z)$ related to $V(z)$ or $I(z)$ respectively.

This coupling can be removed by taking the second differential of Eqn. A.14 and substituting into Eqn. A.16, and by taking the second differential of Eqn. A.16 and substituting into Eqn. A.14.

This results in two second order differential equations, given as:

$$\frac{d^2V(z)}{dz^2} = V(z)(R + i\omega L)(G + i\omega C) = \kappa^2 V(z), \tag{A.17}$$

$$\frac{d^2I(z)}{dz^2} = I(z)(R + i\omega L)(G + i\omega C) = \kappa^2 I(z), \tag{A.18}$$

where $\kappa^2 = (R + i\omega L)(G + i\omega C)$.

Solutions for $V(z)$ and $I(z)$ can now be found, enabling the determination of Z for the loaded material.

A.2.3 Impedance Z of the loaded material

The equations determined for the voltage and current are both second order differential equations therefore ansatz of the form:

$$V(z) = V_0 e^{\kappa z} \qquad \text{and} \qquad I(z) = I_0 e^{\kappa z},$$

can be suggested as solutions, giving:

$$\frac{dV(z)}{dz} = \kappa V_0 e^{\kappa z} \qquad \text{and} \qquad \frac{d^2V(z)}{dz^2} = \kappa^2 V_0 e^{\kappa z}, \tag{A.19}$$

$$\frac{dI(z)}{dz} = \kappa I_0 e^{\kappa z} \qquad \text{and} \qquad \frac{d^2I(z)}{dz^2} = \kappa^2 I_0 e^{\kappa z}. \tag{A.20}$$

However, the question arises as to whether this solution uses $+\kappa$ or $-\kappa$. Expressing each of the voltage and current waves as:

$$\begin{aligned} V(z) &= V^+ + V^- = V_0^+ e^{-\kappa z} + V_0^- e^{\kappa z}, \\ I(z) &= I^+ + I^- = I_0^+ e^{-\kappa z} + I_0^- e^{\kappa z}, \end{aligned} \tag{A.21}$$

where the + sign represents waves travelling in the forward $+z$ direction ($e^{-\kappa z}$ is conventional notation for a wave propagating in this direction as this ensures the wave diminishes in amplitude), and the $-$ sign represents waves travelling in the backwards $-z$ direction, and by setting the sign in front of κ, κ can be forced to be positive and thus:

$$\kappa = +\sqrt{(R + i\omega L)(G + i\omega C)}. \tag{A.22}$$

By inserting the voltage solution from Eqn. A.21 into Eqn. A.19, $\frac{dV(z)}{dz}$ can be determined as:

$$\begin{aligned}\frac{dV(z)}{dz} &= \frac{d(V_0^+ e^{-\kappa z} + V_0^- e^{\kappa z})}{dz}, \\ &= \frac{d(V_0^+ e^{-\kappa z})}{dz} + \frac{d(V_0^- e^{\kappa z})}{dz}, \\ &= -\kappa V_0^+ e^{-\kappa z} + \kappa V_0^- e^{\kappa z}, \\ &= -\kappa(V_0^+ e^{-\kappa z} - V_0^- e^{\kappa z}).\end{aligned}$$

Equation A.14 shows this is equal to:

$$\frac{dV(z)}{dz} = -(R + i\omega L)I(z).$$

Inserting κ from Eqn. A.22 results in:

$$-\kappa(V_0^+ e^{-\kappa z} - V_0^- e^{\kappa z}) = -(R + i\omega L)I(z). \tag{A.23}$$

This enables the current at z to be expressed as:

$$\begin{aligned}I(z) &= \frac{\kappa}{(R + i\omega L)}(V_0^+ e^{-\kappa z} - V_0^- e^{\kappa z}), \\ &= \frac{\kappa}{(R + i\omega L)}(V^+ - V^-).\end{aligned} \tag{A.24}$$

$V(z)$ and $I(z)$ have now been determined (with the associated impedance $Z = V(z)/I(z)$). However, caution needs to be taken here as the forward and backwards travelling waves need to be dealt with individually.

The characteristic impedance of the empty system must be the same in both directions, thus:

$$\frac{V^+}{I^+} = Z_0 = \frac{V^-}{I^-},$$

where $V^+ = V_0^+ e^{-\kappa z}$ and $I^+ = I_0^+ e^{-\kappa z} = \frac{\kappa}{(R+i\omega L)} V^+$. This gives:

$$Z_0 = \frac{V^+}{I^+} = \frac{V^+}{V^+}\frac{(R+i\omega L)}{\kappa} = \frac{(R+i\omega L)}{\sqrt{(R+i\omega L)(G+i\omega C)}} = \sqrt{\frac{(R+i\omega L)}{(G+i\omega C)}}. \tag{A.25}$$

For the coaxial system, where [134, 136]:

$$L = \frac{\mu ln(b/a)}{2\pi} \qquad \text{and} \qquad C = \frac{2\pi\varepsilon}{ln(b/a)},$$

where a and b are the radii of the inner and outer conductors respectively, the impedance of a lossless ($R = G = 0$) material is given as:

$$Z = \sqrt{\frac{L}{C}} = \frac{ln(b/a)}{2\pi}\sqrt{\frac{\mu}{\varepsilon}},$$

and κ is equal to:

$$\kappa = \sqrt{(i\omega L)(i\omega C)} = i\omega\sqrt{LC} = i\omega\sqrt{\varepsilon\mu}. \tag{A.26}$$

Using the linearity of the material, $\varepsilon = \varepsilon_0\varepsilon_r$ and $\mu = \mu_0\mu_r$. Z is therefore expressed as:

$$Z = \frac{ln(b/a)}{2\pi}\sqrt{\frac{\mu}{\varepsilon}} = \frac{ln(b/a)}{2\pi}\sqrt{\frac{\mu_0}{\varepsilon_0}}\sqrt{\frac{\mu_r}{\varepsilon_r}} = Z_0\sqrt{\frac{\mu_r}{\varepsilon_r}}. \tag{A.27}$$

This equation relates the impedance of the load to its material properties ε_r and μ_r. However, these properties are not directly measurable.

The impedance of the load can be determined by utilising the reflection coefficient Γ. This is a measure of the amount of the wave reflected off the load if the load length in the direction of wave propagation was infinite.

This is determined as the ratio of the forward voltage V^+ to the reflected voltage V^- (backward wave):

$$\Gamma = \frac{V^+}{V^-}. \tag{A.28}$$

Therefore $V^- = \Gamma V^+$ and $V(z)$ can be rewritten from Eqn. A.21 as:

$$\begin{aligned} V(z) &= V^+ + V^-, \\ V(z) &= V^+ + \Gamma V^+, \\ V(z) &= V^+(1+\Gamma). \end{aligned} \tag{A.29}$$

This gives an expression for the voltage at z in terms of Γ.

The current in terms of Γ can be determined by inserting Eqn. A.25 into Eqn. A.24, giving:

$$I(z) = \frac{V^+ - V^-}{Z_0} = \frac{V^+(1-\Gamma)}{Z_0}. \tag{A.30}$$

Using $Z = V(z)/I(z)$ gives:

$$Z = \frac{V(z)}{I(z)} = \frac{V^+(1+\Gamma)}{\frac{V^+(1-\Gamma)}{Z_0}} = \frac{1+\Gamma}{1-\Gamma} Z_0. \tag{A.31}$$

Rearranging this for Γ gives:

$$\Gamma = \frac{Z - Z_0}{Z + Z_0}. \tag{A.32}$$

Inserting the result from Eqn. A.27 obtains:

$$\Gamma = \frac{Z - Z_0}{Z + Z_0} = \frac{\sqrt{\mu_r/\varepsilon_r} - 1}{\sqrt{\mu_r/\varepsilon_r} + 1}. \tag{A.33}$$

This is Eqn. 1 in the Nicolson-Ross paper and gives a value of the reflection coefficient Γ in terms of the constitutive parameters ε and μ.

A.2.4 Scattering Parameters

The previous section focused on an infinite d, and from this determined the value for the refection coefficient Γ.

However, in reality there is no such thing as an infinite system. This section introduces the transmission coefficient, T (the Nicolson-Ross paper called this z, but this a rather unhelpful assignment as impedances are denoted by Z and the wave is travelling in the $+z$ direction).

Again referring back to Fig. A.1, a wave propagating from A to B through the material can be written:

$$T = e^{-ik_z d}, \tag{A.34}$$

where k_z represents the wavenumber of the incident wave travelling in the z direction. The wavenumber $k = \omega/v$ where ω is the angular frequency of the wave and v is the speed of propagation and equals $1/\sqrt{\mu\varepsilon} = c/\sqrt{\mu_r\varepsilon_r}$. This means the transmission coefficient can be written as:

$$T = e^{-i(\omega/c)d\sqrt{\mu_r\varepsilon_r}}. \tag{A.35}$$

Creating a signal flow diagram for the system shown in Fig. A.1 shows more easily how the voltage and current flow around the circuit, enabling easier determination of their values. This signal flow diagram can be seen in Fig. A.3.

Scattering parameters determine the amount of a wave that propagates forward or backwards after passing over a Device Under Testing (DUT). A

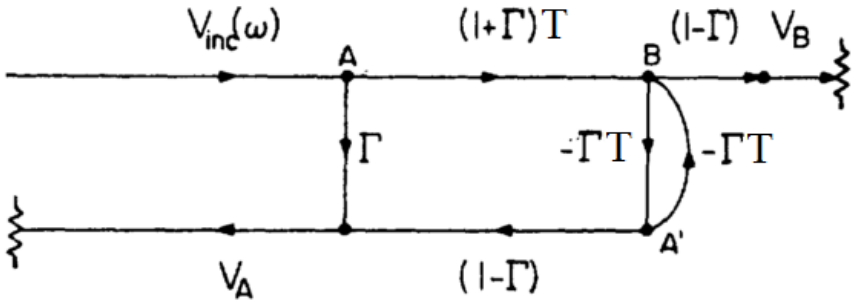

Figure A.3: Signal Flow Diagram for the system outlined in Fig. A.1

schematic showing how the scattering parameters are defined in relation to incident and outgoing waves is shown in Fig. A.4.

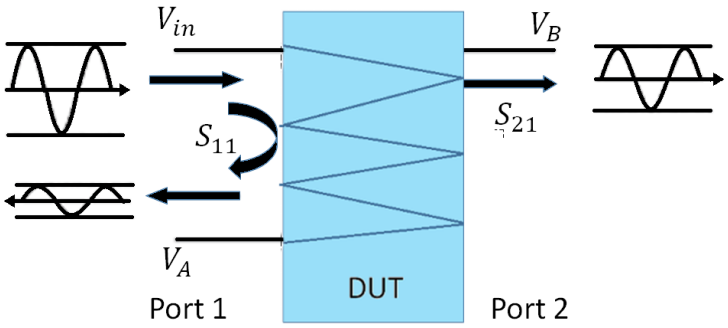

Figure A.4: Schematic demonstrating how scattering parameters are determined.

For the system of interest there is no incident wave (from the right hand side), so $S_{12} = S_{22} = 0$. The scattering parameters S_{11} and S_{21} are defined as the ratios of the reflected voltage to incident voltage, and transmitted voltage to incident voltage respectively:

$$S_{11} = \frac{V_A}{V_{inc}(\omega)} \qquad \text{and} \qquad S_{21} = \frac{V_B}{V_{inc}(\omega)}. \tag{A.36}$$

To make the derivation easier the signal flow diagram can be reduced down further, removing the self-loop between A' and B, as seen in Fig. A.5.

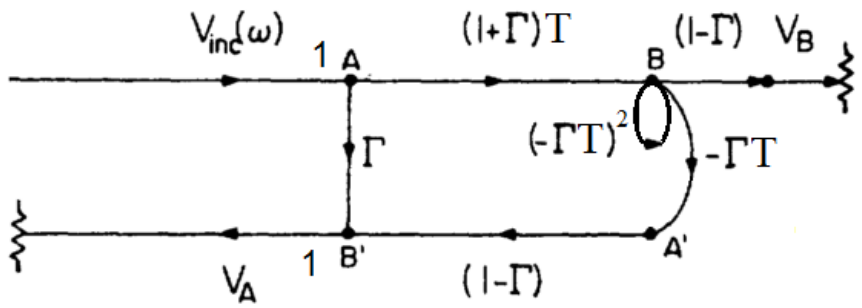

Figure A.5: Reduced Signal Flow Diagram for the system outlined in Fig. A.1

V_A is then calculated (previous node $\times$ path coefficient for all arrows pointing into a node) as:

$$
\begin{aligned}
V_A &= 1 \cdot B' \qquad \text{where,} \\
B' &= \Gamma A + (1-\Gamma)A', \\
A &= 1 \cdot V_{inc}, \\
A' &= (-\Gamma T)B, \\
B &= (1+\Gamma)TA + (-\Gamma T)^2 B \rightarrow B = \frac{(1+\Gamma)TA}{1-(-\Gamma T)^2}.
\end{aligned}
$$

Altogether, this gives:

$$
\begin{aligned}
S_{11} = \frac{V_A}{V_{inc}} &= \Gamma + \frac{(1-\Gamma)(-\Gamma T)(1+\Gamma)T}{1-\Gamma^2 T^2}, \\
&= \Gamma\left(1 - \frac{(1-\Gamma^2)T^2}{1-\Gamma^2 T^2}\right), \\
S_{11} &= \frac{\Gamma(1-T^2)}{1-\Gamma^2 T^2}. \qquad \text{(A.37)}
\end{aligned}
$$

This is Eqn. 4 in the Nicolson-Ross paper and gives the scattering parameter S_{11} in terms of the reflection and transmission coefficients.

Also note that it now becomes clear that for an infinite system ($T = 0$), $S_{11} = \Gamma$.

V_B can be calculated in a similar manner:

$$V_B = (1 - \Gamma) \cdot B,$$

giving:

$$\begin{aligned} S_{21} = \frac{V_B}{V_{inc}} &= \frac{(1-\Gamma)(1+\Gamma)T}{1-\Gamma^2T^2}, \\ S_{21} &= \frac{(1-\Gamma^2)T}{1-\Gamma^2T^2}. \end{aligned} \tag{A.38}$$

This is Eqn. 3 in the Nicolson-Ross paper and relates S_{21} to the reflection and transmission coefficients.

Also note that it now becomes clear that for a system with no reflections ($\Gamma = 0$), $S_{21} = T$.

This results in two equations (A.37 and A.38) with two unknowns (Γ and T; S_{11} and S_{21} can be directly measured) so Γ can be determined by solving simultaneous equations.

Start by setting $V_1 = S_{21} + S_{11}$. This gives:

$$\begin{aligned} V_1 &= \frac{T - \Gamma^2T + \Gamma - \Gamma T^2}{1 - T^2\Gamma^2}, \\ &= \frac{(T+\Gamma)(1-\Gamma T)}{(1+\Gamma T)(1-\Gamma T)}, \\ &= \frac{T+\Gamma}{1+\Gamma T}. \end{aligned} \tag{A.39}$$

Setting $V_2 = S_{21} - S_{11}$ gives:

$$\begin{aligned} V_2 &= \frac{(1-\Gamma^2)T-(1-T^2)\Gamma}{1-T^2\Gamma^2}, \\ &= \frac{(T-\Gamma)(1+\Gamma T)}{(1-\Gamma T)(1+\Gamma T)}, \\ &= \frac{T-\Gamma}{1-\Gamma T}. \end{aligned} \tag{A.40}$$

Rearranging A.39 for T and inserting this into A.40 gives:

$$V_2 = \frac{V_1-\Gamma-\Gamma(1-\Gamma V_1)}{1-\Gamma V_1-\Gamma(V_1-\Gamma)}.$$

Rearranging for Γ gives:

$$\begin{aligned} \Gamma^2 - 2\Gamma\left(\frac{1-V_1V_2}{V_1-V_2}\right) + \frac{V_1-V_2}{V_1-V_2} = 0, \\ \Gamma^2 - 2\Gamma X + 1 = 0, \end{aligned} \tag{A.41}$$

where X is defined as:

$$X \equiv \frac{1-V_1V_2}{V_1-V_2} = \frac{1+S_{11}^2-S_{21}^2}{2S_{11}}. \tag{A.42}$$

Equation A.41 is a quadratic equation, solved using $\Gamma = \frac{-b\pm\sqrt{b^2-4ac}}{2a}$ where a and b are the coefficients in front of the Γ^2 and Γ terms, and c is the independent term. This gives:

$$\Gamma = X \pm \sqrt{X^2-1} = \frac{1+S_{11}^2-S_{21}^2}{2S_{11}} \pm \sqrt{\left(\frac{1+S_{11}^2-S_{21}^2}{2S_{11}}\right)^2 - 1}. \tag{A.43}$$

To determine the correct sign of the square root the material is assumed passive since only one choice of sign satisfies $|\Gamma| \leq 1$ (else the material would be amplifying the wave with no incident energy source, breaking conservation of energy). This shows that Γ is related to the physically measurable quantities S_{11} and S_{21}.

Once Γ has been correctly determined, Eqn. A.39 can be used to determine T, giving:

$$T = \frac{V_1 - \Gamma}{1 - V_1\Gamma} = \frac{S_{11} + S_{21} - \Gamma}{1 - (S_{11} + S_{21})\Gamma}. \tag{A.44}$$

The final step in this derivation is to relate μ_r and ε_r to the scattering parameters S_{11} and S_{21}. Rearranging Eqn. A.33 results in:

$$\frac{\mu_r}{\varepsilon_r} = \left(\frac{1+\Gamma}{1-\Gamma}\right)^2 = c_1, \tag{A.45}$$

and rearranging Eqn. A.35 gives:

$$\mu_r\varepsilon_r = -\left(\frac{c}{\omega d} ln(1/T)\right)^2 = c_2. \tag{A.46}$$

Multiplying Eqns. A.45 and A.46 yields:

$$\mu_r = \sqrt{c_1 c_2} \qquad \text{and} \qquad \varepsilon_r = \sqrt{c_2/c_1}, \tag{A.47}$$

thus showing that complex values of permittivity and permeability can be determined by measurements of the scattering parameters.

Note here that issues with this method of extraction can already be seen; when S_{11} approaches zero the value for Γ becomes unstable as the solution to Eq. A.43 becomes infinite. This issue, in practise, can be resolved by making the material thickness (d) as small as possible (a thickness of less than half a wavelength), though this does increase the uncertainties in the scattering parameter measurements [137].

A.2.5 Weir Extension

The Nicolson-Ross paper produced an extraction technique for ε_r and μ_r in the Time Domain; Weir's method determines ε_r and μ_r in the Frequency Domain. The main issue, according to Weir, is that in the Time Domain a Fourier transform is required to determine ε_r and μ_r from the measured transient response. The other issue is that the frequency values which ε_r and μ_r can be determined are band-limited due to the timed response of the pulse and its repetition frequency. The final issue with the Nicolson-Ross technique is that it produces multi-valued solutions resulting from the ambiguity in Γ, resulting in ambiguities in determining the phase shift over the material for transmission frequencies of $n\lambda/2$.

To solve these issues, Weir's Frequency Domain approach compares the calculated and measured propagating wave through the material. Though this is not very valid for dispersive media (as the concept of group velocity breaks down in regions of anomalous dispersion) it does provide a more rigorous method for determining ε_r and μ_r, removing the frequency dependence on which readings can be taken.

The paper builds on many of the equations already determined in the Nicolson-Ross paper, specifically referring to Eqns. A.43, A.44 for Γ and T respectively, and using Eqns. A.45 and A.46.

Specifically, rearranging Eqn. A.46 and using:

$$\begin{aligned} v &= \frac{1}{\sqrt{\varepsilon\mu}}, \\ &= \frac{1}{\sqrt{\varepsilon_0\mu_0\varepsilon_r\mu_r}}, \\ &= \frac{c}{\sqrt{\varepsilon_r\mu_r}}, \end{aligned} \tag{A.48}$$

where v is the speed of wave propagation in the material and is equal to $\frac{\omega\lambda_g}{2\pi}$ where λ_g is the guide wavelength, results in:

$$\begin{aligned} c_2 = \mu_r\varepsilon_r &= -\left(\frac{c}{\omega d}ln(1/T)\right)^2, \\ \mu_r\varepsilon_r &= \left(\frac{j\lambda_g\sqrt{\varepsilon_r\mu_r}}{2\pi d}ln(1/T)\right)^2, \\ \sqrt{\mu_r\varepsilon_r} &= \frac{j\lambda_g\sqrt{\varepsilon_r\mu_r}}{2\pi d}ln(1/T), \\ \frac{1}{\lambda_g} &= \frac{j}{2\pi d}ln(1/T). \end{aligned} \tag{A.49}$$

However λ_g is also defined as [138]:

$$\begin{aligned} \lambda_g &= \frac{\lambda_0}{\sqrt{(c/v)^2 - (\lambda_0/\lambda_c)^2}}, \\ &= \frac{\lambda_0}{\sqrt{\varepsilon_r\mu_r - (\lambda_0/\lambda_c)^2}}, \end{aligned}$$

where λ_0 is the free-space wavelength and λ_c is the cutoff wavelength.

Inserting this into Eqn. A.49 results in:

$$\begin{aligned} \frac{\sqrt{\varepsilon_r\mu_r - (\lambda_0/\lambda_c)^2}}{\lambda_0} &= \frac{j}{2\pi d}ln(1/T), \\ \sqrt{\frac{\varepsilon_r\mu_r}{\lambda_0^2} - \frac{1}{\lambda_c^2}} &= \frac{j}{2\pi d}ln(1/T), \\ \frac{\varepsilon_r\mu_r}{\lambda_0^2} - \frac{1}{\lambda_c^2} &= -\left(\frac{1}{2\pi d}ln(1/T)\right)^2 = \frac{1}{\Lambda^2}. \end{aligned} \tag{A.50}$$

This is Eqn. 8 in the Weir paper and again relates ε_r and μ_r to the transmission coefficient.

A.3 Smith Adaptation of the NRW approach

The Nicolson-Ross and Weir papers demonstrate how to extract the properties ε and μ from the measured values of S_{11} and S_{21} for a bulk material. This method became the standard technique for extracting these parameters for many years, with improvements made over the years to account for the underlying issues presented, specifically for materials with low loss [139–141].

In 2002, Smith built on this parameter extraction technique by using Pendry's Transfer Matrix Method (TMM - A full description of transfer-matrix derivation can be found in [142] and [143]) for application to effective materials, specifically metamaterials [7], discussed in more detail in his 2005 paper [144]. More on effective materials can be read in Section 3.1. The general principle in Smith's technique is to determine the scattering parameters in terms of the refractive index, n, and the impedance, Z, of the material.

This approach defines a 1D transfer (also known as a transmission or an ABCD-) matrix which relates an incident electromagnetic wave **F** to the outgoing wave **F'** via the equation:

$$\mathbf{F}' = \mathbf{T}\mathbf{F}, \tag{A.51}$$

where:

$$\mathbf{F} = \begin{pmatrix} E \\ H_{red} \end{pmatrix}, \tag{A.52}$$

and E and H_{red} are the complex electric and reduced magnetic fields. The reduced magnetic field has the normalisation $H_{red} = i\omega\mu_0 H$.

Nicolson-Ross and Weir showed that the system can be replaced by an equivalent circuit model, therefore Eqns. A.21 are used to describe the system. However, instead of following the reflection coefficient route, the system can

be described with a transfer matrix. This gives:

$$\begin{bmatrix} V(z) \\ I(z) \end{bmatrix} = \begin{bmatrix} e^{-\kappa z} & e^{\kappa z} \\ \frac{1}{Z_0}e^{-\kappa z} & -\frac{1}{Z_0}e^{\kappa z} \end{bmatrix} \begin{bmatrix} V_0^+ \\ V_0^- \end{bmatrix}. \tag{A.53}$$

Once again referring to Fig. A.1, and evaluating Eqn. A.53 at the A (z=0) and B (z=d) planes gives:

$$\begin{bmatrix} V(0) \\ I(0) \end{bmatrix} = \begin{bmatrix} 1 & 1 \\ \frac{1}{Z_0} & -\frac{1}{Z_0} \end{bmatrix} \begin{bmatrix} V_0^+ \\ V_0^- \end{bmatrix}, \tag{A.54}$$

and:

$$\begin{bmatrix} V(d) \\ I(d) \end{bmatrix} = \begin{bmatrix} e^{-\kappa d} & e^{\kappa d} \\ \frac{1}{Z_0}e^{-\kappa d} & -\frac{1}{Z_0}e^{\kappa d} \end{bmatrix} \begin{bmatrix} V_0^+ \\ V_0^- \end{bmatrix}. \tag{A.55}$$

Rearranging Eqn. A.54 to make V_0^+ and V_0^- the subject gives:

$$\begin{bmatrix} V_0^+ \\ V_0^- \end{bmatrix} = \frac{1}{2}\begin{bmatrix} 1 & Z_0 \\ 1 & -Z_0 \end{bmatrix} \begin{bmatrix} V(0) \\ I(0) \end{bmatrix}, \tag{A.56}$$

and inserting this into Eqn. A.55 results in:

$$\begin{bmatrix} V(d) \\ I(d) \end{bmatrix} = \frac{1}{2}\begin{bmatrix} e^{-\kappa d} & e^{\kappa d} \\ \frac{1}{Z_0}e^{-\kappa d} & -\frac{1}{Z_0}e^{\kappa d} \end{bmatrix} \begin{bmatrix} 1 & Z_0 \\ 1 & -Z_0 \end{bmatrix} \begin{bmatrix} V(0) \\ I(0) \end{bmatrix},$$

$$\begin{bmatrix} V(d) \\ I(d) \end{bmatrix} = \begin{bmatrix} \frac{e^{\kappa d}+e^{-\kappa d}}{2} & -Z_0\frac{e^{\kappa d}-e^{-\kappa d}}{2} \\ -\frac{1}{Z_0}\frac{e^{\kappa d}-e^{-\kappa d}}{2} & \frac{e^{\kappa d}+e^{-\kappa d}}{2} \end{bmatrix} \begin{bmatrix} V(0) \\ I(0) \end{bmatrix}. \tag{A.57}$$

It is useful here to remember what κ is. Equation A.26 says that, for a lossless transmission line, $\kappa = i\omega\sqrt{LC} = i\omega\sqrt{\varepsilon\mu}$. The phase constant β can be defined by:

$$beta = \omega\sqrt{\varepsilon\mu} = \omega\sqrt{\varepsilon_r\varepsilon_0\mu_r\mu_0} = \frac{\omega}{c}\sqrt{\varepsilon_r\mu_r} = nk, \tag{A.58}$$

where k is the wavenumber of the incident wave and n is the refractive index of the material. Inserting $\kappa = i\beta$ into Eqn. A.57 gives:

$$\begin{bmatrix} V(d) \\ I(d) \end{bmatrix} = \begin{bmatrix} \frac{e^{i\beta d}+e^{-i\beta d}}{2} & -Z_0\frac{e^{i\beta d}-e^{-i\beta d}}{2} \\ -\frac{1}{Z_0}\frac{e^{i\beta d}-e^{-i\beta d}}{2} & \frac{e^{i\beta d}+e^{-i\beta d}}{2} \end{bmatrix} \begin{bmatrix} V(0) \\ I(0) \end{bmatrix}. \tag{A.59}$$

Trigonometry denotes:

$$\begin{aligned} cosh(ix) &= \frac{e^{ix}+e^{-ix}}{2} = cos(x) \\ sinh(ix) &= \frac{e^{ix}-e^{-ix}}{2} = isin(x), \end{aligned} \tag{A.60}$$

giving Eqn. A.59 as:

$$\begin{bmatrix} V(d) \\ I(d) \end{bmatrix} = \begin{bmatrix} cos(\beta d) & -Z_0 sin(\beta d) \\ -\frac{1}{Z_0}sin(\beta d) & cos(\beta d) \end{bmatrix} \begin{bmatrix} V(0) \\ I(0) \end{bmatrix}. \tag{A.61}$$

Inserting $Z_0 = \frac{Z}{ik}$ and $\beta = nk$ gives the transmission matrix for a 1D homogeneous slab of material as:

$$\mathbf{T} = \begin{bmatrix} cos(nkd) & -\frac{Z}{k}sin(nkd) \\ \frac{k}{Z}sin(nkd) & cos(nkd) \end{bmatrix}. \tag{A.62}$$

This is Eqn. 3 in Smith's 2005 paper [144].

Recall that $Z = \sqrt{\mu/\varepsilon}$ and that $n^2 = \varepsilon\mu$, therefore ε and μ are determined as:

$$\varepsilon = n/Z \quad ; \quad \mu = nZ. \tag{A.63}$$

Unfortunately, the elements in the $\mathbf{T}$ matrix are not easily accessible by means of experiment. However, by remembering $Z = Z_0 ik$ one can convert these values to the scattering matrix values (pg 192 [138]):

$$\begin{aligned}
S_{11} &= \frac{T_{11} - T_{22} + \left(ikT_{12} - \frac{T_{21}}{ik}\right)}{T_{11} + T_{22} + \left(ikT_{12} + \frac{T_{21}}{ik}\right)}, \\
S_{21} &= \frac{2}{T_{11} + T_{22} + \left(ikT_{12} + \frac{T_{21}}{ik}\right)}, \\
S_{12} &= \frac{2\det(\mathbf{T})}{T_{11} + T_{22} + \left(ikT_{12} + \frac{T_{21}}{ik}\right)}, \\
S_{22} &= \frac{T_{22} - T_{11} + \left(ikT_{12} - \frac{T_{21}}{ik}\right)}{T_{11} + T_{22} + \left(ikT_{12} + \frac{T_{21}}{ik}\right)}.
\end{aligned} \tag{A.64}$$

Inserting the values of T_{11}, T_{12}, T_{21} and T_{22}, where $T_{11} = T_{22} = T_s$ and knowing that $\det(\mathbf{T}) = 1$ gives:

$$\begin{aligned}
S_{12} = S_{21} &= \frac{1}{T_s + \frac{1}{2}(T_{12}ik + T_{21}/ik)}, \\
&= \frac{1}{cos(nkd) + \frac{1}{2}(-iZsin(nkd) - (\frac{i}{Z}sin(nkd))}, \\
&= \frac{1}{cos(nkd) - \frac{isin(nkd)}{2}(Z + \frac{1}{Z})},
\end{aligned} \tag{A.65}$$

and:

$$\begin{aligned}
S_{11} = S_{22} &= \frac{\frac{1}{2}(ikT_{12} - \frac{T_{21}}{ik})}{T_s + \frac{1}{2}(T_{12}ik + T_{21}/ik)}, \\
&= \frac{\frac{1}{2}(-iZsin(nkd) + \frac{i}{Z}sin(nkd))}{cos(nkd) + \frac{1}{2}(-iZsin(nkd) - (\frac{i}{Z}sin(nkd))}, \\
&= \frac{\frac{isin(nkd)}{2}(\frac{1}{Z} - Z)}{cos(nkd) - \frac{isin(nkd)}{2}(Z + \frac{1}{Z})}, \\
&= \frac{isin(nkd)}{2}\left(\frac{1}{Z} - Z\right) \cdot S_{21}.
\end{aligned} \tag{A.66}$$

This gives a relationship between the S_{11}, S_{21} and n and Z as:

$$\frac{S_{11}}{S_{21}} = -\frac{isin(nkd)}{2}\left(Z - \frac{1}{Z}\right). \tag{A.67}$$

This is Eqn. 2 in Smith's 2002 paper [7] [1].

n and Z can be determined by rearranging Eqns. A.65 and A.67. Rearranging Eqn. A.67 to determine n gives:

$$\begin{aligned} cos(nkd) - \frac{isin(nkd)}{2}\left(Z + \frac{1}{Z}\right) &= \frac{1}{S_{21}}, \\ 2cos(nkd) - isin(nkd)\left(Z + \frac{1}{Z}\right) &= \frac{2}{S_{21}}, \\ 2cos(nkd) &= \frac{2}{S_{21}} + isin(nkd)\left(Z + \frac{1}{Z}\right). \end{aligned} \tag{A.68}$$

Rearranging Eqn. A.65 gives:

$$isin(nkd) = -2\frac{S_{11}}{S_{21}}\frac{1}{\left(Z - \frac{1}{Z}\right)}. \tag{A.69}$$

[1] There is ambiguity between Smith's 2002 and 2005 papers when determining this result, as his 2005 paper, Eqn. 8, states that:

$$S_{11} = \frac{isin(nkd)}{2}\left(\frac{1}{Z} - Z\right),$$

without dividing through by S_{21}. This is incorrect as there is indeed a factor of S_{21} missing here.

There is also a sign error in the conversion from the T-matrix parameters to the S_{11} parameter, stating that:

$$S_{11} = \frac{\frac{1}{2}\left(\frac{T_{21}}{ik} - ikT_{12}\right)}{T_s + \frac{1}{2}\left(T_{12} + \frac{T_{21}}{ik}\right)}.$$

This should read:

$$S_{11} = \frac{\frac{1}{2}\left(ikT_{12} - \frac{T_{21}}{ik}\right)}{T_s + \frac{1}{2}\left(T_{12} + \frac{T_{21}}{ik}\right)}.$$

Inserting Eqn. A.69 into Eqn. A.68 gives:

$$cos(nkd) = \frac{2 - 2S_{11}\frac{\left(Z+\frac{1}{Z}\right)}{\left(Z-\frac{1}{Z}\right)}}{2S_{21}}. \tag{A.70}$$

The numerator here can be normalised and simplified by using Eqn. A.42 from the Nicolson-Ross paper, where $X = \frac{1+S_{11}^2-S_{21}^2}{2S_{11}} = \frac{\Gamma^2+1}{2\Gamma} = \frac{\left(Z+\frac{1}{Z}\right)}{\left(Z-\frac{1}{Z}\right)}$ to give:

$$\begin{aligned} cos(nkd) &= \frac{2 - 2S_{11}X}{2S_{21}}, \\ cos(nkd) &= \frac{1 - S_{11}^2 + S_{21}^2}{2S_{21}}, \\ n &= \frac{1}{kd}cos^{-1}\left(\frac{1 - S_{11}^2 + S_{21}^2}{2S_{21}}\right). \end{aligned} \tag{A.71}$$

This is the first part of Eqn. 3 in Smith's 2002 paper.

Equation A.42 is used to determine Z. Rewriting $(Z + \frac{1}{Z}) = (Z^2 + 1)/Z$ and $(Z - \frac{1}{Z}) = (Z^2 - 1)/Z$ gives:

$$\begin{aligned} \frac{Z^2+1}{Z^2-1} = X = \frac{1 + S_{11}^2 - S_{21}^2}{2S_{11}}, \\ Z^2(2S_{11} - 1 - S_{11}^2 + S_{21}^2) = -2S_{11} - 1 - S_{11}^2 + S_{21}^2, \\ Z = \pm\sqrt{\frac{-(S_{11}^2 + 2S_{11} + 1 - S_{21}^2)}{-(S_{11}^2 - 2S_{11} + 1 - S_{21}^2)}}. \end{aligned}$$

Notice here that $S_{11}^2 + 2S_{11} + 1$ and $S_{11}^2 - 2S_{11} + 1$ can be rewritten as $(1 + S_{11})^2$ and $(1 - S_{11})^2$ respectively, resulting in:

$$Z = \pm\sqrt{\frac{(1 + S_{11})^2 - S_{21}^2}{(1 - S_{11})^2 - S_{21}^2}}, \tag{A.72}$$

This is Eqn. 4 in Smith's 2002 paper. n is also determined by:

$$\begin{aligned} n &= \frac{1}{kd} cos^{-1}\left[\frac{1}{2S_{21}}(1 - S_{11}^2 + S_{21}^2)\right], \\ &= \mathrm{Re}\left(\frac{1}{S_{21}}\right) - \frac{1}{2|S_{21}|^2}\left(A_1 S_{11} + A_2 S_{21}\right), \end{aligned} \tag{A.73}$$

where $A_1 = S_{11}^* S_{21} + S_{21}^* S_{11}$ and $A_2 = 1 - |S_{11}|^2 - |S_{21}|^2$ and are both real valued functions that go to zero in lossless materials.

A.4 Absorption and Loss

Appendix A.2 introduced the scattering parameters S_{11} and S_{21}, the reflected/transmitted voltage over the incident voltage:

$$S_{11} = \frac{V_A}{V_{inc}(\omega)} \qquad \text{and} \qquad S_{21} = \frac{V_B}{V_{inc}(\omega)}. \tag{A.74}$$

Rearranging these equations to determine V_A and V_B in terms of these scattering parameters gives:

$$V_A = S_{11} V_{inc} \qquad \text{and} \qquad V_B = S_{21} V_{inc}. \tag{A.75}$$

Due to conservation of energy (therefore power as $[P] = [J]/[s]$) the incident power can be expressed in terms of the reflected, transmitted and lost power as:

$$P_{in} = P_{reflected} + P_{transmitted} + P_{lost}. \tag{A.76}$$

Power is related to voltage by:

$$P = IV = V^2/Z, \tag{A.77}$$

where I represents the current and Z represents the impedance of the system, so the reflected power $P_{reflected}$ and transmitted power $P_{transmitted}$ are determined as:

$$\begin{aligned} P_{reflected} &= V_A^2/Z; && \text{(A.78)} \\ &= (S_{11}V_{inc})^2/Z, && \text{(A.79)} \\ P_{transmitted} &= V_B^2/Z; && \text{(A.80)} \\ &= (S_{21}V_{inc})^2/Z. && \text{(A.81)} \end{aligned}$$

Knowing that $P_{in} = V_{inc}^2/Z$, Eqn. A.76 can be rewritten in its normalised form as:

$$1 = |S_{11}|^2 + |S_{21}|^2 + NormP_{lost}, \tag{A.82}$$

where $NormP_{lost}$ is the normalised power lost, also referred to as the absorptivity. This can be expressed explicitly as [145]:

$$A(\omega) = NormP_{lost} = 1 - |S_{11}|^2 - |S_{21}|^2, \tag{A.83}$$

which is used by Smith in his 2002 paper as A_2 [7]. This is essentially a measure of the power lost from the incident EM wave due to absorption of the incident power by the system, typically through ohmic (resistive) or radiative losses, or due to energy storage within the system itself.

A.5 Bloch-Floquet Theory: Full Derivation

Bloch-Floquet theory is the theorem that describes wave propagation in an infinitely large, periodic medium. Basically, it states that the propagation characteristics of a material can be determined from the analysis of a single unit cell:

$$\Phi(z+p) = e^{\gamma z}F(z) = \Phi(z), \tag{A.84}$$

where Φ is a periodic function of z with a period p, γ is the complex propagation constant of the wave and $F(z)$ is the general solution. This result will be demonstrated here by use of an example outlined in [63].

Consider the propagation of a TE_{10} mode in an infinitely long rectangular waveguide filled with periodically varying dielectric constant $\kappa_0+\kappa_1 cos(2\pi p)$, travelling in the z direction with a harmonic time dependence (proportional to $e^{j\omega t}$), as shown in Fig. A.6.

Figure A.6: Rectangular waveguide loaded with periodically varying dielectric constant.

For a TE mode wave, H_x and H_z can be derived from Eqn. A.3 as:

$$j\omega\mu_0 H_x = \frac{\partial E_y}{\partial z} \quad ; \quad j\omega\mu_0 H_z = -\frac{\partial E_y}{\partial z}. \tag{A.85}$$

The wave equation for EM waves is given by:

$$\nabla^2\mathbf{E} = \frac{1}{c^2}\frac{d^2\mathbf{E}}{dt^2}. \tag{A.86}$$

Rearranging this equation gives:

$$\left(\nabla^2 + \frac{\omega^2}{c^2}\right)\mathbf{E} = 0. \tag{A.87}$$

However given that $\omega/c = k(\omega) = k_0(\omega)n(\omega)$ Eqn. A.87 becomes:

$$\left(\nabla^2 + k^2(\omega)\right)\mathbf{E} = 0. \tag{A.88}$$

Knowing that the dielectric constant varies as $\kappa_0 + \kappa_1 cos\left(\frac{2\pi z}{p}\right)$, and by letting E_y vary as $\psi(z) sin\left(\frac{\pi x}{a}\right)$ where a is the largest cross-sectional dimension of the waveguide, one determines:

$$\left[\frac{d^2}{dz^2} + k_0^2\left(\kappa_0 + \kappa_1 cos\left(\frac{2\pi z}{p}\right)\right) - \frac{\pi^2}{a^2}\right]\psi(z) = 0. \tag{A.89}$$

Since $\psi(z)$ is a solution to this equation, $\psi(z+p)$ is also a solution due to the evenness of the cosine function:

$$cos\left(\frac{2\pi(z+p)}{p}\right) = cos\left(\frac{2\pi z}{p}\right). \tag{A.90}$$

Eqn.A.89 is a second order equation, therefore there can only be two linearly independent solutions. As $\psi(z)$ is a solution, then $\psi_1(z)$ and $\psi_2(z)$ are also solutions, so the solutions at point p are:

$$\psi_1(z+p) = \alpha_{11}\psi_1(z) + \alpha_{12}\psi_2(z), \tag{A.91}$$

$$\psi_2(z+p) = \alpha_{21}\psi_1(z) + \alpha_{22}\psi_2(z), \tag{A.92}$$

where α_{ij} are suitably determined coefficients.

Therefore the general solution for the system can be written as:

$$F(z) = A\psi_1(z) + B\psi_2(z), \tag{A.93}$$

and $\psi(z+p)$ can be written as,

$$F(z+p) = A\psi_1(z+p) + B\psi_2(z+p). \tag{A.94}$$

Inserting Eqn. A.94 into Eqn. A.92 results in:

$$F(z) = A\psi_1(z) + B\psi_2(z),$$
$$F(z+p) = (A\alpha_{11} + B\alpha_{21})\psi_1(z) + (A\alpha_1 2 + B\alpha_{22})\psi_2(z).$$

As $F(z)$ represents a solution for a wave propagating in the z direction, $F(z+p)$ is expressed as:

$$F(z+p) = e^{-\gamma p}F(z), \tag{A.95}$$

where γ is the propagation constant for the wave and can be real, imaginary or complex.

Therefore:

$$F(z+p) = F(z)e^{-\gamma p} = e^{-\gamma p}(A\psi_1(z) + B\psi_2(z)),$$
$$= (A\alpha_{11} + B\alpha_{21})\psi_1(z) + (A\alpha_1 2 + B\alpha_{22})\psi_2(z). \tag{A.96}$$

Equating coefficients gives:

$$
\begin{aligned}
&e^{-\gamma p}A = (A\alpha_{11} + B\alpha_{21}),\\
&\rightarrow A(\alpha_{11} - e^{-\gamma p} + B\alpha_{21} = 0,\\
&e^{-\gamma p}B = (A\alpha_{12} + B\alpha_{22}),\\
&\rightarrow B(\alpha_{22} - e^{-\gamma p} + A\alpha_{12} = 0.
\end{aligned}
$$

Solving these equations simultaneously enables the non-trivial solutions to be found as:

$$e^{-2\gamma p} - (\alpha_{11} + \alpha_{22})e^{-\gamma p} + (\alpha_{11}\alpha_{22} - \alpha_{12}\alpha_{21}) = 0. \tag{A.97}$$

This is a quadratic equation for $e^{-\gamma p}$, therefore:

$$e^{-\gamma p} = \frac{\alpha_{11} + \alpha_{22}}{2} \pm \left[\left(\frac{\alpha_{11} + \alpha_{22}}{2}\right)^2 - (\alpha_{11}\alpha_{22} - \alpha_{12}\alpha_{21})\right]^{1/2}. \tag{A.98}$$

Setting $\alpha_{11}\alpha_{22} - \alpha_{12}\alpha_{21} = \Delta$ gives:

$$
\begin{aligned}
\left(\frac{\alpha_{11} + \alpha_{22}}{2}\right)^2 - \left(\frac{\alpha_{11} + \alpha_{22}}{2}\right)^2 + \Delta = \Delta,\\
\left(\frac{\alpha_{11} + \alpha_{22}}{2}\right)^2 - \left[\left(\frac{\alpha_{11} + \alpha_{22}}{2}\right)^2 - \Delta\right] = \Delta,\\
\frac{1}{\Delta}\left(\frac{\alpha_{11} + \alpha_{22}}{2}\right)^2 - \left[\frac{1}{\Delta}\left(\frac{\alpha_{11} + \alpha_{22}}{2}\right)^2 - 1\right] = 1,\\
\left(\frac{\alpha_{11} + \alpha_{22}}{2\Delta^{1/2}}\right)^2 - \left[\left(\frac{1}{\Delta}\left(\frac{\alpha_{11} + \alpha_{22}}{2}\right)^2 - 1\right)^{1/2}\right]^2 = 1,
\end{aligned}
$$

where $\left(\frac{\alpha_{11}+\alpha_{22}}{2\Delta^{1/2}}\right) = cosh(\theta)$ and $\left(\frac{1}{\Delta}\left(\frac{\alpha_{11}+\alpha_{22}}{2}\right)^2 - 1\right)^{1/2} = sinh(\theta)$.

This gives:

$$cosh^2(\theta) - sinh^2(\theta) = 1. \tag{A.99}$$

Therefore Eqn. A.98 is re-expressed as:

$$\begin{aligned} e^{-\gamma p} &= \Delta^{1/2} cosh(\theta) \pm \Delta^{1/2} sinh(\theta), \\ &= \Delta e^{\pm\theta} = e^{\pm\theta + (1/2) ln\Delta}. \end{aligned} \tag{A.100}$$

This shows that γ can be real, imaginary or complex. If $\Delta = 1$, then if γ is a solution, so is $-\gamma$ and $\gamma \pm j2m\pi/p$ where m is any integer.

Saying that the solution at $p = 0$ is:

$$\Phi(z) = e^{\gamma z} F(z), \tag{A.101}$$

then the solution at a point p in the periodic medium is:

$$\begin{aligned} \Phi(z+p) &= e^{\gamma(z+p)} F(z+p), \\ &= e^{\gamma p} e^{\gamma z} F(z+p), \\ &= e^{\gamma p} e^{\gamma z} e^{-\gamma p} F(z) \\ &= e^{\gamma z} F(z), \\ &= \Phi(z). \end{aligned}$$

This shows that the general solution of Eqn. A.89 is of the form $F(z) = e^{\pm\gamma z}\Phi(z)$.

Appendix B

Excess Graphs and Figures

B.1 HFSS Infinite Systems - Empty vs Loaded

The plots in this section compare the simulations of infinite unit cells, both without (empty) and with (loaded) the engineered unit cell design. These simulations show that the presence of the designed unit cell results in an altered behaviour of the incident wave, resulting with the emergence of a resonance peak at 10GHz.

B.2 COMSOL: Finer Frequency Step Simulations

When running a benchmarking simulation to compare the results produced by HFSS and COMSOL, a number of different frequency steps were attempted over the range of 9-10.5GHz. The frequency step that was settled on was 0.01GHz, as this simulation ran well and did not produce any warnings or errors. However, this only results in 150 data points, which, compared to HFSS's 15001, feels rather insufficient. A frequency step of 0.001GHz (which would have resulted in 1500 data points) was attempted,

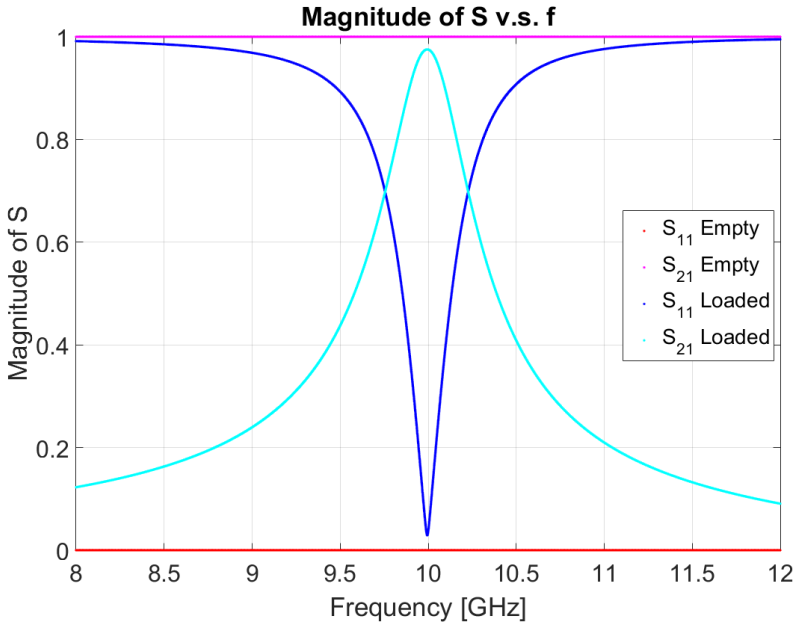

Figure B.1: Plot comparing the magnitude of the scattering parameters for the empty and loaded infinite systems in HFSS.

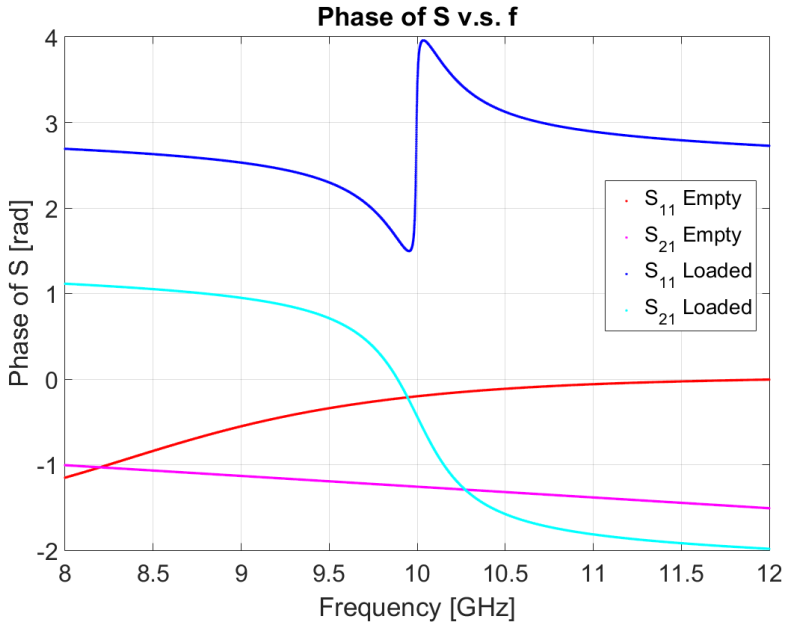

Figure B.2: Plot comparing the phase of the scattering parameters for the empty and loaded infinite systems in HFSS.

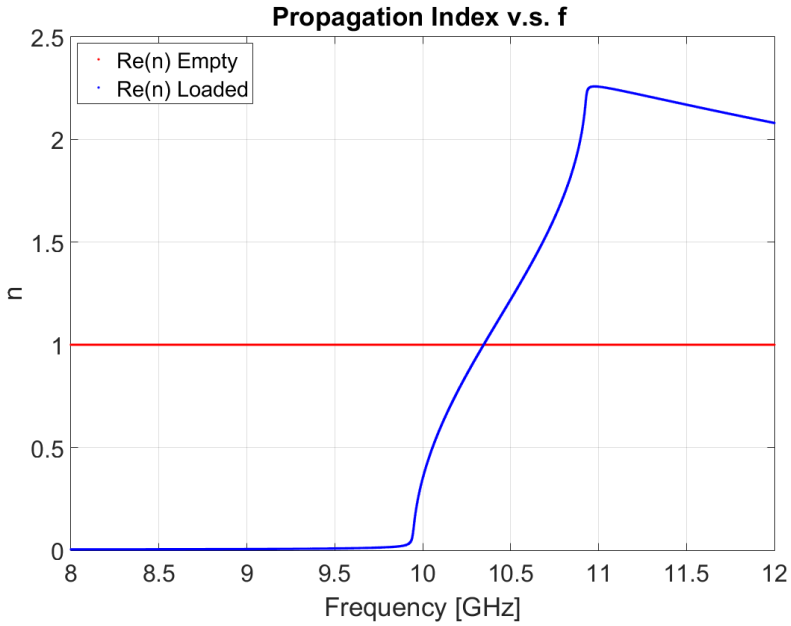

Figure B.3: Plot comparing the refractive indices for the empty and loaded infinite systems.

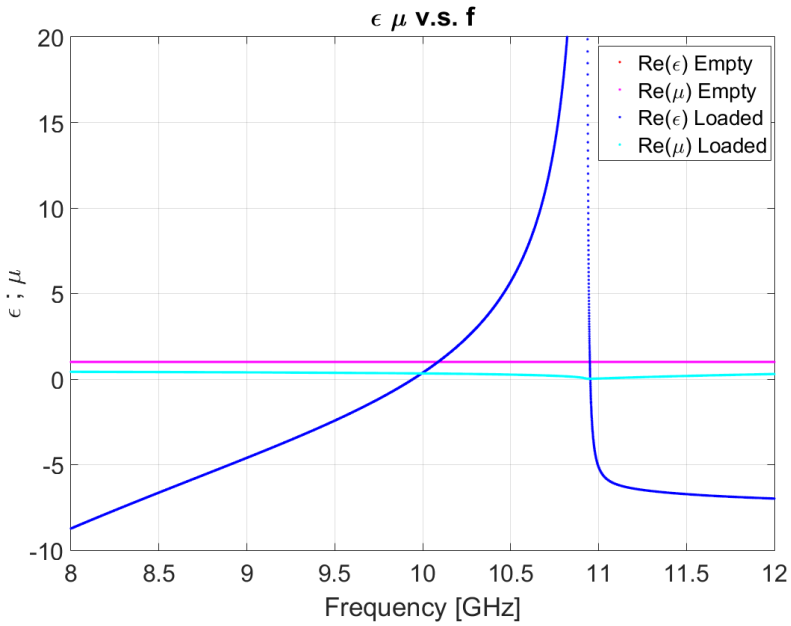

Figure B.4: Plot comparing the ε_r and μ_r for the empty and loaded infinite systems.

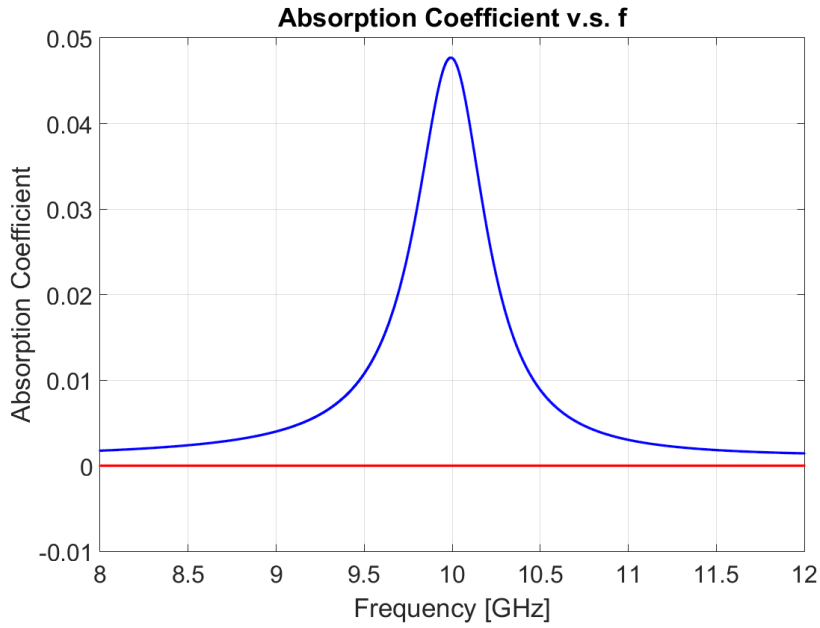

Figure B.5: Plot comparing the absorption coefficients for the empty and loaded infinite systems.

however this failed to converge on an answer and as such resulted in the simulation ceasing.

That said, COMSOL seems to determine a final solution at each frequency step before moving on to the next frequency step, so upon looking at the produced output one can see that very many of the data points were in-fact determined before the simulation stopped. This can be seen in Fig. B.6,

By plotting the successful frequencies against those obtained by HFSS, as shown in Fig. B.7, showing that the frequency difference between the two simulations is less than predicted with the 0.01GHz simulations (only being 0.07GHz low).

This enables 2 conclusions: 1) The COMSOL simulation may eventually converge on the results produced by HFSS, or 2) COMSOL's results may

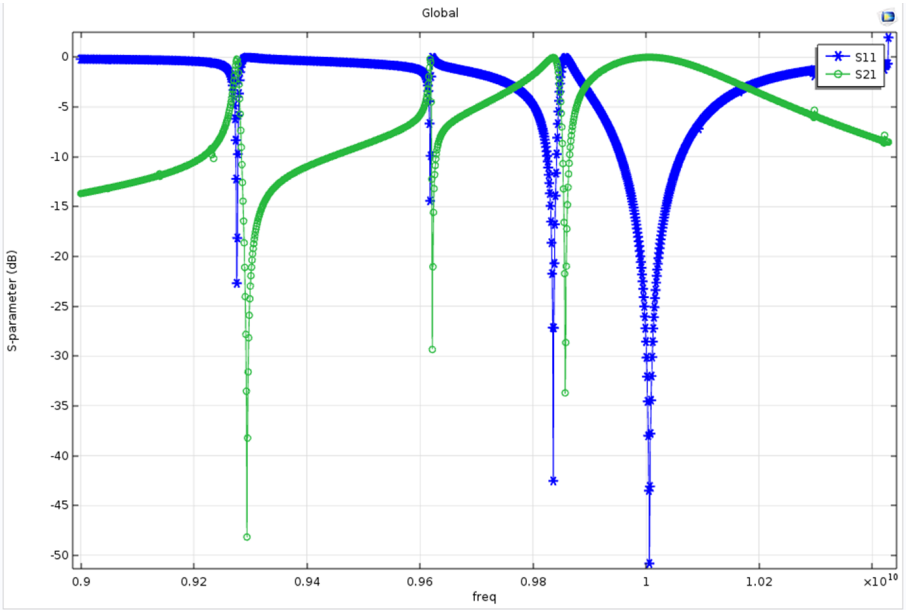

Figure B.6: Plot showing the Scattering Parameters S_{11} and S_{21} as determined by COMSOL. Solutions seem to have been obtained for frequencies up to 10.43GHz, which unfortunately did not converge, causing the simulation to stop.

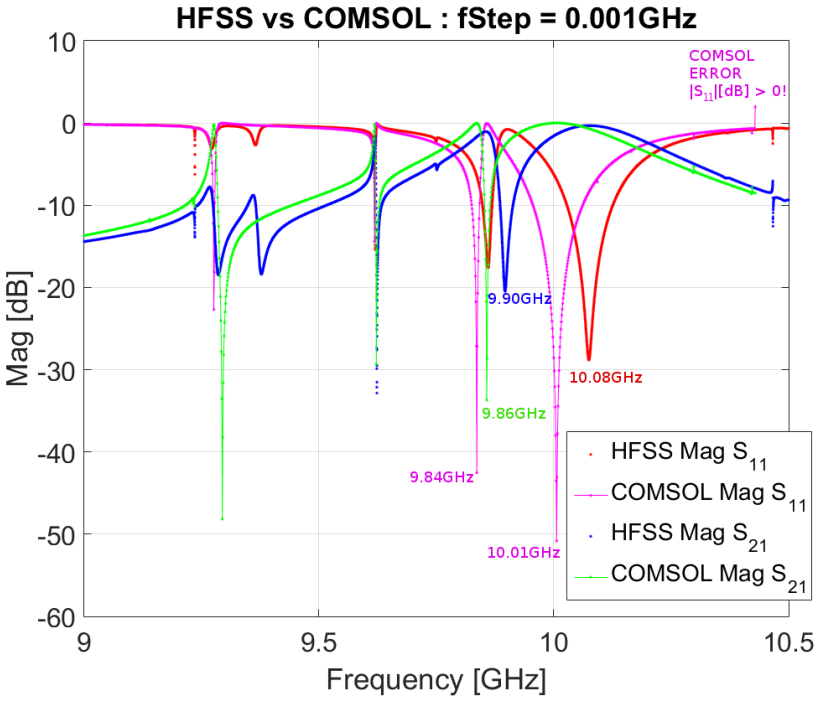

Figure B.7: Plot showing the Scattering Parameters S_{11} and S_{21} as determined by COMSOL (1479 data points) and HFSS (15001 data points).

remain in this region. Note that the original infinite unit cell design was made to have a resonant frequency at 10GHz, so this would mean that COMSOL was actually *better* than HFSS in this particular case.

To check whether this data was able to produce a suitable absorption plot, the absorption was calculated and can be seen in Fig. B.8. This shows quite clearly that there are regions where the simulation ran ok, but that there are also many spurious spikes (single data points) in the predicted absorption, probably highlighting data points which did not converge suitably well.

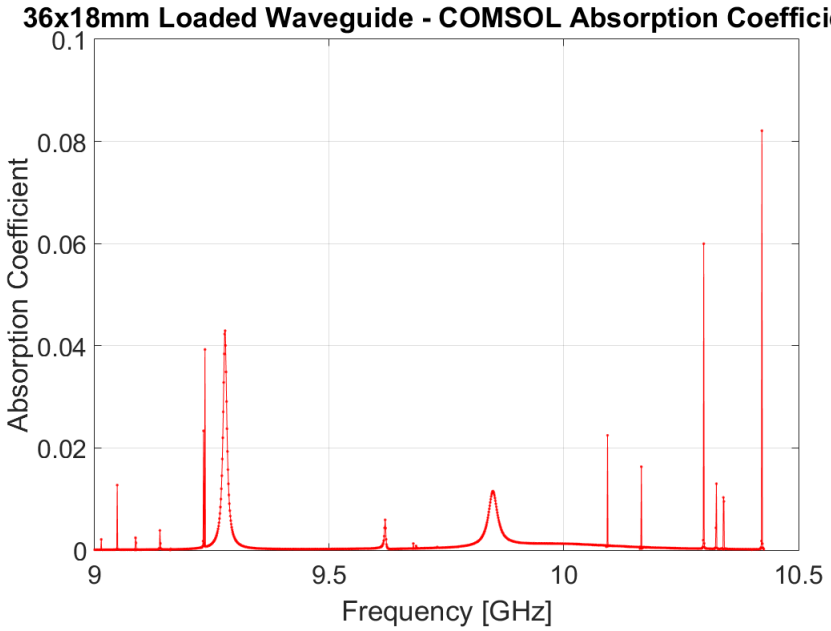

Figure B.8: Absorption plot produced from the S_{11} and S_{21} data from COMSOL.

B.3 COMSOL Heating: Time evolution 0 to 20 seconds

Figure B.9 shows the time evolution of the heating simulation for a 1W 10.03GHz wave in 1 second intervals over 20 seconds.

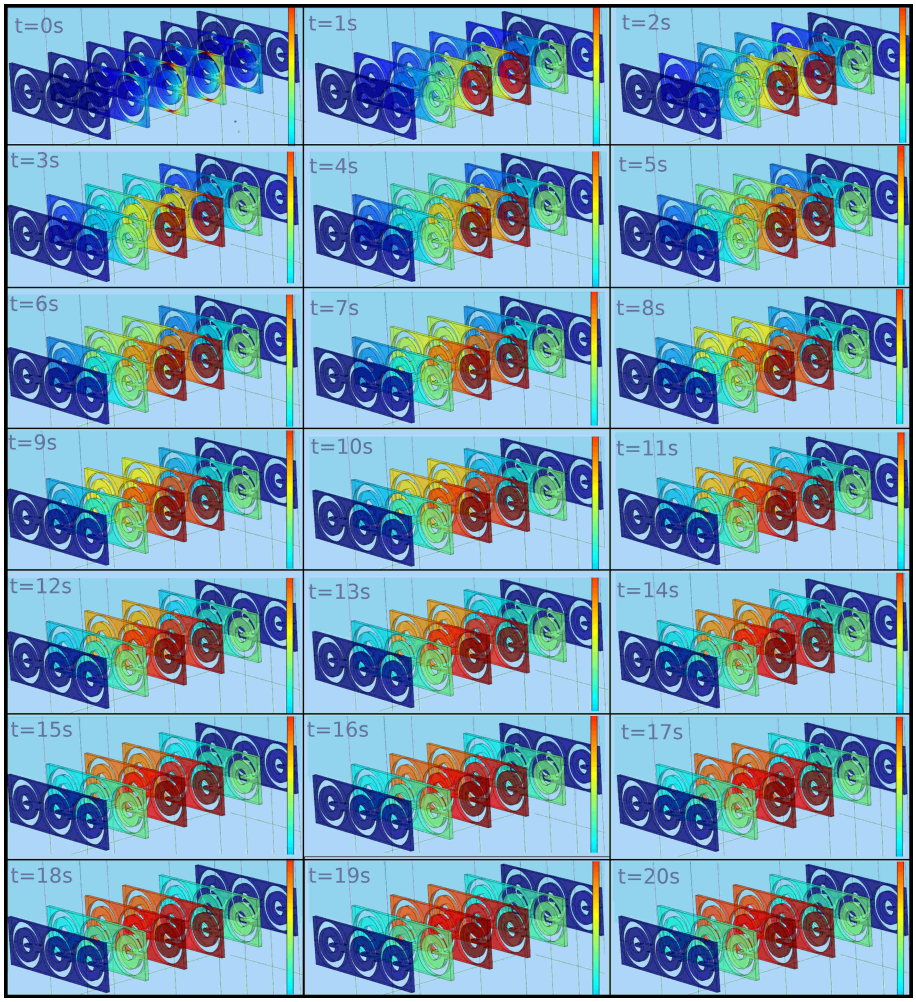

Figure B.9: Surface plots showing the heating of the structure over 20 seconds.

Appendix C

Papers and Publications

C.1 Conferences Contributions

2014

"Characterising Properties and Loss in High Power Metamaterials", Research Festival, Huddersfield, 2.4.2014 (poster)

"Characterising Properties and Loss in High Power Metamaterials", High Power Lasers at the forefront of SCIence and TECHnology (HPLSCITECH), Strathclyde, 3-4.4.2014 (presentation)

"Characterising Properties and Loss in High Power Metamaterials", IOP Particle And Beams Group Meeting, London, 8.4.2014 (poster)

"Characterising The RF Properties of Metamaterials", National Vacuum Electronics Conference, Daresbury, Warrington, 5.6.14 (presentation)

"Effects of High Power on Microwave Metamaterials", Metamaterials2014, The 8th International Congress on Advanced Electromagnetic Materials in Microwaves and Optics, Copenhagen, 25.8.2014 (poster)

"Effects of High Power on Microwave Metamaterials", IOP Novel Materials and Nanostructures for Particle Accelerators Presentation, Daresbury, Warrington, 29.10.2014 (presentation)

2015

"Effects of High Power on Microwave Metamaterials", IOP Particle And Beams Group Meeting, Strathclyde, 14.4.2015 (poster, **WON IOP poster prize**)

"Artificial Materials: ε and μ Near Zero", The 42nd IEEE International Conference On Plasma Science, Antalya, Turkey, 24-28.5.2015 (poster)

"Artificial Material: ε and μ Near Zero", Research Festival, Huddersfield, 13.11.2015 (poster)

"Artificial Material Design", National Vacuum Electronics Conference, Strathclyde, 18.11.2015 (presentation)

"Artificial materials for high power microwave applications", Union Radio-Scientifique Internationale, Festival of Radio Science, Manchester, 16.12.2015 (presentation **WON Presentation Prize**)

2016

"Tailoring the Electromagnetic Properties of an Artificial Material", IOP Particle And Beams Group Meeting, Huddersfield, 8.4.2016 (poster)

"Wave Particle Cherenkov Interactions mediated via Novel Materials", the 7th International Particle Accelerator Conference, Busan, Korea, 9-13.2015 (poster and conference paper)

"Artificial Material Design for High Power Applications", EuroEM, London, 11-14.7.2016 (presentation)

"Artificial Material Design for High Power Applications", National Vacuum Electronics Conference, Lancaster, 18.7.2016 (presentation)

2017

"Artificial Materials for High Power Applications", National Vacuum Electronics Conference, Huddersfield 26.09.2017 (presentation)

C.2 Publications

8th International Congress on Advanced Electromagnetic Materials in Microwaves and Optics - Metamaterials 2014
Copenhagen, Denmark, 25-30 August 2014

Effects of High Power on Microwave Metamaterials

R. Seviour[1], Y. S. Tan[1] and A. Hopper[1]

[1]University of Huddersfield, Institute for Accelerator Applications, Queensfield, HD1 3DH, Huddersfield, UK
aimee.hopper@hud.ac.uk

***Abstract* – In this paper we examine experimentally and numerically the effect of exposing a metamaterial to relatively high-power EM waves. We show that a metamaterial consisting of a conventional Split Ring Resonator on an FR4 substrate can undergo combustion when exposed to 1W of RF. We compare the experimental results to numerical simulations, showing that numerical models can be accurately used to predict the thermal behaviour of metamaterials under exposure to high-power RF.**

I. Introduction

Microwave metamaterials have shown promise in numerous low power applications, ranging from strip lines to antennas. Metamaterials allow microwave designers to obtain electromagnetic characteristics not typically available in nature, leading to new behaviour, as well as reductions in the size of typical devices. High Power Microwave (HPM) technologies ($> 100W$) have in the past drawn inspiration from the conventional microwave community. Metamaterials have received little attention in the HPM area, with the exception of work considering a Cerenkov maser [1] as well as novel research investigating the use of a metamaterial Traveling Wave Tube (TWT) [2]. In the case of the Cerenkov maser, the metamaterial acts to produce, within a given frequency band, nearly the same characteristics as a conventional dielectric, but with an all-metallic structure. In the case of the TWT, the metamaterial introduces new regimes of operation unavailable with standard slow wave structures. In contrast to electron beams numerous authors have considered the interaction of single charges with metamaterials. Importantly, metamaterials offer two key advantages for HPM source design. Firstly, the possibility of exploiting new forms of interaction previously unavailable for microwave source design [2]. Additionally, they offer a path to reduce the dimensions of standard HPM sources and components, gaining significant size advantages for the source designer [2]. However both hinge on finding sub-wavelength structures in configurations that can withstand the harsh operating environment of a HPM device.

This paper explores the ability of metamaterials to withstand and respond to high-power microwave operation. This work involved examining the interactions of the EM field with the metamaterial and the resulting losses and heating, and the effect this had on the operational parameters of the metamaterial unit cell. The thermal and mechanical forces the metamaterial experiences arise due to the interaction between the macroscopic structure of the unit cell and the applied EM wave.

II. Methodology

To investigate the effects of EM heating on metamaterials we considered a system consisting of a standard piece of X-band waveguide with a block of metamaterial placed inside. The intention was to validate numerical simulations with an experimental comparison. After validation, the numerical models can be expanded to consider other metamaterial geometries/materials with a high degree of confidence. The initial metamaterial considered was of the most common form, a unit-cell consisting of an SRR on FR4 PCB, with a single strip line on the reverse side of the PCB, as shown in Fig. 1.

To enable the numerical thermal analysis, the force the EM wave applies to the whole structure must first be determined. The energy released into the structure, which results in heating, by the EM wave, is determined from the time averaged losses inherent to metallic and dielectric components on a molecular level. Due to the complexity of calculating these losses, the commercial simulation packages HFSS and ANSYS were utilised [3, 4].

8th International Congress on Advanced Electromagnetic Materials in Microwaves and Optics - Metamaterials 2014
Copenhagen, Denmark, 25-30 August 2014

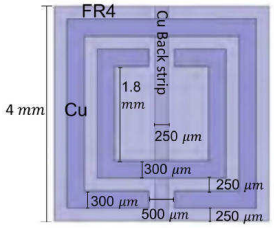

Fig. 1: The SRR geometry considered in this paper, consisting of a Cu SRR ($30\mu m$ thick) deposited on FR4 dielectric substrate, with a Cu track ($30\mu m$ thick) on the reverse side of the substrate.

HFSS is a 3D full-wave EM field solver, utilising the FEM, with adaptive meshing, approach to solve the EM wave-structure interaction. These EM results were imported into ANSYS to calculate the thermal dependent behaviour corresponding to losses from HFSS. This response is used to calculate the metallic and dielectric losses on an element by element case. The metallic loss (P_{le}) and dielectric loss (P_{ld}) are given by;

$$P_{le} = \sqrt{\frac{\omega\mu_0}{8\sigma}} \int_s |\bar{H}_t|^2 ds \tag{1}$$

$$P_{ld} = \frac{\mathrm{Im}(\epsilon_r)\omega}{2} \int_V |\bar{E}|^2 dV \tag{2}$$

where ω is angular frequency, μ_0 is the permeability of free space, σ is the conductivity and $\bar{H}_t$ denotes tangential magnetic field. ϵ_r is the relative permittivity, and denotes electric field. For the thermal analysis it is only necessary to simulate a single unit cell of the metamaterial, not the entire structure. For the simulation the unit cell was discretized into 30K elements, the steady-state loss density was calculated at each element, with a 10W EM plane wave at 10 GHz incident upon the structure. The permittivity and permeability of structure was measured and these results indicated the structure has negative refraction at 10 GHz.

III. Results

The loss density results for the SRR exposed to 1W of RF power at 10 GHz are shown in (left) Fig. 2, and the temperature profile for the SRR is shown (right) in Fig. 2. As seen the peak temperature is predicted to exceed 600 Celsius, which is the combustion point of the FR4 PCB.

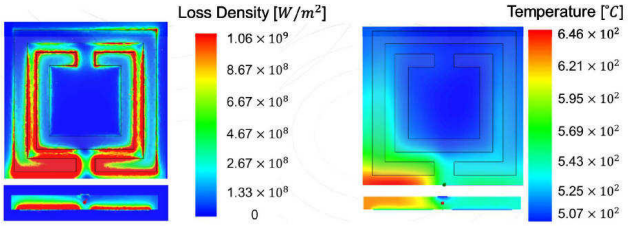

Fig. 2: Left, HFSS results of the loss density for the SRR shown in Fig. 1. Right, ANSYS determined temperature using the loss density from the HFSS simulation.

To confirm the results of Fig. 2 and validate the numerical model, an experiment was conducted using SRR unit-cells fabricated to the exact specifications shown in Fig. 1. The SRR was loaded into a two-port section of X-band waveguide and exposed to 1W RF at 10 GHz for 15 seconds. The waveguide at port 1 was connected by

8th International Congress on Advanced Electromagnetic Materials in Microwaves and Optics - Metamaterials 2014
Copenhagen, Denmark, 25-30 August 2014

coaxial cable to a TMD **PTX 8206** TWT amplifier capable of supplying $0 - 100$W cts (140KW pulsed) RF at frequencies between $6 - 18$ GHz. Port 2 was connected to an Agilent USB power meter, both ports and cables matched to 50Ω impedance. This configuration allowed high-power RF to flow through the waveguide across an interaction region that can be loaded with an arbitrary metamaterial.

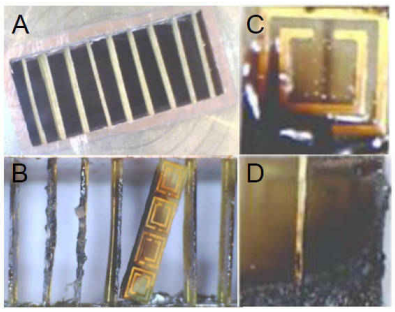

Fig. 3: (A) shows the cross section of the waveguide initially loaded with the metamaterial.(B) shows the cross section of the waveguide loaded with the metamaterial after exposure to 1W of RF at 10 GHz. (C) & (D) show the resulting damage to an individual unit cell of (B).

The waveguide was loaded with 9 strips of metamaterial, each strip consisting of 4 unit-cells (SRRs). Fig. 3 shows the experimental results and the SRR before exposure to 1W and after in the waveguide, and the effects of heating on a single SRR. As seen the distribution of the combustion pattern from the experimental results on a single SRR (Fig. 3 (C) & (D)) is in very good agreement with the combustion patterns predicted by the numerical model, results shown in Fig. 2. As seen in Fig. 3 (C) & (D) the areas of the SRR which show combustion marks match the areas from the numerical simulation (Fig. 2) where the SRR temperature was predicted to exceed 600 Celsius, the combustion point of the FR4 substrate.

IV. Conclusion

In this paper we have examined the effect of exposing a specific metamaterial to a 1 W EM wave, both experimentally and numerically. We have shown that the numerical FEM approach using both HFSS and ANSYS can accurately predict the thermal behaviour of a metamaterial structure, with a comparison to experimental results. We have shown that both simulation and experimental results demonstrate that conventional metamaterial realisation is not suitable for HPM applications in excess of 1 W. Although not presented in this paper (due to space) the above validated numerical technique has been used to consider differing substrate materials (FR6, Quartz, etc) and different geometries (CSRR, EIT, etc). Additionally the effects of thermal expansion on the metamaterial unit-cell have been performed and the effect this deformation has on the properties of the metamaterial has been calculated, the results of this work will be the subject of a subsequent publication.

Acknowledgement

The Authors would like to thank the Airforce Office of Scientific Research for their support of this work under grant FA8655-13-1-2111.

References

[1] Shiffler et. al. "A Cerenkov-like Maser Based on a Metamaterial Structure", Plasma Science, IEEE Transactions on , vol.38, no.6, pp.1462-1465, 2010
[2] Y. S. Tan and R. Seviour, "Wave energy amplification in a metamaterial-based traveling-wave structure", *Europhysics Letters*, vol. 87, p. 34005, 2009.
[3] High Frequency Structure Simulator(HFSS), Ansoft Corporation, Pittsburgh, PA.Ver.12.1,2010.
[4] ANSYS Workbench, ANSYS Inc., Canonsburg, PA.Ver.12.1,2009.

TUPOY024 Proceedings of IPAC2016, Busan, Korea

WAVE PARTICLE CHERENKOV INTERACTIONS MEDIATED VIA NOVEL MATERIALS

A. Hopper*, R. Seviour, IIAA, University of Huddersfield, Huddersfield, UK

Abstract

Currently there is an increasing interest in dielectric wall accelerators. These work by slowing the speed of an EM wave to match the velocity of a particle beam, allowing wave-beam interactions, accelerating the beam. However conventional dielectric materials have limited interaction regions, so wave-beam energy transfer is minimal.

In this paper we consider Artificial Materials (AMs), as slow wave structures, in the presence of charged particle beams to engineer Inverse-Cherenkov acceleration. AMs are periodic constructs whose properties depend on their sub-wavelength geometry rather than their material composition, and can be engineered to give an arbitrary dispersion relation. We show that Metamaterials, one example of an AM, can mediate an Inverse-Cherenkov interaction, but break down in high power environments due to high absorption. We consider AMs with low constitutive parameters and show they can exhibit low absorption whilst maintaining the ability to have a user defined dispersion relation, and mediate a wave-beam interaction leading to Inverse-Cherenkov acceleration.

INTRODUCTION

Artificial Materials (AMs) are periodic structures whose characteristic properties are determined by their sub-wavelength unit-cell structure rather than their material composition. This results in the material appearing homogeneous over certain wavelengths (adhering to the effective medium condition) allowing the use of the abstract bulk properties of permittivity (ϵ) and permeability (μ), defined from the constitutive relations,

$$\mathbf{D} = \epsilon\mathbf{E} \tag{1}$$

$$\mathbf{B} = \mu\mathbf{H} \tag{2}$$

where **D** and **B** represent the electric and magnetic flux densities, and **E** and **H** represent the electric and magnetic fields.

By manipulating the specific geometry of the unit-cells we can engineer the dispersion relation of the material to exhibit novel electromagnetic properties, such as engineering an arbitrary phase shift of an incident EM wave.

By inserting AMs into slow wave structures such as Folded Waveguide Travelling Wave Tubes (FWTWTs), (see Fig. 1), the AM can be optimised to maximise regions of energy transfer between a charged particle beam and an incident EM wave.

This is achieved by matching the velocity of the wave at the interaction points to the speed of the charged particle beam, called the synchronicity condition. When this occurs

* aimee.hopper@hud.ac.uk

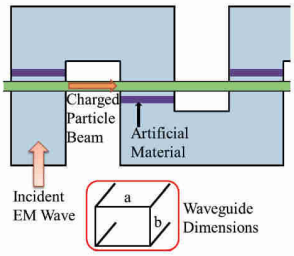

Figure 1: A Folded Waveguide Traveling Wave Tube loaded with the Artificial Material. The incident wave enters from the bottom of the waveguide and travels along the serpentine structure, whereas the charged particle beam passes through the centre of the structure.

energy can transfer between the wave and beam, with the power transferred determined from Madey's Theorem [1] as

$$\Delta P = \frac{\omega^2\mu}{\beta_0}\frac{L^3}{2ab}Z^2\frac{d}{dx}\left(\frac{sin^2(X)}{X^2}\right)\frac{c}{\gamma^3}\frac{1}{v_e^3}(mc^2 I_b/e) \tag{3}$$

where

$Z = \frac{e}{mc^2}\frac{b}{p}sinc(\beta_n'\frac{b}{2})$,

$\gamma = 1 + V_{acc}/m_0c^2$,

$X = \left(\frac{\omega}{v_e} - \beta_n'\right)\frac{L}{2}$.

β_0 is the TE_{01} rectangular waveguide propagation constant, v_e is the velocity of the charged particle beam, I_b is the beam current, m is the mass of the particle, β_n' is the loaded propagation constant and V_{acc} is the acceleration voltage of the beam.

A plot of Eq. 3 with varying V_{acc} of an electron beam can be seen in Fig. 2, where positive power gain shows where the device will operate as a wave amplifier, and negative power gain shows where energy will be imparted into the beam, achieving Inverse-Cherenkov acceleration.

Unfortunately there are limitations with using the existing AM designs, as discussed in the next section. We continue on to discuss a new design aimed at reducing these loss issues whilst still enabling interactions between wave and beam, before concluding with some remarks and future aims.

PREVIOUS WORK

Simulations were conducted to determine the thermal characteristics of an existing AM design [2]: a unit-cell consisting of two copper square Split-Ring Resonators (SRRs) on an FR4 PCB backplate with a copper strip-line along the reverse. This AM was simulated when loaded in a waveguide.

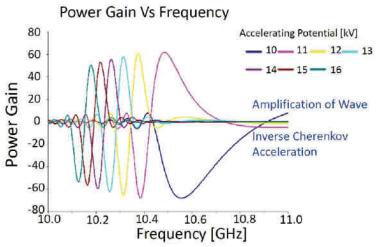

Figure 2: The change in power for the incident wave when interacting with an electron beam, for varying accelerating voltages [1].

Using the simulation packages HFSS and ANSYS [3,4], the time averaged losses inherent to the split rings and dielectric backplate could be determined. These losses are caused by energy being stored in the SRR structure, resulting in heating.

HFSS is a 3D full-wave EM field solver with adaptive meshing, which uses the FEM method to solve wave-structure interactions. The bulk AM was simulated in HFSS to determine the complete loss density map and the results from the EM simulations were imported into ANSYS. Thermal analysis only required the loss density for single unit-cells to determine that cells thermal profile. The metallic losses (P_{lm}) and dielectric losses (P_{ld}) are given by

$$P_{lm} = \sqrt{\frac{\omega\mu_0}{8\sigma}} \int_s |\mathbf{H}_t|^2 ds \tag{4}$$

$$P_{ld} = \frac{Im(\epsilon_r)\omega}{2} \int_V |\mathbf{E}|^2 dV \tag{5}$$

where ω is the angular frequency of the incident wave, μ_0 is the permeability of free space, σ is the conductivity, $\mathbf{H}_t$ is the tangential magnetic field, ϵ_r is the relative permittivity and $\mathbf{E}$ is the electric field [5].

The simulations exposed the AM structure to 1 W of power at 10 GHz, the frequency where the largest μ response is observed, and predicted temperatures exceeding 600 °C (the combustion point of FR4), shown in Fig. 3a.

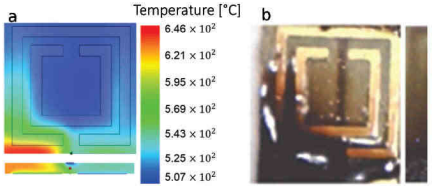

Figure 3: a) Image showing the HFSS/ANSYS predictions for the thermal heating of the unit-cell. b) Experimental results after exposing the fabricated unit-cell to 1W of RF power at 10 GHz [2].

To test the validity of these predictions, the AM was fabricated and exposed to 1 W of RF power at 10 GHz. After 15 seconds the AM began to combust, showing that temperatures exceeding 600 °C had been reached, see Fig. 3b. By comparing the combustion pattern of the experimental unit-cell to the corresponding simulation unit-cell, we can see that the experiment does indeed validate the simulation method used.

By looking at the loss plot, (see Fig. 4), determined by $Loss = 1 - |S_{11}^2| - |S_{21}^2|$, we can see that the operating frequency lies directly on the peak loss (0.3) for this system, caused by energy storage due to resonance. This storage of energy increases until breakdown occurs.

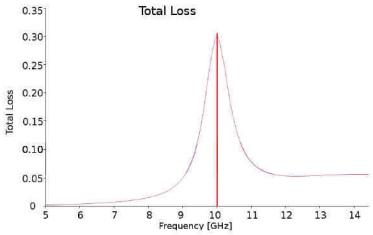

Figure 4: Plot of the total losses for the Artificial Material tested, showing a peak loss of 0.3.

RESULTS

Simulations in HFSS of an optimised geometry were run, and the scattering parameters S_{11} (related to reflection) and S_{21} (related to transmission) were extracted. Figure 5 shows the geometry of the unit-cell, where the EM wave is incident from below the unit-cell.

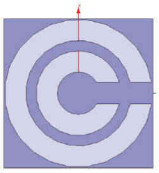

Figure 5: Geometry of the Optimised Unit-Cell.

By using a Nicholson-Ross-Weir based extraction technique [6,7] we can extract the relative ϵ_r and μ_r for the AM. These can be seen in Fig. 6, with ϵ_r values as low as -0.02 (see inset) being predicted.

We can see that the predicted losses in the X-band region are below 0.05 (see Fig. 7), significantly less than the 0.3 observed in the previous case. This suggests that this optimised unit-cell geometry will withstand significantly higher powers than the original design.

Figure 8 shows the dispersion plot (determined using Smith's technique [8]) for this geometry. 20, 25 and 30 keV

ISBN 978-3-95450-147-2

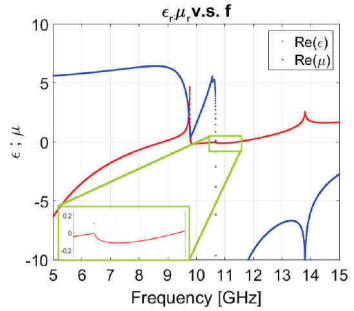

Figure 6: ϵ and μ of the Optimised Unit-Cell, showing low values of ϵ_r are achievable.

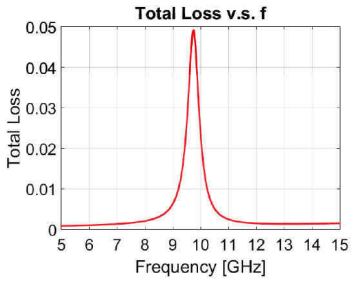

Figure 7: Plot of the losses for the Optimised Unit-Cell, showing losses of less than 0.05 over the investigated frequency range.

electron beam lines are shown, along with the light line. Intersections between the dispersion plot and the beam lines suggest regions where energy transfer between beam and wave can occur. From this plot we observe that forward wave interactions with a 20-30 keV electron beam are possible around 9 GHz, and backward wave interactions are possible around 11GHz, suggesting the possible dual-use of this AM in the X-band region, all occurring with losses of less than 0.05.

CONCLUSIONS

In this paper numerical simulations have shown that Artificial Materials (AMs) provide a route into producing devices with engineerable properties. This enables the user to tailor the dispersion relation to achieve beam-wave interactions, producing desired effects such as Inverse-Cherenkov acceleration. By manipulating the geometry of the constituent unit-cells, the user can optimise energy transfer while keeping losses to a minimum. The material presented here suggests successful high power operation, with the possibility of both forward and backward wave operation.

To establish the feasibility of this design, further simulations characterising the thermal behaviour of this AM need

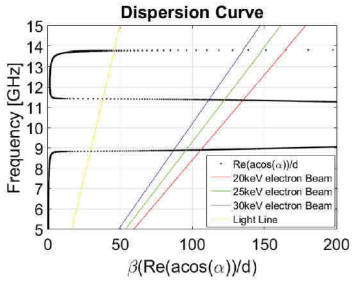

Figure 8: ω-β plot for the Optimised Unit-Cell, showing interactions regions around 9 GHz (forward-wave) and 11 GHz (backward-wave).

to be produced. Particle In Cell (PIC) simulations need to be produced investigating whether the material will successfully interact with the charged particle beam, and ensuring issues like charge build-up are not a problem. Finally, the AM will need to be fabricated and tested in both low and high power environments to ensure it demonstrates successful energy transfer, and successful Inverse-Cherenkov acceleration.

ACKNOWLEDGEMENT

The authors would like to thank the AFOSR and the EPSRC for their financial support for this work.

REFERENCES

[1] Y.S. Tan and R. Seviour, "Wave Energy Amplification in a Metamaterial based Traveling Wave Structure", *EPL* (Europhysics Letters), vol. 87, no. 3, p.34005, 2009.

[2] R.Seviour, Y. S. Tan, and A. Hopper. "Effects of High Power on Microwave Metamaterials" in *Advanced Electromagnetic Materials in Microwaves and Optics (METAMATERIALS), 8th International Congress on*, Copenhagen, Denmark, August 2014, pp. 142-144.

[3] High Frequency Structure Simulator(HFSS), Ansoft Corporation, Pittsburgh, PA.Ver.12.1, 2010.

[4] ANSYS Workbench, ANSYS Inc., Canonsburg, PA.Ver.12.1, 2009.

[5] M. Sabbagh, "Electromagnetic-Thermal Analysis Study Based on HFSS-ANSYS Link", *Electrical Engineering and Computer Science Technical Reports*. Paper 46, 2011.

[6] A. M. Nicolson, and G. F. Ross. "Measurement of the Intrinsic Properties of Materials by Time-Domain Techniques" *Instrumentation and Measurement, IEEE Transactions on*, vol. 19, no. 4 pp. 377-382. 1970.

[7] W. B. Weir, "Automatic Measurement of Complex Dielectric Constant and Permeability at Microwave Frequencies" *Proceedings of the IEEE* vol. 62, no. 1, pp. 33-36. 1974.

[8] D. R. Smith, S. Schultz, P. Markoš, and C. M. Soukoulis. "Determination of Effective Permittivity and Permeability of Metamaterials from Reflection and Transmission Coefficients", *Phys.Rev. B*, vol. 65, no. 19, p. 195104. 2002.

932nd URSI GASS, Montreal, 19-26 August 2017

Metamaterials for MIMO

R. Seviour(1) and A. Hopper(1),
(1) University of Huddersfield, Huddersfield, UK

Abstract

Since their first realization the development of metamaterial based devices and applications has gained an increasing level of interest. These materials offer the opportunity to specifically engineer the materials ability to, control, enhance and suppress EM wave propagation though and near these materials, either in a specific direction or altogether. These materials have been used to construct a range of novel microwave devices such as antennas [1,2], phase-shifters [3], couplers [4], broadband compact power-dividers [5] and other devices such as beam steerers, modulators, band-pass filters and lenses.

More recently researchers have considered the use of metamaterials for MIMO application, either as antenna or parasitic/absorptive elements to control interference. In this paper we present an overview of metamaterials, looking at design, fabrication, and characterization. Focused towards the ability of metamaterials to offer a tailored EM mm-wave response for novel MIMO and 5G applications.

1. Introduction

The ability of engineers to develop new RF technologies is largely limited only by the EM properties of available materials. For over 100 years materials with specific RF properties, such as Polytetraflufoethylene (Teflon) and $Hf0_2$, have been artificial synthesised at the molecular level and used by Engineers, to modify EM wave propagation and interactions in devices. The interaction between EM wave and material is described via the constuitive relations, in a simplistic form are:

$$\begin{aligned} D(k,\omega) &= \varepsilon(k,\omega)E(k,\omega) \\ B(k,\omega) &= \mu(k,\omega)H(k,\omega) \end{aligned} \quad (1)$$

the permittivity (ε) and the permeability (μ) are the averaged EM response functions of the molecules in the material to the electric component (ε) and the magnetic component (μ). These response functions are averaged over all molecules in a volume $\sim\lambda^3$, an approximation that holds well into ultraviolet even for rare gases. Molecular synthesised EM materials have led to the creation of a range of novel RF technologies, although the parameter range these materials can access is limited. To expand this range researchers have developed artificial composite structures with, periodic, sub-wavelength inclusions. These inclusions appear, to the incident RF, identical to giant molecules with a large polarizability. Enabling the EM interaction with these collective inclusions to be described in terms of the "homogenised" abstracted bulk material parameters permittivity and permeability, treating the structure as an "effective media" or an "artificial material".

2. Artificial Materials

Research into artificial materials began in the 1890s, when Rayleigh considered an array of subwavelength small metallic spheres as a continuous medium[6]. The first applications of Artificial materials appeared in 1940s with the pioneering work of Kock who created Artificial Dielectrics from arrays of sub-wavelength metallic structures (spheres, rods, plates) to form Dielectric Lenses[7]. Although all these effective media either had a negative permittivity (permeability) and positive permeability (permittivity), or both permittivity and permeability were positive. The important point is that there are no naturally occurring materials that have a simultaneous negative permittivity and permeability. These double negative materials are referred to as metamaterials, a term first coined by Walser 1999, who defined a metamaterial as "...macroscopic composites having man-made, three-dimensional, periodic cellular architecture designed to produce an optimised combination, not available in nature, of two or more responses to specific excitation". The first systematic theoretical study of metamaterials is attributed to Veselago[8]. His theoretical study showed that for a monochromatic uniform plane wave in such a medium the direction of the Poynting vector is antiparallel to the direction of the phase velocity, as well as presenting the possibility of a lens constructed from this material.

2.1 Artificial Atoms

Pendry[9] presented the key sub-wavelength elements that could be used to construct the unit-cells (artificial atoms) of a metamaterial. The Split Ring Resonator (SRR) remains the meta-atom of choice for researchers, where the basic geometry remains the same as that originally proposed by Schelkunoff in 1950. Figure 1 (a) shows the double SRR designed by Pendry[9]. For a system of SRRs to be considered an "artificial materials" each unit-cell (individual SRR) must be less than $\lambda/10$ in size, and have at least enough unit-cells to hold one wavelength. These

size constraints ensure we meet the homogeneity condition necessary to treat our system as an effective media.

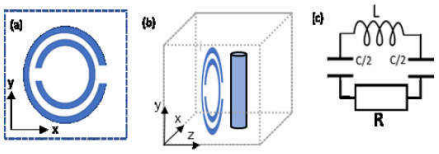

Figure 1. (a) double SRR geometry building block, and an array of SRRs. (b) combined SRR with wire array. (c) the equivalent circuit diagram from the SRR shown in (a).

Starting with just a "single ring" of the form shown in figure 1, without the "split" in the ring the interaction would be purely inductive (non-resonant), resulting in a weakly diamagnetic system (permeability< 1). The "split" prevents the current circulating, causing charge to collect (a capacitance), forming an equivalent LCR resonant circuit, shown in figure 1(c). The behaviour of this system is dominated by the resonance from the outer SRR, where the inner SRR offers greater control over the meta-atom parameters. As the EM field induced by the outer, dominate, SRR in the inner SRR opposes the inducing field. Suppressing the electric dipole moment, allowing the magnetic comment to dominate creating by design permeabilites >> 1.

The inductance is relatively easy to determine as $L \approx 2\mu_0 r$, whereas the capacitance is complicated by the additional capacitive effects from the gap that separates the two SRRs. Although the capacitance of the split rings can be approximated by $C \approx \pi\varepsilon_0 rt/2d$, t is the combined width of the rings and d the separation between the rings. From this we estimate the resonant frequency of the meta-atom as $\omega_0 = (1/(L+R/j\omega_0)C)^{1/2}$. From which we can determine the effective permeability of a material formed from a lattice of these individual sub-wavelength SRRs [10]:

$$\mu_{eff}(\omega) = 1 + \frac{\pi^2 r^4 \mu_0}{V\left(\omega_0^2/\omega^2 - 1\right)L} \qquad (2)$$

Where V is the unitcell volume for our individual meta-atom. The second element of our meta-atom, used to control the effective permittivity in the unit cell is a simple wire, shown combined with the SRR in figure 1(b). The effective permittivity of the wire is given by $\varepsilon_{eff} = 1 - \omega_p^2/\omega^2$, where ω_p is the plasma frequency of electrons in the wire. If we assume a lossless wire, then the wire array can be modelled as an array of inductors, with inductance L. In this case the effective permittivity becomes;

$$\varepsilon_{eff}(\omega) = 1 - \frac{1}{d^2\omega^2\varepsilon_0 L} \qquad (3)$$

This approach does not take into account electric coupling or the bianisotropic nature of the material. Although it does enable us, at least to 1st order, to gain useful insights into how changes in geometry will change the effective permeability of our artificial material, i.e. $\omega_0/\omega < 1$ results in a negative permeability. This approach enables us to establish the broad dimensions of a geometry that will produce a response at the appropriate frequency required.

3. Parameter Determination

In this section we determine the effective permittivity and permeability from measurements of the scattering parameters (S-parameters). The approach used is a variant of the Nicolson-Ross-Weir NRW approached adapted by Smith [11] to account for possible negative responses in the real components of the permittivity and permeability. The NRW uses a closed form expression allowing the complex form of the permittivity and permeability to be determined directly from S-parameter measurements. In addition the NRW technique is relatively robust to experimental error. Assuming the material is a free-standing slab (thickness d) surrounded by a vacuum, with normal incident plane waves, then the S-parameters S21 and S11 are given by;

$$S_{21} = \left[\cos(nkd) - \frac{i}{2}\left(Z + \frac{1}{Z}\right)\sin(nkd)\right]^{-1}$$
$$S_{11} = -\frac{i}{2}\left(Z + \frac{1}{Z}\right)\sin(nkd)\,.\,S_{21} \qquad (4)$$

$k = 2\pi/\lambda_0$ is the free space wave vector, $Z = Z' + iZ''$ the impedance of the material, and $n = n' + n''$ the refractive index. Inverting these equations we find,

$$Z = \pm\left[\frac{(1+S_{11})^2 - S_{21}^2}{(1-S_{11})^2 - S_{21}^2}\right]^{1/2} \qquad (5)$$

$$n' = \pm\frac{1}{kd}\Re\left[cos^{-1}\left(\frac{1 - S_{11}^2 + S_{21}^2}{2S_{11}^2}\right)\right] + \frac{2\pi m}{kd}$$
$$n'' = \pm\frac{1}{kd}\Im\left[cos^{-1}\left(\frac{1 - S_{11}^2 + S_{21}^2}{2S_{11}^2}\right)\right] \qquad (6)$$

Where the permittivity and permeability can be found directly, $\varepsilon_{eff} = n/Z$ and $\mu_{eff} = nZ$. The complication of course is in choosing the root and branch of the above equations. For a passive media the imaginary components of ε_{eff}, μ_{eff}, n and the real component Z must be positive (except at points of anti-resonances). The inverse cosine introduces some ambiguity into the imaginary component of n. To constrain the solution we ensure that n' is continuous across the frequency range.

4. Metamaterial Sheet

To investigate wave transport we model an infinite sheet of metamaterial using HFSS, the commercial finite element method solver for electromagnetic structures from Ansys. This is achieved by modelling the unit cell geometry shown in figure 2, using Bloch-Floquet boundary conditions to create the infinite sheet. To demonstrate the bi-isotropic behaviour of SRR based materials we consider wave

propagation in two planes relative to the unit cell geometry, perpendicular figure 2(a) and parallel figure 2(b). The unit cell consists of a double Cu square SRR on an FR4 substrate with Cu wire strip on the back. Total unit cell size 3mm, the Cu track of the SRR has a 200μm width and is 2mm long.

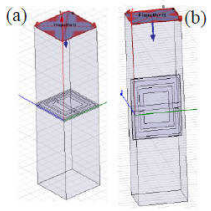

Figure 2. Meta-atom unit cell, wave propagation from the top (blue arrow) to the bottom Bloch-Floquet boundary conditions on all other sides. (a) propagation perpendicular to SRR. (b) propagation parallel to SRR.

The simulation was conducted in the frequency domain to determine the S-parameters both parallel and perpendicular to the structure. Using equations 5 and 6 to calculate the permittivity and permeability, shown in figures 3(a) and (b), for perpendicular and parallel wave propagation respectively. Figures 3(c) and (d) show the Absorption coefficient determined from the refractive index.

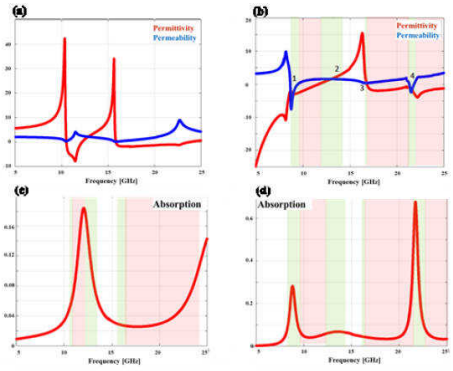

Figure 3. Permittivity and permeability (a) and (b), for perpendicular and parallel wave propagation respectively. (c) and (d) the Absorption coefficient.

From figure 3 we see the bi-isotropic nature of the metamaterial configuration, where regions of positive/negative permittivity and permeability are dependent on both direction of propagation and frequency. Likewise the Absorption shows a marked difference depending on direction, for example at 9 GHz the Absorption coefficient is 0.03 for perpendicular transport, whereas for parallel transport the Absorption coefficient is 0.5. More interesting information can be gleamed from the dispersion relation for the material, which of course also displays the direction/frequency dependence, shown in figure 4. The dispersion behaviour has many interesting features, extreme slow wave velocity and negative dispersion. Note the cusps in figure 4 relate to high dispersive regions, the group velocity $V_g \approx \partial\omega/\partial k$ only holds true for non-dispersive media. A key aspect from figure 4 for different directions of propagation we notice band gaps where for specific frequencies wave propagation is not possible.

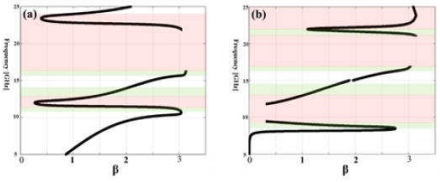

Figure 4. Dispersion relation for (a) perpendicular and (b) parallel wave propagation.

5. MIMO

A major advantage of using mm-waves around 60 GHz is the Gigabit data rates that can be achieved. This is a prime driver in creating a growing interest in MIMO research at this frequency. Although working at 60 GHz presents major challenges, in particular for MIMO systems where compactness and low-weight are a necessary feature in antenna design. This situation is exacerbated by the very short wavelengths (~5mm) at 60 GHz, which gives rise to several issues around the design and fabrication of the multiple antenna elements in MIMO arrays. As the antenna elements are generally placed between λ/8 - λ/2 apart, at this frequency mutual coupling between antenna elements is a common problem in antenna. Where reducing this electromagnetic coupling between antenna elements is a challenging design task, and an active area of research.

Research into the suppression of mutual coupling between antennas has being an area of active research for around 40 years. For example, in [12] the use of a lossless network between input and the antenna ports is used, where the mutual coupling antenna impedance is purely reactive at resonance to isolate antennas from each other. Or using transmission lines as antenna decouplers [13,14]. Other approaches have used resonant defects and slits in the ground plane to confine resonate states [15,16,17]. As well as metamaterial and EM band-gap approaches [18].

All the above approaches focused on mutual coupling suppression at 3GHz and below, including the metamaterials approach (1-1.6 GHz). Attempting to scale these approaches to higher frequencies, especially 60GHz introduces its own issues. Although a correctly designed optimised metamaterial substrates for MIMO antennas can

be used to control and mitigate the mutual coupling that arises between individual antenna elements even at 60 GHz and above. As we have discussed metamaterials can be engineered with very specific properties, both frequency and direction of propagation specific. For example, we can use metamaterial constructs as a substrate for MIMO antennas designed to operate parasitically at the points of coupling, designed with spatially, directional, localised frequency band-gaps. We can even take the approaches used previously and design materials to implement these approaches at 60 GHz. For example using the type of structure presented in section 5, scaled to 60 GHz, orientated correctly EM should lead to a suppression of EM interaction across the material with an Absorption coefficient of 0.8, inside a band-gap, in the plane between antenna elements, whilst perpendicular to the antenna elements the Absorption coefficient is ~0.03.

Fabrication at these frequencies can also be an issue, as to ensure homogeneity, so that our system can be treated as a material, each unit-cell must be less than $\lambda/10$. Hence at 60 GHz we need our unit-cell to be smaller than 500μm, with features around 50μm. Fabrication of structures with this feature size can be fabricated with conventional lithographic processes. Currently these lithographic processes are restricted to the fabrication of 2-dimensional objects. This does place a certain level of restriction on the range of structures that can be fabricated.

6. References

1. C. Caloz, T. Itoh, Microwave Symposium Digest, IEEE MTT-S International Microwave Symposium, vol. 1, June 2003, pp. 195-198.

2. F. Qureshi, M. Antoniades, G.V. Eleftheriades, IEEE Antenna Wireless Propagation Lett. 4 (2005) p. 333-336.

3. M. Antoniades, G.V. Eleftheriades, IEEE Antennas Wireless Propagation Lett. 2 (7) (2003) p. 103-106.

4. C. Caloz, A. Sanada, T. Itoh, IEEE Trans. Microwave Theory Techniques 52 (3) (2004) p. 980-992.

5. M. Antoniades, G.V. Eleftheriades, IEEE Microwave Guided Wave Lett. 15 (11) (2005) p. 808-810.

6. Rayleigh (1892) *Phil. Mag*, **5** (34), 481.

7. Kock, W.E. (1948) *Bell System Technical J*, **27**, 58.

8. Veselago, V.G. (1967) *Usp. Fiz. Nauk*, **92**, 517–526.

9. Pendry J.B., Holden A.J., D.R. and Stewart, W. (1999). *IEEE Trans Microw Theory Tech*, **47**, 2075–2084.

10. Marques R., F.M. and Rafii-El-Idrissi, R. (2002). *Phys Rev B*, **65** (144440).

11. D. R. Smith, D. C. Vier, T.K. and Soukoulis, C.M. (2005). *Phys. Rev. E*, **71** (036617).

12. J. Andersen and H. Rasmussen, IEEE Trans. Antennas Propag., vol. 24, no. 6, pp. 841–846, Nov. 1976.

13. S.-C. Chen, Y.-S. Wang, and S.-J. Chung, IEEE Trans. Antennas Propag., vol. 56, no. 12, pp. 3650–3658, Dec. 2008.

14. S. Dossche, S. Blanch, and J. Romeu, Proc. IEEE/ACES Int. Conf. on Wireless Communications and Applied Computational Electromagnetics, Apr. 2005, pp. 849–852.

15. C. Volmer, J. Weber, R. Stephan, K. Blau, and M. Hein, IEEE Trans. Antennas Propag., vol. 56, no. 2, pp. 360–370, Feb. 2008.

16. P. J. Ferrer, J. M. Gonzalez-Arbesu, and J. Romeu, Microw. Opt. Tech. Letts., vol. 50, no. 5, pp. 1414–1417, May 2008.

17. M. M. Bait-Suwailam, M. S. Boybay, and O. M. Ramahi, Proc. 13th Int. Symp. on Antenna Technology and Applied Electromagnetics (ANTEM/URSI), Feb. 2009, pp. 1–4.

18. D. Sievenpiper, L. Zhang, R. Broas, N. Alexopolous, and E. Yablonovitch, IEEE Trans. Microw. Theory Tech., vol. 47, no. 11, pp. 2059–2074, Nov. 1999.

19. M. Bait-Suwailam, IEEE TRANS. Antennas and Propagation, 58, 9, 2010